Study of the Structural Properties and Control of Degradation Rate for Biodegradable Metallic Stents using Cold Spray

Rajib Barua

Department of Mechanical Engineering
Faculty of Engineering
McGill University
Montreal

July 2015

A thesis submitted to McGill University in partial fulfillment of the requirements of the degree of Doctor of Philosophy

To my family

Table of Contents

Table of Contents iii
List of Figures v
List of Tables viii
List of Abbreviations ix
Glossary xi
Abstract xiii
Abrégé xv
Chapter 1. Introduction 1
  1.1 Background 1
    1.1.1 Coronary Artery Disease and its Current Treatments 1
    1.1.2 Stents: Innovation, Developments and Limitations 2
    1.1.3 Biodegradable Stent 3
      1.1.3.1 Bio-absorbable Stent 4
      1.1.3.2 Bio-corrodible Stent 5
    1.1.4 Cold Spray as a Technique for Manufacturing Degradable Stents 10
      1.1.4.1 Process Overview 10
      1.1.4.2 Bonding Mechanism on Cold Spray 11
      1.1.4.3 Cold Sprayability 12
      1.1.4.4 Cold Spray as a Manufacturing Technique for Stent Material 15
      1.1.4.5 Microgalvanic Corrosion Effect: A Concept for Fabricating Degradable Stent 16
      1.1.4.6 Mixed Powders: Cold Spraying and Corrosion 18
  1.2 Research Objectives 19
    1.2.1 Specific Aim 1: 19
    1.2.2 Specific Aim 2: 19
    1.2.3 Specific Aim 3: 19
  1.3 Organization of the Thesis 20
Chapter 2. Cold Sprayability of Mixed Coatings 21
  2.1 Introduction 21
  2.2 Materials and Methods 22
    2.2.1 Feedstock Powders 22
    2.2.2 Cold Spray Parameters and Process Overview 24
    2.2.3 Coating Characterizations 26
  2.3 Results and Discussions 27
    2.3.1 Characterization of Feedstock Powders 27
      2.3.1.1 Composition 27
      2.3.1.2 Size Distribution 27
      2.3.1.3 Microstructure 30
      2.3.1.4 Microhardness 33
      2.3.1.5 Phase Identification 34
    2.3.2 Outcome of Cold Spray Process 36
      2.3.2.1 Deposition Efficiencies for Different Mixed Conditions 36
      2.3.2.2 Particle Impact Velocity Calculation 39
    2.3.3 Coating Characterization 43
      2.3.3.1 Coating Composition 43
      2.3.3.2 Porosity and Microstructure of as-Sprayed Coatings 47
      2.3.3.3 Microhardness of as-Sprayed Coatings and Powders 49
      2.3.3.4 Phase Observations of as-Sprayed Coatings 50
  2.4 Conclusions 52
Chapter 3. Structural Properties Cold Sprayed Materials 53
  3.1 Introduction 53

3.2 Materials and Methods 53
  3.2.1 Micro-shear Punch Test 54
  3.2.2 Tensile Test 55
3.3 Results and Discussions 58
  3.3.1 Changes of Porosity with Heat Treatment 58
  3.3.2 Changes of Microhardness with Heat Treatment 63
  3.3.3 Micro Shear Punch Testing of Coatings 65
  3.3.4 Tensile Testing of the Heat Treated Coatings 74
3.4 Conclusions 80
Chapter 4. Corrosion Investigation 82
4.1 Introduction 82
4.2 Materials and Methods 83
  4.2.1 Corrosion Rate Measurement by Static Immersion Test 84
  4.2.2 Corrosion Rate Measurement by Polarization Test 85
  4.2.3 Corrosion Rate Measurement by Galvanic Corrosion Test 87
  4.2.4 Characterization of Degraded Products 90
4.3 Results and Discussion 90
  4.3.1 Static Immersion Test 90
  4.3.2 Polarization Test 97
  4.3.3 Galvanic Corrosion Test 104
  4.3.4 Characterization of the Degraded Products 107
4.4 Empirical Equation for Corrosion Rate Estimation of Mixed Coatings 118
4.5 Corrosion Mechanism 120
4.6 Conclusion 121
Chapter 5. Stent Fabrication and Future Work 123
5.1 Introduction 123
5.2 Experimental Details 123
5.3 Manufacturing Process of Stents 126
5.4 Recommendations for the Future Plan 130
Chapter 6. Discussion 132
6.1 Difficulties 133
6.2 Challenges 133
6.3 Limitations 134
6.4 Future work 135
Chapter 7. Conclusions 137
References 141
Appendix A 149
Appendix B 150
Appendix C 152
Appendix D 154
Appendix E 156

List of Figures

Figure 1.1: Biotronik coronary stent (a) non-expanded and (b) expanded, adapted with permission from reference [35] and [36], respectively 6
Figure 1.2: (a) Implanted iron stent and (b) X-Ray photomicrograph of iron stent from Biotronik, Inc., adapted with permission from references [41] and [40], respectively 8
Figure 1.3: Schematic diagram of cold spray process 10
Figure 1.4: Deposition process (a) shear loading and (b) jetting, adapted with permission from [53] 12
Figure 1.5: (a) Schematic diagram showing the relation between deposition efficiency and particle velocity and (b) schematic diagram of the window of deposition, modified from [58] and [59], respectively 14
Figure 1.6: Schematic diagram of particle and critical impact velocities as a function of particle size, modified from [53] 14
Figure 1.7: Galvanic series in seawater flowing at 2.4-4 m/s for 5-15 days at 15-30^{0}C, reproduced from ASTM G82-98, modified from [65] 17
Figure 2.1: Cold spray process to fabricate mixed coatings; powder mixing either (a) rolling mixture or (b) rotating tumbler, (c) KINETICS 4000 cold spray system (d) as-sprayed coating with cutting directions shown with arrows, (d) EDM cut coating strip with substrate and (e) coating without substrate cut with diamond cutter 24
Figure 2.2: Particle size distribution of 316L powders of (a) lot 1, (b) lot 2 and (c) lot 3 28
Figure 2.3: Particle size distribution of CP Fe powders of (a) lot 1, (b) lot 2 and (c) lot 3 29
Figure 2.4: SEM of powders (a) 316L lot 1, (b) CP Fe lot 1, (c) 316L lot 2, (d) CP Fe lot 2, (e) 316L lot 3 and (f) CP Fe lot 3 31
Figure 2.5: Optical microscopy images of polished and etched powders: (a) 316L lot 1, (b) 316L lot 2 (c) 316L lot 3, (d) CP Fe lot 1, (e) CP Fe lot 2 and (f) CP Fe lot 3 32
Figure 2.6: SEM of 80wt%CP Fe mixed powders at (a) low and (b) high magnification 33
Figure 2.7: Average microhardness of CP Fe and 316L powders of all lots 34
Figure 2.8: XRD pattern of feedstock powders (a) lot 1 and (b) lot 2 and lot 3 35
Figure 2.9: Theoretical and experimental deposition efficiency of coatings with increasing wt% of CP Fe 37
Figure 2.10: Comparison of the particle velocities of mixed powders when changing the gas inlet temperatures from (a) 700^{0}C to (b) 800^{0}C at 4 MPa 40
Figure 2.11: Comparison of particle velocities of (a) 40wt%Fe and (b) 90wt%Fe mixed powders with changing pressure at 800^{0}C gas temperature 41
Figure 2.12: Best fit curves of particle velocity as a function of wt% of Fe for (a) 4 MPa, 700°C and (b) 4 MPa, 800°C spray condition 42
Figure 2.13: Comparison of expected and experimental chemical composition of (a) iron, (b) chromium and (c) nickel 46
Figure 2.14: Cross-sections of as-sprayed coatings (a) 316L, (b) CP Fe, (c) 20wt%Fe, (d) 50wt%Fe, (e) 80wt%Fe and (f) 80wt%Fe lot 3 48
Figure 2.15: Average porosity of as-sprayed coatings 49
Figure 2.16: Average micro-hardness ($HV_{0.05}$) of as-sprayed coatings 50
Figure 2.17: XRD of as-sprayed coatings showing the peaks for identified phases 51
Figure 3.1: Shear punch tests (a) MTS machine and (b) test procedure center 55
Figure 3.2: Schematic of ASTM E8 specified tensile coupons (dimensions are shown in millimeters) 56
Figure 3.3: Processing of the tensile coupons (a) argon atmosphere furnace (b) air cooling after heat treatment (c) Grinding and (d) tensile coupons 57
Figure 3.4: (a) MTS tensile testing machines (b) tensile test procedure 57
Figure 3.5: Change of porosity with heat treatment 59
Figure 3.6: Average with standard deviations of porosities of pure coatings 59
Figure 3.7: Optical microstructure of 316L at (a) 400°C, (b) 800°C, (c) 1000°C, (d) 1100°C and CP Fe at (e) 400°C, (f) 800°C, (g) 1000°C and 1100°C 60
Figure 3.8: Average with standard deviations of porosities of mixed coatings 61

Figure 3.9: Optical microstructure of 20wt%Fe at (a) 400°C, (b) 800°C, (c) 1000°C, (d) 1100°C and 50wt%Fe at (e) 400°C, (f) 800°C, (g) 1000°C and (h) 1100°C 62
Figure 3.10: Optical microstructure of 80wt%Fe at (a)400°C, (b)800°C, (c) 1000°C, 80wt%Fe lot 3 at (e) 400°C, (f)800°C, (g) 1100°C and (h) 20wt%Fe lot 3 at 1100°C 63
Figure 3.11: Average micro-hardness of as-sprayed and heat treated coatings for CP Fe and 316L 64
Figure 3.12: Force vs. displacement curves of shear punch test for 316L at different annealing temperature 66
Figure 3.13: Force vs. displacement curves of shear punch test for 20wt%Fe at different annealing temperature 66
Figure 3.14: Force vs. displacement curves of shear punch test for 50wt%Fe at different annealing temperature 67
Figure 3.15: Force vs. displacement curves of shear punch test for 80wt%Fe at different annealing temperature 67
Figure 3.16: Force vs. displacement curves of shear punch test for CP Fe at different annealing temperature 68
Figure 3.17: Shear strength vs. % area in reduction curve for 316L (all the trials are generated with triplicates) 70
Figure 3.18: Shear strength vs. % area in reduction curve for 20wt%Fe (all the trials are generated with triplicates) 70
Figure 3.19: Shear strength vs. % area in reduction curve for 50wt%Fe (all the trials are generated with triplicates) 71
Figure 3.20: Shear strength vs. % area in reduction curve for 80wt%Fe (all the trials are generated with triplicates) 71
Figure 3.21: Shear strength vs. % reduction in area curve for CP Fe (all the trials are generated with triplicates) 72
Figure 3.22: SEM images of the shear punch test fractured microstructure for CP Fe at ×4000 magnification factor 73
Figure 3.23: SEM images of the Shear punch test microstructure for 80wt%Fe at ×4200 magnification factor 73
Figure 3.24: Mean shear strength vs. % R.A. curve for 20wt%Fe lot 3 at 1100°C shear punch test 74
Figure 3.25: Mean tensile stress vs. strain curve for 20wt%Fe lot 3 tensile coupons annealed at 1100°C (all the trials are generated with triplicates) 75
Figure 3.26: Mean shear strength vs. % R.A. curve for 80wt%Fe lot 3 at 1100°C shear punch test (all the trials are generated with triplicates) 75
Figure 3.27: Mean tensile stress vs. strain curve for 80wt%Fe lot 3 tensile coupons annealed at 1100°C (all the trials are generated with triplicates) 76
Figure 3.28: Fractured microstructure of 80wt%Fe at (a) ×100 and (b) ×5000 magnification factor 77
Figure 3.29: Fractured microstructure of 20wt%Fe at (a) ×100 and (b) ×5000 magnification factor 78
Figure 4.1: Pourbaix diagram of Fe in body fluid analogue, reproduced from [91] 82
Figure 4.2: Set-up for the laboratory immersion test 84
Figure 4.3: Set-up for the potentiodynamic polarization test 85
Figure 4.4: Schematic illustration of mixed potential theory 89
Figure 4.5: Rate of mass loss of as-sprayed coatings obtained with immersion test 90
Figure 4.6: Corrosion rate of as-sprayed coatings obtained with immersion test 91
Figure 4.7: Effect of microgalvanic corrosion on the as-sprayed coatings 93
Figure 4.8: pH values of testing solutions with immersion time 94
Figure 4.9: Rate of mass loss of heat treated coatings found from immersion test 95
Figure 4.10: Corrosion rate of heat treated coatings found from immersion test 96
Figure 4.11: Effect of microgalvanic corrosion on annealed coatings 97
Figure 4.12: Open circuit potential test of as-sprayed coatings 98
Figure 4.13: Polarization curves of as-sprayed coatings 99
Figure 4.14: Comparison of corrosion rate (in mmpy) from immersion and polarization tests of as-sprayed coatings 100
Figure 4.15: Open circuit potential tests of heat treated coatings 101
Figure 4.16: Polarization curves of heat treated coatings 102

Figure 4.17: Comparison of corrosion rates from immersion and polarization tests of annealed coatings .103
Figure 4.18: Current vs. time from galvanic corrosion tests of as-sprayed coatings 104
Figure 4.19: Current vs. time from galvanic corrosion tests of heat treated coatings 105
Figure 4.20: Average rates of mass loss for the mixed coatings from galvanic corrosion coupled with 316L (1:1 area ratio) 106
Figure 4.21: Average galvanic corrosion rates for the mixed coatings coupled with 316L (1:1 area ratio) 106
Figure 4.22: Characterization of the corrosion products with XRD 107
Figure 4.23: SEM image of 20wt%Fe after galvanic corrosion showing initiation of pitting (red circle) and initiation of corrosion from the cracked (blue circle) portion of the surface 109
Figure 4.24: Energy dispersive spectral analysis on corroded 20wt%Fe coating.......................................110
Figure 4.25: EDS elemental mappings of (a) C, (b) O, (c) Na, (d) Si, (e) P and (f) Cl on 20Fe after corrosion test 111
Figure 4.26: EDS elemental mappings of (a) K, (b) Cr, (c) Mn, (d) Fe, (e) Ni and (f) Mo on 20Fe after corrosion test 112
Figure 4.27: SEM image of degraded 80wt%Fe showing network of pits throughout the surface 113
Figure 4.28: Energy dispersive spectral analysis on corroded 80wt%Fe surface 114
Figure 4.29: EDS elemental mappings of (a) C, (b) O, (c) Na, (d) Si, (e) P and (f) Cl on 80wt%Fe after corrosion test 115
Figure 4.30: EDS elemental mappings of (a) K, (b) Cr, (c) Mn, (d) Fe, (e) Ni and (f) Mo on 80wt%Fe after corrosion test 116
Figure 4.31: 80wt%Fe coating after 5 week immersion test showing disintegration of the surface from large pits 117
Figure 4.32: Polynomial fit for annealed immersion corrosion tests showing average corrosion rate 118
Figure 4.33: Polynomial fit for annealed polarization corrosion tests showing average corrosion rate 119
Figure 4.34: An exponential fit for immersion corrosion tests showing the average corrosion rate 120
Figure 5.1: Cold spray with rods showing (a) jaw with a motor (b) mandrel and (c) spray gun 124
Figure 5.2: 80wt%Fe mixed powders deposited on a rod substrate showing (a) coating deposited on the substrate and (b) substrate 126
Figure 5.3: (a) Heat treatment effort of coatings with rod and (b) stent minitubes prepared after femto laser cutting...128
Figure 5.4: (a) Minitubes after EDM and (b) laser cut stents 129
Figure 5.5: Flow chart for stent fabrication 130
Figure 5.6: Laser cut stent after electro-polishing from 80wt%Fe mixed coating with a stent thickness of about 150 μm...131

List of Tables

Table 1.1: Mechanical and corrosion properties of currently investigated permanent and degradable materials, reproduced from [30, 60] 15
Table 2.1: Spray conditions used to fabricate coatings using KINETICS 4000 cold spray system....25
Table 2.2: Spray conditions used for the velocity measurement using Plasma Giken (PCS-800) spray system....25
Table 2.3: Composition of 316L and CP Fe powders (in weight %)....27
Table 2.4: Particle size distribution of different lot powders....30
Table 2.5: Percentages of phases in 316L and CP Fe powders 36
Table 2.6: Deposition efficiency (DE) calculation of coatings with lot 1 powders....37
Table 2.7: Deposition efficiency (DE) calculation of coatings with lot 3 powders....38
Table 2.8: Chemical composition of lot 1 coatings found from ICP-OES (in wt %) 44
Table 2.9: CP Fe (wt %) on mixed coatings....47
Table 2.10: Phase percentage of ferrite and austenite on as-sprayed coatings 51
Table 3.1: Regression factor calculation from tensile and shear punch test of lot 3 coatings 79
Table 3.2: Estimation of tensile strengths (MPa) of annealed coatings of lot 1 79
Table 4.1: Composition of Hank's physiological solution, reproduced from Appendix E 83
Table 4.2: Corrosion rates obtained from immersion testing (in mmpy) for as-sprayed coatings....91
Table 4.3: Corrosion rate found from immersion test (in mmpy) for annealed coatings....95
Table 4.4: Polarization criteria of as-sprayed coatings....100
Table 4.5: Polarization criteria of heat treated samples....103
Table 4.6: Corrosion compounds identified with XRD....108
Table 4.7: Empirical constants for the quadratic model 119
Table 5.1: Parameters used for rod coatings....125

List of Abbreviations

M	Molar mass (g/mol)
ρ	Density (g/cm^3)
F	Faraday's constant
mpy	Mils (1/1000 inch) per year
mmpy	Millimeter per year (mm/yr or mmyr^{-1})
i_{couple}	Couple current density (μA/cm^2)
i	Net current density (μA/cm^2)
i_a	Anodic current density (μA/cm^2)
i_c	Cathodic current density (μA/cm^2)
β_c	Cathodic Tafel slope
β_a	Anodic Tafel slope
z	Number of electrons
R	Universal gas constant
T	Temperature (°C)
i_0	Exchange current density (μA/cm^2)
E_0	Equilibrium potential (volt)
η	Overpotential (E-E_0)
K	Constant (8.76×10^{-4})
W	Mass loss (mg)

A	Sample area (cm^2)
CR	Corrosion rate
t	Elapsed time (hour)
EW	Equivalent weight
i_{corr}	Corrosion current density ($\mu A/cm^2$)

Glossary

Acute gain: The immediate change in minimal lumen diameter before and after procedural intervention.

Anastomosis: Surgical connection between two blood vessels.

Aneurysm: Swelling or expansion or dilation of part of a blood vessel or cardiac chamber.

Atherosclerosis: A chronic accumulation of lipids (cholesterol and fatty acid) inside artery walls.

Binary restenosis rate: ≥50% luminal narrowing at follow up.

Catheter: Medical devices that can be inserted in the body to treat diseases or perform a surgical procedure.

Cytokines: Cell signaling molecules that help inter cell communication in immune responses and stimulate cell movement towards inflammation or infection sites.

Dual antiplatelet therapy: The combination of aspirin and second anticlotting medication from thienopyridine analogs: clopidogrel, ticlopidine or prasugrel to reduce the risk of blood clots following stent implantation.

Embolization: The process or condition by which a blood vessel or organ is obstructed by embolus or by other mass. Usually surgical implantation in to circulatory system obstructs specific blood vessel.

Fibrin: A network of white insoluble elastic proteins from fibrinogen which can trap red blood cells and platelets during blood clotting is called fibrin.

Foam cells: Formed when macrophages absorb excessively high amount of cholesterols and fats.

Late loss: The difference between main lumen diameters immediately after stent deployment and at follow up. Positive remodeling equals negative late loss.

Low density lipoprotein: Transport proteins that carry cholesterol it where it needs to go.

Lymphocyte: White blood cell.

Magnetic Resonance Imaging: An imaging modality that uses a magnetic field and radio frequency to detect organs and structures inside the body based on their hydrogen content.

Monocytes and macrophages: Monocytes are a type of white blood cells (leukocytes) produced in the bone marrow.

Myocardial infarction: Necrosis of heart muscle due to lack of blood supply.

Necrosis: Death of cells or tissues through injury or disease.

Nital: A mixture of nitric acid and ethyl alcohol.

Plaque: A fatty deposit inside artery wall.

Restenosis and in-stent restenosis: Stenosis is an abnormal narrowing of a blood vessel. Restenosis is the recurrence of stenosis after a procedure. In-stent restenosis is the recurrent blockage or narrowing of a previously implanted stent.

Revascularization: Restoration of blood flow to the heart.

Extracellular matrix: It is composed of proteins, minerals and certain carbohydrates.

Stent recoil (absolute): Recoil is defined as stent area at post procedure minus stent area at follow up.

Stent: Mesh-like tubular scaffold to hold the artery open and restore blood flow to the heart muscle.

Stent thrombosis: The sudden blockage of coronary artery by a blood clot.

Transferrin: A beta globulin that combines with and transports iron.

Tunica intima: The innermost layer of a blood vessel.

Tunica media: The intermediate layer of blood vessel.

Vasoconstriction: Active narrowing of blood vessels.

Vasodilator: Medications that dilate blood vessels.

Abstract

There is considerable interest in fabricating stents with degradable materials to avoid the disadvantages of permanent stents such as stent fracture. The focus of this thesis is on forming degradable materials consisting of mixtures of two metal powders and determining their rate of galvanic corrosion. To fabricate degradable coatings suitable for producing a stent, the cold gas dynamic spray technique is used to combine the two powders into a single low-porosity layer. Stainless steel (316L SS) and commercial purity iron (CP Fe) powders are mixed together and sprayed onto a metallic substrate in order to produce an amalgamate material. In terms of cold sprayability, spraying the single component 316L powder leads to a higher deposition efficiency (DE) as compared to CP Fe powder (72% vs. 33%), but the porosities remain low (about 1%). It is observed that spraying a mixture of 20wt% CP Fe and 80wt% 316L results in a DE of 43%. Increasing the percentage of CP Fe in the mixture to 50% does not change the DE significantly, although a further increase to 80% results in a DE of 66%. The porosities of the mixed coatings remain low in all cases. These observations may be related to differences in the hardness of the 316L and CP Fe powders. As-sprayed mixed coatings exhibit microhardness values between the range of microhardness of 316L and CP Fe coatings. Also, the effect of mixing does not result in any decrease in the shear strength of as-sprayed coatings as compared to the shear strength of as-sprayed 316L and CP Fe coatings. It is found that annealing the coating relieves work hardening by recrystallization, reduces porosity, and promotes sintering. Shear punch test results indicate that annealed mixed coatings attain shear strengths of that of 316L (455 MPa) with approximately 15% decrease in the reduction in area. Reduction of the work hardening in both 316L and CP Fe particles increases the coating ductility. The 20wt% Fe coatings exhibit 23% ductility, which is sufficient to be used for a degradable stent. Immersion and potentiodynamic polarization tests of the as-sprayed coatings indicate no significant difference in the corrosion rates of 100wt%Fe, 80wt%Fe and 50wt%Fe, which indicates that the corrosion rate of iron is increasing with increasing 316L in the composite material, assuming that iron is the only component which is corroding. This indicates that galvanic corrosion is accelerating the corrosion rate of iron in the mixed coatings. After heat treatment, the corrosion rate generally decreases primarily due to the reduction of pores, which reduces the surface area that is responsible for the higher corrosion rate of the as-sprayed coatings. X-ray diffraction (XRD) tests show that iron oxide forms after degradation. Energy dispersive X-Ray spectroscopy (EDS) also indicates the formation of iron oxides on the mixed coatings which reduces the corrosion rate with time. Considerable pitting is observed on the iron particles after the degradation tests, which indicates that chlorides are pitting the surface of mixed coatings. Overall, the use of the cold spray technique for forming an amalgamate material subject to galvanic corrosion appears to be a potential method for the fabrication of degradable stent. Further clinical investigations are required to validate the performance of such stents.

Abrégé

Il y a actuellement un intérêt considérable pour la fabrication de stents faits à partir de matériaux dégradables afin d'éviter les désavantages des stents permanents tel que la fracture. L'objectif de cette thèse consiste à générer des matériaux dégradables constitués d'un mélange de deux poudres métalliques et déterminer leur taux de corrosion galvanique. Dans le but de fabriquer un revêtement dégradable approprié pour un stent, la technique de projection à froid est utilisée pour combiner les deux poudres en une couche avec faible porosité. Les poudres utilisées sont l'acier inoxydable 316L SS et le fer de pureté commercialle (CP Fe). Celles-ci sont mélangées et pulvérisées sur un substrat métallique. En ce qui concerne la déposition, la poudre 316L produit une meilleure efficacité de dépôts (DE) que le CP Fe (72% contre 33%), mais la porosité des deux reste basse (environ 1%). La déposition d'un mélange comprenant 20% en poids de CP Fe et 80% de 316L produit une DE de 43%. On observe que l'augmentation du pourcentage de CP Fe dans le mélange à 50% ne change pas la DE significativement; cela dit, une augmentation à 80% résulte en une DE de 66%. La porosité des différents mélanges de revêtements reste très faible dans tout les cas. Ces observations peuvent être liées à la différence de dureté entre la poudre de 316L et celle de CP Fe. Les revêtements déposés des mélanges démontrent des valeurs de micro-dureté se situant entre la gamme de micro-dureté du revêtement pulvérisé de 316L et celle du CP Fe. De plus, l'effet du mélange ne résulte en aucune diminution de la résistance de cisaillement des revêtements comparé à la résistance de cisaillement des revêtements de 316L et CP Fe respectivement. On a trouvé que le recuit du revêtement améliore l'écrouissage par recristallisation, réduit la porosité et favorise le frittage. Les résultats des tests de perforation montrent que les revêtements recuits atteignent des résistances au cisaillement comparable à celles du 316L (455 MPa). Une réduction de l'écrouissage des particules de 316L et CP Fe accroit la ductilité du revêtement. Les revêtements contenant 20% en poids de CP Fe démontrent 23% de ductilité, ce qui est suffisant pour l'application à un stent dégradable. Les tests d'immersion et de polarisation potentiodynamique des revêtements indiquent aucune différence significative dans les taux de corrosion pour les

mélanges de 100%, 80% et 50% en poids de CP Fe, ce qui indique que la vitesse de corrosion du fer augmente avec l'augmentation de 316L dans le matériau composite, en supposant que le fer est le seul composant qui corrode. Ceci indique que la corrosion galvanique accélère le vitesse de corrosion du fer dans le revêtement du mélange. Suite au traitement thermique, le taux de corrosion diminue, en général, principalement en raison de la réduction des pores, ce qui réduit la surface de contact qui contribue à la vitesse de corrosion la plus élevée des revêtements. Les tests de diffraction de rayons-X (XRD) démontrent que l’oxyde de fer se forme après la dégradation. La spectroscopie de rayons-X à dispersion d’énergie (EDS) indique également une formation d’oxyde de fer dans les revêtements pulvérisés, ce qui réduit le taux de corrosion. Suite au tests de dégradation, qui permettent d’identifier que le chlore creuse la surface du revêtement, plusieurs creux importants sont observés sur les particules de fer. Dans l'ensemble, l'utilisation de la technique de projection à froid pour former un matériau présentant une corrosion galvanique semble être un procédé prometteur pour la fabrication de stents biodégradables. D'autres essais cliniques sont nécessaires pour valider les performances de ces stents.

Acknowledgement

I wish to express my sincere gratitude to the persons without whom it would not be possible to complete this work. First of all, I want to express my gratitude to my supervisor, Dr. Rosaire Mongrain, for his continued guidance, encouragement, financial support and valuable advice throughout this research work. I would also like to thank Dr. David Frost, co-supervisor, for financial support and for giving him the right balance of flexibility and drive to attain the set goals. Thanks also to Dr. Stephen Yue, for providing his laboratory facilities, invaluable advice and financial support over the years.

I am greatly indebted to my post-docs friends for their help, encouragements, and discussions. My special thanks are to Dr. Huseyin Aydin and Dr. Sriraman Rajagopalan. Dr. Aydin was always available for discussions whenever I needed and kindly had performed so many works from the beginning to ending to this project. Dr. Sriraman introduced me to the corrosion measurement techniques and helped me with the set-ups. Here I list the name of my colleagues who helped me a lot during my stay at McGill: Abu Syed Humayun Kabir, Dr. Sazol Kumar Das, Clodualdo Jr. Aranas, Binhan Sun, Tong Wang, Bikram Konar, Dr. Manas Paliwal and Xingchen Liu.

Finally, I would like to thank my parents for their love and mental support. I am also grateful to my family for their guidance, suggestion, happiness and moral supports.

Above all, I thank to God, Almighty for His love and mercy.

Last but not the least; I thank Dr. Olivier Bertrand, Laval University and Claude Belleville, Opsens Inc. for their financial support on this research.

Statement of Original Contribution

The main contributions from this research can be summarized:

1. Development of the concept of using cold gas dynamic spray to fabricate degradable stent materials.
2. Cold spray has been utilized for the first time to obtain intermixed coatings of 316L and CP Fe powder.
3. Confirmation and assessment of cold sprayability (deposition efficiency, porosity and microhardness) of the 316L/CP Fe mixed coatings.
4. The use of the regression factor to estimate tensile strength from micro shear strength on cold sprayed material.
5. Tensile and micro shear punch testing for 316L/CP Fe intermix coatings.
6. Characterization of corrosion (static immersion and polarization) of the 316L/CP Fe intermixed coatings.
7. Characterization of the galvanic couple of 316L/CP Fe intermixed coatings and 316L.
8. Development of a stent prototyping protocol using the cold spray technique.

Chapter 1. Introduction

1.1 Background

Stents are implanted to reopen a blocked artery. Current stents that range from bare-metal to drug-eluting are permanent. Stent thrombosis and stent fractures are current known limitations associated with permanent stents. The research of this thesis is an effort to develop a degradable stent which employs controlled galvanic corrosion effect. Stents fabricated from a noble and a less noble material exhibit both general and accelerated corrosion. This chapter describes the limitations of permanent stents and recent developments of degradable stents. Further, it presents how the cold spray procedure is used to fabricate a degradable stent.

1.1.1 Coronary Artery Disease and its Current Treatments

Coronary artery disease is responsible for approximately seven million deaths worldwide yearly, which represents approximately 13.3% of all deaths in 2010 [1]. It is mostly caused by atherosclerosis, a chronic development of fibrous materials inside the artery. Atherosclerosis starts by concentrated low-density lipoprotein formation in the bloodstream due to genetics or consumption of foods rich in cholesterol. Monocytes oxidize low-density lipoprotein instead of migrating damaged cells away from any injury site and accumulate lipid-laden macrophages referred to as foam cells. Foam cells form fatty streaks accumulating in the tunica intima and deliver pro-inflammatory cytokines which migrate smooth muscle cells from tunica media to intima. Smooth muscle cells proliferate and accumulate fibrous matrix around foam cells. Smooth muscle cells and foam cells die and form the fibrous cap. Gradual plaque formation narrows the lumen and can cause angina. Weakened fibrous cap may fracture by continuous exposure to cyclic mechanical loading effect which can impede blood flow to the myocardium. This phenomenon is known as myocardial infarction [2].

Coronary artery disease can be treated either by coronary artery by-pass graft surgery or percutaneous coronary intervention. Healthy veins or arteries are grafted or connected usually from the arm (radial artery), leg (saphenous vein) or chest (thoracic artery) to bypass blocked coronary arteries and restore normal blood flow to the myocardium in by-pass surgery. Percutaneous coronary intervention is a catheter based non-surgical treatment to restore blood flow to myocardium using balloon angioplasty or stent placement [2].

1.1.2 Stents: Innovation, Developments and Limitations

Dotter *et al.* reported teflon dilating catheter, stainless steel and spiral nitinol coil implanted in animal arteries from 1964 to early 1980s [3-5]. Gruentzig *et al.* invented balloon angioplasty in 1977 [6]. Here, a small deflated balloon passes from the wrist (radial artery) or groin (femoral artery) through coronary lesion, inflates and compresses the plaque and restores blood flow after deflating and removing the balloon [2]. It is associated with a 40% restenosis rate within the first six months after angioplasty [7]. A stent or metallic mesh-like tubular scaffold is mounted on the balloon. Inflation of the balloon expands the stent and reopens the blocked artery. As the balloon deflates, the stent that has undergone permanent deformation and holds the artery open. Palmaz *et al.* implanted the first stainless steel graft in canine arteries in 1985 [8].

Despite the success of bare metal stent implantation in human coronary arteries in 1986, early stent thrombosis (blockage of vessel by a blood clot) was observed in up to 18% at the treatment site within the first two weeks following angioplasty [9]. The use of dual antiplatelet therapy during and after angioplasty reduces the risk of stent thrombosis to less than 1% [10]. In-stent intimal hyperplasia or thickening of vessel intima can cause stent stenosis during first 3-6 months after stenting in 20-30% of the cases [11]. These rates led to the development of drug eluting stents. The first generation of drug-eluting stent coatings releases anti-proliferative drugs (sirulimus/rapamycin or paclitaxel) from permanent polymers on the vessel surface to control smooth muscle cell proliferation [12].

Although a drug-eluting stent can reduce intimal hyperplasia, it hampers the growth of the endothelium and the metal can induce thrombosis [12]. Bare metal and drug-eluting stents reduce in-stent restenosis rate to 20-25% [13] and 3.2-13.6%, respectively, both stents exhibit a similar rate of stent thrombosis for up to one year [14]. However, the

BASKET-LATE trial reported that the incidence of stent thrombosis in drug-eluting stents is 2.6% compared to 1.3% in bare metal stents between 7-18 months after stent deployment [15]. Sirolimus eluting stents are associated with 6.26% mortality rate compared to 3.91% for bare metal stents. Similarly, paclitaxel eluting stents are associated with 3.28% mortality rate compared to 2.84% for bare metal stents [16].

Stent fracture is another problem observed after stent implantation. Clinical and autopsy studies report approximately 1-2% [17] and 29% [18] incidence, respectively, of stent fracture after stent implantation. About 5% are associated with adverse effects such as inflammation, stent thrombosis and in stent restenosis [19]. The right coronary artery exhibits the highest (56.4%) incidence of stent fracture compared to the 30.4% incidence for the left anterior descending artery possibly due to the cyclic loading of the right coronary artery [20]. Multiple stent fracture with transection and gap in the stent body occurs with the longest duration times after implantation (from 11-1800 days) [18]. Since stent fracture correlates with anatomical location and implantation time, it is associated with a fatigue process. All implanted stents under combined loading conditions (higher curvature, bending and contraction) eventually lead to stent fracture. Materials with higher ultimate strength or biodegradable materials could be potential solutions to solve the stent fracture and thrombosis problem [21]. For example, the second-generation drug-eluting stents introduce a thinner cobalt chromium stent and the third generation drug eluting stents include additional property of being completely biodegradable [22].

1.1.3 Biodegradable Stent

The purpose of a stent is to form a scaffold which restores blood perfusion and allows healing and complete re-endothelialization of the vessel. The presence of a stent thereafter may cause certain complications including in-stent restenosis or late-stent thrombosis. The idea of a biodegradable stent is to provide short-term scaffolding of the vessel and then progressively reabsorb. Biodegradable stents allow the possibility of future surgical intervention such as for repeat revascularization. It eliminates late stent thrombosis, limits the use of antiplatelet therapy [23]. In addition, biodegradable stents are suitable for complex anatomy where permanent stents are difficult to implant and would be vulnerable to fractures [24]. Biodegradable stents are classified as bio-absorbable (mainly polymeric) or bio-corrodible stents. Biodegradable polymers are used to fabricate most of the biodegradable stents to date and they are also called bio-resorbable stents as the degradation products are removed from the body by cellular activity. Bio-corrodible stents, on the other hand, would form water-soluble material under physiological conditions.

1.1.3.1 Bio-absorbable Stent

The first biodegradable Poly-L-Lactide stent was implanted by Stack *et al.* at Duke University in 1988 [25]. However, manufacturing difficulties due to the loss of radial strength and molecular weight from the polymer chain introduced inflammation and stent fracture, respectively. In addition, long-term compatibility issues and chronic swelling of the stents limited their widespread use. The Igaki-Tamai stent, the first implanted stent in a human, used high molecular weight Poly-L-Lactide to limit inflammation and exhibited good tensile properties [26]. Hydrolyzation of the covalent bond and crystalline structure of Poly-L-Lactide reduces the molecular weight and radial strength, respectively, to lactic acid. Finally, it is metabolized through the Krebs cycle and excreted as carbon dioxide and water. A trial with 50 patients with 63 implantations exhibited 21% and 19% restenosis rate at six and at nine months, respectively [27]. The REVA stent from Reva Medical Inc., San Diego, CA, USA, was developed from bio-absorbable tyrosine-derived polycarbonate which also degrades through the Krebs cycle and maintains a high molecular weight. A trial with 27 patients resulted in higher retreatment of stented lesions in 4-6 months due to restenosis [22]. The BTI stent from Bio-absorbable Therapeutics Inc., Menlo Park, CA, USA, was developed from sirolimus coated with poly (anhydride ester) backbone and salicylic acid polymer to exhibit different absorption rates over time. A trial with 8 patients resulted in higher intimal hyperplasia [22]. A bio-absorbable vascular scaffold (BVS) everolimus eluting stent from Abott Vascular, Santa Clara, CA, USA, made of Poly-L-Lactide acid backbone with poly (D, L-lactic acid) polymer and everolimus resulted in the highest number of human clinical trials to date. A trial with 30 patients has shown a moderate 11.5% restenosis rate after six months but a higher late luminal area reduction during follow up (0.65 mm^2 in 6 month vs. 0.1 mm^2 in 4 month) compared to a Palmaz stent [23, 28]. Two orders of lower strength seem to late luminal area reduction during follow up. Thick struts may also impede flows through the vessel. Local inflammation and lack of radioopacity are additional limitations to bio-absorbable stents [24].

1.1.3.2 Bio-corrodible Stent

Bio-corrodible stent materials should possess a minimum of 490 MPa ultimate strength required for ASTM F138 and 40% elongation, the maximum plastic deformation for a SS316L stent [29]. On the other hand, the degradation rate should be between pure iron which is 0.2 mmpy and magnesium which is 5-10 mmpy [30]. Ideally, the degradability should be controllable to adjust to the desired duration. Magnesium and iron-based alloys are currently investigated for bio-corrodible stents [31]. In addition, bio-corrodible materials should have long term biocompatibility and should be non-toxic.

Magnesium based Bio-corrodible Stents

Magnesium (ii) cation is the fourth major in human body and the typical human dietary intake is 250-380 mg/day [32]. In addition to its low thrombogenicity and good biocompatibility, it is a co-factor of many enzymes and also a tissue structural constituent. After its first application to ligate radial artery in 1878, it was also used in the twentieth century to connect blood vessels. In addition, magnesium wires are used to induce thrombogenicity for favoring intravascular clotting in aneurysm treatment. It shows rapid degradation in a chloride solution and may result in intimal formation due to tissue overload with degradation products and loss of mechanical integrity in a short time period [33]. The AE21 alloy (magnesium alloy with 2wt% aluminum and 1wt% rare earth elements) was first used in coronary arteries in 11 pigs in 2003 and a follow up was performed up to two months based on 50% mass loss. Early intimal proliferation was reduced by later vessel diameter increase (positive remodeling) with no signs of thrombogenicity. The bio-corrosion reduced the mechanical integrity [34]. An improved absorbable magnesium alloy stent was developed from a WE43 alloy (magnesium alloy with <5wt% zirconium, <5wt% yttrium and <5wt% rare earth element) by Biotronik, Germany is shown in Figure 1.1.

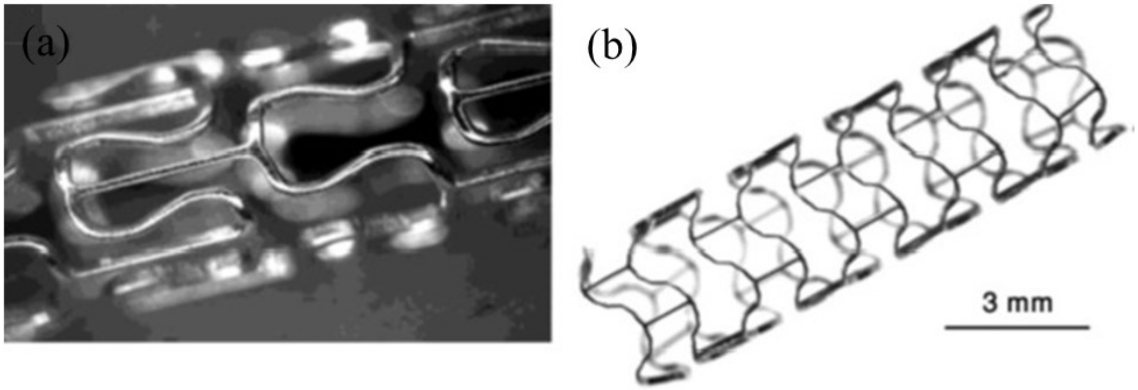

Figure 1.1: Biotronik coronary stent (a) non-expanded and (b) expanded, adapted with permission from reference [35] and [36], respectively

Preclinical studies of absorbable magnesium alloy stents in coronary arteries of 33 mini pigs exhibited favorable vessel diameter increase (positive remodeling) compared to 316L stents after a 12 week period [37]. Another preclinical study implanted WE43 stents in porcine coronary arteries for three months in 2006. The results indicated less intimal area compared to 316L stents with no signs of inflammation, thrombosis or vessel obstruction [33].

An absorbable magnesium stent from Biotronik was successfully implanted in the left pulmonary artery of a six week old premature baby in 2005. Angiographic follow-up revealed complete degradation of the stent after five months without in-stent restenosis or intimal hyperplasia. Later, two absorbable magnesium stents were implanted to a three-week-old baby suffering from critically narrowed aorta in 2006. Later in 2007, 71 absorbable magnesium stents were implanted in the coronary arteries of 63 patients in the PROGRESS-AMS trial. Radial support was lost within a few days and a 50% restenosis rate was observed after four months with a loss of radial support within days without sign of thrombosis and myocardial infarction [22]. Similar outcomes were obtained with 74 absorbable magnesium stent vs 75 bare metal stents implanted to treat chronic limb ischemia in a total of 117 patients in 2009. The patency rate of magnesium stents was significantly lower with a higher binary restenosis rate compared to bare metal stents after a six-month follow up [38]. Based on those results, it has been stated that absorbable magnesium alloy stents might not be an ideal stent for adults but might be a potential stent for pediatric applications. A high corrosion rate is responsible for the reduction of radial strength and polymeric layers have been added to recent absorbable magnesium stent for controlling the degradation. Currently magnesium is alloyed with lithium, zirconium, calcium, zinc, manganese and rare earth elements to improve their ductility, although these investigations are still in progress [33].

Iron based Bio-corrodible Stent

Iron is a major constituent (70%) of red blood cells and the typical human dietary intake of iron is 6-40 mg/day [32]. The faster ion transferring ability of iron makes them a useful component of cytochromes, enzymes, hemoglobin and myoglobin. The high elastic modulus of iron leads to high radial strength. The high ductility of iron eases the stent implantation procedure. The bio-corrodible NOR-1 stents were implanted in 16 New Zealand white rabbits in 2001 (Figure 1.2(a)). Investigations did not show any signs of stent thrombosis, intimal proliferation, inflammatory response or systemic toxicity in the 6-18 month angiographic follow-ups [33]. Both iron and 316L control stents were implanted in descending aortas of 27 pigs in 2006. The results revealed no significant difference in terms of intimal proliferation between stents with no pronounced inflammation [39]. Nine iron and eight cobalt chromium control stents were implanted in porcine coronary arteries in 2008. The iron stents (shown in Figure 1.2(b)) did not exhibit any luminal area reduction, vessel blockage or stent thrombosis [40].

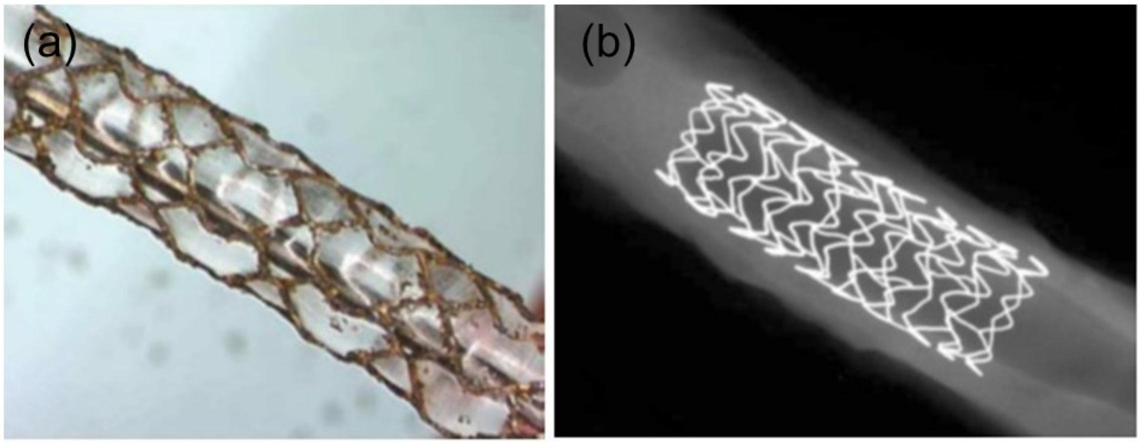

Figure 1.2: (a) Implanted iron stent and (b) X-Ray photomicrograph of iron stent from Biotronik, Inc., adapted with permission from references [41] and [40], respectively

Iron and magnesium wires were implanted on an artery lumen and artery wall to evaluate the corrosion behavior of stent materials in 2011. The corrosion products, hematite and magnetite were confirmed. However, blood-contacting surfaces experienced reduced corrosion compared to the arterial wall contacting surfaces because the existence of iron is less present in flowing blood compared to the flowing conditions in the stagnant arterial wall [42]. In vitro indication of irons' inhibition on human vascular smooth muscle cell proliferation was also investigated in 2013. The results indicate that Fe^{2+} and Fe^{3+} exert a concentration dependent suppressive effect on the vascular aortic smooth muscle cell proliferation [43]. Further, a 28 day-long clinical trial was performed on 8 nitriding iron stents and eight Cobalt-Chromium control stents in coronary arteries of 8 mini-swine. The results indicate no significant differences in intimal area, intimal thickness and percentage area stenosis between iron and control stents. Moreover, iron stents provide better intimal coverage than control stents which indicates their better re-endothelialization capacity [44].

The findings from the above review emphasize the need to investigate corrosion rate and improved strength and elongation. Iron with 20 to 35wt% manganese alloys manufactured using powder metallurgy was investigated first in 2004. Less noble manganese was added in the alloy to make the coating susceptible to corrosion. Outcomes indicate existence of antiferromagnetic single austenite phase with 5.3-2.1%

porosity. Tensile tests reveal 208-228 MPa yield strength, 548-568 MPa ultimate strength and a 27-32% elongation. Dynamic degradation tests indicate that iron and manganese releases per day are below metal specific blood toxicity levels. Uniform corrosion initiates from grain boundaries. The corrosion rate found from potentiodynamic polarization and static immersion after 7 days are 0.44 and 0.26 mmpy, respectively [31]. Fe-10Mn-1Pd alloy produced in a vacuum induction furnace was designed based on the idea that the addition of manganese would make the coating susceptible to corrosion and the noble element palladium to generate finely dispersed intermediate phases that will induce some micro galvanic corrosion by acting as a cathode. The results exhibited an accelerated corrosion rate (0.19 vs 0.1 mmpy) in a static immersion test and a one order of magnitude higher corrosion rate compared to pure iron in electrochemical impedance spectroscopy. In addition to the accelerated corrosion rate, the particle hardening mechanism improves the yield and tensile strength by forming intermetallic phases and decreases percentage elongation to 2-8% [45]. Binary alloying of iron with up to 3wt% of Mn, Co, Al, W, Sn and B was investigated using a vacuum induction furnace. Other than Sn, all binary alloys exhibited improved yield and tensile strength with similar corrosion rates compared to pure iron. A vacuum induction furnace was also used to prepare shape memory iron alloy Fe30Mn6Si which exhibited improved mechanical properties with a 0.3 mmpy corrosion rate using potentiodynamic polarization tests. Although most of these alloys are biocompatible, the average grain size is ≥100 microns. It is believed that smaller grains provide better yield and tensile strength and would be more susceptible to corrosive attack. Annealed electroformed iron provides finer grains (2-8 μm) and results in improved tensile and yield strengths than pure iron. Although the average in-vitro corrosion rate can be accelerated from 0.46 to 1.22 mmpy by altering the electrodeposition current density, it is not well understood why the formation of the degradation layer exhibited significantly lower corrosion rates of 0.23-0.28 mmpy in static immersion tests [30].

1.1.4 Cold Spray as a Technique for Manufacturing Degradable Stents

1.1.4.1 Process Overview

The cold gas dynamic spray or cold spray is a solid state high kinetic energy surface coating technique developed by Papyrin *et al.* [46] in the mid-1980s when coating was observed during wind tunnel experiments using metal particles. Figure 1.3 shows a schematic diagram of the cold spray process. High pressure compressed gas *e.g.* nitrogen, helium or air, is diverted into two channels. In one channel, the gas goes through the powder feeder to carry the metallic powder towards the spray gun.

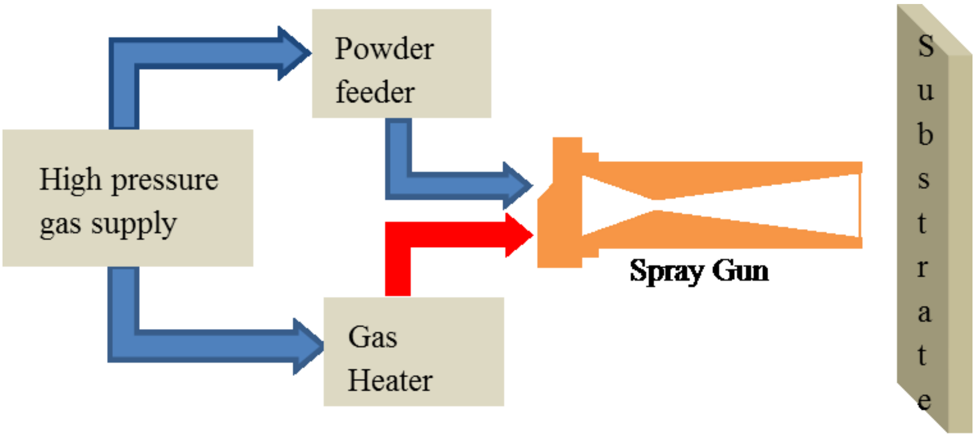

Figure 1.3: Schematic diagram of cold spray process

In the other channel, the gas goes through a heater. This gas is heated up and eventually reaches the spray gun as well. Finally, the metallic powder is accelerated to supersonic velocity through a converging/ diverging nozzle and eventually impacts onto a substrate and a coating is formed [47].

In comparison to the thermal spray processes, the particle temperature before impact on the substrate is lower than the melting temperature of powder. So, particle deposition is mainly due to their high kinetic energy upon impact which minimizes oxidation, phase transformation, grain growth and thermal stresses of the coatings. Therefore, cold sprayed hydroxyapatite coating is introduced for orthopedic implants [48]. As-sprayed coatings exhibit fine grain structure [49] and can coarsen a little even with the heat associated with conventional laser machining [30] which may decrease mechanical fatigue and provide material integrity required for the stent application. Grain size reduction improves wear properties of the materials [50]. Low ductility due to severe work-hardening of particles during the deposition process [51] can be improved by annealing.

The cold spray process mitigates any heating effect (e.g. grain growth) [51] due to subsequent laser machining in stent fabrication [52]. In comparison to the thermal spray processes, the particle temperature before impact on the substrate is much lower than the melting temperature of powder in cold spray. So, particle deposition is mainly due to their high kinetic energy upon impact which minimizes oxidation, phase transformation, grain growth and thermal stresses of the coatings.

1.1.4.2 Bonding Mechanism on Cold Spray

Presently, the concept of adiabatic shear instability is proposed as the bonding mechanism in cold spray. Briefly, when a particle impacts onto the substrate, a shear load is generated, shown in Figure 1.4(a). The shear load accelerates and causes localized shear deformation, which cause disruptions of thin oxide surface films on both the particle and the substrate, thus, creating an intimate confocal contact allowing bonding to occur [53].

Adiabatic shear instability locally dominates thermal softening over strain and strain rate hardening. This leads to a discontinuous jump in temperature and strain and an immediate breakdown of stress. This phenomenon leads to lateral jetting of the material, as shown in Figure 1.4(b) [53].

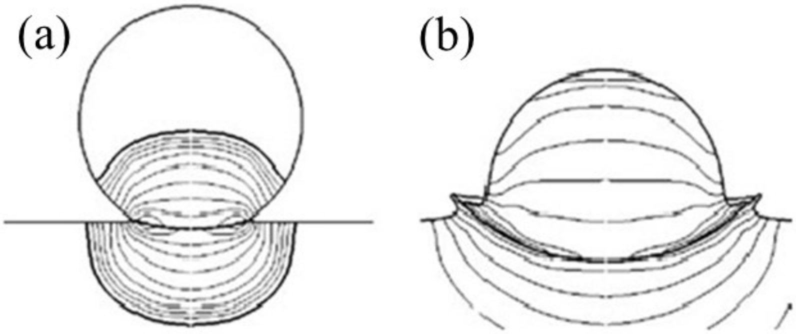

Figure 1.4: Deposition process (a) shear loading and (b) jetting, adapted with permission from [53]

There is also the possibility of physical interlocking of particles. Impacting particle forms a lip of substrate which partially envelops the particle. This phenomenon is known as interlocking and it is observed both at particle-substrate and inter-particle interfaces [54].

1.1.4.3 Cold Sprayability

It is not all particles impacting on the substrate that necessarily deposit. The term "cold sprayability" is introduced to define the conditions under which a coating is formed. Critical velocity, deposition efficiency, porosity and mechanical properties of the coatings are the metrics of cold sprayability [55]. Critical velocity is defined as the minimum velocity above which the particles adhere onto the substrate. Deposition efficiency is the ratio of the mass of particles that have successfully deposited onto the substrate over the total mass of particles projected [46], *i.e.,*

$$DE = \frac{m_s}{M_p} \qquad [1.1]$$

Here, m_s is the difference between the final and initial masses of the substrate and M_p is the total mass of the initial feedstock particles. The porosity is the ratio of area of the pores over the total area of observation of the resulting coating [56], *i.e.*:

$$Porosity = \frac{Area\ of\ pores}{Total\ area\ of\ coating\ under\ observation} \times 100\% \qquad [1.2]$$

Figure 1.5(a) illustrates that if the particle velocity is lower than the critical velocity, v_{cr}, then either the particles impact and bounce back from the substrate or they hit the substrate and cause surface erosion. Particles only adhere if the particle velocity exceeds v_{cr}. The critical velocity is estimated using following empirical equation [57]:

$$v_{cr} = 667 - 14\rho + 0.08T_m + 0.1\sigma_u - 0.4T_i \qquad [1.3]$$

It is seen from Equation 1.3 that v_{cr} is dependent on the density (ρ), melting point T_m, ultimate strength (σ_u) and initial temperature of the particle (T_i). Critical velocity also depends on particle size partly because smaller particles transfer heat better than larger particles which increase the critical velocity.

Increasing the cold sprayability means an increase in deposition efficiency and a decrease in porosity. Increasing the spray process intensity (i.e. gas temperature and pressure) increases particle velocity, which increases deposition efficiency and decreases porosity. However, the effect of velocity is also a function of process variables; *i.e.*, increasing the velocity by pressure only, even though the increment in velocity is the same [55].

In general, particle velocity decreases as particle size increases for a particular condition of gas, gas temperature and pressure but bow shock effect decelerates very fine particles. Heat dissipation effects and lower levels of oxidation in higher particle sizes decrease deposition efficiency [53]. Figure 1.5(b) shows that a cold spray “deposition window” exists, bounded by a minimum critical velocity and a maximum erosion velocity above which a deposition layer is not formed [53]. The deposition efficiency can also be shown in terms of particle size. Figure 1.6 is a schematic diagram showing the effect of particle size on particle impact velocity (v_{impact}) and v_{cr} for a given set of cold spray process conditions.

Obviously, the deposition window is the size range over which v_{impact} is greater than v_{cr}. There is a subset of particle sizes within this range where the difference between v_{impact} and v_{cr} is maximized and this is considered as the optimum particle size range.

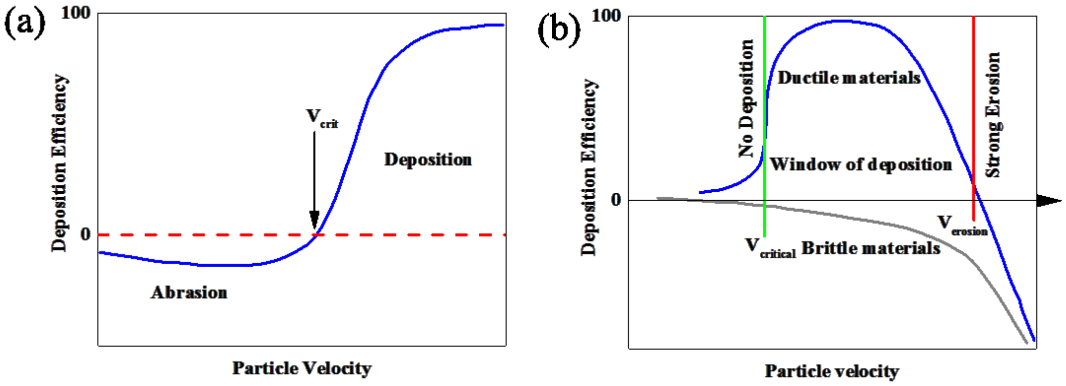

Figure 1.5: (a) Schematic diagram showing the relation between deposition efficiency and particle velocity and (b) schematic diagram of the window of deposition, modified from [58] and [59], respectively

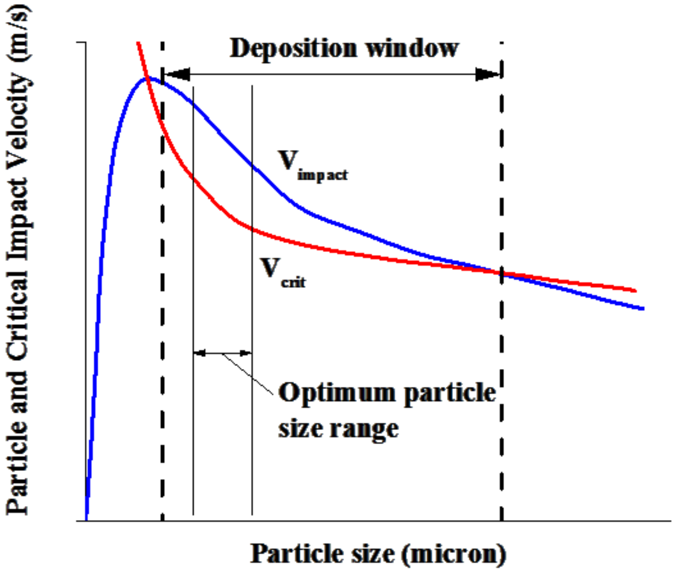

Figure 1.6: Schematic diagram of particle and critical impact velocities as a function of particle size, modified from [53]

1.1.4.4 Cold Spray as a Manufacturing Technique for Stent Material

There are no definite optimal values for stent manufacturing. However, the key desirable properties for ideal metallic stents are high tensile strength and high ductility. In general, a high elastic modulus (*E*) is needed to limit stent recoil after insertion and expansion of the stent. The elastic modulus, *E* also influences radial strength and resistance to buckling. A low yield strength (σ_y) is needed to enable the expansion of a stent at low balloon pressures. A high tensile strength (σ_{ut}) is needed to obtain the desired radial strength with a minimum stent volume. A high tensile strength implies the strut thickness may be minimized. A high ductility is needed to ensure the longevity of the stent and enable it to withstand periodic deformation under heart pulsation and a and high ($E \times t^3$) is required to get high buckling resistance [60]. Table 1.1 lists the mechanical and corrosion properties of some of the degradable and permanent stent materials currently investigated, as reproduced from [30, 60].

Table 1.1: Mechanical and corrosion properties of currently investigated permanent and degradable materials, reproduced from [30, 60]

Coatings	**Yield Strength (MPa)**	**Tensile strength (MPa)**	**Elongation (%)**	**In vitro corrosion rate (mmpy)**	**Average Grain Size (µm)**
316L	190	490	40	~	12-30
Co-Cr, L605	500	1000	46	~	<32
Armco®Fe	150	200	40	0.19	40
Fe-35Mn	230	430	30	0.44	<100
Electroformed Fe	270	290	18	0.46-1.22	2-8
Pure Mg	20	86	13	407	-
WE43	195	280	2	1.35	10

* Corrosion rates are measured by potentiodynamic polarization technique.

The cold spray method could potentially be used to fabricate materials for stents due to the high velocity and low temperature range, which reduces thermally induced harmful effects commonly observed in thermal spray coatings. Moreover, the small grain size of cold sprayed materials leads to enhanced mechanical properties. Austenitic stainless steel, 316L, is considered to be the reference material for stents. Gas atomized 316L powder was sprayed on steel substrates using nitrogen and helium gas with 40 bar inlet gas pressure at 700ºC inlet gas temperature. Coatings with steel substrate were heat treated from 400-1100ºC for 1 hour to improve ductility. The lower particle velocity due to nitrogen resulted in a low level porosity (up to 1.6%) and a reasonable deposition efficiency of about 78%. Annealing at 1100ºC for 1 hour reduced the porosity to 0.2% and resulted in a 433 MPa tensile strength and 23% ductility [61]. 316L powder was sprayed on both stainless steel and aluminum substrates using nitrogen gas with the same spray parameters as reported in [61]. Less deformation of particles were observed for coatings with aluminum substrate with high as-sprayed porosity (3.5-4%) compared to porosity for coatings on steel substrate (1.2-2.9%). Conversion of continuous inter-particle boundary to reduced amount of fine pores at annealed coatings exhibit 1-1.9% porosity, 511 MPa tensile strength and 37% ductility [62]. 316L powder spray coatings on Al7075-T6 substrates were optimized with varying inlet gas pressure between 20-40 bar, inlet gas temperature between 400 to 800ºC and keeping standoff distance at 40 mm, gun speed at 500 mm/s and powder feed rate at 33g/min. The results indicate 89.2% deposition efficiency at 800ºC gas temperature and 40 bar gas pressure combination [63]. These results support the use of 316L for stent applications.

1.1.4.5 Microgalvanic Corrosion Effect: A Concept for Fabricating Degradable Stent

Reactive coatings need to be prepared in order to induce corrosion susceptibility of the coating. So far, aluminum is the most reactive powder that has been cold sprayed (Figure 1.7) but is considered to be toxic [64]. However, the concept of micro-galvanic corrosion could potentially be applied to fabricate degradable coatings.

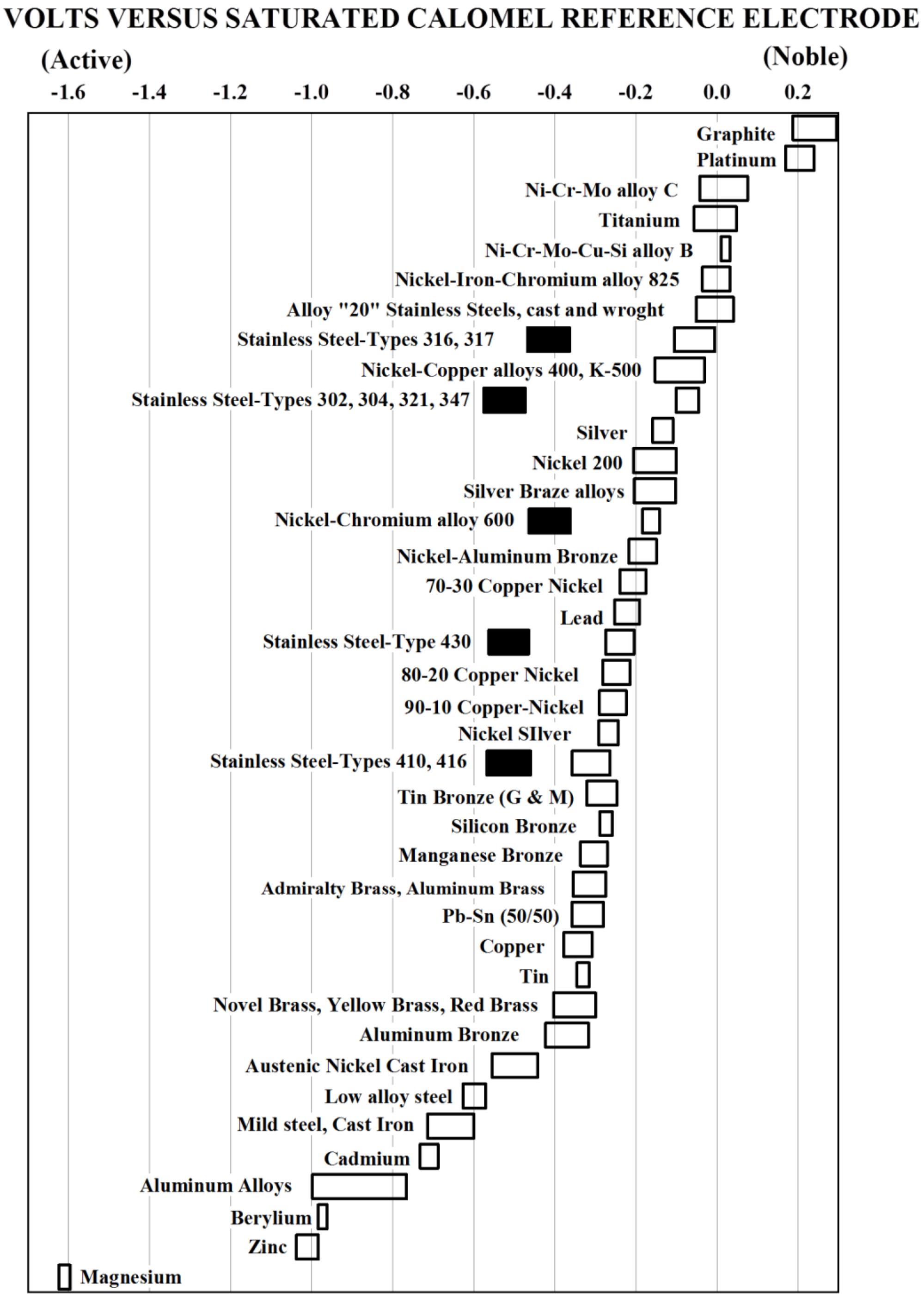

Figure 1.7: Galvanic series in seawater flowing at 2.4-4 m/s for 5-15 days at 15-30^{0}C, reproduced from ASTM G82-98, modified from [65]

Two different electrically coupled metals or alloys exposed to an electrolyte exhibit galvanic or bimetallic corrosion. The less noble metal or anode corrodes and the more noble metal or cathode is protected. Corrosion of steel at steel-copper joint tubing in a domestic water heater or corrosion of aluminum at an aluminum-steel junction in car registration plates are common examples of galvanic corrosion. The galvanic corrosion series shown in Figure 1.7 indicates that any metal or alloy below another in the galvanic table will undergo corrosion when both are in electrical contact in sea water. In order to prepare coatings with dissimilar materials combining a reactive and a noble powder, cold spraying of a mixture of dissimilar powders is performed.

1.1.4.6 Mixed Powders: Cold Spraying and Corrosion

Cold spraying of mixed powders has potential basic issues in that the cold sprayabilities of each component will be different, and, for a given set of process conditions, the velocities of each component powder will be different. Thus one component of the mixture may reach the substrate faster than the other component which might lead to an inhomogeneous coating. Also, the component with the lower cold sprayability may adversely affect the cold sprayability of the mixture. However, recent work has shown that in some cases the cold sprayability of the mixed powder is better than that of individual components and there is no sign of any serious inhomogeneity issues [66].

Limited biomedical alloys have the potential for mixed powder applications, with regard to micro-galvanic corrosion [67]. Cobalt-chromium, L605 powder was mixed with 316L powder in order to explore the possibility of micro-galvanic corrosion [68]. Mixtures of cobalt powder in 25, 33.3 and 50wt% were sprayed on steel substrates. The 25wt% and 33.3 wt% coatings exhibited very low porosity (less than 1.6%) with reasonable deposition efficiencies of 77% and 50%, respectively. However, the 50wt%L605 mixture had only 9% deposition efficiency. Following annealing at 1100°C for 1 hour, the 25wt% and 33.3wt% coatings exhibited ultimate tensile strength of 650MPa with 19% of ductility.

The mixed coatings exhibited a higher corrosion resistance compared to single component 316L coatings, which was attributed to low porosity. It seems that galvanic corrosion effect was negated by improved porosity [68].

1.2 Research Objectives

1.2.1 Specific Aim 1:

To prepare a mixed material from cold spray using a combination of noble and less noble metallic powders from the galvanic series and investigate the effect of cold spray process (inlet gas pressure and temperature) and powder characteristics (i.e. composition, microstructure, morphology, size and size distribution) on the properties of the resulting material generation (deposition efficiency, porosity and mechanical properties).

Hypothesis: It is possible to fabricate a cold sprayable mixed material with the appropriate mechanical properties for stent application.

1.2.2 Specific Aim 2:

To investigate the structural properties of biodegradable materials after thermal treated for stent application.

Hypothesis: It is possible to adjust the mechanical properties of the material with thermal treatment for achieving suitable mechanical and microstructural properties to provide mechanical integrity for stent application.

1.2.3 Specific Aim 3:

To measure the corrosion rate of the resulting material, compare the mass losses from galvanic corrosion and characterize the general corrosion rate and degradation product.

Hypothesis: Galvanic corrosion effect could potentially intensify or change the corrosion rate of intermixed compounds. It’s possible to fabricate galvanic couple that provides metallic degradability.

1.3 Organization of the Thesis

This thesis consists of six chapters. It starts by an introduction (chapter 1) continued to cold spray ability of the as sprayed coatings (chapter 2), effects of heat treatment on the mechanical and microstructural properties of the coatings (chapter 3), degradation properties with characterization of as sprayed and heat treated coatings (chapter 4), stent fabrication and future work (chapter 5) and conclusion (chapter 6).

The first chapter is an overall introduction of the thesis including research hypotheses and objectives. Literature reviews are presented for each topic. It starts with a brief overview of cardiovascular disease and the current limitations of permanent stents. A review of degradable stents is then presented. The cold spray process is presented as a manufacturing technique for generating materials for degradable stent inducing a galvanic corrosion. It is followed by a presentation of the hypotheses and related objectives.

The second chapter explains how cold sprayability is affected by the powder characteristics and the process intensity (gas pressure and temperature).

The third chapter explains how the mechanical and microstructural properties are affected by the heat treatment of sprayed coatings.

The fourth chapter describes the degradation properties of the as sprayed and heat treated materials with a characterization of the degraded products.

The fifth chapter presents the stent fabrication techniques and prototyped stents from cold spray and the current status of the manufactured stent.

Chapter six discusses the overall project with difficulties, challenges, limitations and future plans for the continuation of this doctoral study.

Chapter seven concludes the thesis works, describes about the fulfillment of the objectives intended to do and explains originality of this thesis.

Chapter 2. **Cold Sprayability of Mixed Coatings**

This chapter explains the effect of cold spray parameters (inlet gas pressure and temperature) and powder characteristics (*i.e.,* composition, microstructure, morphology, size and size distribution) on the cold sprayability of mixed coatings.

2.1 Introduction

The last two sub-sections in chapter one (1.1.4.4 and 1.1.4.5) described the possibilities and limitations of the use of multi-material sprays to obtain mixed coatings. The present chapter describes how cold sprayability is affected by cold spray parameters (inlet gas pressure and temperature) and particle characteristics on the mixed coatings to fulfil objective 1 of the thesis. The rationale to select specific powders for the mixed spray to explore galvanic corrosion effects are biocompatibility, cold sprayability with physical properties of the powders and the effect of microgalvanic corrosion of the mixed powders. In order to meet the requirements of a stent, the galvanic table is used as a reference in order to choose two metals such that the mixed coating could potentially degrade with the galvanic corrosion effect and hence accelerate the general corrosion rate of the coating. The galvanic table, as shown in Figure 1.7, indicates that mild steel or cast iron is a potential active material, after magnesium, zinc, beryllium, aluminum alloy and cadmium. In addition, mild steel or cast iron maintains a substantial potential difference with respect to austenitic stainless steel 316L, which is the reference material for stent fabrication.

In order to meet the challenges, biocompatibility of the mixed metals is first followed. Cadmium is one of the most toxic metals being responsible for lung cancer, kidney damage, bone damage and chronic obstructive pulmonary disease [69]. Short and long term beryllium exposure causes lung inflammation and chronic beryllium disease, respectively. Only 1 nanogram/gram of beryllium exists in human blood at normal levels because chronic exposure to beryllium causes lung cancer [70]. Aluminum is a possible candidate powders for the mixed coating but aluminum is highly neurotoxic and is suspected of leading to neurodegenerative disorders [64].

Cold sprayability of the mixed powder in addition to physical properties (*e.g.,* density, melting temperature etc.) issues are then reviewed after observing the potential difference between the powders from the galvanic table. If 316L is used as the non-reactive powder for the mixed coating, magnesium or zinc are not ideal for cold spray mixed powders because of their low density and melting point compared to 316L [71, 72]. These different attributes may lead to inhomogeneous coatings or clogging of the nozzle (due to melting). Also, magnesium is potentially explosive in powder form and could be a serious problem when cold spraying.

Pure iron is found to be the most suitable powder because the physical properties of pure iron and 316L powders are reasonably close. Pure iron maintains a 0.855 volt potential difference when coupled to austenitic stainless steel in seawater [73]. Therefore, pure iron and austenitic stainless steel (316L) powders are selected as the most appropriate for generating a mixed coating with the cold spray technique.

In this research, the cold gas dynamic spray technique is used to spray micron-sized particles onto flat metallic or cylindrical substrates. Stainless steel, (316L) powder is mixed with commercially pure iron powder (denoted CP Fe) (by weight of Fe, 0%, 20%, 50% and 80% and 100% are considered) and sprayed onto aluminum or steel substrates to induce the galvanic corrosion effect on the as-sprayed composite. Impact velocities are estimated for different inlet pressure and gas temperature conditions. The deposition efficiency for specific conditions is measured. The porosity, microhardness and phase identification of as-sprayed coatings and the corresponding powders are characterized by optical microscopy, microhardness and x-ray diffractometer, respectively.

2.2 Materials and Methods

2.2.1 Feedstock Powders

Powders are characterized on the basis of their particle composition, size distribution and microstructure. Lots 1, 2 and 3 represent powders provided from the manufacturer in 2012, 2013 and 2014, respectively. Both pure iron and 316L powders were purchased from Sandvik Osprey Limited, UK.

The chemical compositions were determined to validate the compositions reported by the manufacturer. Inductively coupled plasma optical emission spectroscopy (ICP-OES) analyzer, ICP 6000 series ICP-OES from Thermo fisher Scientific Inc. was used to measure the elemental concentration in the powder samples. Here, weighed powders are completely digested with a hydrochloric acid and nitric acid mixture and the solution is then sprayed into radio-frequency (RF) argon plasma. Extremely high temperatures (approximately 10,000°K) at the ICP core dries the sprayed solution and atomic emission emitted from the argon plasma is transmitted to the wavelength selection device and the actual chemical composition is transmitted to an output device [74]. The carbon content was measured separately according to the standard ASTM-E1019 (combustion) test method because carbon escapes from the solution by forming carbon dioxide during digestion based ICP sample preparation. Here, elemental carbon forms carbon dioxide during decomposition of the substance in the oxygen stream. Carbon dioxide is measured by absorbing it in a chromatographic column consisting of a specific zeolite which elevates after carbon dioxide absorption [75].

A laser diffraction particle size distribution analyzer, LA-920, HORIBA was used to measure the particle size distributions of the 316L and iron powders. When the laser beam passes through the dispersed particles (isopropanol is used to disperse the powders), smaller particles exhibit higher diffraction angles compared to larger particles. A laser diffraction analyzer calculates the particle size distribution from the angular variation of scattered light made by ranges of powders using the refractive index of the particular powders.

The powder microstructure was characterized with a Field Emission Gun Scanning Electron Microscope (Philips-XL30 and Hitachi SU3500).

The microhardness of the powders was determined with a Vickers Microhardness tester (Clark, ClemexTM CMT) with a load of 10 gram. A minimum of 20 measurements were taken at random locations. Cold mounted powders were ground with 600, 800 and 1200 grit paper followed by polishing with 0.3 micron alumina and 20 nm colloidal silica suspensions. They were etched with 2% nital.

The initial phases of the powders were detected with a Bruker D8 X-ray diffractometer with Co Kα radiation, 40 mA current, 40kV voltage and 0.02^0/sec scan rate. Eva software was used to quantify ferrite and austenite phases of the powders.

2.2.2 Cold Spray Parameters and Process Overview

A KINETICS® 4000 cold spray system (Sulzer Metco, Westbury, NY) with nitrogen as the propellant gas and a MOC24 nozzle was used to produce coatings at National Research Council (NRC), Boucherville, QC. A rolling mixer without balls or rotating tumbler with balls was used for an hour to mix the 316L and iron particles. Substrates were grit blasted with a 24 grit alumina before spray to increase coating adhesion. Pure and mixed powders were calibrated in order to determine powder feed rate for each coatings. Details of the fabrication process are given in Figure 2.1. Powder is sprayed on substrate according to spray conditions shown in Table 2.1.

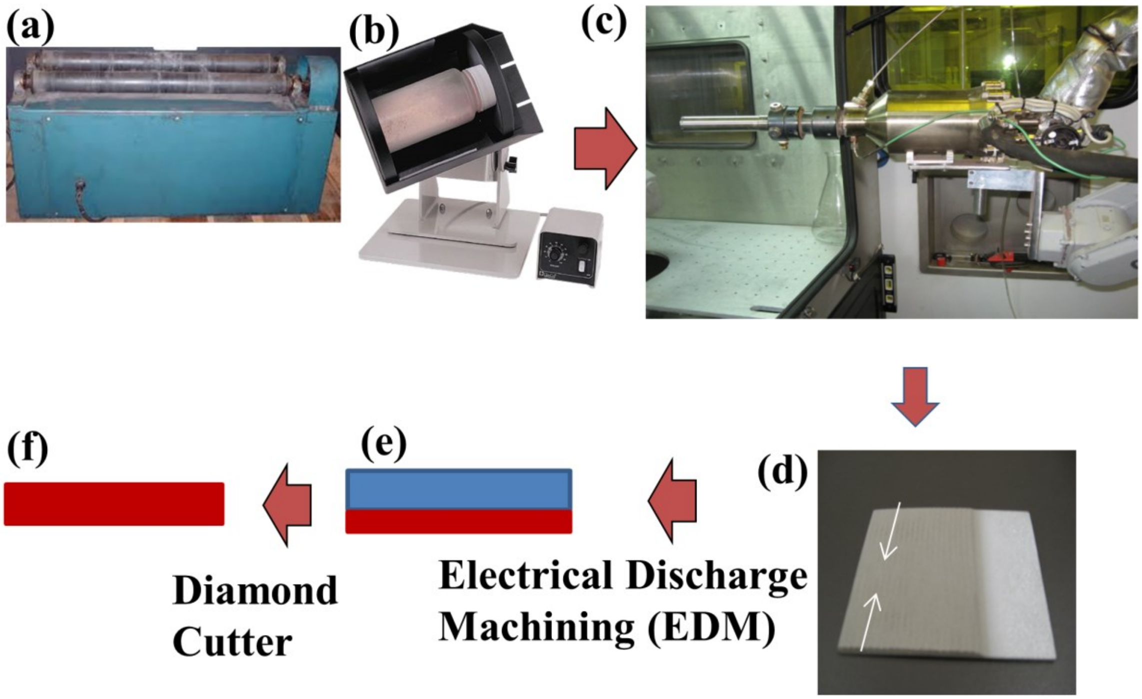

Figure 2.1: Cold spray process to fabricate mixed coatings; powder mixing either (a) rolling mixture or (b) rotating tumbler, (c) KINETICS 4000 cold spray system (d) as-sprayed coating with cutting directions shown with arrows, (d) EDM cut coating strip with substrate and (e) coating without substrate cut with diamond cutter

Spray conditions for velocity measurements are shown in Table 2.2.

Table 2.1: Spray conditions used to fabricate coatings using KINETICS 4000 cold spray system

Powders	**Powder lot**	**Gun Traverse Speed (mm/sec)**	**Gas Temp (°C)**	**Pressure (MPa)**	**Feed Rate (gm/min)**	**Stand-off (mm)**
316L	1	300	700	4	21.2	80
CP-Fe	1	300	700	4	24.1	80
20wt%Fe	1	300	700	4	20.7	80
50wt%Fe	1	300	700	4	19.5	80
80wt%Fe	1	300	700	4	24.1	80
20wt%Fe_3	3	300	700	4	30	80
80wt%Fe_3	3	300	750	4	29	40

Table 2.2: Spray conditions used for the velocity measurement using Plasma Giken (PCS-800) spray system

Powders	**Powder lot**	**Gun Traverse Speed (mm/sec)**	**Gas Temp (°C)**	**Pressure (MPa)**	**Feed Rate (gm/min)**	**Stand-off (mm)**
CP-Fe	2	300	700-800	4-5	36	80
90wt%Fe	2	300	700-800	4	36	80
80wt%Fe	2	300	700-800	4	36	80
65wt%Fe_3	2	300	700-800	4	27	80
40wt%Fe_3	2	300	700-800	4-5	29	40

Coatings are deposited on 100 mm×100 mm× 3 mm aluminum, Al6061 and mild steel, 1020CR substrates. The particle velocity was measured prior to the form coating. An electric discharge machine (EDM) was used to cut the coating with substrate. Finally a diamond cutter is used to remove the substrate from the coating.

The deposition efficiency was calculated for lot 1 and lot 3 coatings. Spray conditions were varied to produce better deposition efficiencies and reduce the coating porosity.

Nozzle clogging problems were identified on lot 2 mixed coating fabrications, so deposition efficiency calculations are not shown. In addition, coatings fabricated with lot 2 powders were used to fabricate stents; so these were not subjected to microstructural and mechanical characterization. Lot 1 coatings were successful apart from the nozzle clogging issues with 80wt%Fe coatings. This problem led us to use Plasma Giken PCS-800 cold spray system (Plasma Giken Company Ltd, Tokyo, Japan) with nitrogen as the propellant gas and the PNDO-10-30S glass nozzle was used to measure the particle velocity avoiding clogging problem.

2.2.3 Coating Characterizations

Inductively Coupled Plasma (ICP) and the combustion based ASTM-E1019 methods were used to measure the chemical composition and the carbon content of the coatings.

Porosity of the as-sprayed coatings was determined with a Nikon Epiphot 200 microscopy equipped with Clemex vision software. Cross sections were ground with 120, 240, 400, 600, 800 and 1200 grit paper and polished with 0.3 μm alumina and 20 nm colloidal silica suspensions. Images were recorded at 200X magnification and more than 15 images were studied for each coating.

Microhardness of coatings are performed with Vickers Microhardness tester (Clark, Clemex^{TM} CMT) at a load of 50 gram. A minimum of 20 measurements were taken at random locations after the porosity measurements had been made.

Alloy phases of the as-sprayed coatings were observed with a Bruker D8 x-ray diffractometer maintaining same parameters as for the powders.

2.3 Results and Discussions

2.3.1 Characterization of Feedstock Powders

2.3.1.1 Composition

The measured chemical compositions of all the powders are shown in Table 2.3. Compositions of all 316L lots are within the allowable ranges. However, the commercial purity irons have Fe contents that are somewhat lower than that of Armco® iron, which is a minimum of 99.85%Fe [76]. Armco® iron being the industry standard for commercial purity iron.

The main difference between these Fe lots and Armco® iron appears to be relatively high levels of manganese and silicon, which may be due to the processing of iron powders [77]. However, lot 3 Fe is in fact mild steel since it contains 0.16wt% carbon, which is an order of magnitude higher than the other two lots.

Table 2.3: Composition of 316L and CP Fe powders (in weight %)

Lot	**Powder**	**Fe**	**Cr**	**Mn**	**Mo**	**Ni**	**Si**	**C**
1	316L	68.71	16.36	1.41	2.33	10.90	0.28	0.014
1	CP Fe	99.29	0.07	0.37	0.02	0.11	0.14	0.032
2	316L	67.37	17.00	1.41	2.47	11.39	0.34	0.019
2	CP Fe	99.27	0.06	0.35	0.02	0.10	0.20	0.031
3	316L	68.76	16.24	1.32	2.40	10.90	0.35	0.013
3	CP Fe	99.00	0.03	0.70	0.00	0.03	0.07	0.16

2.3.1.2 Size Distribution

Figures 2.2 and 2.3 represents particle size distribution curves for the different powder batches. Average and standard deviations of particle sizes are listed in Table 2.4:

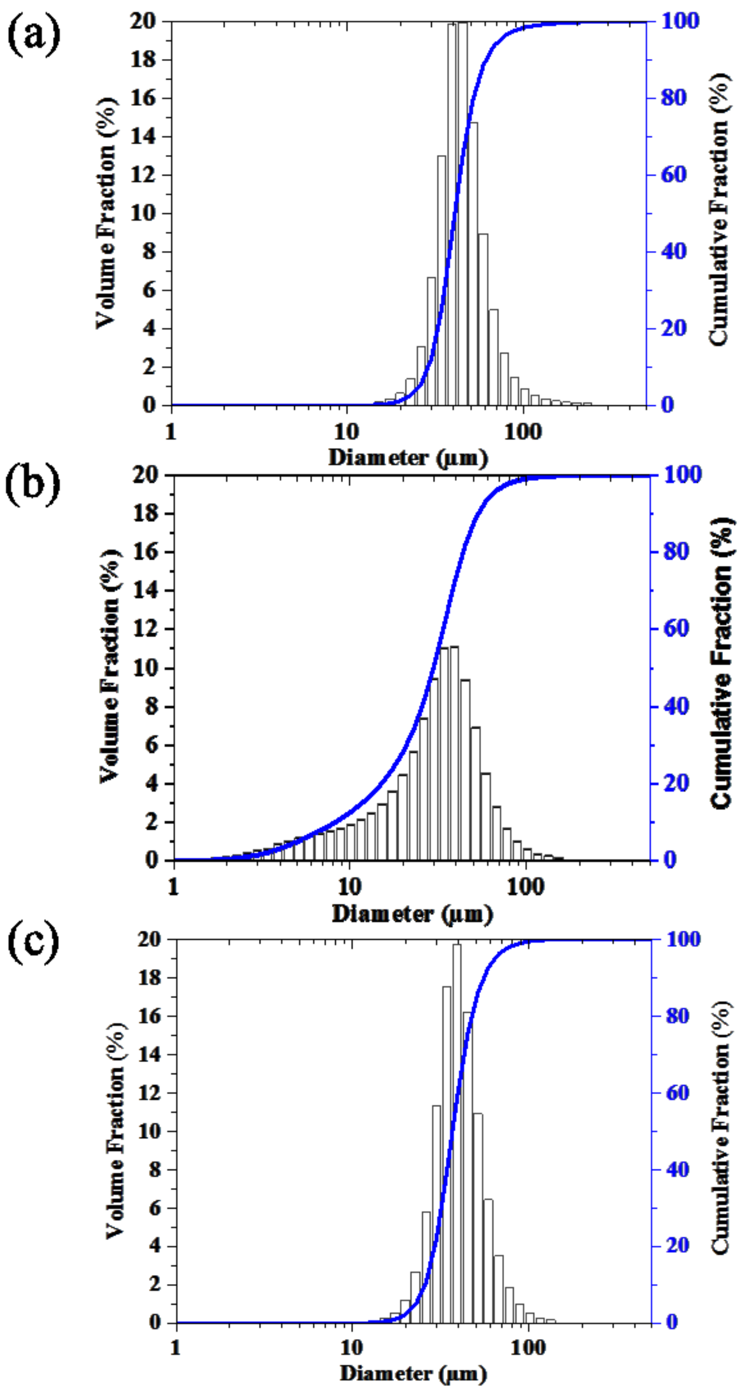

Figure 2.2: Particle size distribution of 316L powders of (a) lot 1, (b) lot 2 and (c) lot 3

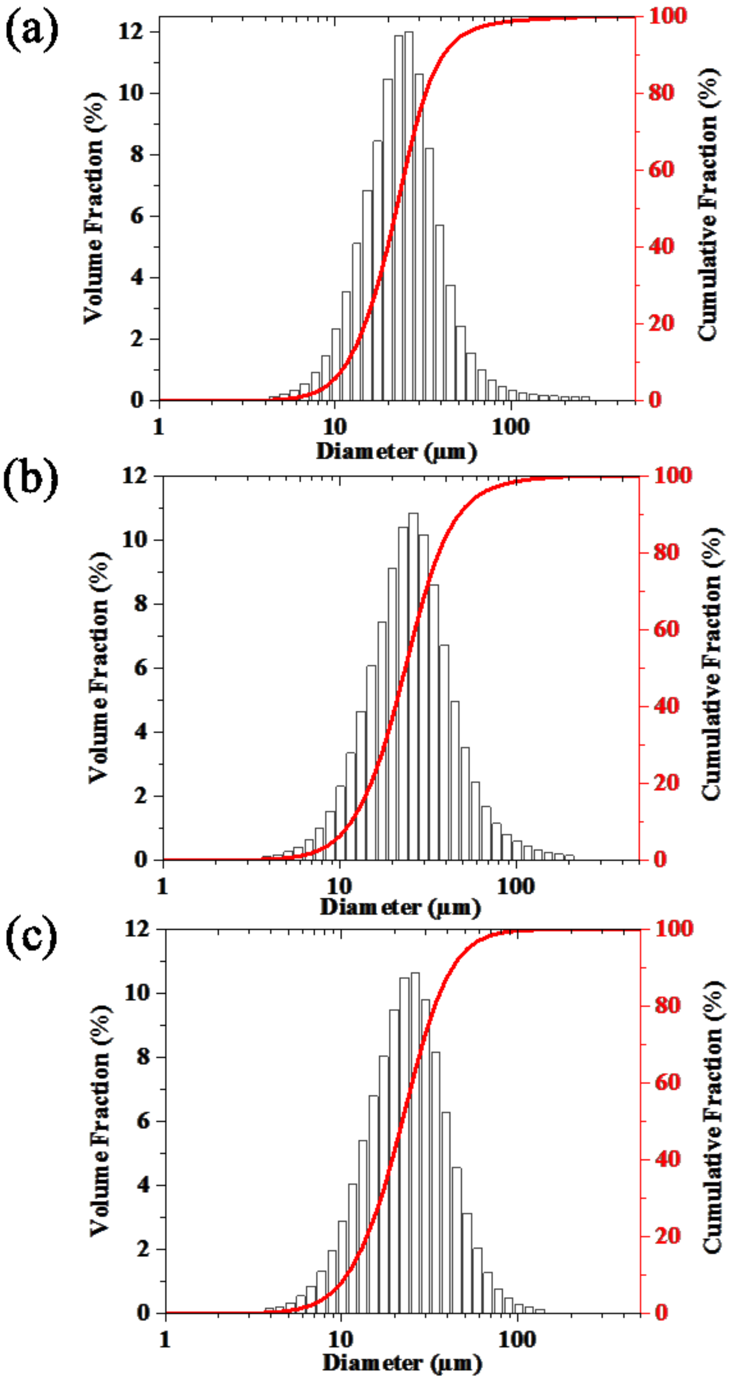

Figure 2.3: Particle size distribution of CP Fe powders of (a) lot 1, (b) lot 2 and (c) lot 3

Table 2.4: Particle size distribution of different lot powders

Powders	**Powder lot**	**Average diameter (µm)**	**Standard deviation (µm)**	**D10 (µm)**	**D50 (µm)**	**D90 (µm)**
316L	1	43.74	16.95	28.56	40.64	60.95
316L	2	31.56	19.59	8.21	29.44	54.11
316L	3	39.27	13.83	25.37	36.56	54.86
CP Fe	1	23.21	12.58	11.50	21.41	38.24
CP Fe	2	26.65	18.45	11.61	23.38	44.72
CP Fe	3	25.15	14.57	10.75	22.26	42.65

These data indicate that iron powders are relatively finer than 316L powders and will therefore achieve higher particle velocities than coarser 316L particles. The powder size distributions are shown in Figures 2.2(b) and the only point of interest is that the lot 2 316L powders have a large amount of fines.

2.3.1.3 Microstructure

Scanning electron microscopy of feedstock powders is shown in Figure 2.4. It is seen that the gas atomized 316L and CP Fe powders are mostly spherical in shape. There are three levels of powder roughness. 316L lot 1 and CP Fe lot 2 are very rough due to fine powders agglomerating onto coarse ones; the other Fe lots are very smooth and 316L lot 3 is in between two levels of roughness. Rougher particles will tend to have higher velocities for a given set of cold spray conditions, although these particular powders have higher powder sizes because of agglomeration, and this may reduce particle velocity. The rough surface may also favor higher deposition rates through physical interlocking particle bonding.

Optical cross-sections of 316L and CP Fe powders are shown in Figure 2.5. Figures 2.5(d), 2.5(e) and 2.5(f) indicate the appearance of some needle like structures which are the characteristics of martensitic microstructures. Nital did not reveal any microstructural details of 316L because 316L is resistant to nital.

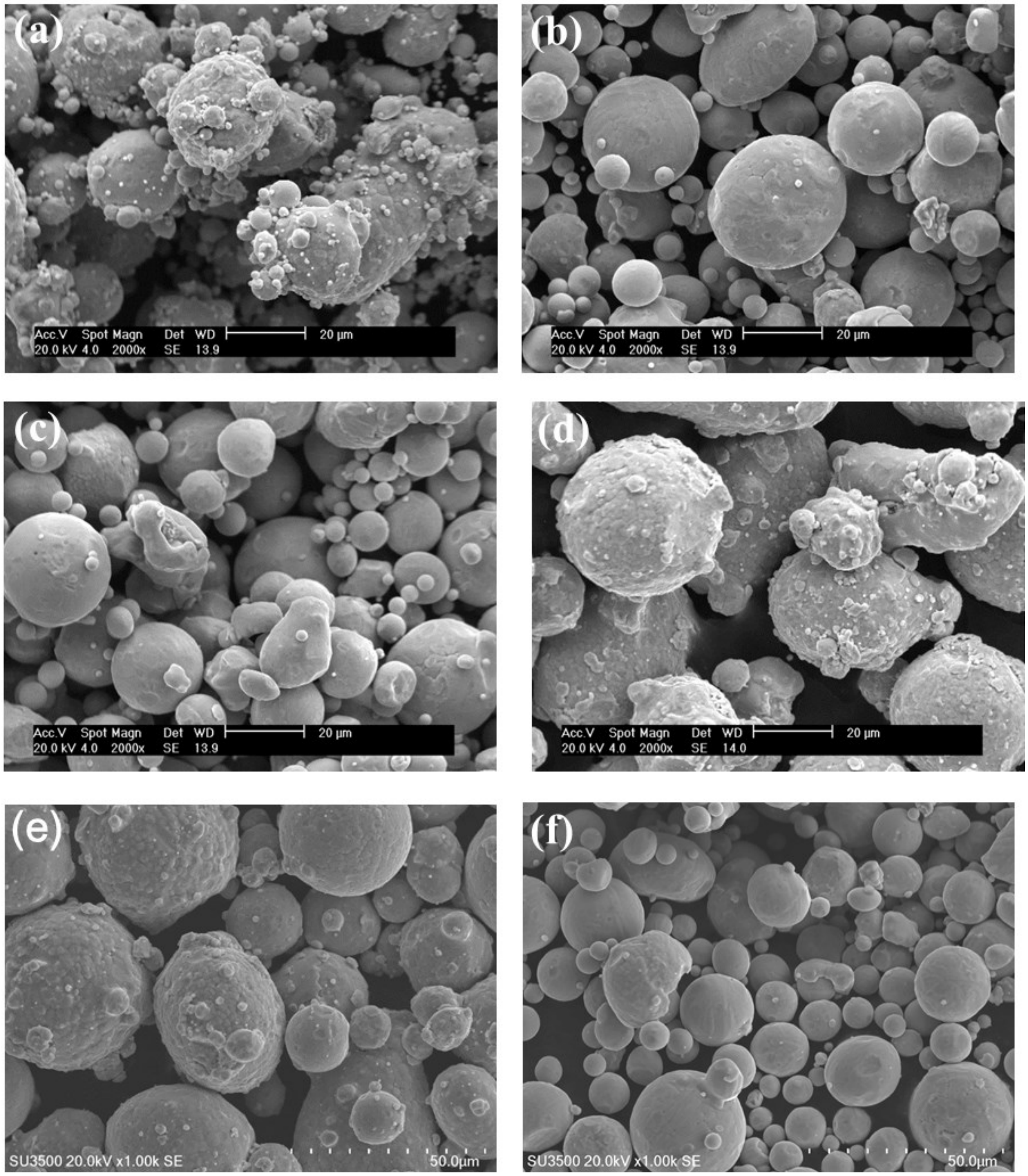

Figure 2.4: SEM of powders (a) 316L lot 1, (b) CP Fe lot 1, (c) 316L lot 2, (d) CP Fe lot 2, (e) 316L lot 3 and (f) CP Fe lot 3

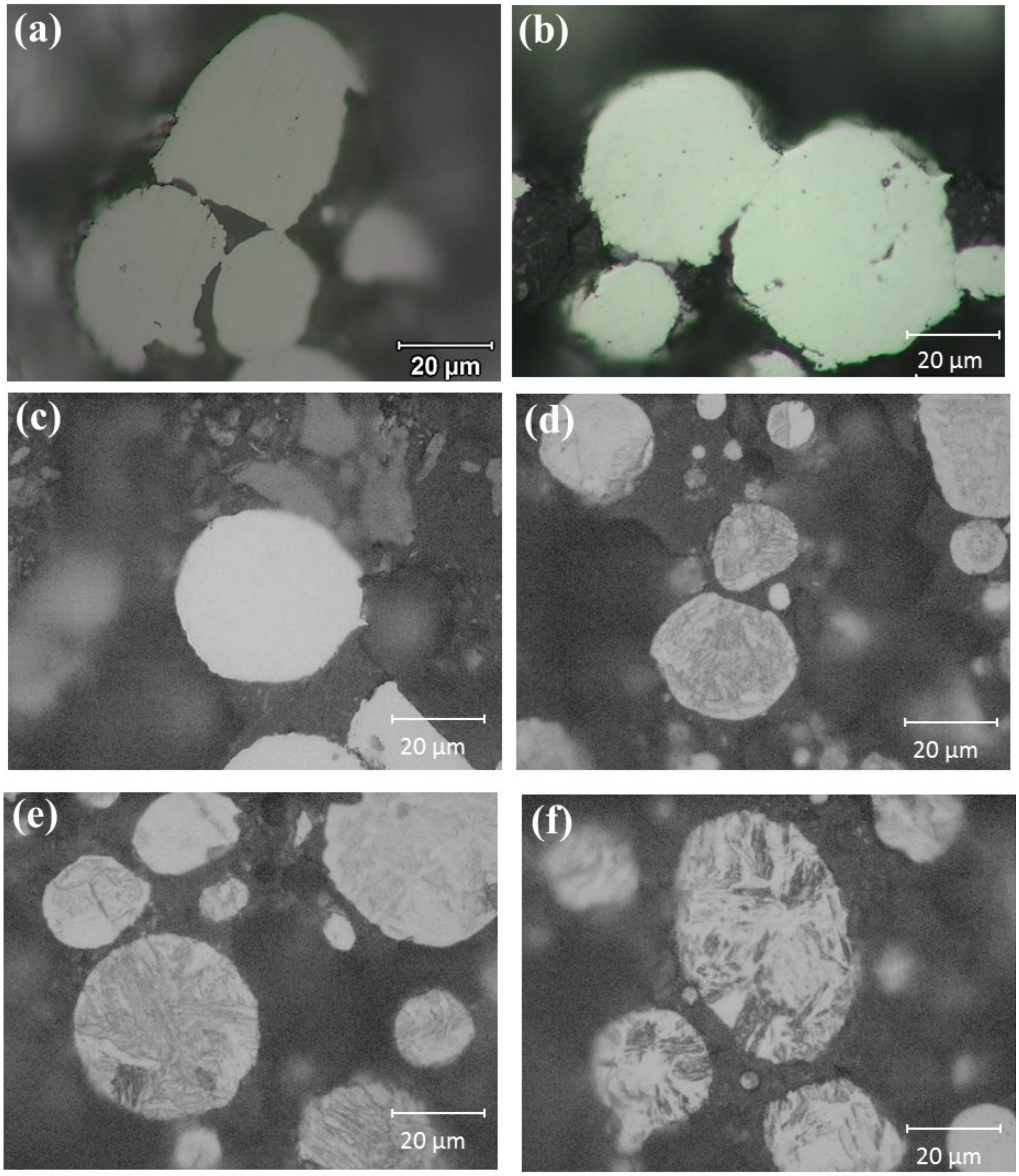

Figure 2.5: Optical microscopy images of polished and etched powders: (a) 316L lot 1, (b) 316L lot 2 (c) 316L lot 3, (d) CP Fe lot 1, (e) CP Fe lot 2 and (f) CP Fe lot 3

Scanning electron microscopy of the mixed lot 3 powders (80wt% CP Fe and 20wt% 316L) is shown in Figure 2.6. It is seen that 316L powders are scattered on the surface indicating that the powders are thoroughly mixed. 316L powders can be easily distinguished from the CP Fe powders by higher particle size of the former.

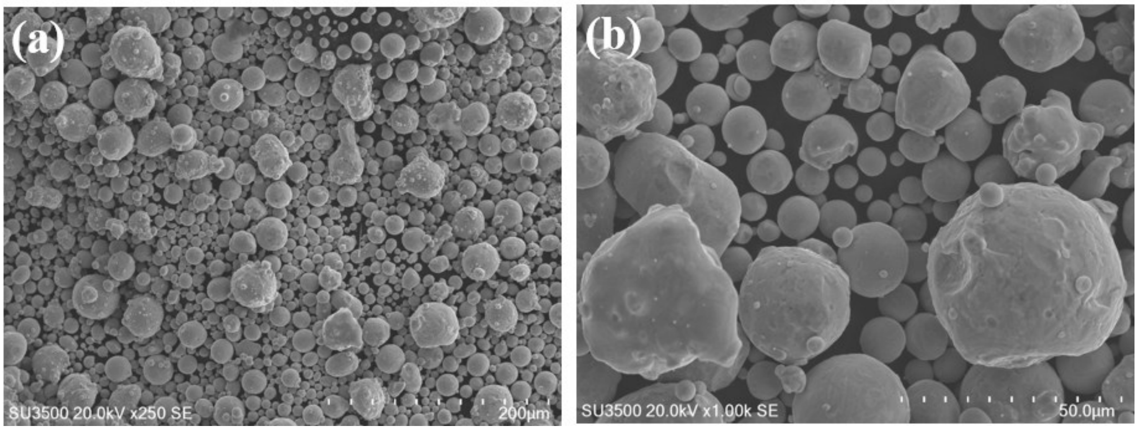

Figure 2.6: SEM of 80wt%CP Fe mixed powders at (a) low and (b) high magnification

2.3.1.4 Microhardness

Microhardness values of powders from lot 1 to 3 are shown in Figure 2.7. The higher hardness values of the iron powders ($287.71\pm33.35\text{HV}_{0.01,}$ $296.58\pm28.1_{0.01}$ and $375.46\pm31.45\text{HV}_{0.01}$ for lots 1, 2 and 3 CP Fe powders, respectively) are also an indication for the martensitic transformation from ferrite. Note that lot 3, which is a mild steel, has the highest hardness, which can also be attributed to more martensite and harder martensite because of the high carbon level. The hardness of elemental iron and bulk 316L has been reported previously at a level of 150 and 155 HV, respectively[78, 79]. Although the image analysis does not indicate a martensitic transformation in 316L powders, the high hardness values of 316L powders ($226.4\pm31.66\text{HV}_{0.01,}$ $236.87\pm28.11_{0.01}$ and $238.92\pm13.91\text{HV}_{0.01}$ for lots 1, 2 and 3 316L powders, respectively) are an indication of martensitic transformations [80]. Irregularly sized 316L powder has been reported to exhibit a hardness value of $185\pm15\text{HV}_{0.01}$ [61], which is also higher than the bulk 316L value, but much lower than the 316L used in this work. Martensite could form as a result of the very high cooling rates in powder processing even with carbon levels as low as lots 1 and 2 CP Fe; the carbon content of lot 3 CP Fe is high enough to comfortably form some martensite during quenching. Martensite formation in 316L is much more difficult because of the stability of the austenite phase, so it would be surprising to see martensite formed in any quantity. In fact, in welding studies according to the 316L composition used in this work, the likelihood of any martensite forming is very low [81].

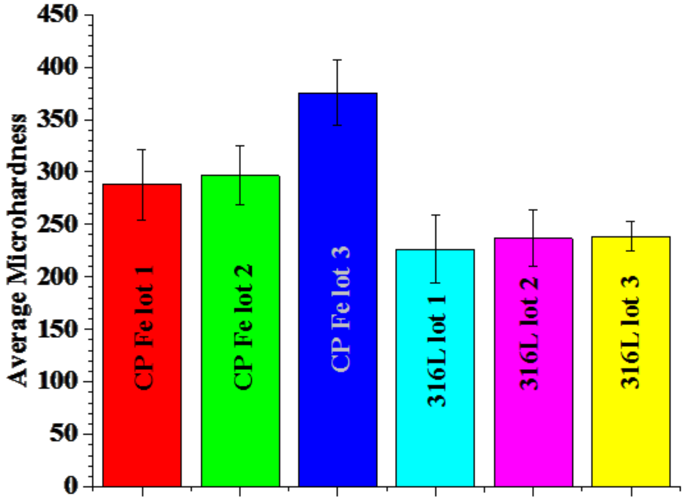

Figure 2.7: Average microhardness of CP Fe and 316L powders of all lots

2.3.1.5 Phase Identification

Figure 2.8(a) and 2.8(b) presents XRD patterns obtained for the lot 1 to lot 3 powders.

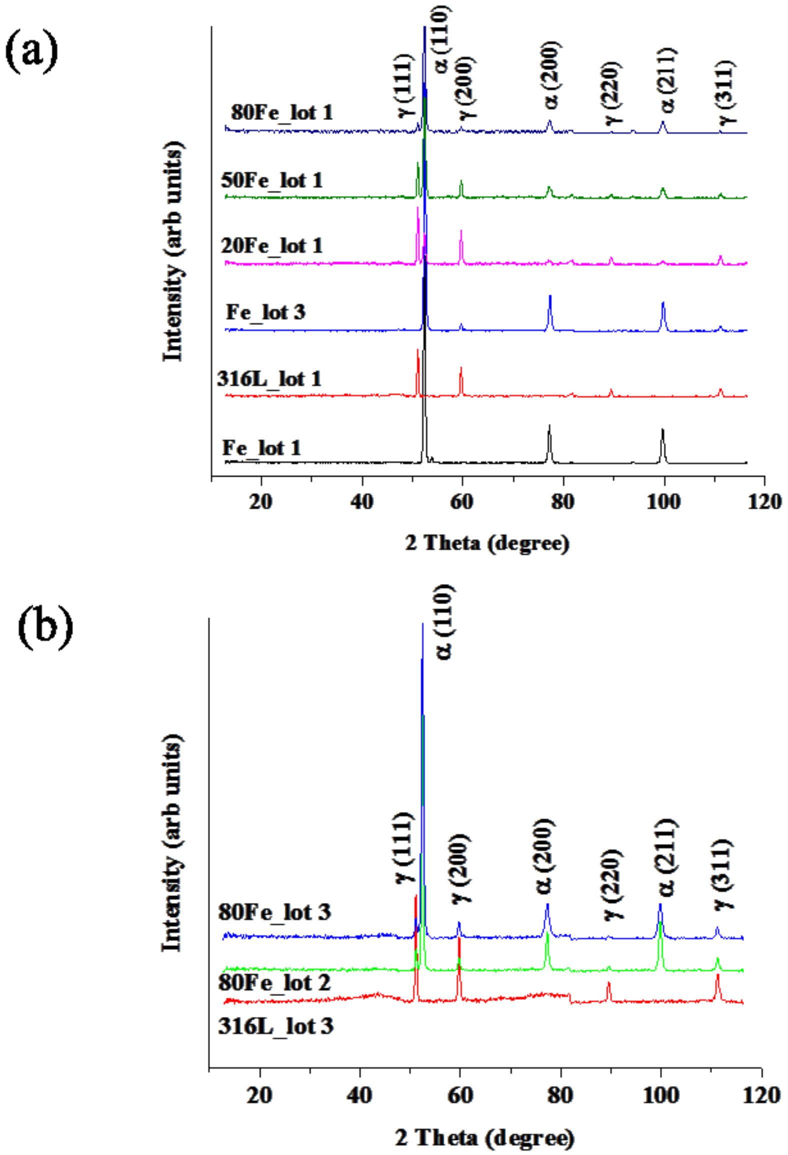

Figure 2.8: XRD pattern of feedstock powders (a) lot 1 and (b) lot 2 and lot 3

Figures 2.8(a) and 2.8(b) are XRD patterns obtained for the lot 1 to lot 3 powders, with a pattern from the 50-50 mixed powder. ICDD (The international center for diffraction data) patterns 00-033-0397 mainly match with 316L powder, which is basically face-centered cubic austenite. ICDD pattern 03-065-4899 matches with CP Fe pattern which is basically a body-centered alpha iron compound. The quantitative measurements of ferrite and austenite are in Table 2.5. Note that there is a small amount of 'ferrite' in the 316L, which might be martensite. Martensite, which is body centered tetragonal, cannot be normally distinguished from BCC ferrite by XRD, hence cannot be resolved in the CP Fe powders, which reveal 100% ‘ferrite’. The mixed powders were also subjected to XRD to see if any changes had occurred during mixing, and the XRD reveals both patterns of face-centered cubic and body-centered cubic phases. However, Table 2.5 shows that there is a considerable loss of austenite due to mixing. Assuming this is not due to physically ‘losing’ 316L, this loss of austenite can only be due to a transformation of austenite to ferrite during mixing, probably due to strain induced transformation [82].

Table 2.5: Percentages of phases in 316L and CP Fe powders

Coatings	**Percentages of Phases (%)**	
	Ferrite (α)	**Austenite(γ)**
316L_lot 1	7.9±0.4	92.1±0.3
CP Fe_lot 1	100.0±0.0	0.0±0.0
20Fe_lot 1	34.1±0.6	65.9±0.4
50Fe_lot 1	65.9±0.4	34.8±0.5
80Fe_lot 1	91.0±0.5	9.0±0.6

2.3.2 Outcome of Cold Spray Process

2.3.2.1 Deposition Efficiencies for Different Mixed Conditions

The deposition efficiency is calculated based on Equation 1 and shown in Table 2.6 for lot 1 powders. The gas temperature was 700°C and pressure was 4MPa. The 316L and CP Fe powders exhibit the highest and lowest deposition efficiencies, respectively, and the mixed powders exhibit deposition efficiencies, somewhere in between as shown in Figure 2.9. The 316L powder shows a better DE possibly because it has a lower hardness and also it is face centered cubic, which generally illustrates easier plastic flow compared to BCC. However, the 316L particle size is larger, which would reduce the velocity of the particle. However, this negative effect seems to have been more than compensated by the favourable mechanical properties.

Table 2.6: Deposition efficiency (DE) calculation of coatings with lot 1 powders

Sl. No.	**Plate length (mm)**	**Gun Speed (mm/s)**	**No. of passes**	**No. of Returns**	**Feed Rate (gm/min)**	**Mass feed (gm)**	**Mass Deposited (gm)**	**DE (%)**
316L	100	300	47	40	21.2	221.42	159.40	71.99
20Fe	100	300	60	40	24.1	321.33	137.90	42.91
50Fe	100	300	57	40	20.7	262.20	126.20	48.13
80Fe	100	300	40	40	19.5	173.33	114.95	66.32
Fe	100	300	60	40	24.1	321.33	105.00	32.68

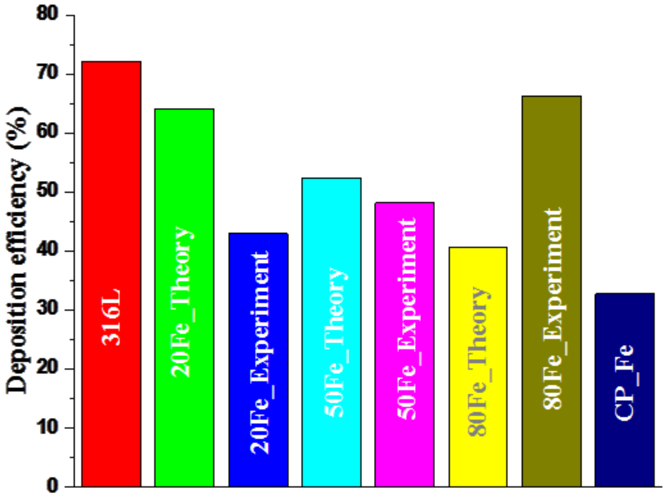

Figure 2.9: Theoretical and experimental deposition efficiency of coatings with increasing wt% of CP Fe

Also shown in Figure 2.8 are the predicted DEs of the mixtures calculated from the weighted averages of the powders in the mixtures. Only in the case of the 50-50 mixture does the prediction reasonably match the experiment; the other mixtures exhibit very large differences between prediction and experiment. At least qualitatively, the expectation of adding a powder with a better DE to one with a poorer DE is to increase the DE of the mixture. In fact this has been shown to be the case by Yue *et al.* [83] who showed a very strong effect of mixing powders, similar to the result in Figure 2.8 of adding 20% 316L to Fe, leading to a DE close to that of 100% 316L. It is not known why such a small amount of 316L should give such a large increase in DE, but it might be connected with differences in hardness of the CP Fe and 316L leading to higher strains at the interfaces between the different powders, promoting bonding and therefore DE in this way. However, the DEs of the mixtures decrease quite significantly with increasing 316L, remaining fairly constant for 50 and 80 wt% 316L. In fact, it is most surprising to see that the experimental DEs are even lower than predicted from the weighted averages. These results contradict the concept of the effect of particles of different hardnesses interacting at the interfaces in a beneficial manner, which was used to explain the 20% 316L result. At present, there is no explanation for these results.

The deposition efficiency for lot 2 powders is shown in Table 2.7. The gas temperature was 750°C and the pressure was 4.9MPa. These values were used because the values used for lot 1 powders led to zero DE. The main difference in the lot 3 powders is the much higher hardness of the CP Fe (which is in fact a mild steel), and it is this increase in hardness that is assumed to be the major factor in the decrease in DE of these mixtures. Even though the data of table 2.7 is generated at different cold spray parameters, it is interesting to note that the effect of adding 20% 316L to CP Fe is no different than the effect of adding 20% CP Fe to 316L, which is totally different from the lot 1 powders.

Table 2.7: Deposition efficiency (DE) calculation of coatings with lot 3 powders

Sl. No.	**Plate length (mm)**	**Gun Speed (mm/s)**	**No. of passes**	**No. of Returns**	**Feed Rate (gm/min)**	**Mass feed (gm)**	**Mass Deposited (gm)**	**DE (%)**
20Fe	150	300	30	40	30	300.00	158.90	52.97
80Fe	100	300	1	10	29	3.22	1.62	50.27

2.3.2.2 Particle Impact Velocity Calculation

In order to examine the effect of mixing on powder velocity, lot 2 powders were run in a Plasma Giken PCS-800 cold spray system (Plasma Giken Company Ltd, Tokyo, Japan) with nitrogen as propellant gas. The reason that the gun was changed was to avoid nozzle clogging, which had been a problem with the Kinetics gun. As can be seen in Figure 2.10, adding 316L decreases the powder velocity mainly because the 316L has larger particle sizes. It is not known if these measurements represent an average speed of all particles or an average of the two different particles; however, it seems more likely that the velocity of the two powders are different in the mixture, so these values represent the average of the 2 different particles. In other words, the CP Fe particles are probably moving at a higher velocity than the 316L particles in the mixture. It is not known what effect this might have on the cold spray outcome (i.e. DE and porosity).

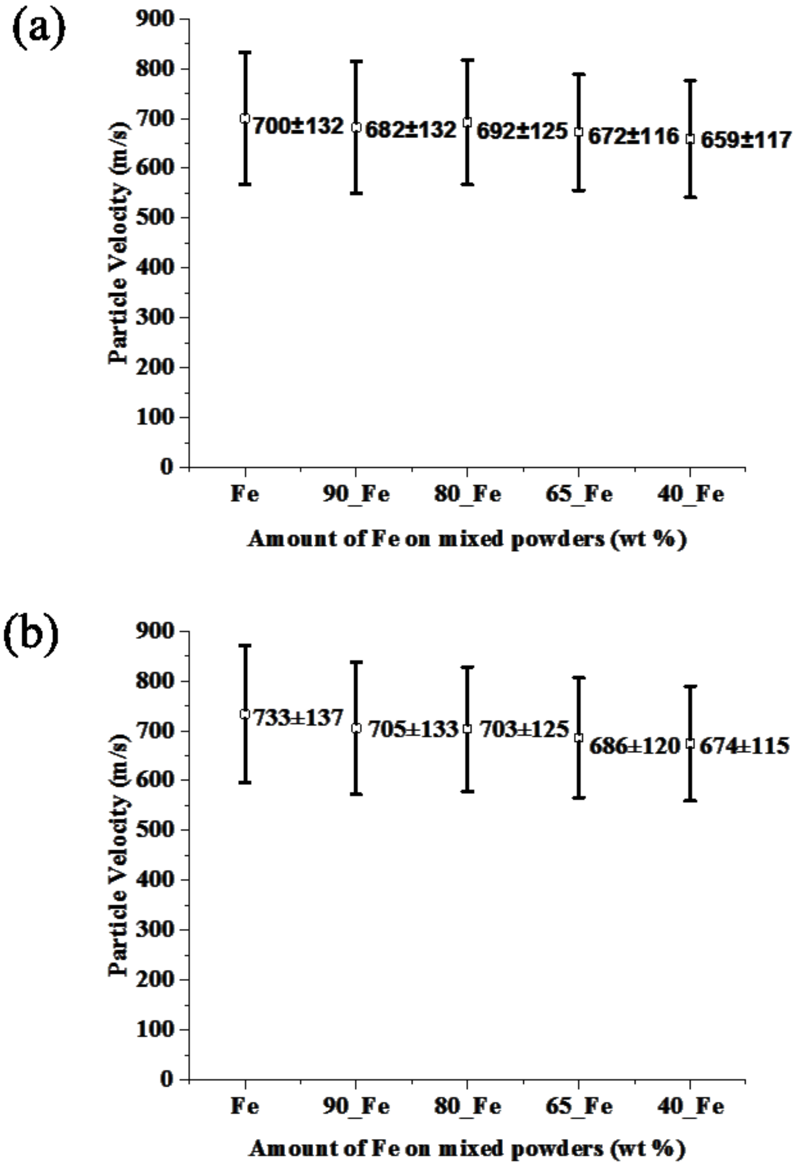

Figure 2.10: Comparison of the particle velocities of mixed powders when changing the gas inlet temperatures from (a) 700^0C to (b) 800^0C at 4 MPa

Keeping spray parameters as same as Table 2.2, PNDO-10-30S glass nozzle was used to avoid clogging. Gas inlet temperatures were increased from 700ºC to 800ºC and inlet pressure was increased from 4 to 5 MPa. The results, shown in Fig. 2.11, reveal what appears to be a relatively small effect of increasing these parameters to the levels described. This type of velocity change was required to increase the DE of lot 3 powders from zero to 50%, which suggests that these velocities are close to the critical velocity for all these powders.

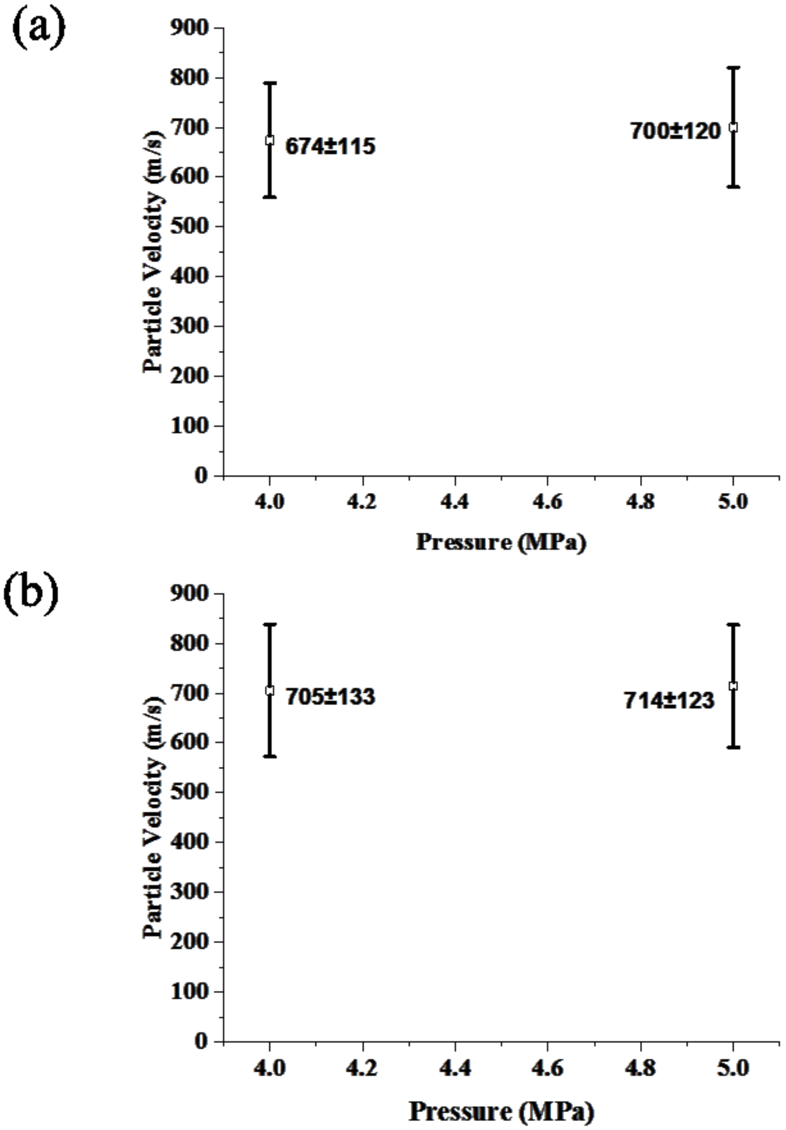

Figure 2.11: Comparison of particle velocities of (a) 40wt%Fe and (b) 90wt%Fe mixed powders with changing pressure at 800^{0}C gas temperature

Figure 2.12 indicates a linear effect of composition on velocity, unlike the effect on DE. Therefore, there is no strong link between DE and velocity in the case of mixing.

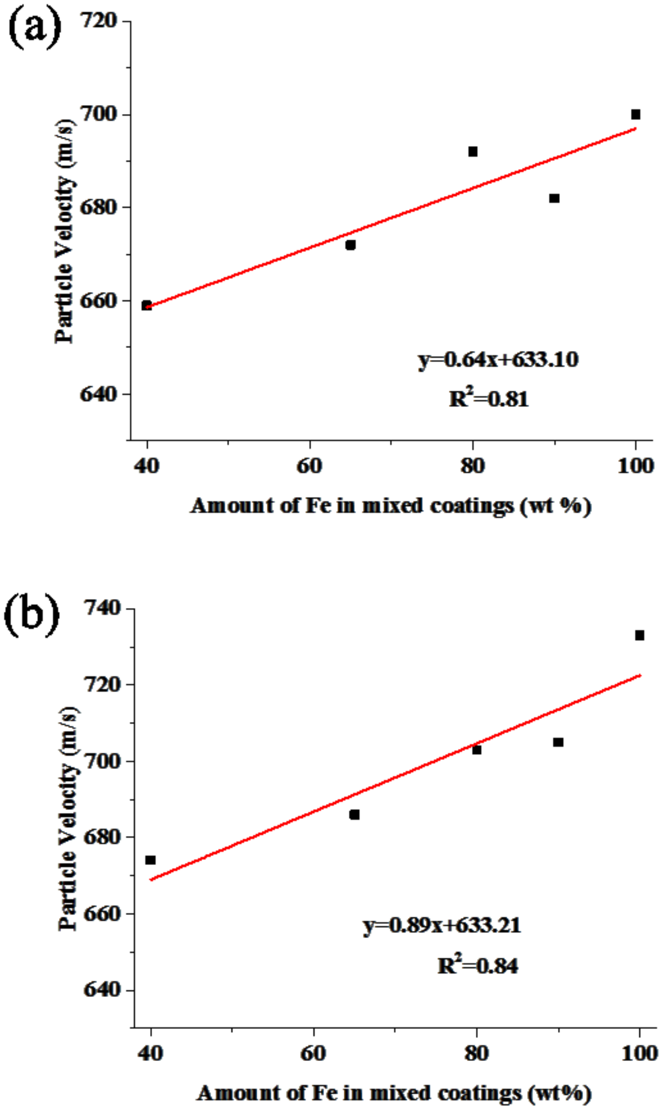

Figure 2.12: Best fit curves of particle velocity as a function of wt% of Fe for (a) 4 MPa, 700°C and (b) 4 MPa, 800°C spray condition

The particle velocity obtained from the cold spray systems gradually decrease with an increasing coarse 316L in the mixture. Considering the average velocities found in Figure 2.10, a linear fit through the data points is shown in Figure 2.11 which indicates that the particle velocity increases approximately linearly with wt% of Fe. Extrapolating the lines shown in Figure 2.12 to 0wt%Fe suggests that the particular impact velocity for pure 316L powder would be about 633 m/s. Particle velocities for spherical +20-45 µm (D_{50}= 27 µm) 316L powders have been previously reported to be 649±102 m/s under similar spray conditions [62], which is consistent with the present results.

Below a certain critical velocity under specific condition, the deposition efficiency drops sharply and a coating is not formed. This critical velocity can be calculated without considering the particle size effect as shown in Equation 1.3 but experimental reports suggest that the size of the impacting particles may affect the critical velocity. As a result, a number of empirical equations have been developed which are applicable for specific materials and spray conditions. Among those, an empirical equation has been developed by T. Schmidt *et.al.* [53] for 316L particles for the specific conditions (*e.g.* 3 MPa pressure and 300°C gas temperature with nitrogen gas) considering the effect of particle size, *i.e.,*

$$v_{crit} = 950.\, d_{particle}^{-0.14} \qquad [2.1]$$

Equation 2.1 suggests that for particles ranging in size from 15-45 micron would have within critical velocities ranging from 650-557 m/s. Although Equation 2.1 is empirical, it suggests that impact velocities found in present conditions are close to the critical velocity.

2.3.3 Coating Characterization

2.3.3.1 Coating Composition

Table 2.8 represents the actual chemical composition of mixed coatings.

Table 2.8: Chemical composition of lot 1 coatings found from ICP-OES (in wt %)

Powder	**Fe**	**Cr**	**Mn**	**Mo**	**Ni**	**Si**	**C**
316L Bulk	70.71	18.50	1.77	0.37	8.41	0.19	0.047
316L	68.70	16.25	1.43	2.20	10.93	0.44	0.057
20Fe	73.17	13.93	1.26	1.90	9.39	0.32	0.039
50Fe	83.29	9.18	0.95	0.13	6.25	0.19	0.040
80Fe	91.75	4.05	0.61	0.57	2.79	0.17	0.050
CP Fe	99.23	0.07	0.37	0.04	0.12	0.10	0.068

Based on the compositions of pure iron and 316L powders, a mass balance has been made to obtain the expected mass fraction of the major elements of each coating. These values are referred to as ‘expected Fe’ or ‘expected Cr’ and so on.

A comparison between the expected mass fraction values and the experimental values of iron, chromium and nickel within the various powder mixtures is shown in Figure 2.12. In addition, an estimate is made of the wt % of CP Fe within the mixed coatings. For example, suppose the CP Fe and 316L powders contain 0.11 and 10.90 wt % Ni, respectively. Hence, the expected amount of nickel in 20wt%Fe coating will be 0.2×0.11+0.8×10.90 or 8.74%. The amount of nickel is found experimentally from ICP-OES to be 9.39% for 20wt%Fe coatings. Now, the weight percentage of the expected amount (e.g., 0.2 and 0.8) is altered so that the expected values are equal to the experimental composition to two decimal places.

The results are given in the chart in Table 2.9. Figure 2.13 indicates that the mixed coatings contain a lower amount of iron than the iron content of mixed powder that is originally sprayed. Also, the mixed coatings contain a larger amount of chromium and nickel relative to the contents of the mixed powder. Chromium and nickel are contributed mostly from the 316L powder whereas the iron comes from both the 316L and CP Fe powders. In conclusion, the higher elemental chromium and nickel in the mixed coatings indicates that 316L powders have a higher deposition efficiency than the CP Fe powder.

However, it is found from this calculation that the amount of CP Fe in the mixed coatings is always 5-7% less than the as-mixed powders. Since the DE of 100% CP Fe is 33% vs 72% for 316L, this ‘loss’ of CP Fe due to spraying seems rather low. Furthermore, above 20% 316L, it has been shown that the DE of the mixtures is lower than predicted by weighted averages. Therefore, the DE characteristics, including retention of CP Fe cannot be explained on the basis of the DE characteristics of one powder, but needs to be explained on the basis of the mixture. Unfortunately more work is required to understand these results.

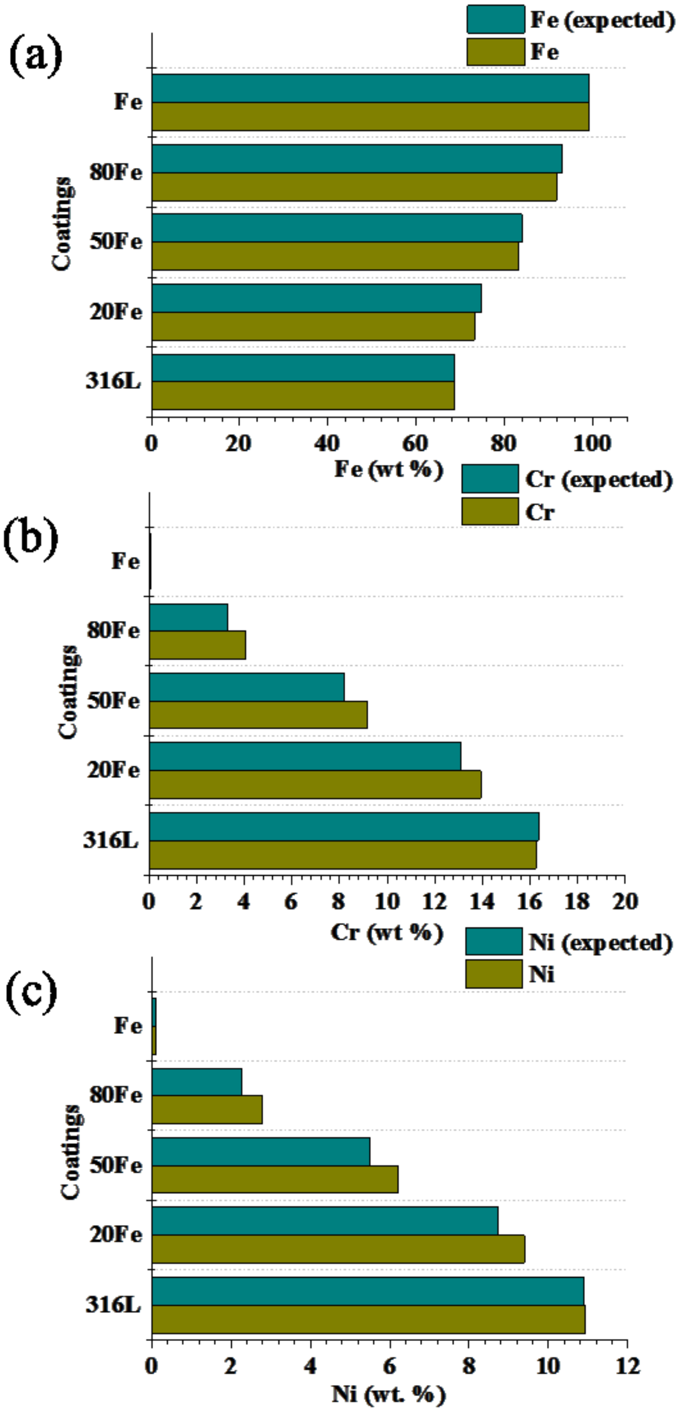

Figure 2.13: Comparison of expected and experimental chemical composition of (a) iron, (b) chromium and (c) nickel

Table 2.9: CP Fe (wt %) on mixed coatings

Coatings	**Calculated wt% of CP Fe in coatings based on powders'**		
	Fe Content (%)	**Cr content (%)**	**Ni Content (%)**
20Fe	14.59	14.91	13.97
50Fe	47.72	44.04	43.33
80Fe	75.44	75.52	75.10

2.3.3.2 Porosity and Microstructure of as-Sprayed Coatings

Figure 2.14 shows images of the as-polished cross sections of the mixed coatings and Figure 2.15 presents the as-sprayed porosity of mixed coatings using lot 1 and lot 3 powders.

The results shown in Figure 2.15 indicate that the as-sprayed porosity of both pure and mixed coating is very low, possibly due to the ease of plastic flow of these two cubic crystallographies. It is possible that the higher particle velocity for CP Fe relative to 316L leads to more higher plastic deformation of the powder, which lowers the resulting porosity of the coatings. Lot 3 CP Fe exhibits the highest porosity probably due to it having the highest hardness.

As-sprayed porosity values of 3.5-4% and 1.2-2.9% have been reported for spherical 316L powders coatings on aluminum and steel substrates, respectively, using similar cold spray parameters [62]. Another study with similar spray conditions produced coating with a 1.6% and 0.2% porosity for irregular 316L powders on a steel substrate using nitrogen and helium as the carrier gases, respectively [61]. The effect of mixing particles on the porosity is a difficult parameter to quantify because of the very low porosity of these powders, but increasing 316L tends to increase porosity.

In terms of microstructures, there are very fine 'dots' in the CP Fe (Figure 2.13(b)) which may be an artefact of specimen preparation. It is clear that both powders have lost their sphericity. However, the morphology of the particles is not even elliptical, which might be expected if the sphere was simply flattened. Therefore, the deformation is being influenced by crystallography, which is to be expected. There is no significant change in the morphologies of the deformed particles when the ‘matrix’ is changed, e.g. comparing 2.14(c) to 2.14(e), the change from a softer matrix to a harder one has not changed the general morphology of the deformed particles. As well, increasing the hardness of the the CP Fe (from lot 1 to lot 3, i.e. 2.14(e) vs 2.14(f)) also has no significant effect on the morphologies.

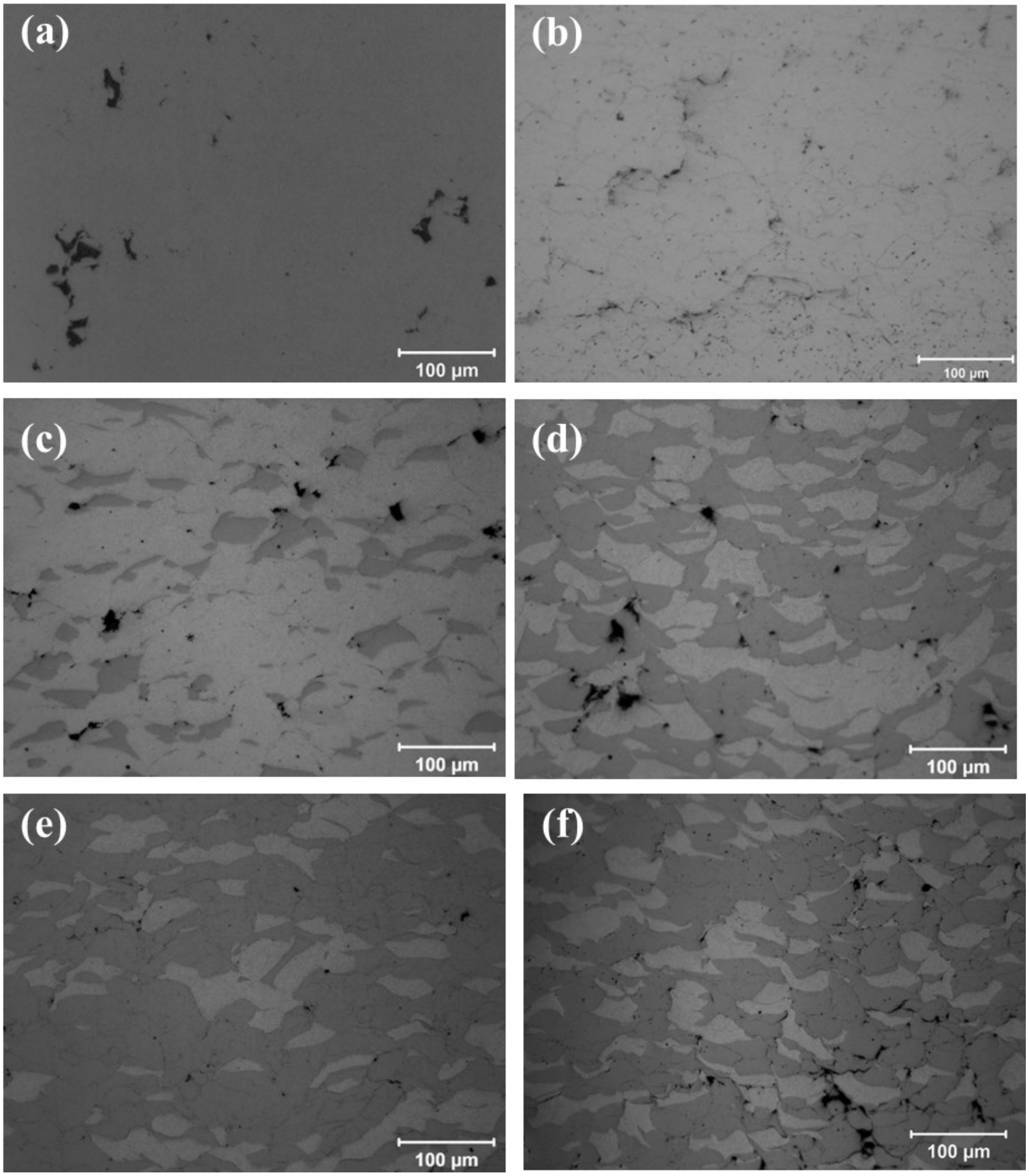

Figure 2.14: Cross-sections of as-sprayed coatings (a) 316L, (b) CP Fe, (c) 20wt%Fe, (d) 50wt%Fe, (e) 80wt%Fe and (f) 80wt%Fe lot 3

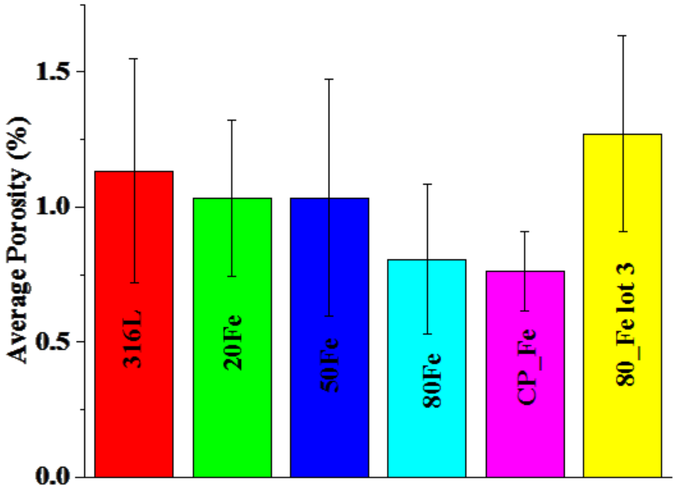

Figure 2.15: Average porosity of as-sprayed coatings

2.3.3.3 Microhardness of as-Sprayed Coatings and Powders

The microhardness of the as-sprayed mixed coatings of lot 1 and lot 3 is shown in Figure 2.16. The work hardening associated with particle deformation during the spray process increases the microhardness of the as-sprayed 316L coatings compared with the 316L powders, which were shown in Figure 2.7 (*i.e.* 226 $HV_{0.05}$ vs 391 $HV_{0.05}$ for 316L powders and coatings, respectively). Similarly the as-sprayed CP Fe coatings also exhibit a higher microhardness than the original CP Fe powder (287.71 $HV_{0.05}$ vs. 347 $HV_{0.05}$ for CP Fe powders and coatings, respectively). The relative change in microhardness during the spraying process is greater for 316L than CP Fe (*i.e.,* 1.72 vs. 1.2 times respectively). However, there is the possibility of an austenite to martensite transformation during mixing, thus the effect of spraying in terms of work hardening the 316L may be less than 1.72. It has been reported previously that a smaller increase in work hardening increases the coating porosity [51], but this was not observed in research.

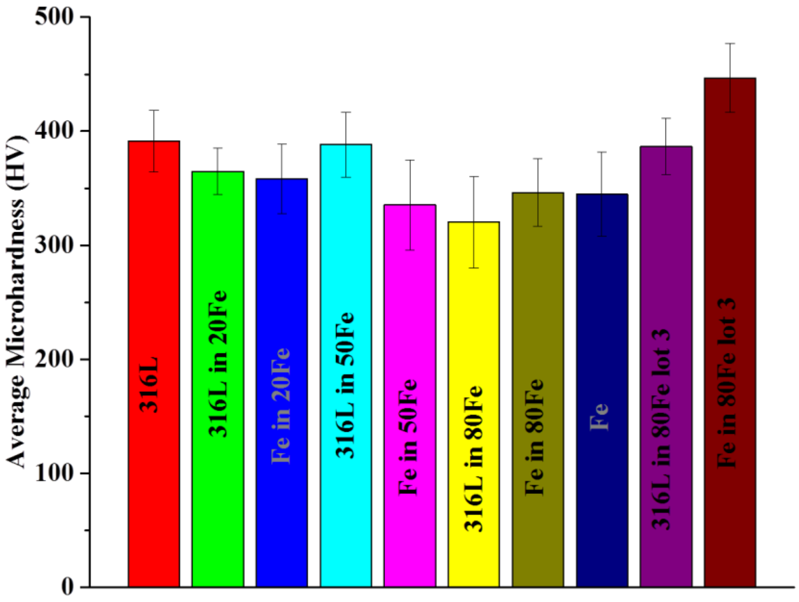

Figure 2.16: Average micro-hardness ($HV_{0.05}$) of as-sprayed coatings

The effect of mixing on microhardness seems negligible for CP Fe but appears to decrease the work hardening in the 316L, reaching its lowest value in the 20% 316L coating. This might be due to some stress shielding provided by the harder CP Fe particles, preventing tamping of the 316L due to subsequent cold spray layers.

2.3.3.4 Phase Observations of as-Sprayed Coatings

Figure 2.17 presents XRD spectra of as-sprayed coatings. Comparing Figure 2.16 with Figure 2.8(a), it can be stated that similar diffraction patterns are exhibited for the powder and as-sprayed coatings. The percentage of ferrite and austenite phase for various coating is presented in Table 2.10. It is observed from Table 2.10 that mixed coatings exhibit lower austenite percentages as compared to the as-mixed powders. This may also be due to strain induced transformation of austenite to martensite during cold spraying.

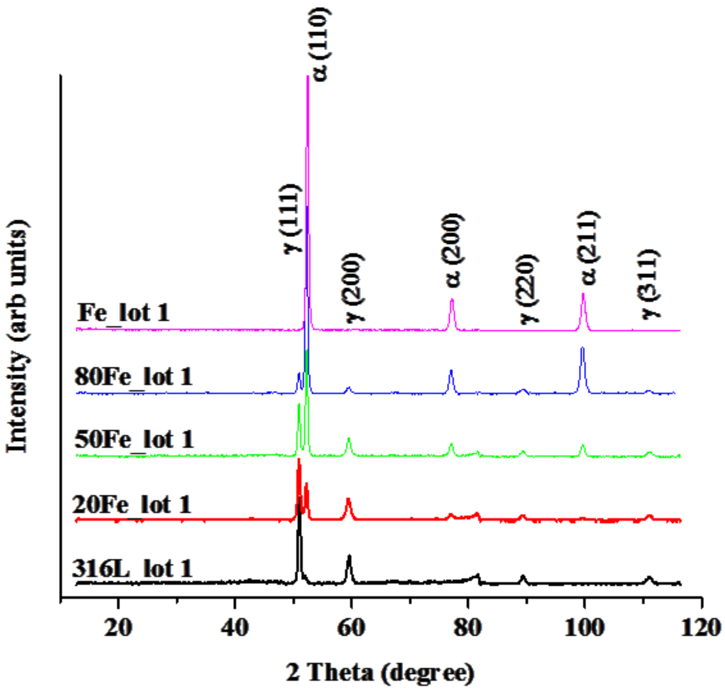

Figure 2.17: XRD of as-sprayed coatings showing the peaks for identified phases

Table 2.10: Phase percentage of ferrite and austenite on as-sprayed coatings

Coatings	Percentages of Phases (%)	
	Ferrite (α)	Austenite(γ)
316L_lot 1	6.2±0.5	93.8±0.2
Fe_lot 1	100.0±0.0	0.0±0.0
20Fe_lot 1	41.4±0.4	58.6±0.4
50Fe_lot 1	78.5±0.3	21.5±0.5
80Fe_lot 1	92.2±0.7	7.8±0.5

Due to the severe plastic deformation, the cold spray process induces residual stress. Residual stress is the distribution of internal stress imposed on the coatings during powder consolidation. In general, internal stress generation may result in deviations in the XRD peaks [84], although this is not observed here.

2.4 Conclusions

The following observations were presented in this chapter:

a. Microhardness values and optical images indicated the presence of martensite in both the 316L and CP Fe powders, which may affect the deposition efficiency of pure and mixed coatings.

b. After mixing, the amount of austenite was reduced, suggesting that some of the austenite had transformed to martensite.

c. DE of 316L was 72%, which was much higher than that of the CP Fe (32%). This may be attributed to the higher hardness of the CP Fe.

d. DE of the 20wt% 316L mixture was much higher than calculated from the weighted average, but the DEs of the 50 and 80wt% 316L mixtures was much lower than predicted.

e. The mixed powders lost about 5 to 7% CP Fe after spraying, due to the lower DE of CP Fe. However, the large difference (more than twice) in deposition efficiency for pure 316L powder vs. CP Fe powder is not consistent with the deposition efficiency of mixed powders. As well, the austenite level in the coating was lower than for the as-mixed powder, suggesting more austenite had undergone strain induced transformation during spraying.

f. The porosity of all coatings was extremely low, possibly due to the ‘easy’ plastic flow properties of the cubic crystallographies of the two powders.

g. Increasing 316L decreased the velocity of the mixed powders probably due to the larger 316L particles. However, the increase in microhardness after impact is lower for CP Fe (1.2 vs. 1.7) than 316L. However, the hardness of the as-mixed powders was not measured and it may be that, if austenite did transform to martensite during mixing, the work hardening during cold spraying is lower than stated.

Chapter 3. **Structural Properties Cold Sprayed Materials**

3.1 Introduction

Conventional as-sprayed coatings exhibit large pores with a network of interlocked splats and cracked boundaries [51]. Incomplete interparticle bonding is observed for as-sprayed coatings due to the effect of work hardening [61]. When a spray coated sample is heat treated, the incomplete interparticle bonding and large pore structure is converted to continuous interparticle bonding with well-distributed fine pores throughout the microstructure. The heat treatment causes the recovery and recrystallization of work hardened grains [61], and in general improves the mechanical properties of materials to be used for stents. In the present chapter, test results will be presented which illustrate the effect of heat treating on the material properties of the spray-coated stent material.

As noted earlier, the key desirable properties for degradable metallic stents are high tensile strength with high ductility and high corrosion rate. The tensile strength with ductility and in vitro degradation rates for common stent materials are given in Table 1.1. It states that iron-based degradable stent materials exhibit better mechanical properties but slower degradation rates than magnesium-based stents which have the highest degradation rates by several orders of magnitude. In this chapter, tests to characterize material properties of as-sprayed and heat treated coatings will be presented.

3.2 Materials and Methods

Coatings prepared with lot 1 and lot 3 powders were used for the tests described in this chapter. Porosity and Microhardness test details were given in chapter 2. The mechanical tests were carried out using static test equipment including micro shear punch and tensile tests. An MTS hydraulic machine with anvils and pressure bars was used for both the micro shear punch and tensile tests of the coatings, respectively. Finally, the morphology of the fractured surfaces was characterized using a Hitachi SU3500 scanning electron microscope.

3.2.1 Micro-shear Punch Test

Lot 1 powders were sprayed on an aluminum substrate, but the substrate was deformed in such a way that tensile specimens could not be produced. Thus, shear punch tests were performed instead of tensile tests since, the deformation and failure behavior of both tests are analogous [85]. The idea of shear punch test was first reported in Lucas *et al.* [86] and the test has been adapted and improved by Huseyin *et al.* [87]. Load-displacement curves obtained from micro shear punch test can be correlated with conventional tensile test to obtain yield and ultimate tensile strength of the coatings [87]. Specimen preparation is very simple in shear punch test and a greater volume of material deformation is tested compared to a microhardness test [85]. However, a non-uniform deformation zone is produced with a highly complex stress-strain state in shear punch test. Thus, a complete force-displacement curve cannot be converted to stress-strain curve. Instead, the yield and ultimate tensile strengths can be reported rather than the entire force-displacement curve [87]. The equipment used for the micro shear punch test is shown in Figure 3.1.

Micro shear punch test is a straight forward test based on the blanking operation. Here, a flat, cylindrical punch of 1.55 mm diameter is forced to punch a hole in a flat, thin sample. The sample was clamped on a die with a 2 mm diameter holes centered to the punch. A load cell connected beneath the specimen transfers shearing action on the sample to load-displacement curve. In the micro shear punch test, the strain rate was kept constant at 0.001 s^{-1}. The sample size was 10 mm by 4 mm, with 0.60-0.85 mm thick coatings are prepared for the micro shear punch test. The average shear stress, τ is related to shear force, F as follows [87]:

$$\tau = \frac{F}{2\pi r t} \qquad [3.1]$$

Where, t is the sample thickness and r is the average radius of shear punch and die hole. Considering shear punch test results in pure shear stress, τ under pure shear load F applied by a shear punch of average radius, r on a sample of thickness, t. The yield and ultimate tensile strength (σ_y and σ_{ul}) are mainly related to the yield and ultimate shear punch force (F_y and F_{ul}), respectively, as follows [87]:

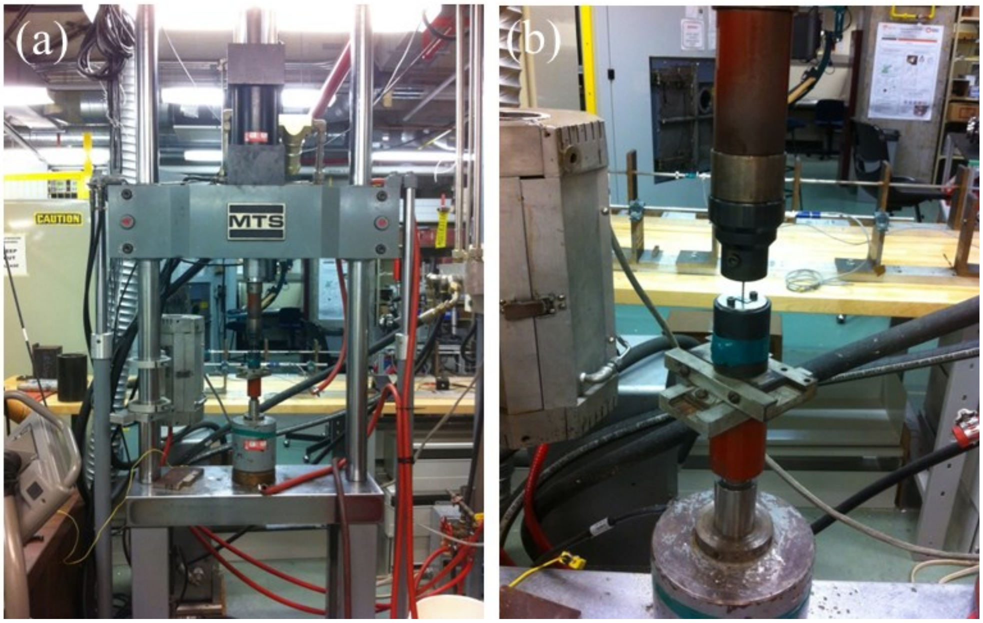

Figure 3.1: Shear punch tests (a) MTS machine and (b) test procedure center

$$\sigma_{y,ut} = C.\tau_{y,ut} = C[\frac{F_{y,ut}}{2\pi rt}] \quad [3.2]$$

$$R.A. = \frac{D_f}{t} \quad [3.3]$$

Where, *R.A.* is the tensile reduction in area, D_f is the failure shear punch displacement, and *C* is the regression factor. *R.A.* indicates the range of ductility being 0 for completely brittle and 1 for completely ductile.

3.2.2 Tensile Test

Tensile test samples were machined according to ASTM E-8 sub-standard size with a strain rate of 0.001 s^{-1}. Jaw-type grips were used to hold the sample for tensile tests on the MTS hydraulic testing machine. Figure 3.2 is a schematic illustration of the specimen for tensile testing, with the longitudinal direction along spray direction.

The highly work-hardened state of an as-sprayed coating results in a significant loss of material ductility. Annealing is performed to relieve the work-hardening of coatings so that the fabricated materials and stents will have a sufficient amount of ductility to withstand the deformation from cyclic loading after stent deployment. Here, the coating is annealed after spraying in a temperature-controlled ThermCraft box furnace (model: XSB-8-8-12-C, Winston-Salem, NC, USA). Prior to testing, the coating samples were wrapped with a steel sheet and annealed at 1100^0C for 1 hour in an argon gas environment to minimize oxidation of the coating. After one hour had elapsed, the sample remained in the oven for a further 30 minute while the oven temperature was reduced. After the 30 minutes had elapsed, the sample was removed from the oven and allowed to cool to room temperature. The sample was then ground to flatten the surface. After grinding, coupons were fabricated using electrical discharge machining, EDM (108521 Canada Inc., Montreal-Nord, QC, Canada). Photographs of the various steps in the fabrication process are shown in Figure 3.3.

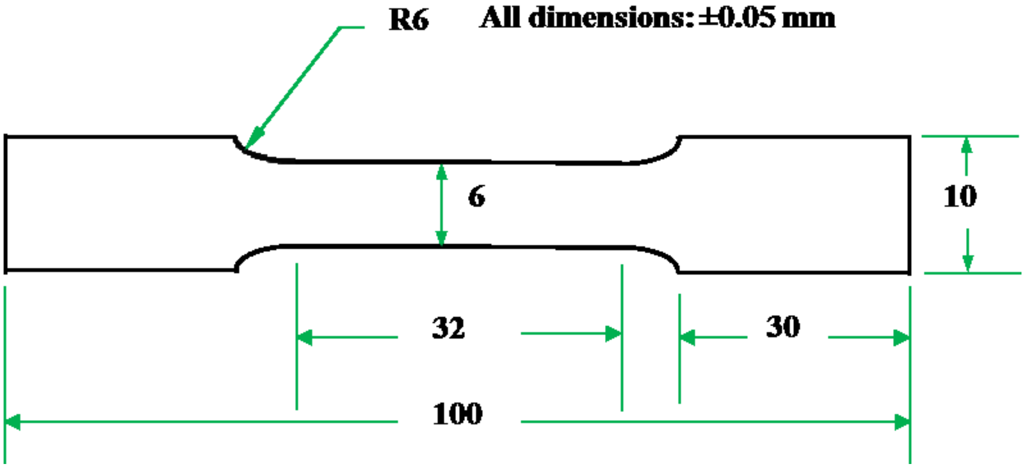

Figure 3.2: Schematic of ASTM E8 specified tensile coupons (dimensions are shown in millimeters)

The samples were then polished in order to eliminate any micro-cracks on the surface. Photographs of the MTS machine used for the tensile test including a close-up view of a clamped sample are shown in Figure 3.4. The test samples in all the tensile and shear punch tests were preloaded with a force of 100N to maintain the same preload values for all the static tests.

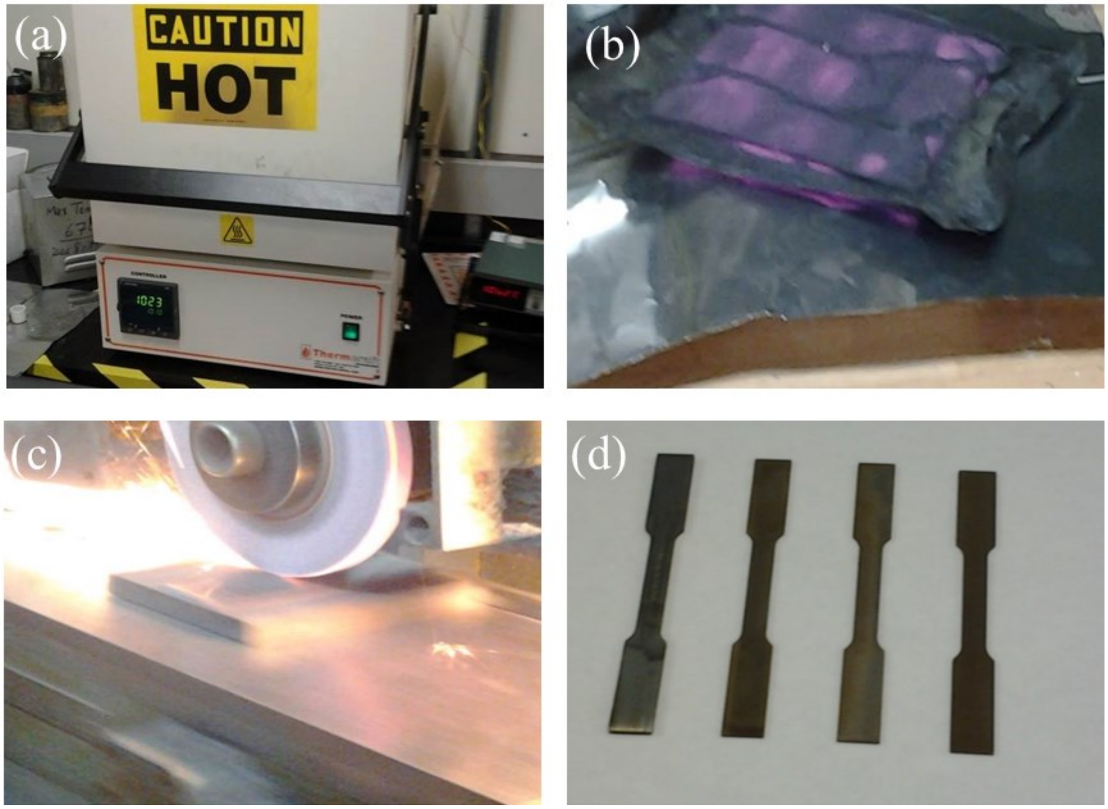

Figure 3.3: Processing of the tensile coupons (a) argon atmosphere furnace (b) air cooling after heat treatment (c) Grinding and (d) tensile coupons

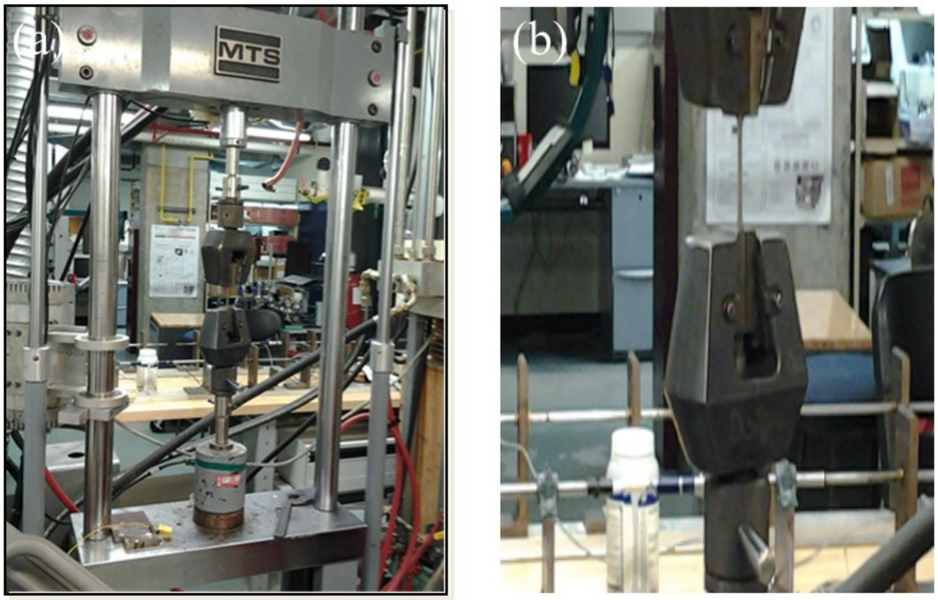

Figure 3.4: (a) MTS tensile testing machines (b) tensile test procedure

3.3 Results and Discussions

3.3.1 Changes of Porosity with Heat Treatment

Figure 3.5 shows the effect of heat treatment temperature on the porosity of samples exposed for 1 hour over temperatures of 400, 800, 1000 and 1100^0C, respectively under an argon atmosphere for one hour. In general, annealing reduces the sample porosity. Significant changes in porosity start to occur above a temperature of about 600^0C because the coatings start to recrystallize above this temperature. All mixed coatings exhibited porosities less than 0.6% after annealing at 1100^0C. This reduction in porosity at 1100°C can be attributed to sintering at bounded inter-particle interfaces.

The highest porosity was observed for the 80wt%Fe_lot 3 samples, *i.e.,* a porosity of 0.54±0.16% after annealing at 1100°C for 1 hour. There were significant batch-to-batch variations, as shown by the 80wt%Fe lot 1 sample which had porosities about one-third less than the lot 3 sample.

For 316L and CP Fe coatings, Figure 3.6 shows the average with standard deviations for multiple porosity measurements with under various heat treatments. The porosity of the 316L coating is initially higher than the CP Fe coating, but drops more rapidly with heat treatment temperature. Figure 3.7 exhibits low magnification optical images of 316L (Figure 3.7(a) to Figure 3.7(d)) and CP Fe (Figure 3.7(e) to Figure 3.7(h)) particles. 316L cross-sections only exhibit pores without any cracks which indicates better inter-particle bonding of 316L. CP Fe, on the other hand, exhibits very few cracks with general pores. Cracks do not reduce even after annealing at 1100°C for one hour.

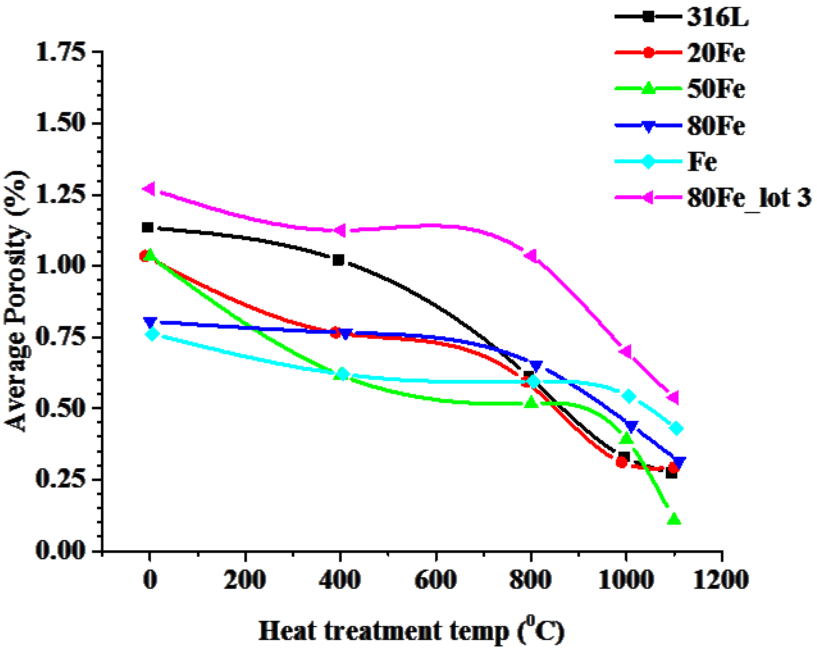

Figure 3.5: Change of porosity with heat treatment

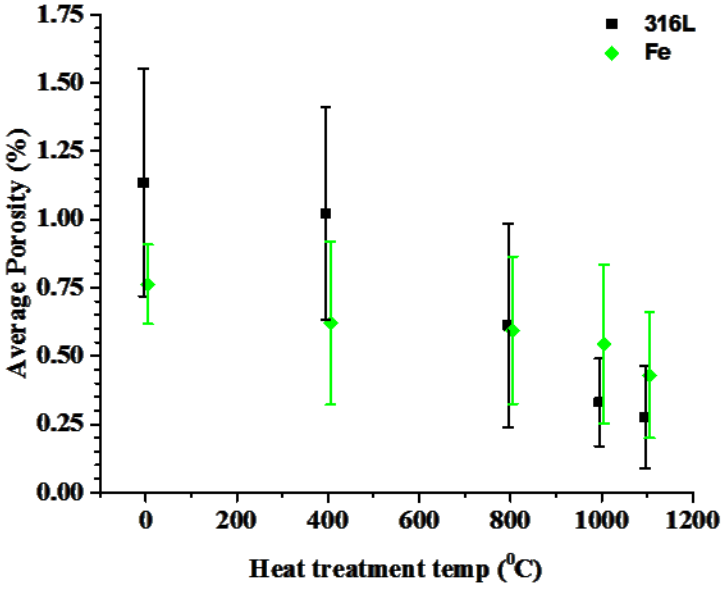

Figure 3.6: Average with standard deviations of porosities of pure coatings

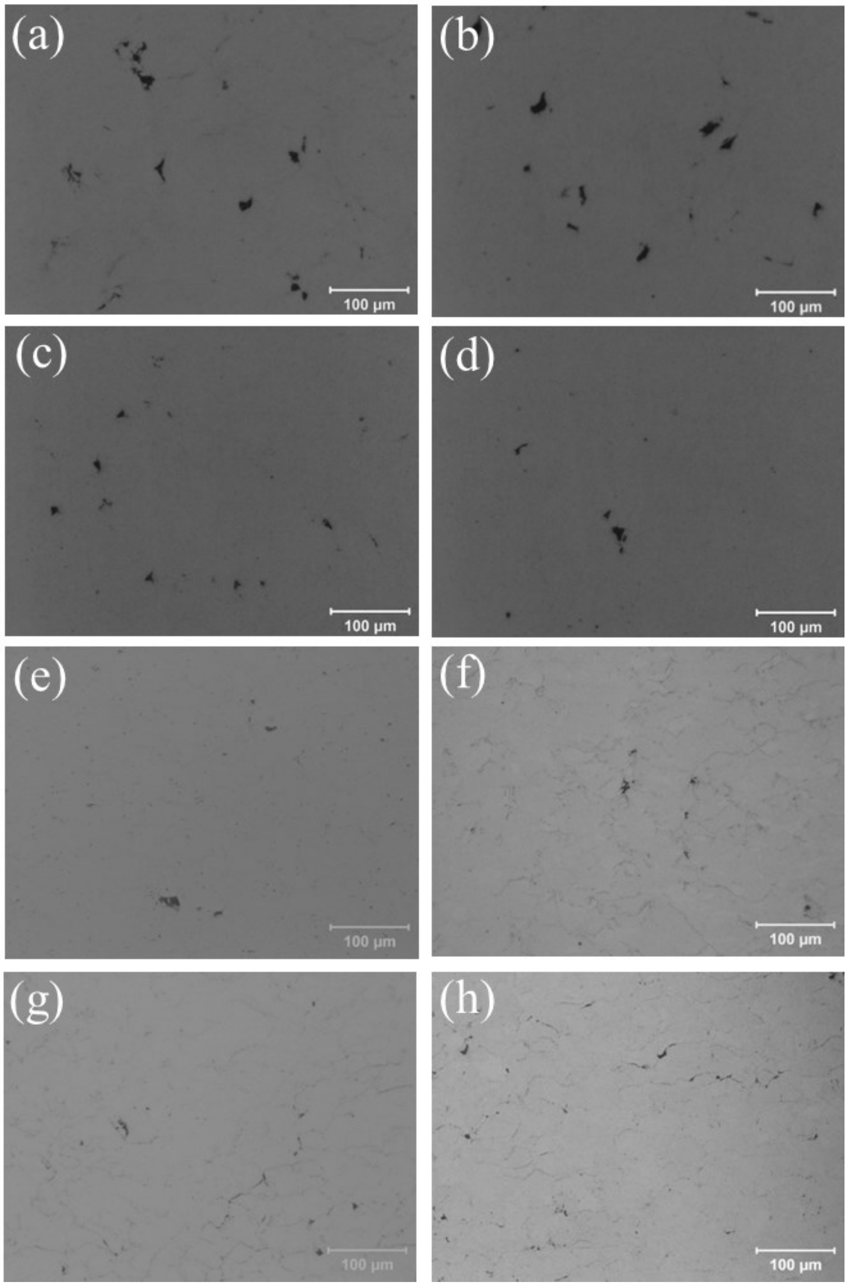

Figure 3.7: Optical microstructure of 316L at (a) 400°C, (b) 800°C, (c) 1000°C, (d) 1100°C and CP Fe at (e) 400°C, (f) 800°C, (g) 1000°C and 1100°C

Figure 3.8 shows that 50wt%Fe mixed coatings have the lowest porosity after heat treatment possibly due to having the maximum CP Fe/316L interfaces, which may facilitate sintering due to higher diffusion activity because of chemical concentration gradients, or perhaps there is more deformation at these interfaces promoting intimate contact between the interfaces. The microstructural observations for all mixed coatings are similar to Figure 3.7.

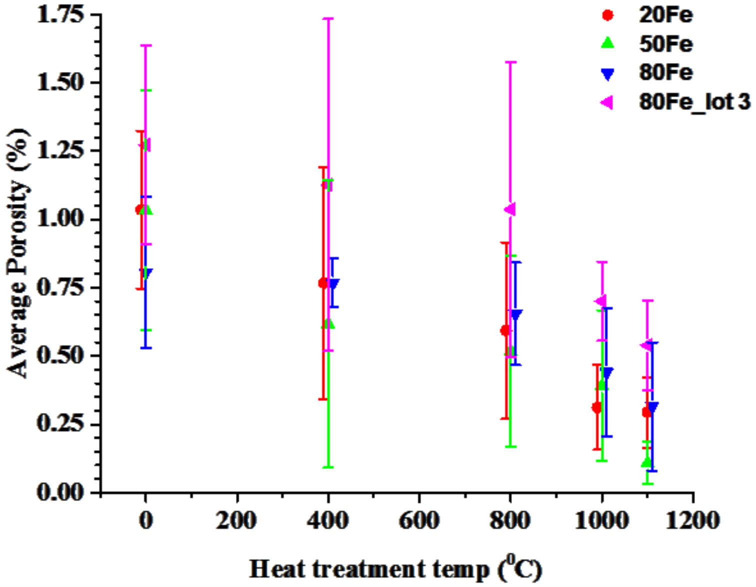

Figure 3.8: Average with standard deviations of porosities of mixed coatings

Figure 3.9 exhibits cross-section of 20wt%Fe and 50wt%Fe. Here, dark and bright areas represent CP Fe and 316L particles, respectively. Continuous coarse pores with a few fine pores and very few cracks are observed. Pores are reduced after heat treatment at 1100°C, cracks were not reduced at all.

For 80wt%Fe, Figure 3.10 exhibits a few cracks among Fe/Fe, Fe/316L and 316L/316L inter-particles along with coarse pores and some fine pores. The number of cracks is higher, which is likely due to the higher amount of CP Fe. The 80wt%Fe lot 3 coatings produced the largest number of cracks and pores. In addition, a network of continuous fine pores was present, as seen in Figure 3.10(g) even after annealing of the sample. Compared to 80wt%Fe lot 3, 20wt%Fe lot 3 coatings exhibit fewer pores and fine cracks after annealing which again illustrates the better cold sprayability of 316L particles in comparison with CP Fe. The deformed particle structure of the mixed coatings observed in Figure 3.9 and 3.10 is also consistent with their relatively low porosity. Other than cracks and pores, very few inclusions are observed.

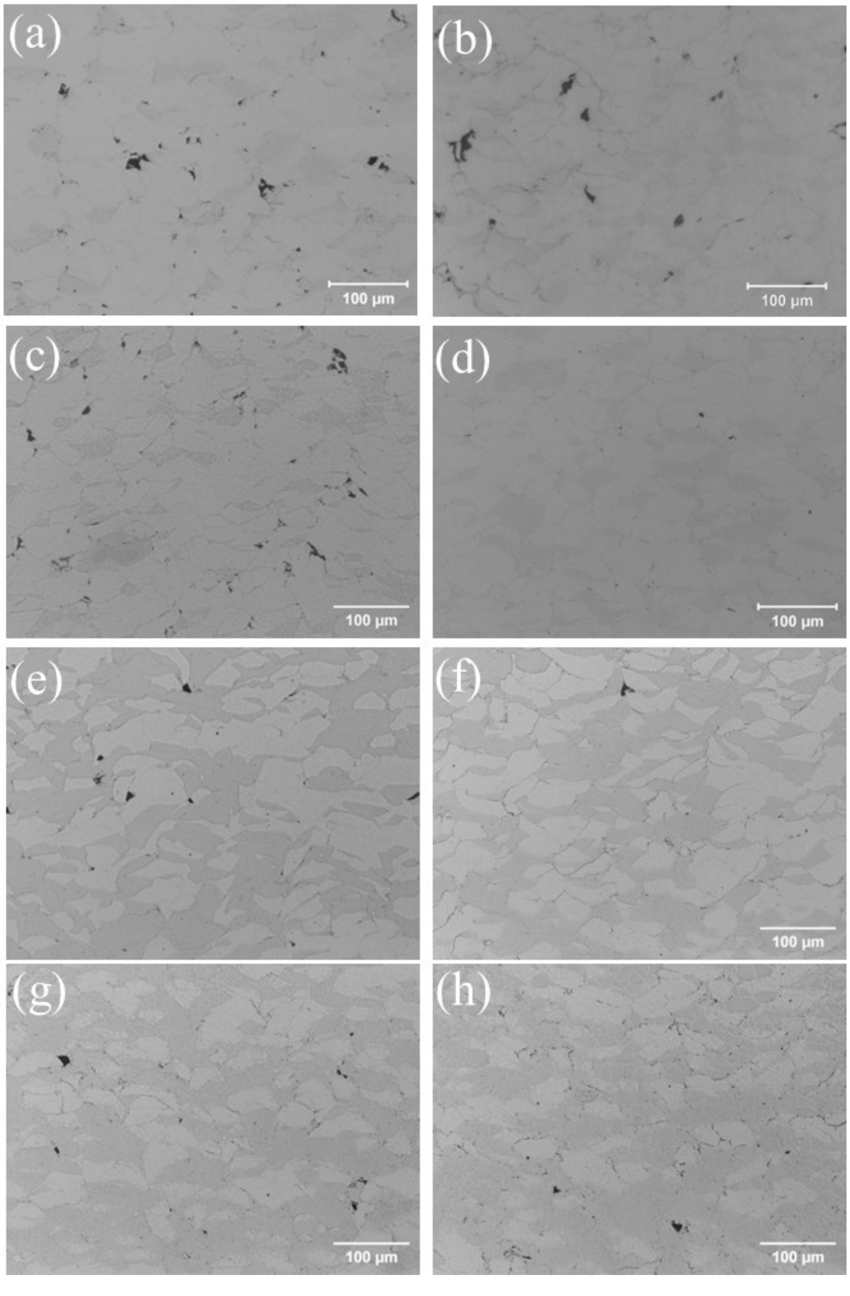

Figure 3.9: Optical microstructure of 20wt%Fe at (a) 400°C, (b) 800°C, (c) 1000°C, (d) 1100°C and 50wt%Fe at (e) 400°C, (f) 800°C, (g) 1000°C and (h) 1100°C

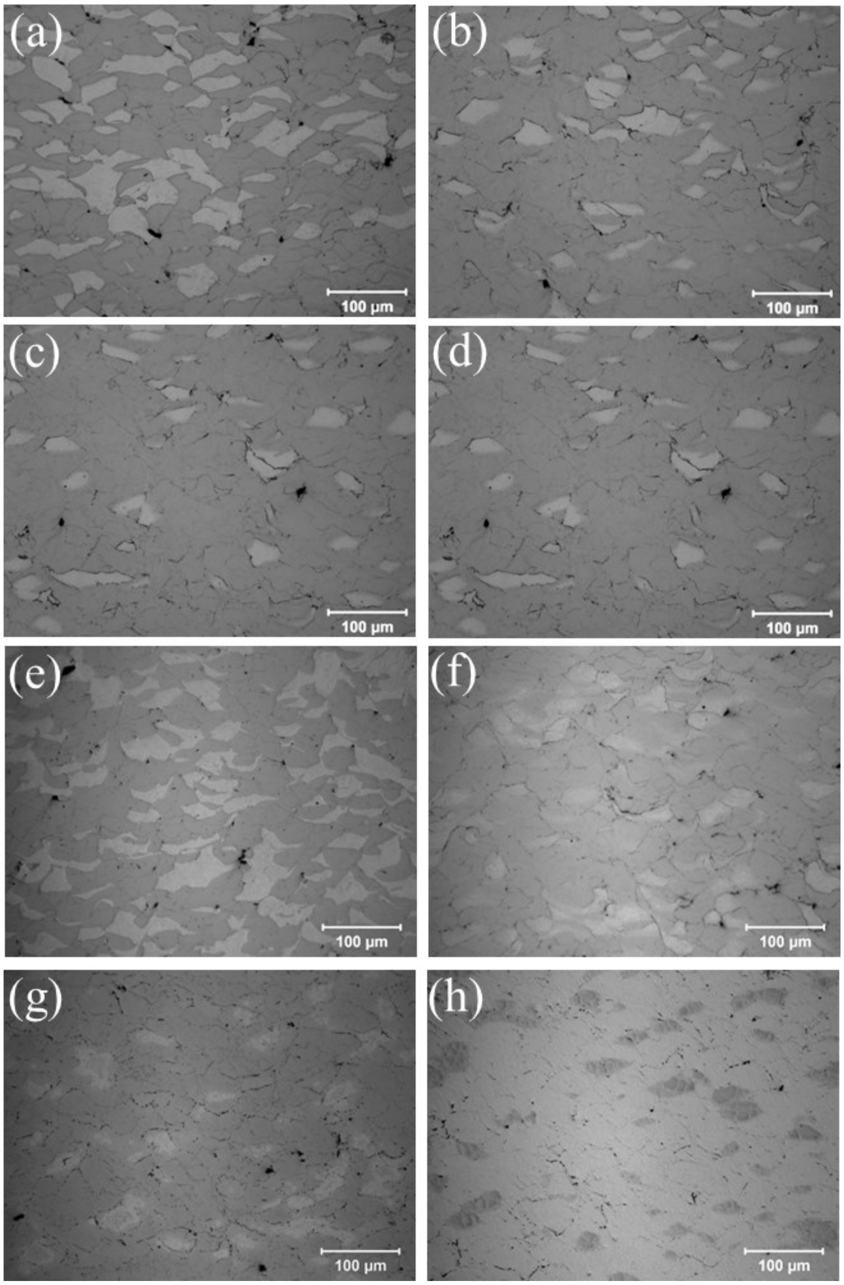

Figure 3.10: Optical microstructure of 80wt%Fe at (a)400°C, (b)800°C, (c) 1000°C, 80wt%Fe lot 3 at (e) 400°C, (f)800°C, (g) 1100°C and (h) 20wt%Fe lot 3 at 1100°C

3.3.2 Changes of Microhardness with Heat Treatment

Figure 3.11 exhibits Vickers microhardness of as-sprayed and heat-treated coatings. The microhardness was tested on both volume fractions in a mixed coating distinguished by optical microscopes attached with the microhardness tester. Here, "Fe in 20Fe" represents the microhardness of Fe in the 20wt%Fe mixed coatings in Figure 3.11.

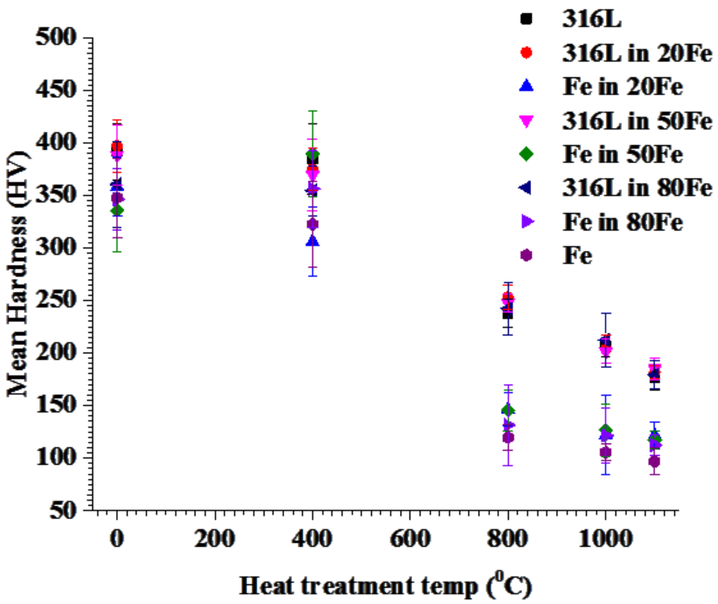

Figure 3.11: Average micro-hardness of as-sprayed and heat treated coatings for CP Fe and 316L

Up to 400 °C there is little effect of temperature on microhardness. Between 400°C and 800°C there is a substantial decrease in microhardness with CP Fe falling below 316L; this difference is maintained to 1100°C. Therefore, the recovery and recrystallization, that occurs from 400 to 800^{0}C releases the work hardening of the sprayed coatings and lowers the hardness. Also, since martensite appears to have been in the microstructures, these heat treatments will also transform the martensite to austenite or ferrite. Therefore, at room temperature the structures are martensite and dislocation free, and stainless steel is harder mainly because of solid solution strengthening.

Stainless steel, 316L coatings always exhibit higher microhardness than CP Fe coatings. Figure 3.11 indicates a sudden drop in microhardness in between 400 to 800^{0}C. However, CP Fe exhibits a larger drop in microhardness from 322.2 to 119.7HV$_{0.05}$

during recrystallization as compared to the drop of microhardness observed for 316L. The higher drop of microhardness after recrystallization in CP Fe can be attributed to the lower plastic deformation and lower dislocation density of CP Fe coatings [68]. The hardness of as-sprayed coatings does not change when they are annealed at 400°C and furthermore, the microhardness does not change significantly when the coating is annealed from 800 to 1100^{0}C. Therefore, the recovery and recrystallization, that occurs from 400 to 800^{0}C releases the work hardening of the sprayed coatings and lowers the hardness starting after the recrystallization temperature of stainless steel which is around 725^{0}C.

The CP Fe has lower microhardness than 316L in all mixed coatings and exhibits a similar softening characteristic as compared to pure coatings. As-sprayed 316L and CP Fe maintain almost the same microhardness and very little change in hardness occurs when mixed coatings are annealed at 400^{0}C. Although the hardness is reduced when annealing at 800°C, a distinction is observed between the hardness of 316L and CP Fe for both pure and mixed coatings. Finally, the hardness reduces to almost bulk Fe or bulk 316L after annealing at 1100^{0}C. 80wt%Fe exhibits a hardness of 112.5±9.6HV and 179.31±12.91HV on CP Fe and 316L particles, respectively inside 80wt%Fe coatings after annealing at 1100°C. Closely similar softening kinetics are observed for 316L/Co-Cr mixed coatings during annealing of mixed coatings [68].

3.3.3 Micro Shear Punch Testing of Coatings

Figure 3.12 to 3.16 exhibit the force-displacement curves for static shear punch tests of pure and mixed coatings for different heat treatment conditions.

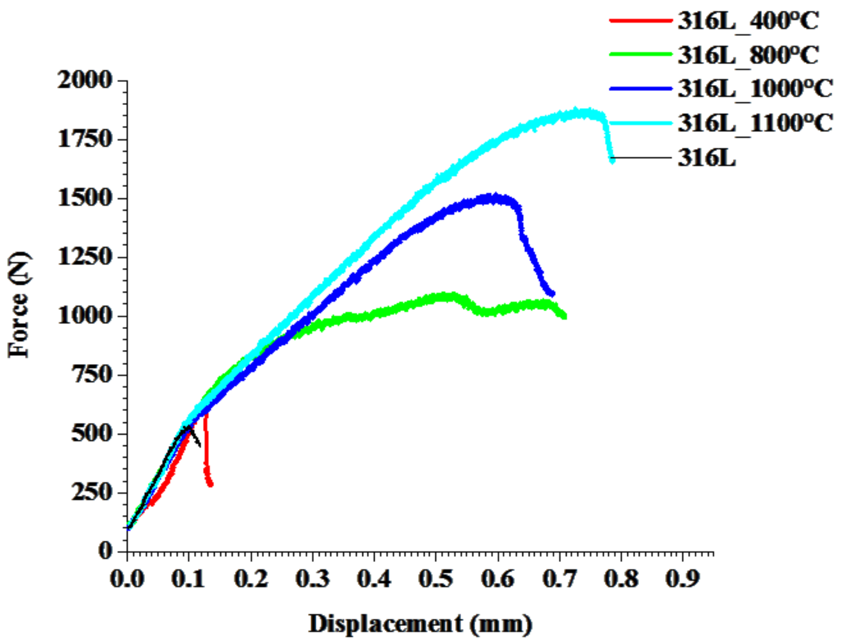

Figure 3.12: Force vs. displacement curves of shear punch test for 316L at different annealing temperature

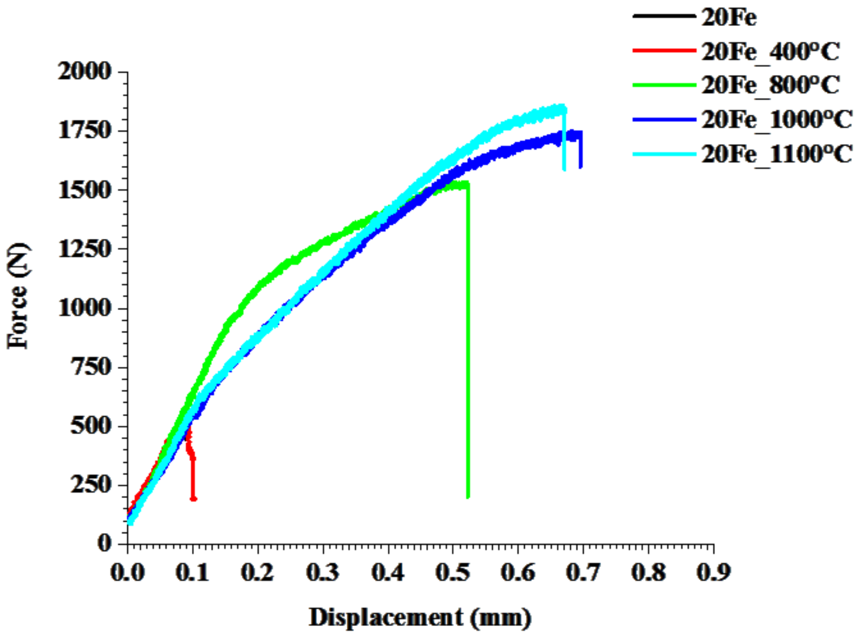

Figure 3.13: Force vs. displacement curves of shear punch test for 20wt%Fe at different annealing temperature

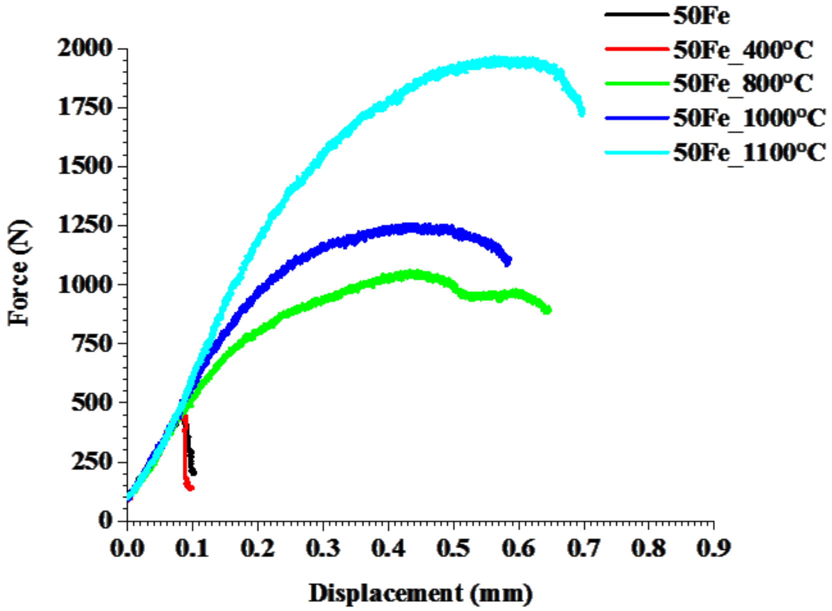

Figure 3.14: Force vs. displacement curves of shear punch test for 50wt%Fe at different annealing temperature

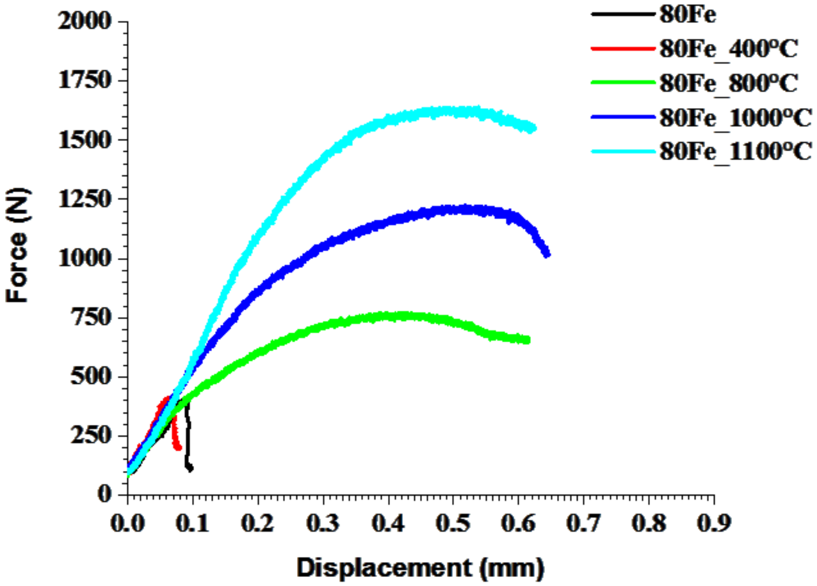

Figure 3.15: Force vs. displacement curves of shear punch test for 80wt%Fe at different annealing temperature

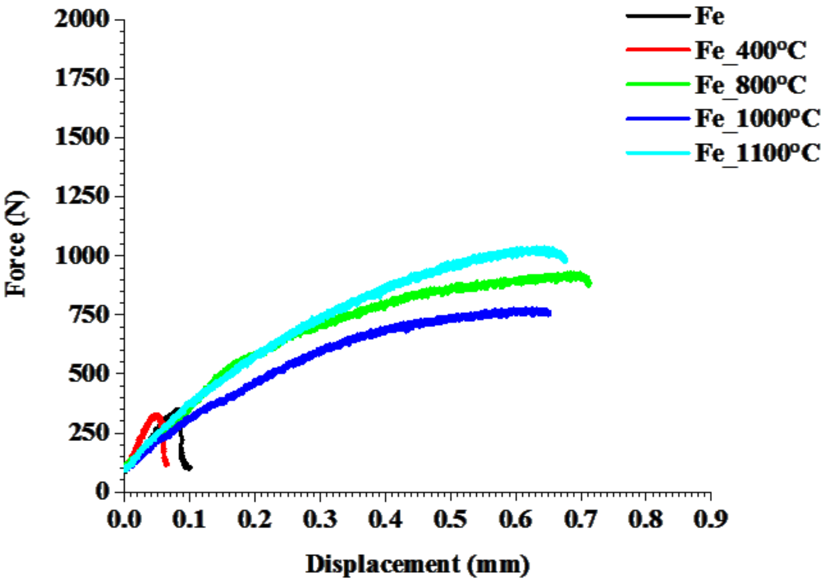

Figure 3.16: Force vs. displacement curves of shear punch test for CP Fe at different annealing temperature

The figures indicate that as-sprayed coatings and annealed coatings at 400^{0}C fracture at low forces and displacements. A significant increase in the force and displacement at fracture is observed when the coating is annealed at 800°C. The maximum force and displacement at fracture is attained for coatings annealed at 1100°C. For the single component coatings, all the flow curves follow the same shape regardless of the annealing temperature. In other words, the fracture strength increases because the ductility is increasing, but the work hardening rate remains the same. For the mixed powders, with increasing annealing temperature, the ductility is increasing but the work hardening rate is also increasing. This suggests there is a significant change in microstructure taking place.

It has been shown that cold spraying leads to work hardening and, in general, annealing of a work hardened structure leads to an increase in ductility because the dislocations are removed allowing dislocation motion to take place. However, in cold spray, there is a further complication of interparticle bonding. In the as-sprayed material, it is likely that the interparticle bonds are very poor and therefore the as-sprayed ductility is very low mainly because of the interparticle bonds, with a very minor effect, if any, of work hardening. This leads to an as-sprayed low strength and low ductility. Annealing then increases the interparticle bond strength by ‘sintering’ and also softens the material be recrystallized. Therefore, the strength increases mainly because the ductility has increased because the interparticle bonding has much improved.

In the single component structures, there will not be many other changes that occur due to annealing, but in the mixed structures there are two rather different metals in terms of flow properties, CP Fe and 316L, as was seen in Figures 3.13 and 3.16. It seems as though the effect of annealing is to transform the properties of the composite from that of CP Fe to that of 316L. This may be because sintering of the respective particles (i.e. Fe/Fe; 316L/316L and Fe/316L) is taking place at different temperatures, so that the structure is transforming from something which has largely one type of sintered structure to one that finally has a mixed bonding character.

As mentioned earlier the shear strength vs. % reduction in area may be determined and is shown in Figures 3.17 to 3.21.

The figures show that shear strength of the coating are concentrated into two regions: one region with shear strength similar to the as-sprayed coating and another region where the heat treatment has significantly increased the shear strength. All coatings exhibit an improvement in the shear strength at 800°C which indicates that sintering has improved ductility. Further improvement in the shear strengths of these coatings indicates a more sintering. Mixed coatings, even with only 20wt% 316L, provide higher or equal shear strength values with a slightly lower reduction in area compared to 100wt% 316L. In addition, CP Fe provides lower shear strength than 316L coatings but both pure coatings exhibit more than 90% reduction in area before ultimate fracture.

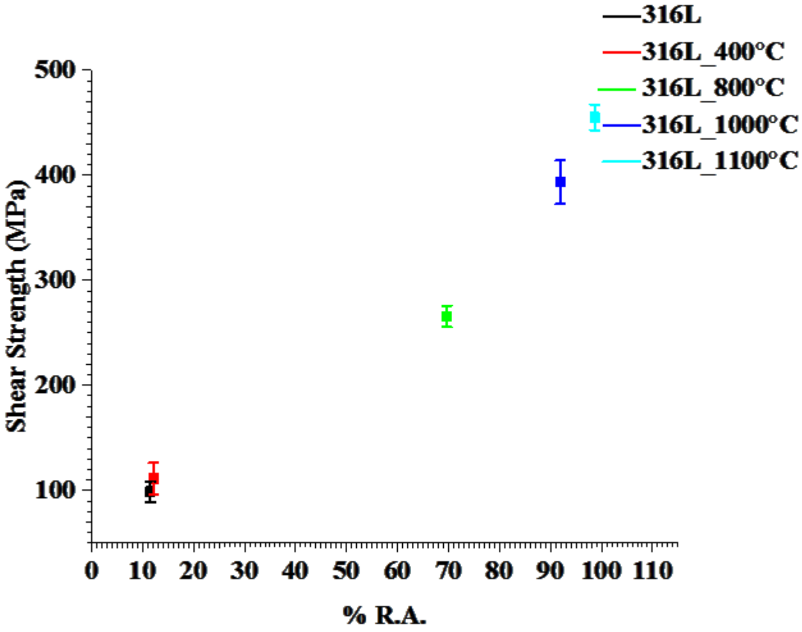

Figure 3.17: Shear strength vs. % area in reduction curve for 316L (all the trials are generated with triplicates)

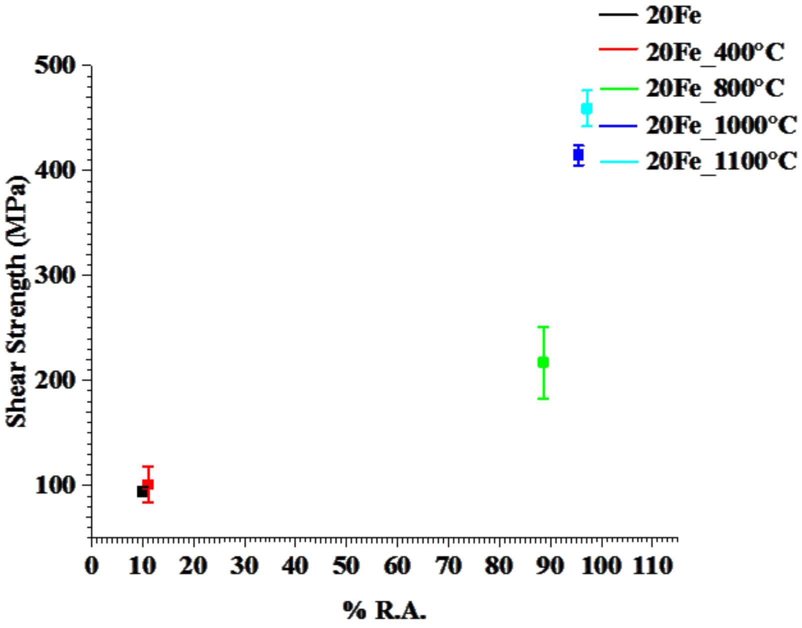

Figure 3.18: Shear strength vs. % area in reduction curve for 20wt%Fe (all the trials are generated with triplicates)

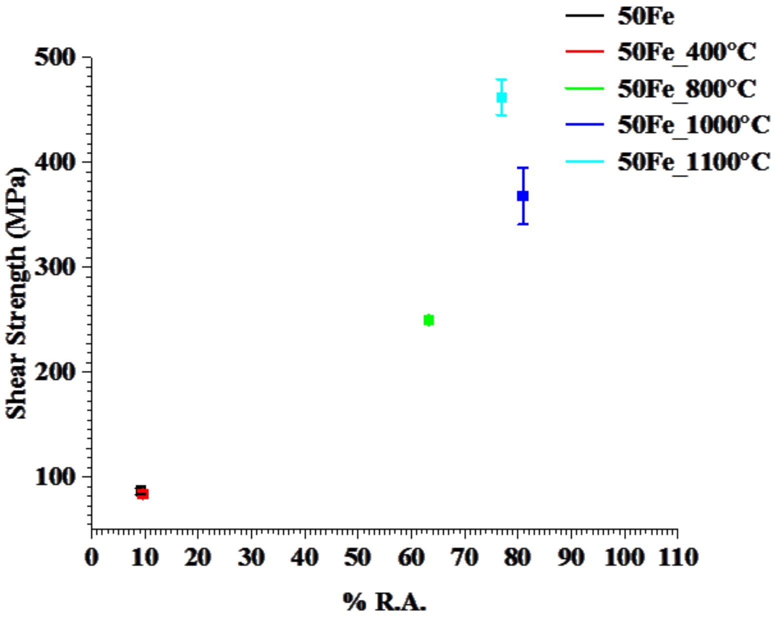

Figure 3.19: Shear strength vs. % area in reduction curve for 50wt%Fe (all the trials are generated with triplicates)

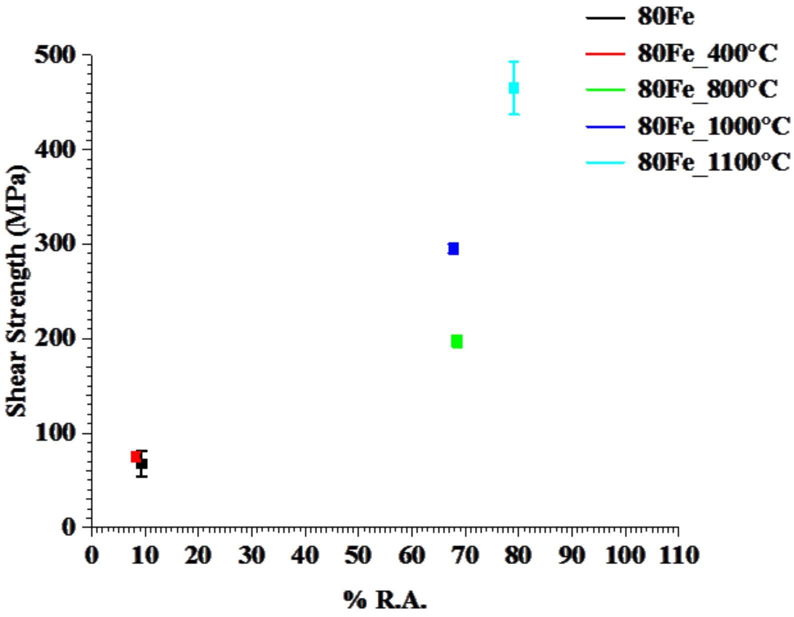

Figure 3.20: Shear strength vs. % area in reduction curve for 80wt%Fe (all the trials are generated with triplicates)

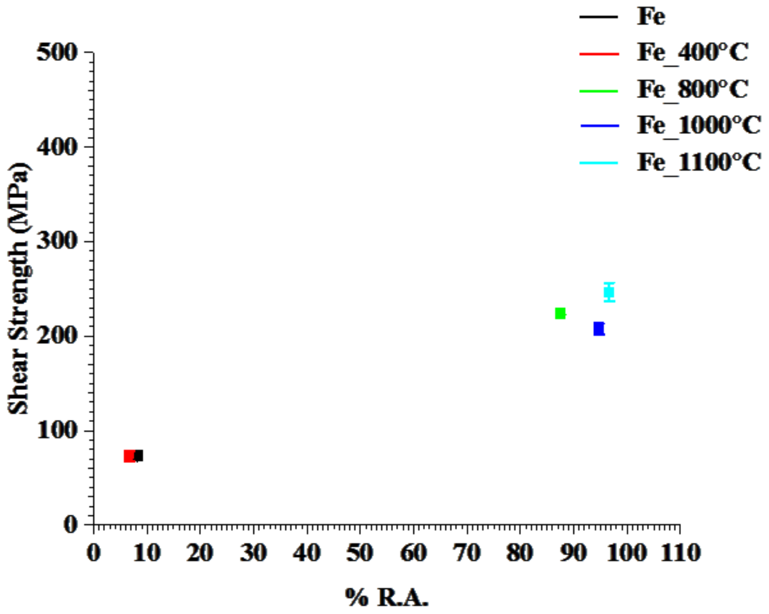

Figure 3.21: Shear strength vs. % reduction in area curve for CP Fe (all the trials are generated with triplicates)

Among the mixed coatings, 20wt%Fe exhibits a higher reduction in area compared to the 50wt%Fe and 80wt%Fe coatings. Also, the CP Fe coating has the highest reduction in area among all other coatings. The fractured surfaces from the shear punch tests are observed using a high resolution scanning electron microscope and the results are shown in Figure 3.22. CP Fe exhibits some dimpled structures which is an indication of ductile behavior whereas, the mixed coatings in general did not exhibit dimpled microstructure. For example, the fractured surface of the 80wt%Fe sample shown in Figure 3.23 exhibits a dimple-like fracture surface, which illustrates excellent metallurgical bonding.

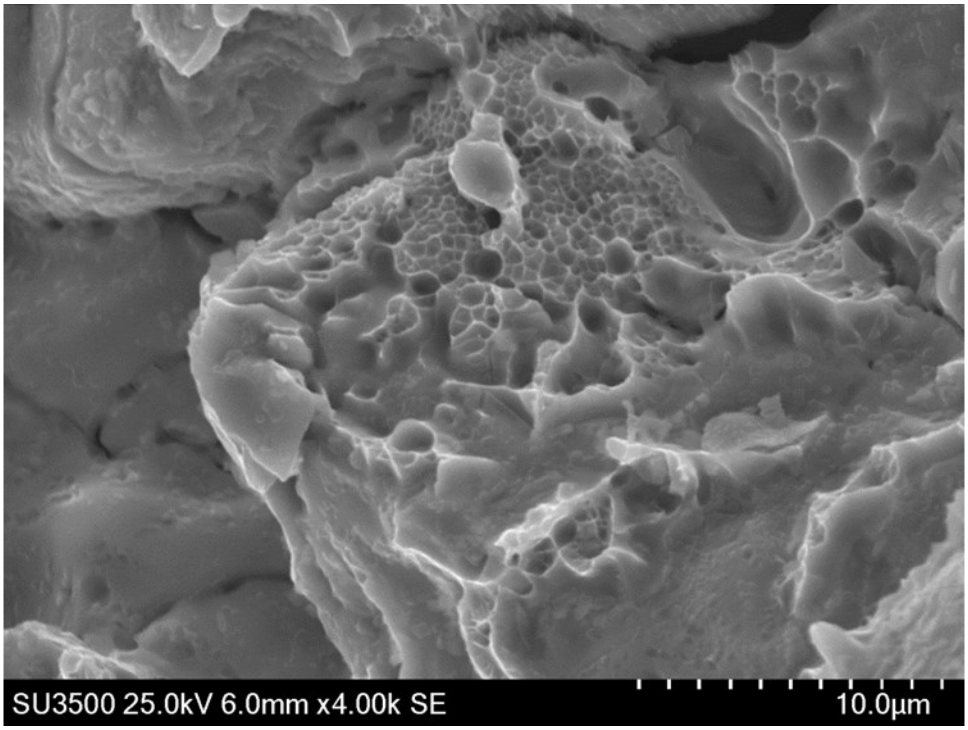

Figure 3.22: SEM images of the shear punch test fractured microstructure for CP Fe at ×4000 magnification factor

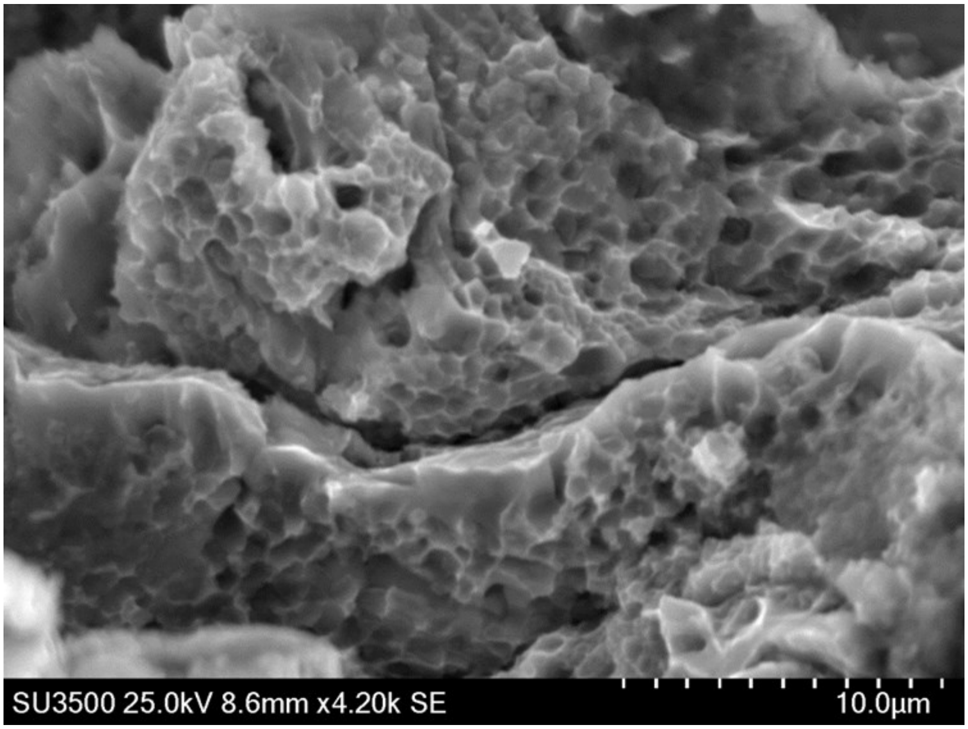

Figure 3.23: SEM images of the Shear punch test microstructure for 80wt%Fe at ×4200 magnification factor

3.3.4 Tensile Testing of the Heat Treated Coatings

Figures 3.24 and 3.25 give a comparison of the shear stress and tensile stress of the 20wt%Fe lot 3 coating annealed at 1100^{0}C for 1 hour. Figure 3.24 shows that the ultimate shear strength is reached after a 90% of reduction in area (*% R.A.*) which indicates a high ductility found from the shear punch test. Figure 3.25 reflects the results of Figure 3.24 indicating around 23% ductility before failure with ductile behavior observed after achieving the yield strength. On the other hand, Figure 3.26 indicates brittle behavior in a static shear punch test with 80wt%Fe lot 3 coating annealed at 1100°C. For this coating, ultimate failure occurs with about 65% reduction in area in contrast with the value of 90% for the 20 wt%Fe lot 3 coating. Figure 3.27 shows that the 80 wt%Fe lot 3 coating attains only 8% ductility before failure from tensile test whereas, in contrast, the 20 wt%Fe coating has a ductility that is more than three times higher before ultimate failure. The increase in tensile strength and ductility observed for the 20wt%Fe lot 3 coating may be attributed to a combination of the effect of recrystallization, sintering of interparticle bonding, and a reduction in dislocation density.

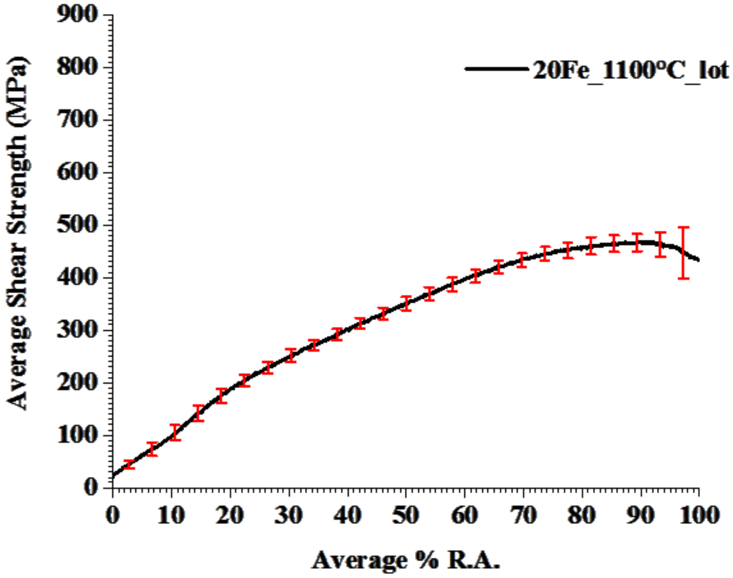

Figure 3.24: Mean shear strength vs. % R.A. curve for 20wt%Fe lot 3 at 1100°C shear punch test

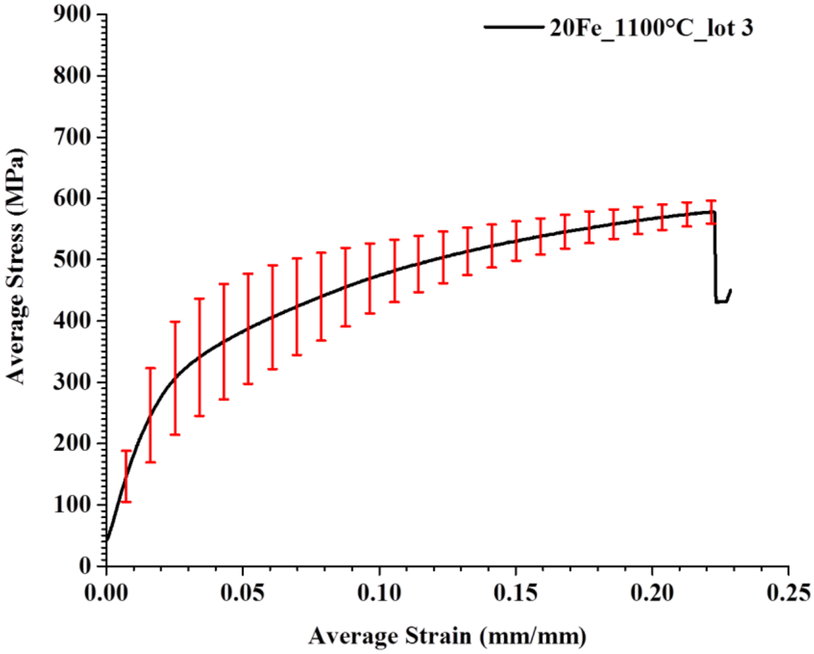

Figure 3.25: Mean tensile stress vs. strain curve for 20wt%Fe lot 3 tensile coupons annealed at 1100°C (all the trials are generated with triplicates)

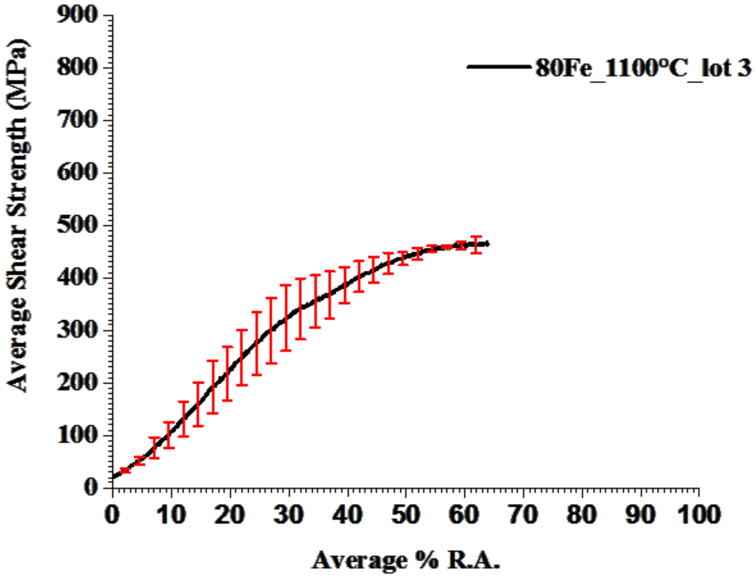

Figure 3.26: Mean shear strength vs. % R.A. curve for 80wt%Fe lot 3 at 1100°C shear punch test (all the trials are generated with triplicates)

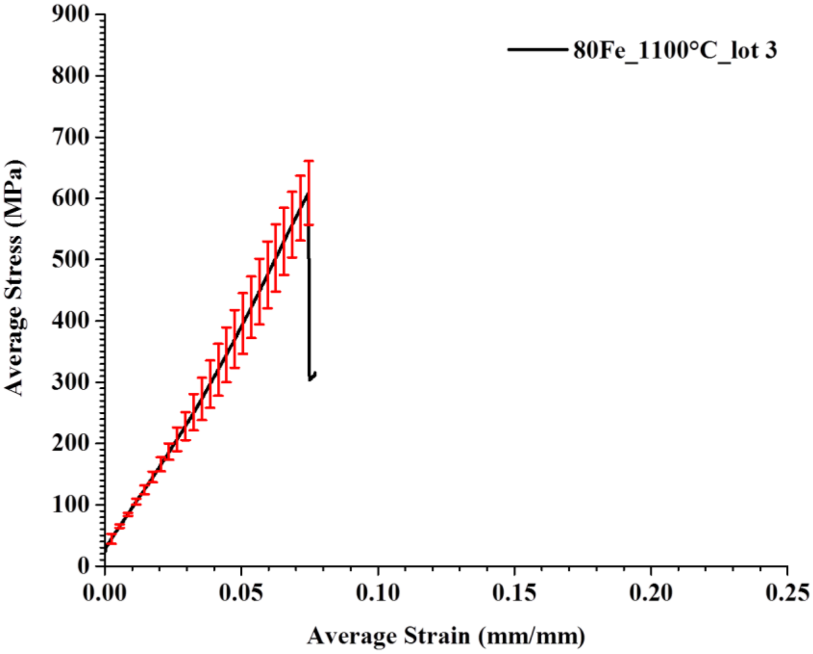

Figure 3.27: Mean tensile stress vs. strain curve for 80wt%Fe lot 3 tensile coupons annealed at 1100°C (all the trials are generated with triplicates)

In order to characterize the fracture behavior of the tensile coupons, SEM analysis was performed on the fractured samples.

Figure 3.28(a) indicates brittle microstructure on the low magnification image of fractured 80wt%Fe lot 3 coatings. The fracture surface also exhibits a continuous array of pores and cracks throughout the surface. In addition, dimpled structures are also observed in Figure 3.28(b). But cracks, holes and pores are also observed inside dimpled structures which are an indication of mixed brittle and ductile behaviors. In comparison to the 80wt%Fe coating, the 20wt%Fe coating exhibits ductile microstructure shown in the low magnification fracture microstructure image in Figure 3.28(a). The influence of the dimpled structures can be observed even in the low magnification images. In addition, cracks and very few pores are observed in the low magnification images. The high magnification image in Figure 3.29(b) indicates a complete network of dimpled microstructures with very few pores. Cracks are observed at the top-right part of Figure 3.29(b) but it is usual for the entire fractured surface observed at the bottom-left part of Figure 3.28(b), as well.

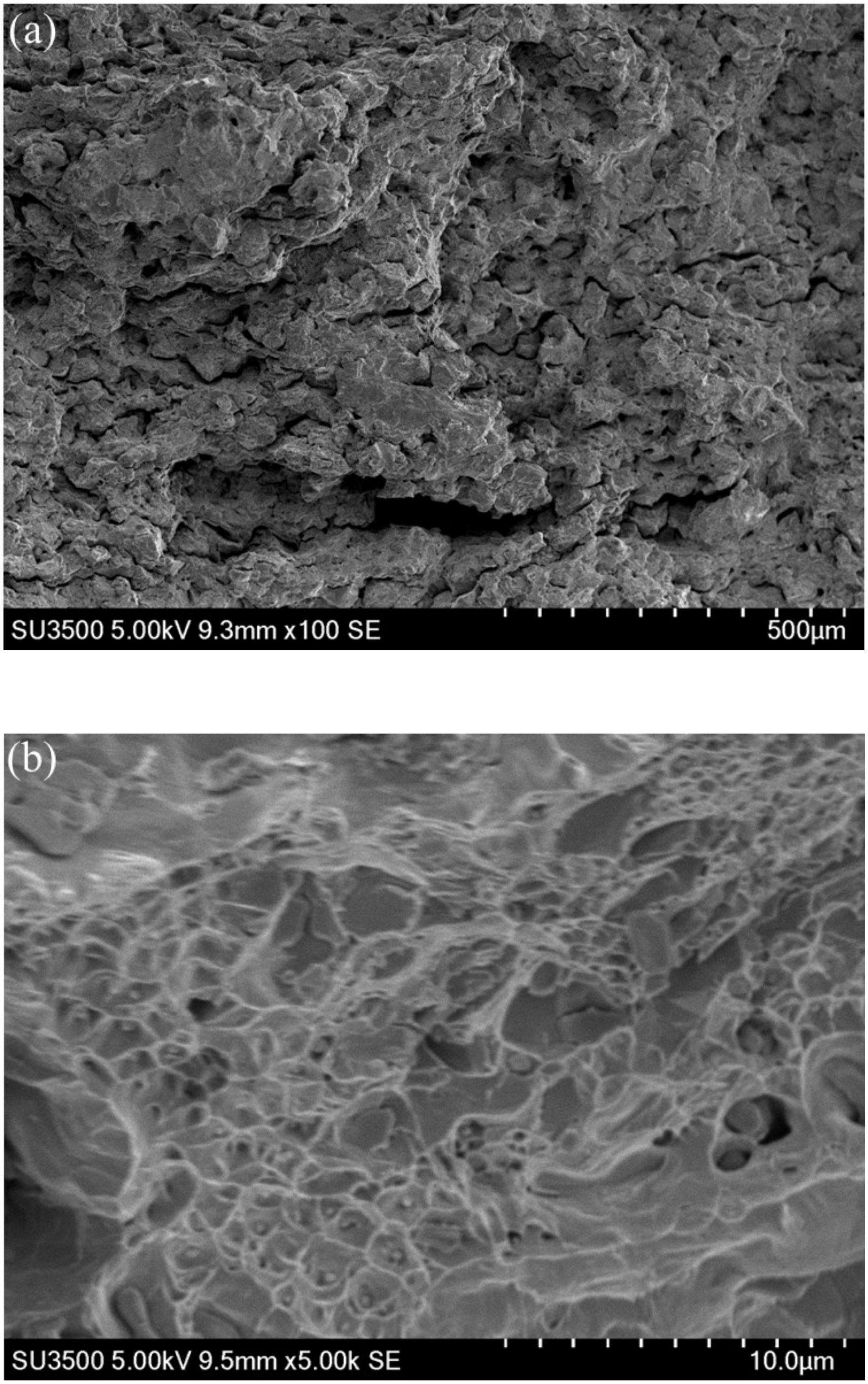

Figure 3.28: Fractured microstructure of 80wt%Fe at (a) ×100 and (b) ×5000 magnification factor

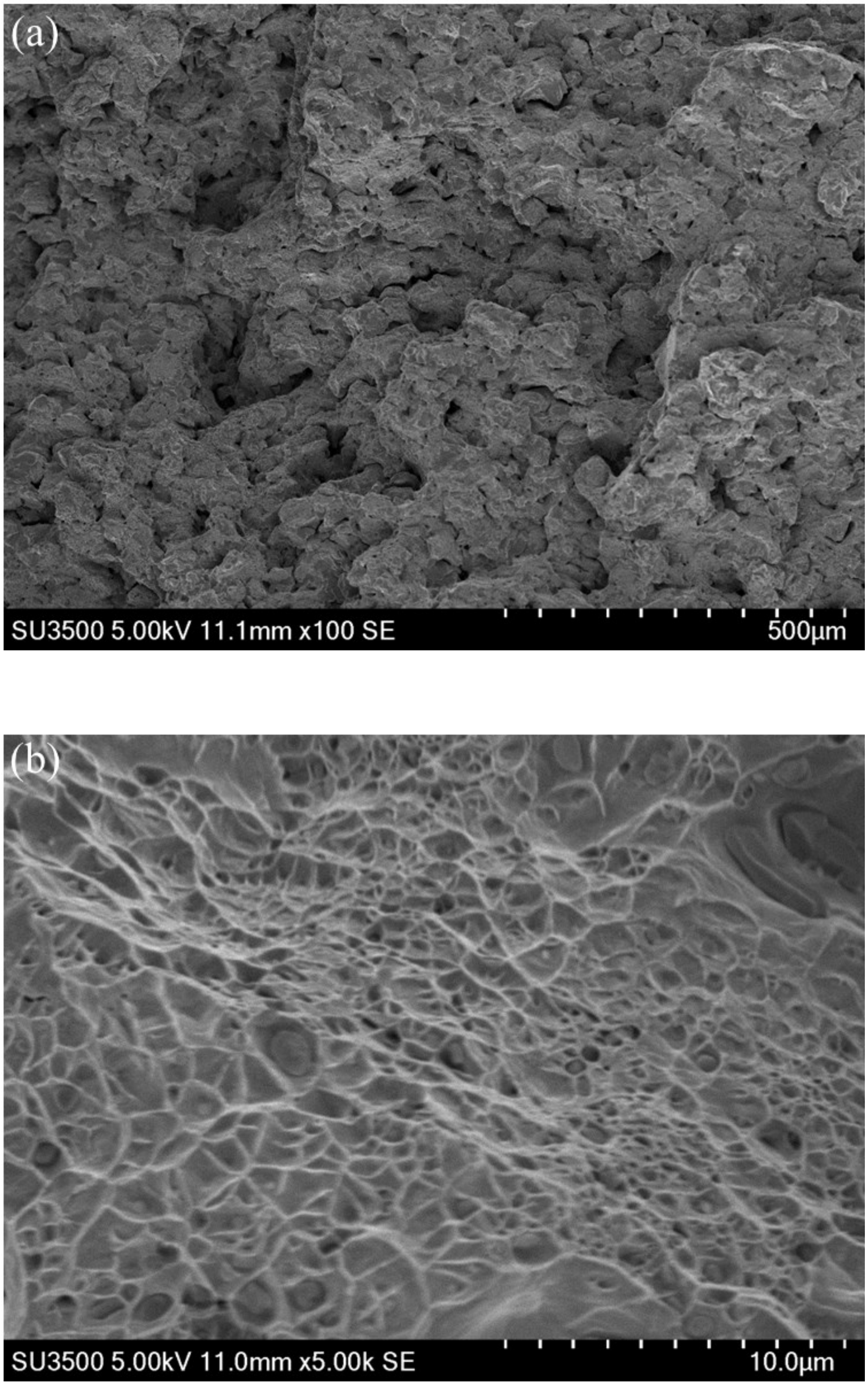

Figure 3.29: Fractured microstructure of 20wt%Fe at (a) ×100 and (b) ×5000 magnification factor

The ultimate tensile vs. ultimate yield strengths and yield tensile vs. yield shear strengths of 20wt%Fe and 80wt%Fe lot 3 coatings are calculated in order to determine a regression factor for the ultimate strength and yield strength. Table 3.1 estimates the regression factor for ultimate and yield strength of mixed coatings of lot 3.

Table 3.1: Regression factor calculation from tensile and shear punch test of lot 3 coatings

Coating	**Shear Strength (MPa)**	**Tensile Strength (MPa)**	**C**	**Mode**
20Fe	468.47±13.65	584.00±18.11	1.25	Ultimate
80Fe	483.87±34.71	629.10±79.19	1.3	Ultimate
20Fe	161.33±11.85	262.33±7.5	1.63	Yield
80Fe	158.00±2.82	227.50±10.61	1.43	Yield

The tensile strength curve for the 80wt%Fe lot 3 coatings did not follow any traditional stress-strain curve as shown in Figure 3.27. However, only shear punch tests were performed for lot 1 coatings. Hence, these regression factors are used to estimate the tensile strength of the mixed coatings of lot 1. Highest C values are taken in order to obtain maximum values that can be estimated. The estimations of the yield and ultimate tensile strengths are shown in Table 3.2:

Table 3.2: Estimation of tensile strengths (MPa) of annealed coatings of lot 1

Coating	**Yield Strength (MPa)**	**Tensile Strength (MPa)**
316L	255.37	591.79
20Fe	245.86	596.98
50Fe	279.27	601.18
80Fe	237.71	604.64
Fe	202.39	320.69

The value of the regression factor, C has been reported to be 1.7 for the yield and 2.2 for the ultimate strength calculation for the bulk 316L [88]. Since the regression factors for the cold-sprayed coatings are unknown, the regression factor is calculated by correlating the tensile and shear punch test results obtained from lot 3 mixed coatings. Then, the correlation factors of lot 3 coatings are used to estimate the tensile properties of lot 1 coatings. Table 3.2 only provides an estimate of the highest tensile strength that may be obtained. From the data in Table 3.2 it may be concluded that the mixed coatings provide satisfactory tensile and yield strength values required for the stent application. Although ductility cannot be stated from the correlation factor, lot 3 coatings on 20wt%Fe provide a satisfactory ductility required for stent application. Although ductility of lot 3 coatings is reported to be only 8%, the tensile properties of 80wt%Fe lot 1 coatings and %reduction in area of the shear punch test indicate that results can be improved by choosing CP Fe instead of CP Fe lot 3 powder.

3.4 Conclusions

The following points summarize the main findings in the chapter:

a. Pores are only exhibited on 316L coatings but other coatings exhibit both pores and cracks at their cross-section. Annealing reduces the number of pores but has little impact on the number of cracks. The presence of pores without cracks is an indication of the better interparticle bonding of 316L at particle interfaces than other coatings.
b. The microhardness is reduced due to a reduction of work hardening by recovery and recrystallization following annealing of the as-sprayed coatings.
c. The shear strength improves after annealing due mainly to sintering, although there is also a small effect of recrystallization. Further improvement can be attributed to either sintering of unbounded interparticles or the reduction of dislocations.
d. The mixed powder coatings undergo a transition in which the work hardening rate of the annealed material increases with increasing annealing temperature. This

may be due to the sintering of different types of interfaces at different temperatures.

e. The lower increase in work hardening of CP Fe powder in 80wt%Fe lot 3 coatings reduces the ultimate strength and ductility of the coatings without affecting the porosity of the coatings.
f. The regression factor found from tensile and shear punch tests provides an estimate satisfactory yield and tensile strength of annealed pure and mixed coatings.

Chapter 4. **Corrosion Investigation**

The stent material must possess a minimum allowable degradation rate in order to be used for a resorbable stent. In vitro tests were performed in order to quantify the material's corrosion rates. This section introduces the rationale for performing corrosion tests, the required methodologies, as well as the results and characterization of the degraded products.

4.1 Introduction

Quantification of degradation rate of implanted iron based stents requires a correlation between the in vitro and in vivo tests [89]. Pourbaix [90] developed a potential vs. pH diagram based on thermodynamic data to predict the propensity of corrosion of a metal in water. A schematic of the potential vs. pH diagram in a body fluid analogue [91] is found in Figure 4.1.

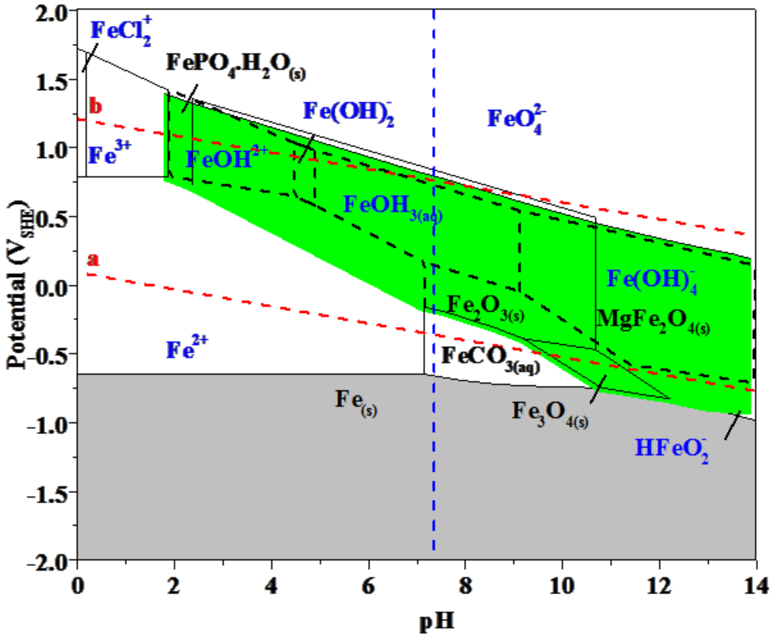

Figure 4.1: Pourbaix diagram of Fe in body fluid analogue, reproduced from [91]

This figure displays the immunity, passivity and corrosion regions of iron with grey, green, and white colored areas, respectively. Aqueous corrosion occurs between diagonal lines a-b, where water is stable. White areas indicate the regions in which corrosion occurs without any stable solid phases. Finally, green area indicates passive region, where iron dissolves into oxides. This passive oxide layer can have further corrosion, depending on the corrosive environment.

Although the Pourbaix diagram can predict metal dissolution in simulated body fluid under equilibrium, the human physiological condition is imbalanced, where organic compounds and ions may significantly impact the in vitro and in vivo corrosion rates [91]. Nevertheless, corrosion rates of as sprayed and heat treated coatings are investigated so that corrosion rates under a non-equilibrium environment may provide information about the corrosion process observed with different iron-based alloys for similar conditions.

4.2 Materials and Methods

A Hank’s physiological solution, SH30588 from Fisher Scientific Canada, was used for all corrosion tests. The composition of Hank’s physiological solution is shown in Table 4.1. Cold sprayed and heat treated (1100°C for 1 hour) coatings were used as samples for the corrosion test.

Table 4.1: Composition of Hank's physiological solution, reproduced from Appendix E

Component	**Concentration (mg/L)**	**Concentration (mmol/L)**
KCl	400	5.37
KH_2PO_4	60	0.44
NaCl	8000	136.89
Na_2HPO_4	47.68	0.34
$C_6H_{12}O_6$	1000	5.55
$NaHCO_3$	350	4.17

The general corrosion rate is calculated using static immersion tests and potentiodynamic polarization technique [89]. Since the mixed coatings are fabricated based on the notion of accelerated corrosion rate due to galvanic effect, a technique to quantify the degree of galvanic corrosion was needed. Mass loss and corrosion rate due to galvanic corrosion is quantified by the galvanic corrosion test.

4.2.1 Corrosion Rate Measurement by Static Immersion Test

Static immersion tests were performed according to ASTM G 31-72 [92] using the test setup shown in Figure 4.2.

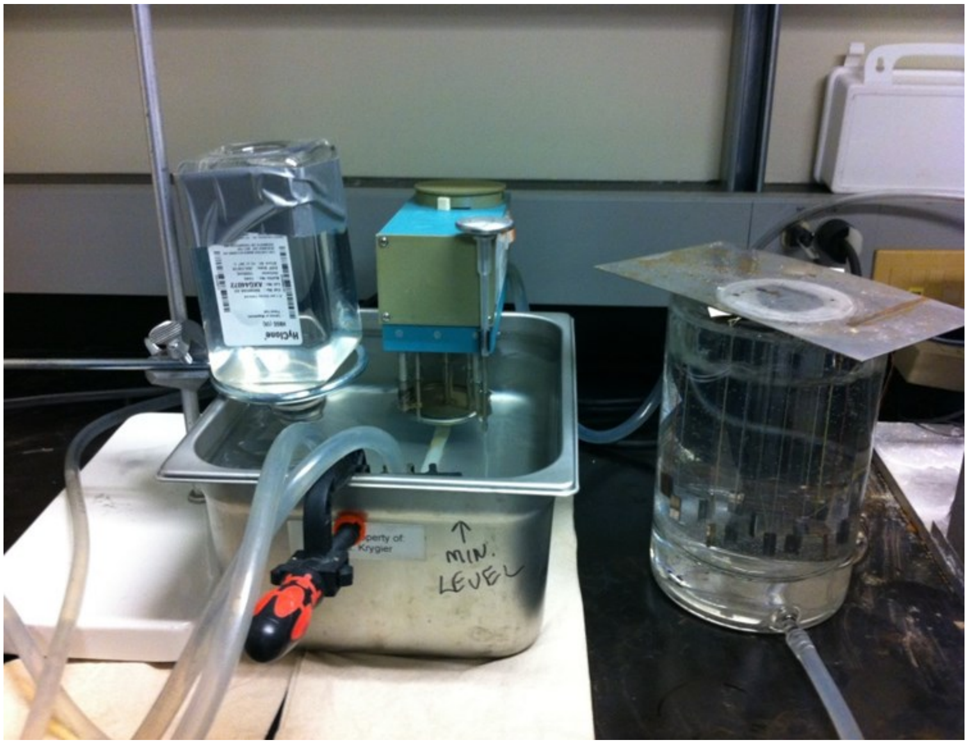

Figure 4.2: Set-up for the laboratory immersion test

A Tempette TE7 pump (Bibby Scientific US, Burlington, NJ, USA) with a heater circulates hot distilled water through a 2 litre reaction beaker. The temperature inside the reaction beaker is maintained at 37 ± 1^0C. Samples are immersed in Hank's physiological solution. An Oakton 6 pH meter was used to monitor the pH and the temperature of the solution. The samples were immersed for seven to nine days, then cleaned, dried every 7-

9 days and continued for up to 45 days. A precise scale (±0.00001 grams) was used to measure the mass loss of each sample.

The corrosion rate was estimated from the mass loss of each sample by using the following equation [92]:

$$Corrosion\ rate = \frac{K \times W}{A \times t \times \rho} \qquad [4.1]$$

Where, the mass loss, W (mg) of a sample of area, A (cm^2) and density, ρ (gm/cm^3) is measured after a specific time interval, t (hour). The value of the constant, K, is 8.76×10^4, for a desired corrosion rate unit of mmpy. Finally, the corrosion rate is converted from one unit to another by using corrosion rate conversion chart in appendix A.

4.2.2 Corrosion Rate Measurement by Polarization Test

Polarization tests were performed according to ASTM G59-97 norm using the test setup shown in Figure 4.3 [93].

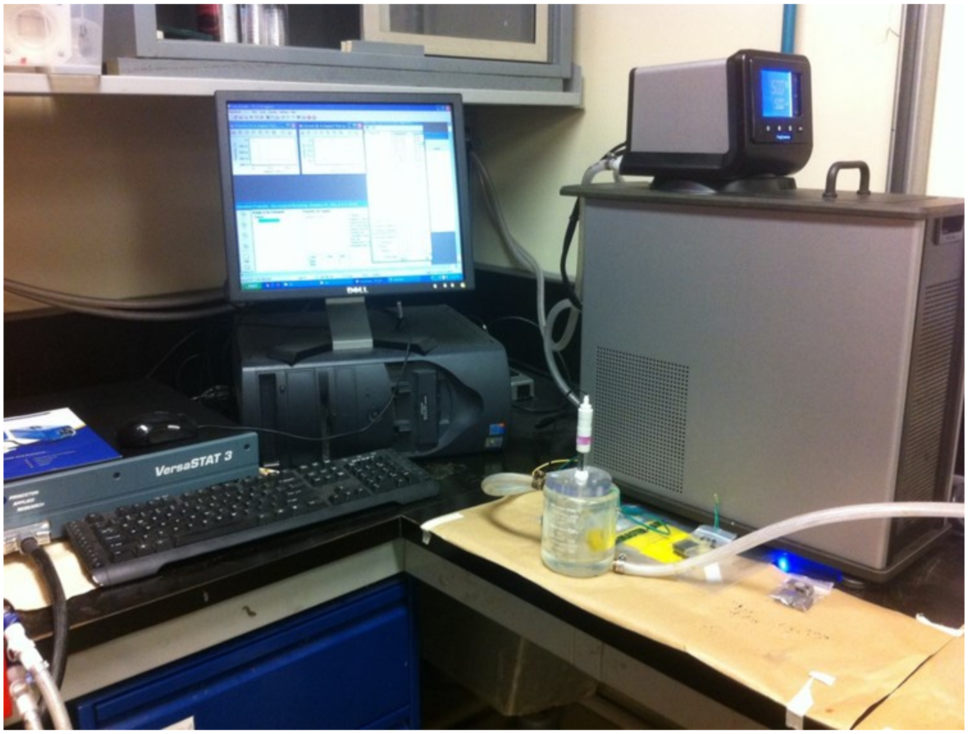

Figure 4.3: Set-up for the potentiodynamic polarization test

VersaStat3 potentiostat (Princeton Applied Research, TN, US) was used with a three electrode setup. A pump with a heater circulates warm distilled water through a 200 mL reaction beaker. The temperature inside the reaction beaker is maintained at 37±1^{0}C. The coatings cold mounted with epoxy were used as a working electrode. Highly corrosion resistant platinum wire is used as an auxiliary electrode. It provides applied current to support an oxidation or reduction reaction without participating within the electrochemical test. A saturated calomel electrode is used as a reference electrode to measure the potential difference between the electrolyte and the working electrode. All three electrodes were immersed in Hank's physiological solution. Open circuit potential (OCP) is recorded for the first 24 hours followed by a potential variation of ±25mV at a 0.167mV/s scan rate.

OCP (E_0) is defined as the reversible equilibrium potential (zero overpotential) of an electrode at its exchange current density (i_0) value. A reduction and oxidation reaction occurs at the same rate as the equilibrium potential of a reaction. Therefore, the anodic and cathodic currents are equal at equilibrium potential. This point is called exchange current, and the rate of electron exchange between the electrodes at equilibrium is called exchange current density (i_0). Overpotential is the potential difference between a working electrode and its open circuit potential. However, when a reaction deviates from its equilibrium state, overpotential develops with different anodic and cathodic current densities. Therefore, the anodic and cathodic current density for a given electrode is given by:

$$i_a = i_0 \exp[\frac{\beta_a zF\eta}{RT}] \qquad [4.2]$$

$$i_c = -i_0 \exp[-\frac{\beta_c zF\eta}{RT}] \qquad [4.3]$$

It follows that the net current density, i, equals the difference between i_a and i_c and constitutes the Butler-Volmer equation:

$$i = i_0[\exp\left(\frac{\beta_a zF\eta}{RT}\right) - \exp\left(-\frac{\beta_c zF\eta}{RT}\right)] \qquad [4.4]$$

Equation 4.4 reduces to the Tafel equation in the case of large overpotential, either anodic or cathodic polarization and is expressed as follows:

$$\eta = \beta log_e \frac{i}{i_0} \qquad [4.5]$$

Where, β represents the Tafel slope of the polarization curve. The Tafel extrapolation technique is used to obtain the Tafel slopes and the corrosion current (i_{corr}) of as-sprayed and heat treated coatings.

Finally, the corrosion rate is calculated using the following equation:

$$CR = 3.27 \times 10^{-3} \frac{i_{corr}EW}{\rho} \qquad [4.6]$$

Where, EW, ρ and i_{corr} are the equivalent weight, density and corrosion current density of the coating, respectively.

4.2.3 Corrosion Rate Measurement by Galvanic Corrosion Test

Since the mixed samples are fabricated based on the notion of an accelerated corrosion rate due to galvanic effect, a technique to quantify galvanic corrosion is important. So, the ASTM G71-81 standard was utilized to evaluate the potential for galvanic corrosion of the mixed coatings using 316L as the other electrode [94]. The stainless steel, 316L powder is a constituent of the mixed coatings, as well, 316L is the golden standard material for a cardiovascular stent. Therefore, 316L was selected as the other electrode to assess whether the fabricated coatings indicate an accelerated corrosion rate, in comparison to 316L. The galvanic corrosion rate was calculated by quantifying the amount of current flow between the working electrode and 316L. The VersaStat3 potentiostat was utilized to induce a galvanic couple using mixed coatings and 316L. Based on this notion, the galvanic corrosion rate was calculated as follows:

$$Galvanic\ corrosion\ rate = \frac{W}{A \times t} \qquad [4.7]$$

The mass loss W was calculated from the following relation:

$$W = \frac{M \times I \times t}{z \times F} \qquad [4.8]$$

Where, M is equal to the atomic mass of the material (gm/mole), I is equal to the current (amp), z is the number of electrons, with z=2 for iron and 316L, F is equal to Faradays constant; 96485.34 amp-sec/mole-e^-s and t is the elapsed time. The galvanic corrosion test provides current flow over time, which is integrated and substituted in Equation 4.8. This method is referred to as the "direct measurement of galvanic corrosion rate" as it directly measures galvanic current with respect to time. This method measures an additional corrosion rate under the freely corroding condition, in addition to the galvanic corrosion rate [95]. Other ways to evaluate galvanic corrosion include mixed potential theory and potential probe methods. Among those, the measurement of galvanic corrosion through mixed potential theory is simple if the potentiodynamic polarization test of materials participating in galvanic corrosion is available. Here, the polarization curves of both materials are superimposed on a same graph as shown in Figure 4.4. The intersection point of the anodic branch of the anode (material with lower E_{corr}) and the cathodic branch of the cathode (material with higher E_{corr}) indicates galvanic couple current density, i_{couple}. Galvanic corrosion rate can be determined with:

$$CR = \frac{M.i_{couple}}{zF\rho} \qquad [4.9]$$

Mixed potential theory, however, only provides good results when the reaction rate of the other two branches are negligible, since the applied current is used instead of utilizing the anodic/cathodic current from the polarization test [95]. In addition, the potential difference between the anode and the cathode should be at least 0.12 V, depending on the slopes of the polarization curves, in order to obtain an adequate estimation of the corrosion rate from mixed potential theory [96].

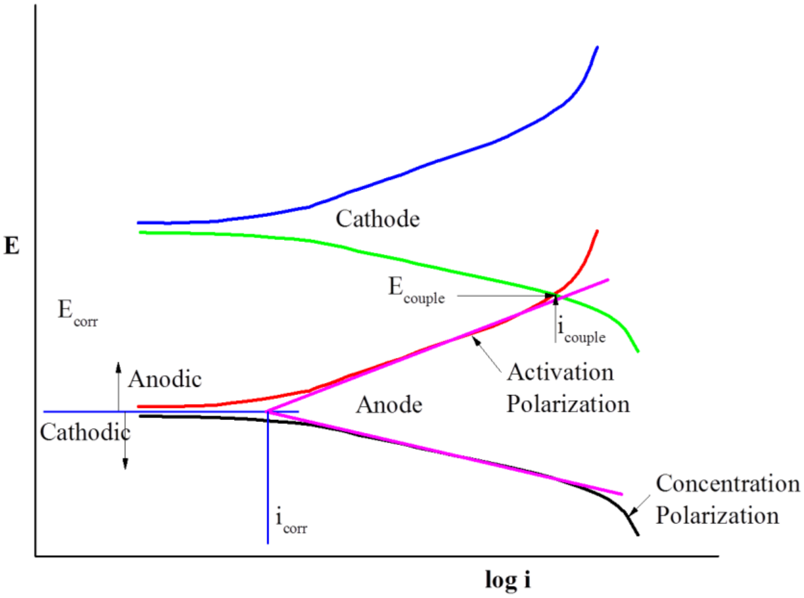

Figure 4.4: Schematic illustration of mixed potential theory

The potential probe method maps local ionic currents between the anode and cathode's surface through scanning or vibrating the electrode. This technique is not used in the current project [95]. However, none of the techniques, discussed here can measure microgalvanic corrosion between CP Fe and 316L particles in a mixed coating. Due to their corrosion characteristics, CP Fe may preferentially corrode with respect to non-reactive 316L. According to the methodologies of galvanic corrosion, it is stated that two dissimilar metals should be in electrical contact to each other. There is no requirement that cathodes and anodes should physically contact each other [97]. However, 316L and CP Fe particles keep in intimate contact with each other, but "microgalvanic corrosion" between two particles in a spray coating is hard to quantify. Microgalvanic corrosion can be estimated by using anodic area instead of the overall area that takes part in general corrosion. This can be done since only the CP Fe inside the mixed coating will corrode, not the entire coating. This can provide an estimation of microgalvanic corrosion between two microparticles in a coating. Henceforth, galvanic corrosion will refer to a corrosion rate that is achieved using working and 316L as electrodes and microgalvanic corrosion rate will indicate the results obtained by the corrosion rate found utilizing the anodic area.

4.2.4 Characterization of Degraded Products

Characterizations of the samples after degradation, was completed, through the use of x-ray diffraction (XRD), stereoscopy, optical microscopy and scanning electron microscopy (SEM) with energy dispersive spectroscopy.

4.3 Results and Discussion

4.3.1 Static Immersion Test

Figure 4.5 represents the rate of mass loss of the as-sprayed coatings determined from the immersion tests. It indicates that the rate of mass loss increased up to 441 hours (18 days, approx.) and then started to reduce. It is also apparent that the rate of mass loss of the mixed coatings with higher percentage of CP Fe is closely similar to the mass loss rate of CP Fe coatings, due to the higher weight percentages of CP Fe.

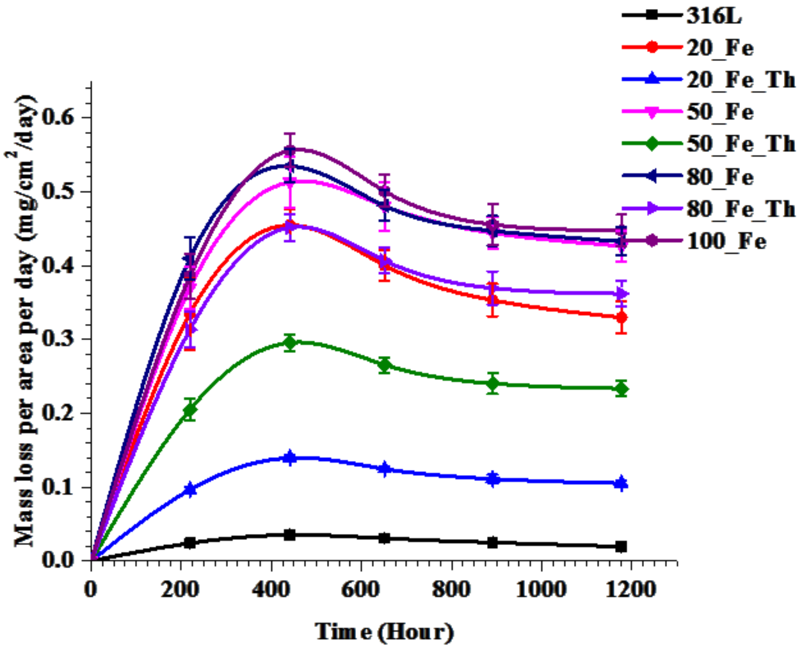

Figure 4.5: Rate of mass loss of as-sprayed coatings obtained with immersion test

Figure 4.6 illustrates the corrosion rate of the as sprayed mixed coatings. It also indicates a reduction of the corrosion rate approximately after 18 days immersed in Hank's solution, similar to observations found in Figure 4.5. A decrease in the corrosion rate after a specific time period, as observed in Figure 4.5 and 4.6, is an indication of the formation of oxide layers, which prohibits further oxidation of the coatings [98]. Table 4.2 states the average corrosion rate after 9 and 18 days of immersion, with standard deviation also reported.

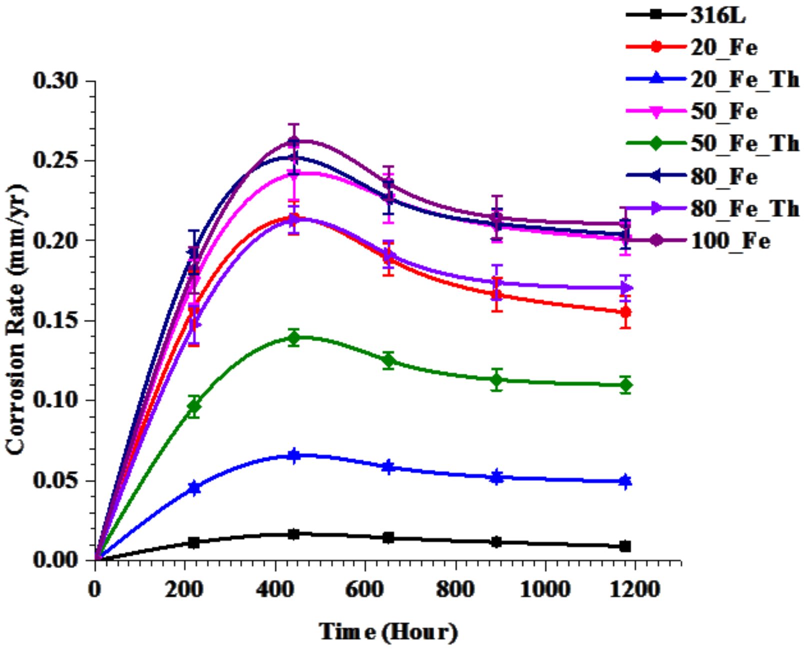

Figure 4.6: Corrosion rate of as-sprayed coatings obtained with immersion test

Table 4.2: Corrosion rates obtained from immersion testing (in mmpy) for as-sprayed coatings

Coatings	**Corrosion Rate (mmpy)**	
	CR$^{9\ days}$	**CR$^{18\ days}$**
316L_lot 1	0.011±0.001	0.017±0.000
20Fe_lot 1	0.16±0.023	0.21±0.014
50Fe_lot 1	0.17±0.010	0.24±0.016
80Fe_lot 1	0.19±0.014	0.25±0.014
100Fe_lot 1	0.18±0.014	0.26±0.011

The accelerated corrosion rates of Fe-35Mn and annealed CTT-Fe (casting and thermo-mechanically treated Fe) at 550^0C from immersion tests are reported as 0.26 and 0.14±0.02 mmpy, respectively after 7 days of immersion in Hank's solution buffered with Hepes. Electroformed Fe (E-Fe) and annealed E-Fe at 550^0C is reported 0.40±0.03 and 0.25±0.02 mmpy respectively after 14 days of immersion [33]. Compared to immersion test results reported in [33] and Table 4.2, it can be stated that the corrosion rates determined in these investigations are comparable to other corrosion rates observed from iron-based alloys. Although electroformed Fe indicates an accelerated corrosion rate (0.4 mmpy), it requires heat treatment to obtain minimal ductility for use in stent applications. The corrosion rate reduces to 0.25 mmpy after one hour of annealing at 550^0C [33]. This could be further reduced if it is annealed at 1100^0C, such as used the annealing temperature in this research. However, the corrosion rate of as-sprayed coating could not be increased more than 0.25 mmpy after 14 days of immersion in Hank's solution. This is largely due to the limitation of the corrosion rate of the constituent materials used for the mixed coating. The corrosion rate of Armco© grade pure iron exhibits an average corrosion rate of about 0.10 mmpy when exposed to 14-28 days in Hank's solution [98]. The corrosion rate of annealed 316L is obtained as 0.0029 mmpy after 24 weeks of immersion in Hank's solution [99]. This is more than one order of magnitude lower than the corrosion rate of as-sprayed 316L (0.0166 mmpy) in 18 days. This can be attributed to its higher porosity among all other as-sprayed mixed coatings. The as-sprayed mixed coatings did not have higher porosities than as-sprayed 316L. The microgalvanic effect on the as-sprayed coatings may be attributed to a higher as-sprayed corrosion rate of mixed coatings. Both Figure 4.5 and 4.6 indicate possibilities of microgalvanic corrosion of the mixed coatings because all of the mixed coatings show a higher experimental corrosion rate as compared to the theoretical (represented as _Th) corrosion rate of the same mixed coatings. The theoretical corrosion rate is calculated by mass balance of the pure coatings at a specific time. The 20wt%Fe coating has the highest difference between the theoretical and experimental corrosion rates and the 80wt%Fe coating has the lowest. This indicates that the effect of microgalvanic corrosion is the highest with the 20wt%Fe coatings and the lowest with the 80wt%Fe coatings.

Considering the fact that only CP Fe inside the coating preferentially corrodes and disintegrates the mixed coatings, the resulting effect of CP Fe on microgalvanic corrosion is shown in Figure 4.7.

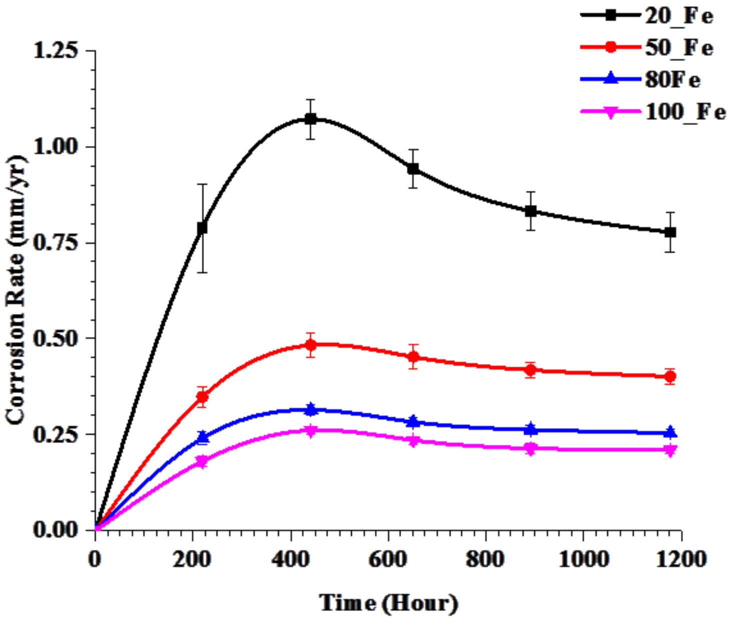

Figure 4.7: Effect of microgalvanic corrosion on the as-sprayed coatings

Figure 4.7 indicates that although the 100wt%Fe and 80wt%Fe coatings exhibit higher corrosion rates among the as-sprayed coatings, the effect of microgalvanic corrosion is the maximum in the 20wt%Fe and the minimum in the 80wt%Fe coatings. This phenomenon can be explained by the area effect on galvanic corrosion. Higher cathodic area increases the corrosion rate of the anode (less noble material) through galvanic coupling, even with a lower potential difference between the cathode and the anode (*i.e.* $\Delta E_{corr} > 50$ mV, minimum). This effect is more severe in diffusion controlled rather than activation controlled cathodic reaction, due to higher slope of the former [100].

The ratio of the solution volume to sample surface area (V/S) is calculated as 37.38 mL/cm^2 which are within the range of 20-40 mL/cm^2, the minimum value set by ASTM G 31-72 standard [92]. Although the exposure time in the electrolytes is identified for corrosion rate in [33], the ratio of solution volume to sample surface area is not reported which might be the most important factor that may affect the rate of corrosion. ASTM

G31-72 standard recommends 20-40 mL/cm^2 in order to avoid any additional change in corrosion rate during the test. An appreciable change in corrosion rate may occur if the degraded products are exhausted or accumulated in the electrolyte which may affect additional degradation [92].

Figure 4.8 indicates the corresponding pH values of the testing physiological solution. The pH values become stable at a value of approximately 7.8 which corresponds to a basic solution. A stable pH value of 7.8 is found from Figure 4.8 and can be explained with the Pourbaix diagram shown in Figure 4.1. It predicts that corrosion products might be formed in the unstable aqueous iron carbonate or passivated iron oxide. A stable range of pH should be maintained in order to mimic in-vitro degradation tests closely similar to the physiological conditions of human blood plasma [98].

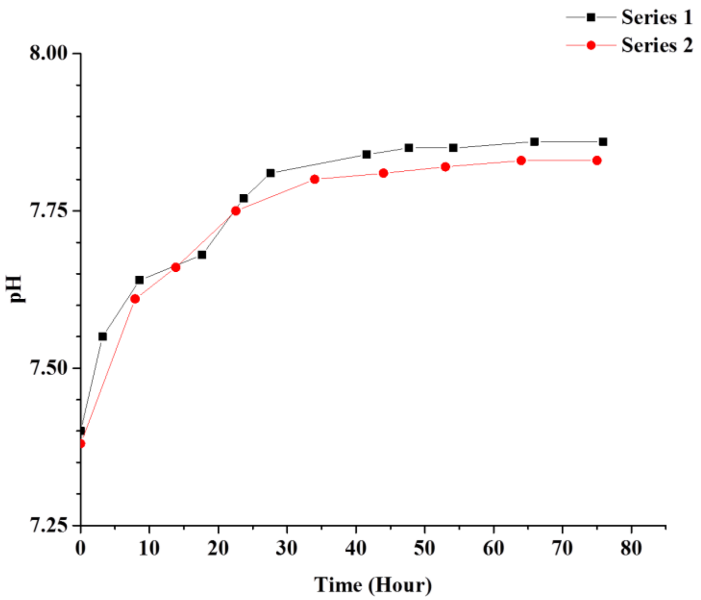

Figure 4.8: pH values of testing solutions with immersion time

Figure 4.9 and 4.10 display the rate of mass loss and the corrosion rate of the heat treated coatings, respectively obtained from the immersion tests. The ratio of solution volume to sample surface area (V/S) is calculated as 34.87 mL/cm^2 which are within the range of 20-40 mL/cm^2, the minimum value set by ASTM G 31-72 standard. It indicates that the rate of mass loss increased up to 17 days and then, it began to decrease. Compared to the rate of mass loss of as-sprayed coatings (Figures 4.5 and 4.6), it is observed that the corrosion rate of the 20wt%Fe coating is substantially reduced after the heat treatment. In contrast, 50wt%Fe and 80wt%Fe coatings present the reduction in corrosion rate after the heat treatment. Table 4.3 reports the average corrosion rate after 8 and 17 days of immersion (with standard deviation):

Table 4.3: Corrosion rate found from immersion test (in mmpy) for annealed coatings

Coatings	**Corrosion Rate (mmpy)**	
	CR$^{9\ \text{days}}$	**CR$^{18\ \text{days}}$**
316L_lot 1	0.011±0.000	0.019±0.000
20Fe_lot 1	0.08±0.006	0.12±0.011
50Fe_lot 1	0.15±0.011	0.22±0.011
80Fe_lot 1	0.17±0.014	0.23±0.011
100Fe_lot 1	0.18±0.011	0.24±0.013

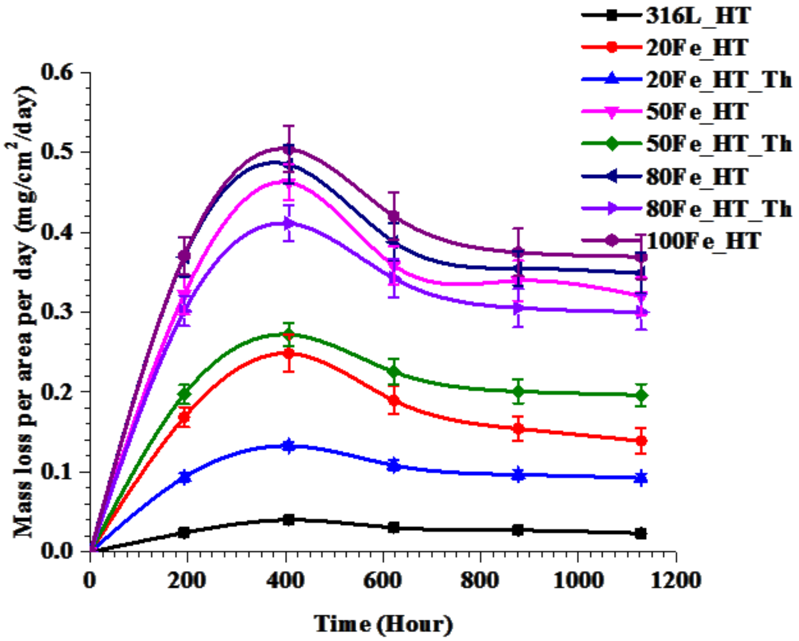

Figure 4.9: Rate of mass loss of heat treated coatings found from immersion test

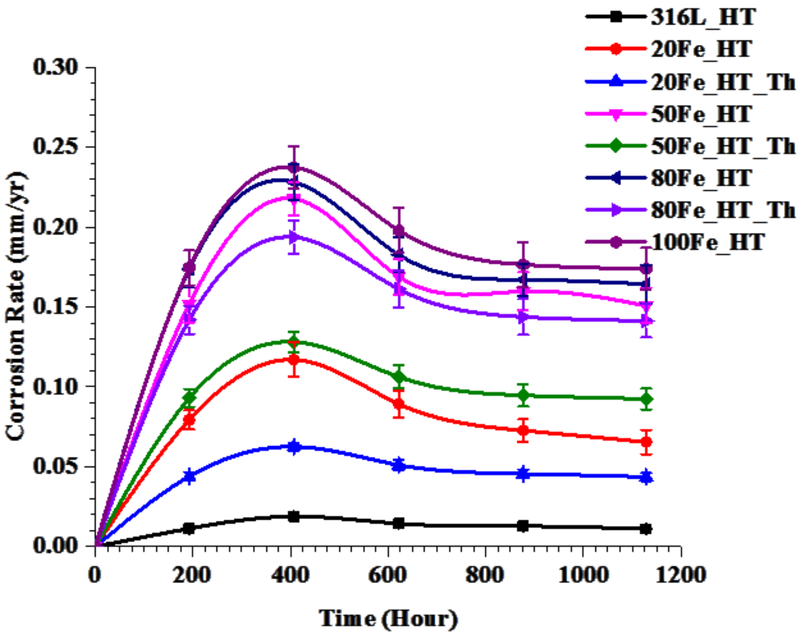

Figure 4.10: Corrosion rate of heat treated coatings found from immersion test

The reduction of the corrosion rate after heat treatment is due to the reduction of porosity after the heat treatment, thereby reducing the overall surface area of the coatings as described by Equation 4.1. This explanation, however, does not describe the corrosion rate of 316L which exhibits approximately the constant corrosion rate before and after annealing. However, it is very difficult to accurately calculate the corrosion rate of materials such as 316L by immersion test. A corrosion rate of only 0.0029 mmpy for annealed 316L after 24 weeks of immersion in physiological solution [99] means that the reduction in porosity after annealing will not substantially reduce the corrosion rate of 316L.

Figure 4.11 illustrates the effect of micro-galvanic corrosion on the annealed mixed coatings. As compared to the as-sprayed coatings in Figure 4.7, it can be stated that annealing reduced the corrosion rate from the microgalvanic corrosion of 20wt%Fe by almost half of that of the as-sprayed 20wt%Fe. Annealing slightly reduces the corrosion rate from microgalvanic corrosion of the 50wt%Fe and 80wt%Fe.

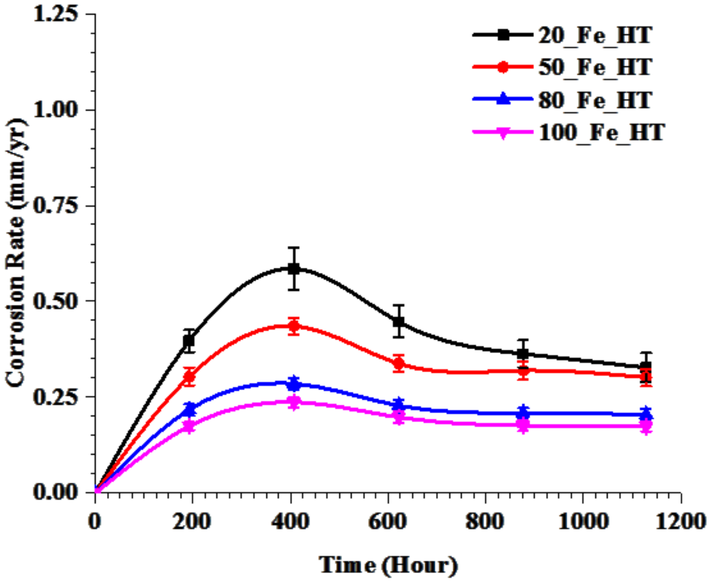

Figure 4.11: Effect of microgalvanic corrosion on annealed coatings

4.3.2 Polarization Test

Figure 4.12 shows open circuit potential of mixed and pure coatings. It is observed that the potential of bulk 316L increases from its initial value before stabilization. The potential of as-sprayed 316L increases for up to 2 hours before stabilizing in physiological solutions. The potential of 50wt%Fe and 80wt%Fe coatings decreases up to 2 hours from its initial value before stabilization. This indicates that a reversible equilibrium potential of the 50wt%Fe and 80wt%Fe coatings at its exchange current density value is close to that of CP Fe coatings. In contrast, the 20wt%Fe coatings decrease initially for up to 2 hours, the beginning to increase before finally stabilizing after 15 hours.

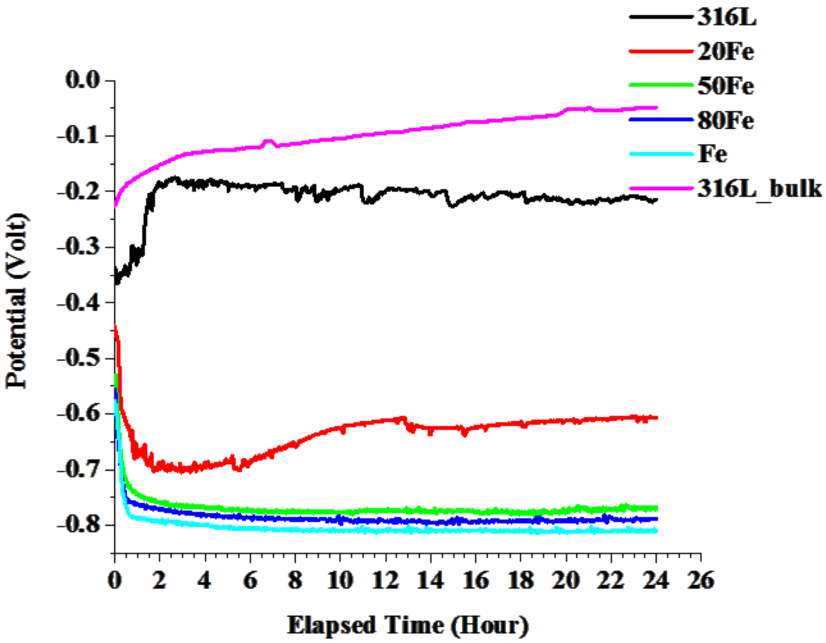

Figure 4.12: Open circuit potential test of as-sprayed coatings

The corrosion process of 316L in Hank's solution is a continuous dissolution and regeneration of passive films. The increase in corrosion resistance of bulk 316L shown in Figure 4.12 initially during the OCP test indicates the formation of stable passive films [101]. The initial increase of the open circuit potential and stabilization thereafter indicates the development and dissolution of a protective oxide layer. The sudden decrease of the open circuit potential and stabilization however, for the 50wt%Fe, 80wt%Fe and CP Fe may be attributed to the initial mass loss due to microgalvanic corrosion followed by a protective oxide layer. The potential drop of the mixed coatings demonstrates that native oxide is thermodynamically unstable in physiological solution. A higher percent of 316L in the 20wt%Fe coatings allows for potential improvements to protect corrosion after an initial potential drop. The 50wt%Fe and 80wt%Fe coatings indicate an initial potential drop from the beginning without having any protective oxide layer before stabilization during open circuit potential test [102].

Figure 4.13 illustrates the potentiodynamic polarization curves of as sprayed mixed and pure coatings.

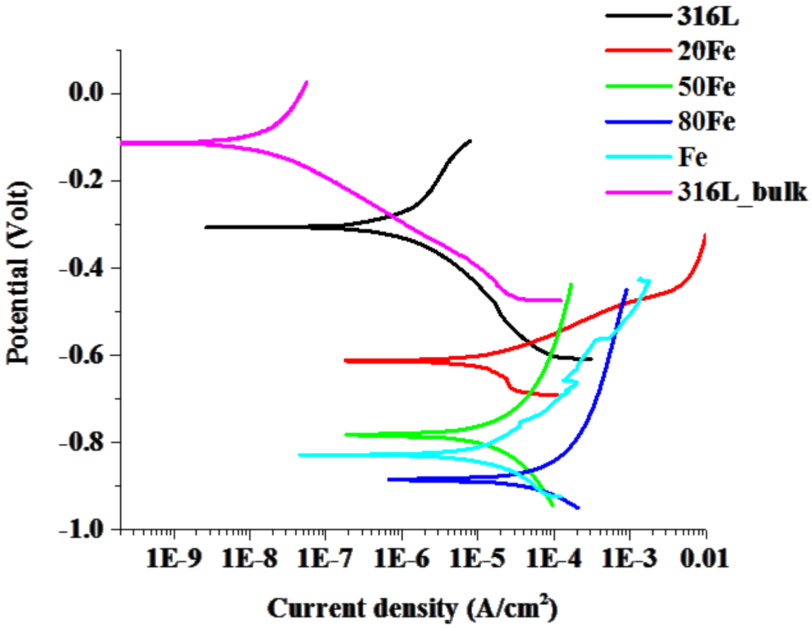

Figure 4.13: Polarization curves of as-sprayed coatings

These results indicate that release of excess electrons in anodic reaction renders the metal potential of mixed and CP Fe coatings more negative as compared to bulk and as-sprayed 316L coatings. Cathodic and anodic branches of polarization curves exhibit active dissolution characteristics for all coatings without any indication of concentration controlled polarization behavior. The results show that anodic dissolution of mixed coatings across the coating-electrolyte interface determines the rate of corrosion [100]. Tafel extrapolation technique is used to find corrosion characteristics (E_{corr}, i_{corr} and corrosion rate) of the mixed and pure coatings, as shown in Table 4.4. This table indicates that all the mixed coatings possess an increase of corrosion rate compared to 316L coatings. Furthermore, the corrosion rates were even higher than CP Fe coatings. The decrease of as sprayed porosity of the mixed coatings reveal that galvanic corrosion is responsible for the increase of the general corrosion rate of the mixed coatings compared to 316L coatings.

Table 4.4: Polarization criteria of as-sprayed coatings

Coating	**Ecorr (mV)**	**i_{corr} (µA/cm^2)**	**CR (mmpy)**
316L Bulk	-86.11±13.12	~	~
316L	-304.25±13.66	0.93±0.09	0.01±0.001
20Fe	616.68±11.77	14.91±3.71	0.18±0.044
50Fe	-749.02±52.4	14.14±1.89	0.17±0.022
80Fe	-768.14±88.35	15.43±3.67	0.18±0.043
CP Fe	-812.57±16.84	13.36±1.72	0.16±0.020

Figure 4.14 summarizes the corrosion rate found from polarization and immersion tests. In this figure, 'I' and 'P' represents the average corrosion rate of as-sprayed coatings obtained from immersion and polarization tests, respectively.

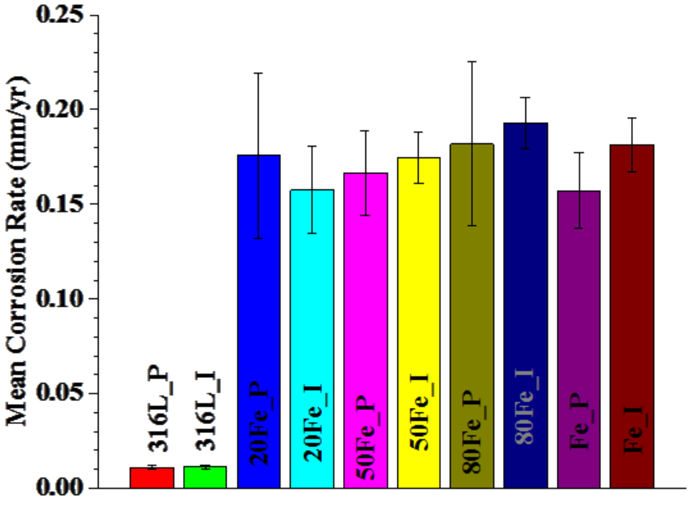

Figure 4.14: Comparison of corrosion rate (in mmpy) from immersion and polarization tests of as-sprayed coatings

The immersion test results after 9 days of immersion are compared with polarization test results. To do so, the duration of the immersion test for materials with moderate or low corrosion rates was estimated with ASTM G31-72 standard according to Equation 4.10 [92]:

$$T = \frac{2000}{Corrosion\ rate\ in\ mpy} \qquad [4.10]$$

Using the highest corrosion rate obtained from the polarization test, calculations using Equation 4.10 indicates that the immersion tests with 225.67 hours of immersion are comparable to polarization tests. Figure 4.14 reveals that the corrosion rate obtained from the immersion and polarization tests are comparable, as they exhibit similar values and similar variabilities. In addition, it is apparent that the mixed coatings can be modified, depending on the desired corrosion rate for future degradable stents. These results confirm that the corrosion rates obtained from both techniques provide data that are reliable.

The effect of the heat treatment on the reduction of corrosion rates is particularly observed for the 20wt%Fe coatings as both the heat treated 316L and the 20wt%Fe coatings exhibit almost the same OCP values, as shown in Figure 4.15.

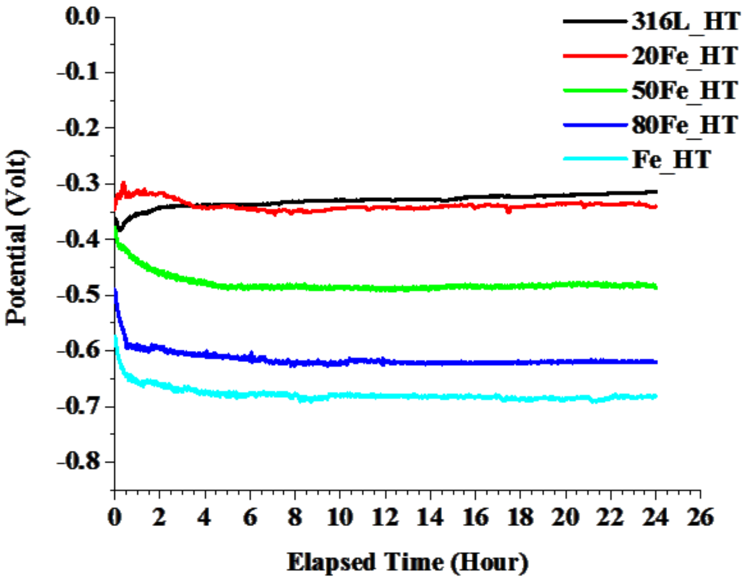

Figure 4.15: Open circuit potential tests of heat treated coatings

The initial potential drops for all mixed and CP Fe coatings, and then stabilizes after 5 hours. In contrast, an increase in potential is observed after 3 hours for the heat treated 316L coatings. The heat treatment reduces the open circuit potential values (Figure 4.15). Activation controlled potential behavior is observed on both cathodic and anodic branches of the polarization curves in Figure 4.16. Tafel extrapolation technique is used to find corrosion characteristics (E_{corr}, i_{corr} and corrosion rate) of the annealed mixed and pure coatings, as shown in Table 4.5.

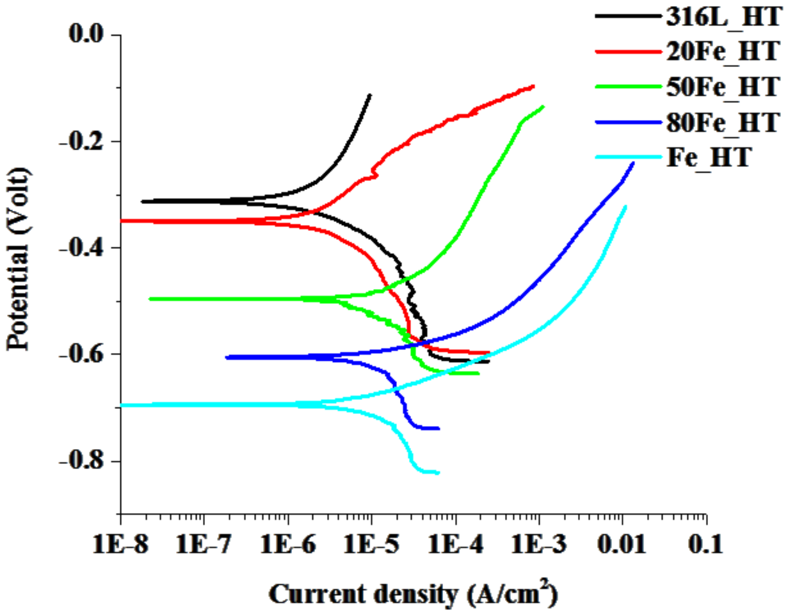

Figure 4.16: Polarization curves of heat treated coatings

A comparison of Figure 4.16 with Figure 4.13 seems to indicate that the release of excess electrons in an anodic reaction is less for heat treated coatings compared to as-sprayed one. This renders the metal potential of mixed coatings less negative as compared to as-sprayed coatings. Table 4.5 lists E_{corr}, i_{corr} and the corrosion rate of heat treated mixed and pure coatings. The comparison of Table 4.5 with Table 4.4 indicates that the use of heat treatment substantially reduces the corrosion rate of 20wt%Fe coatings more than 50% after heat treatment. The 80wt%Fe coatings seems to indicate an accelerated corrosion rate after heat treatment as compared to heat treated CP Fe, though the corrosion rate is decreased as compared to the as-sprayed coatings.

Table 4.5: Polarization criteria of heat treated samples

Coating	Ecorr (mV)	i_{corr} (µA/cm^2)	CR (mmpy)
316L	-307.18±13.12	1.39±0.02	0.02±0.000
20Fe	-372.90±21.03	5.21±1.75	0.06±0.021
50Fe	-501.95±20.07	8.98±0.76	0.11±0.009
80Fe	-582.61±36.28	11.55±0.53	0.14±0.006
CP Fe	-611.57±116.25	11.56±0.47	0.14±0.006

Figure 4.17 compares the corrosion rates of annealed coatings obtained from the immersion and polarization tests. In this figure, 'I' and 'P' represent the average corrosion rates of annealed coatings obtained from immersion and polarization tests, respectively.

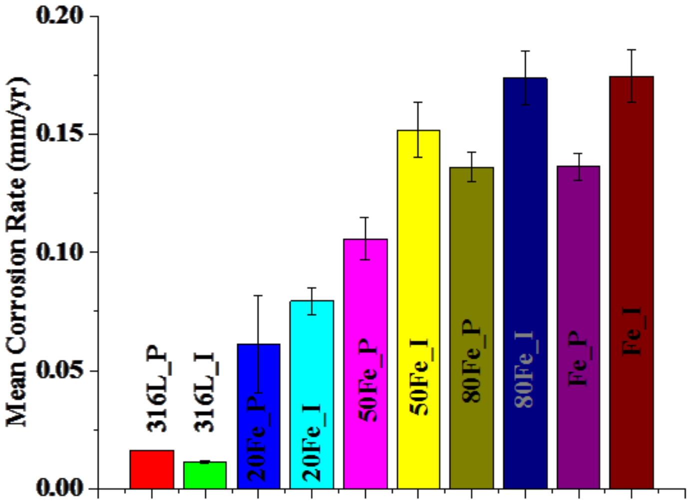

Figure 4.17: Comparison of corrosion rates from immersion and polarization tests of annealed coatings

Comparable corrosion rates are observed for all coatings. Although the 80wt%Fe coating exhibits the highest corrosion rate of all the mixed coatings, it has the lowest microgalvanic effect and lower corrosion rate of constituent coatings. Its corrosion rate is close to that of CP Fe for both the as-sprayed and annealed samples.

4.3.3 Galvanic Corrosion Test

Figure 4.18 and 4.19 illustrate the current flow from the as-sprayed working electrode to 316L and the heat treated working electrode to 316L, respectively. This allows for the calculation of the galvanic corrosion rate between working electrode and 316L at an area ratio of 1:1. Integration of the curve yields the galvanic current over time and results in Equation 4.8. Finally the galvanic corrosion rate is quantified according to Equation 4.7. The working electrode preferentially corrodes in relation to 316L, when galvanic current is positive.

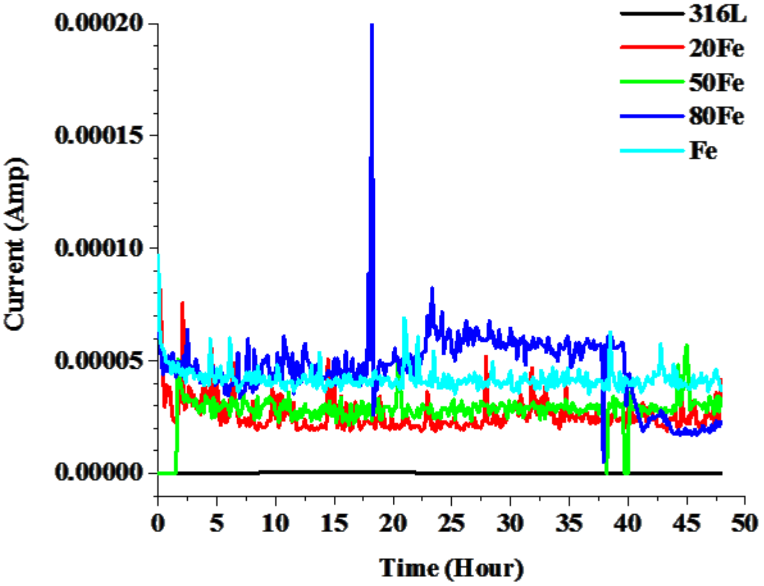

Figure 4.18: Current vs. time from galvanic corrosion tests of as-sprayed coatings

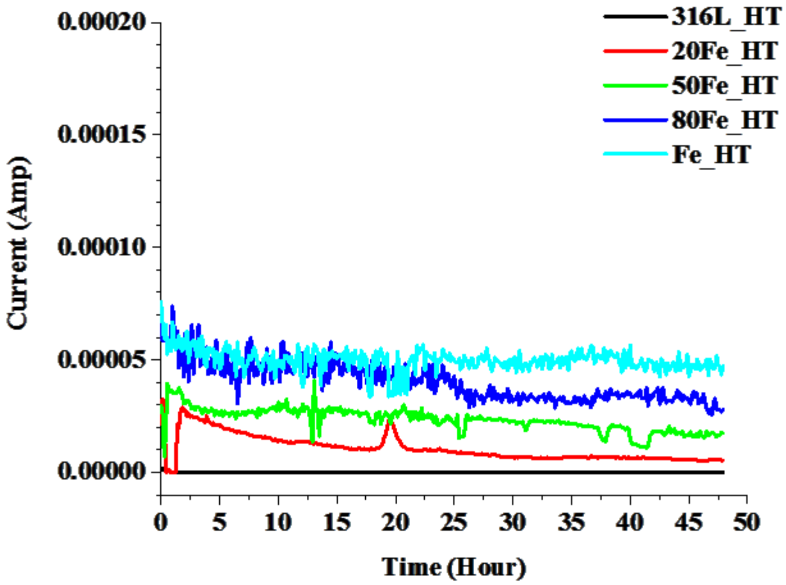

Figure 4.19: Current vs. time from galvanic corrosion tests of heat treated coatings

The galvanic corrosion tests used in this work are direct measurements as shown in Figure 4.18 and 4.19. Figure 4.18 demonstrates that the area under the curve increases when the weight percentage of CP Fe increases in the mixed coatings. The 80wt%Fe coatings have the highest areas. This signifies that the current that flows from the mixed coating to 316L is very close to the current that flows from the CP Fe coatings to 316L. Therefore, the galvanic corrosion rate of the 80wt%Fe/316L couple is very close to the CP Fe/316L couples. Figure 4.19 displays the reduction of current flow for all heat treated coatings. This means a reduction of the couple corrosion rate for the heat treated coatings as compared to the as-sprayed coatings. Figure 4.20 and 4.21 summarize the rate of mass losses and corrosion rates for the mixed coatings due to galvanic corrosion as compared to 316L. The effect of heat treatment on microgalvanic corrosion is evident as a result of a 66% reduction in couple corrosion rate of annealed vs. as-sprayed 20wt%Fe coatings. Although the 80wt%Fe coating exhibits the lowest effect on microgalvanic corrosion, the effect of heat treatment did not substantially reduce the couple potential.

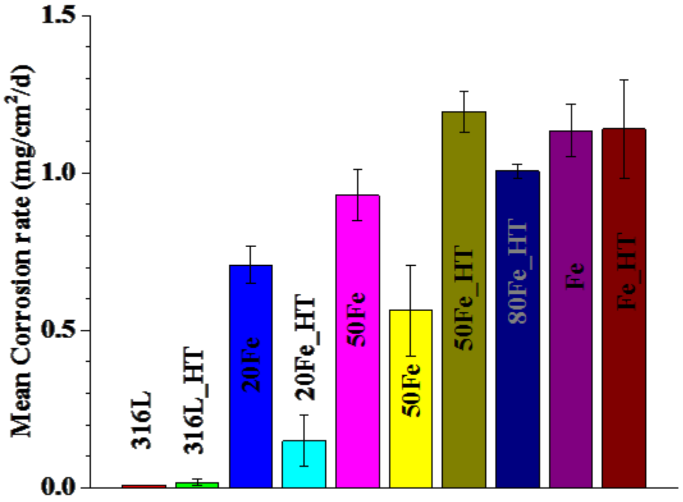

Figure 4.20: Average rates of mass loss for the mixed coatings from galvanic corrosion coupled with 316L (1:1 area ratio)

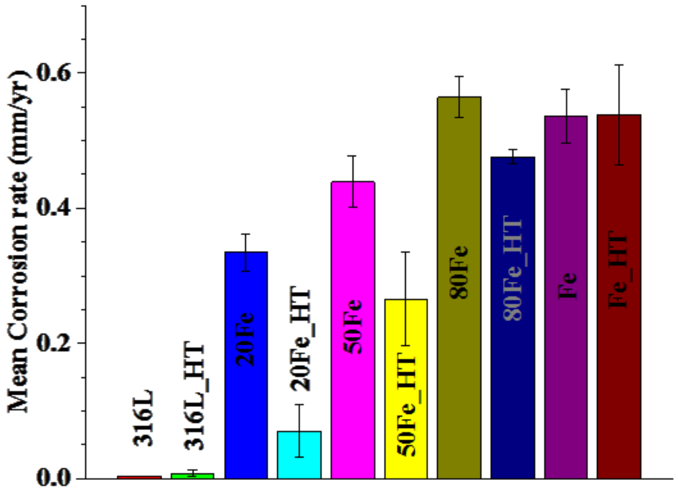

Figure 4.21: Average galvanic corrosion rates for the mixed coatings coupled with 316L (1:1 area ratio)

4.3.4 Characterization of the Degraded Products

The corrosion products were determined using XRD on the coating surface after the immersion test, in Figure 4.22. Comparing Figure 4.22 with the XRD of the as-sprayed coatings in Figure 2.19, similar peaks are identified before and after the corrosion test. This indicates that the corrosion products are originating from the peaks that are observed before the corrosion test.

Table 4.6 lists the degraded products. Figure 4.22 shows that maghemite, an austenitic iron (iii) oxide is predominantly responsible for the corrosion in Hank's physiological solution. Other than maghemite, elemental iron, rokuhnite (hydrated iron (ii) chloride with iron (iii) oxide) contributes to the overall corrosion. Iron (iii) oxide is the stable end product from elemental iron, whereas iron (ii) oxide and Fe_3O_4 are the unstable degradation products between elemental iron and iron (iii) oxide.

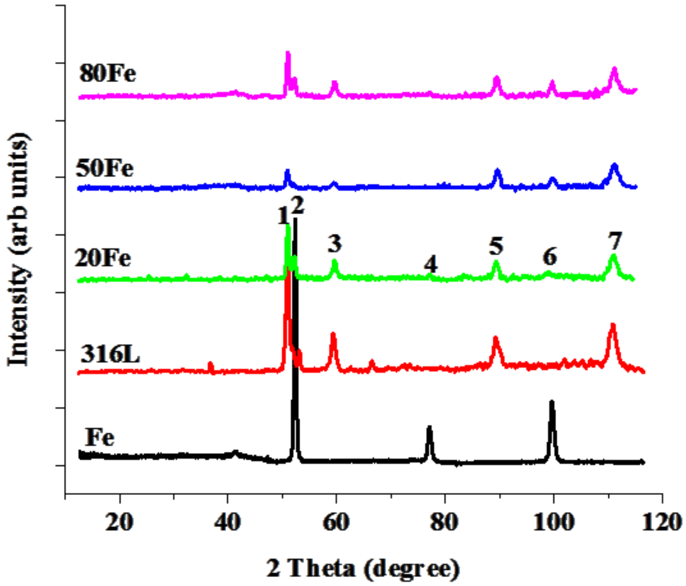

Figure 4.22: Characterization of the corrosion products with XRD

Table 4.6: Corrosion compounds identified with XRD

Peaks	**Compound Name**
1	Maghemite, C + Fe Ni ($Fe_{0.64}Ni_{0.36}$)
2	Fe+Fe_2O_3
3	Rokuhnite, syn $FeCl_2.2H_2O$+Fe_2O_3
4	Fe
5	Rokuhnite, syn $FeCl_2.2H_2O$
6	Fe
7	Maghemite, C+ Maghemite, Q

It is apparent that iron (iii) oxide is the conventional common oxide that takes part in the corrosion of the as-sprayed coatings in Hank's physiological solution. On the other hand, the compounds consisting of Maghemite, elemental iron, iron (iii) oxide and $Fe_{0.64}Ni_{0.36}$ take part in 316L corrosion. The surface analysis with X-Ray Photoelectron spectroscopy (XPS) on the degraded 316L exhibits the formation of iron, chromium and molybdenum oxides after 24 weeks of immersion in Hank's physiological solution [99]. Another XPS study on degraded 316L shows that chromium is the main element of the oxide layer formed after 14 weeks of degradation in a phosphate buffer solution with various concentration of bovine serum albumin [103]. The absence of chromium can be attributed to either insensitivity of XRD equipment or a shorter period of immersion time (6 weeks) in Hank's solution. Degraded 316L samples observed only after 6 weeks of immersion may not indicate existence of chromium oxide on the coating surface and any visual layer of degradation product after 4 weeks were not observed. For other mixtures than 316L, the amount of chromium and molybdenum is reduced, so the potential of forming oxide potential of chromium and molybdenum is also reduced.

Figure 4.23 shows a scanning microscope image of the 20wt%Fe coatings after the galvanic corrosion test. Energy dispersive spectroscopy (EDS) analysis of the surface indicates with the red circle a pitting covered with iron, chlorine, carbon and oxygen. The blue circle indicates a crack with higher chromium percentage, which reveals that 316L starts to disintegrate due to galvanic corrosion.

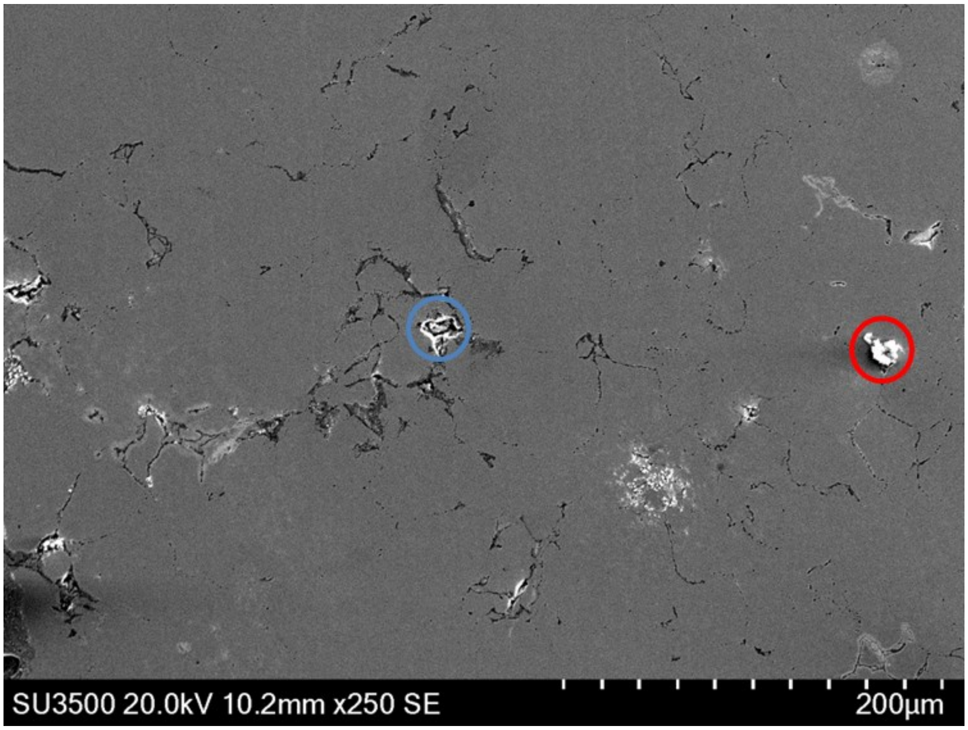

Figure 4.23: SEM image of 20wt%Fe after galvanic corrosion showing initiation of pitting (red circle) and initiation of corrosion from the cracked (blue circle) portion of the surface

Furthermore, the cracked and white spaces contain a higher oxygen concentration than the regular surface area. As a result, oxides initiate from the cracked or porous area.

Figure 4.24 shows the EDX spectrum of Figure 4.23 with the weight percentages of elements found after the completion of the corrosion test. Compared to the weight percentages obtained with ICP-OES (Table 2.8), it indicates that the carbon and oxygen content are introduced which are essentially contaminants and degradation products. The presence of sodium is due to the fact that it is the main component of Hank's solution. The existence of all other elements of the Hank's solution and the degraded surface of 20wt%Fe are depicted in Figures 4.25 and 4.26. Carbon in this surface is actually containment which is found over the entire surface.

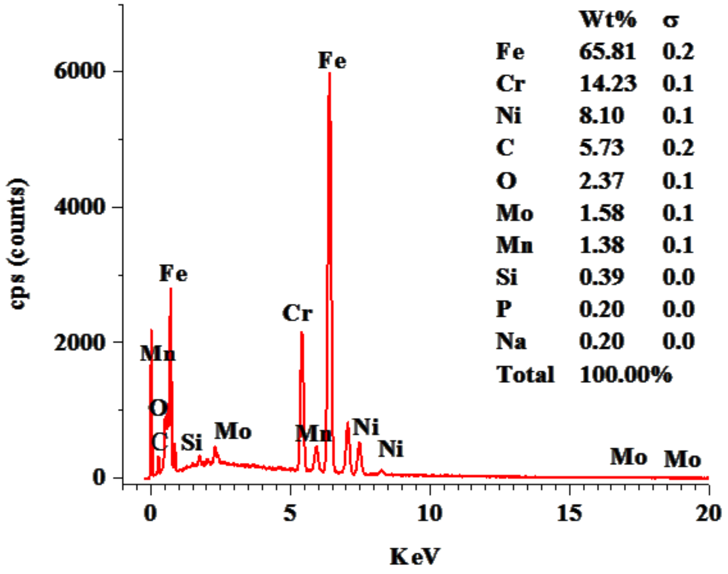

	Wt%	σ
Fe	65.81	0.2
Cr	14.23	0.1
Ni	8.10	0.1
C	5.73	0.2
O	2.37	0.1
Mo	1.58	0.1
Mn	1.38	0.1
Si	0.39	0.0
P	0.20	0.0
Na	0.20	0.0
Total	100.00%	

Figure 4.24: Energy dispersive spectral analysis on corroded 20wt%Fe coating

The oxygen found on the degraded surface is apparent only on the cracked, porous and pit areas. Chlorine is showing only on rare pits (red-circled in Figure 4.23). Silicon is another contaminant that results from polishing the material. The elements inside 20wt%Fe are all visible on the EDS mapping.

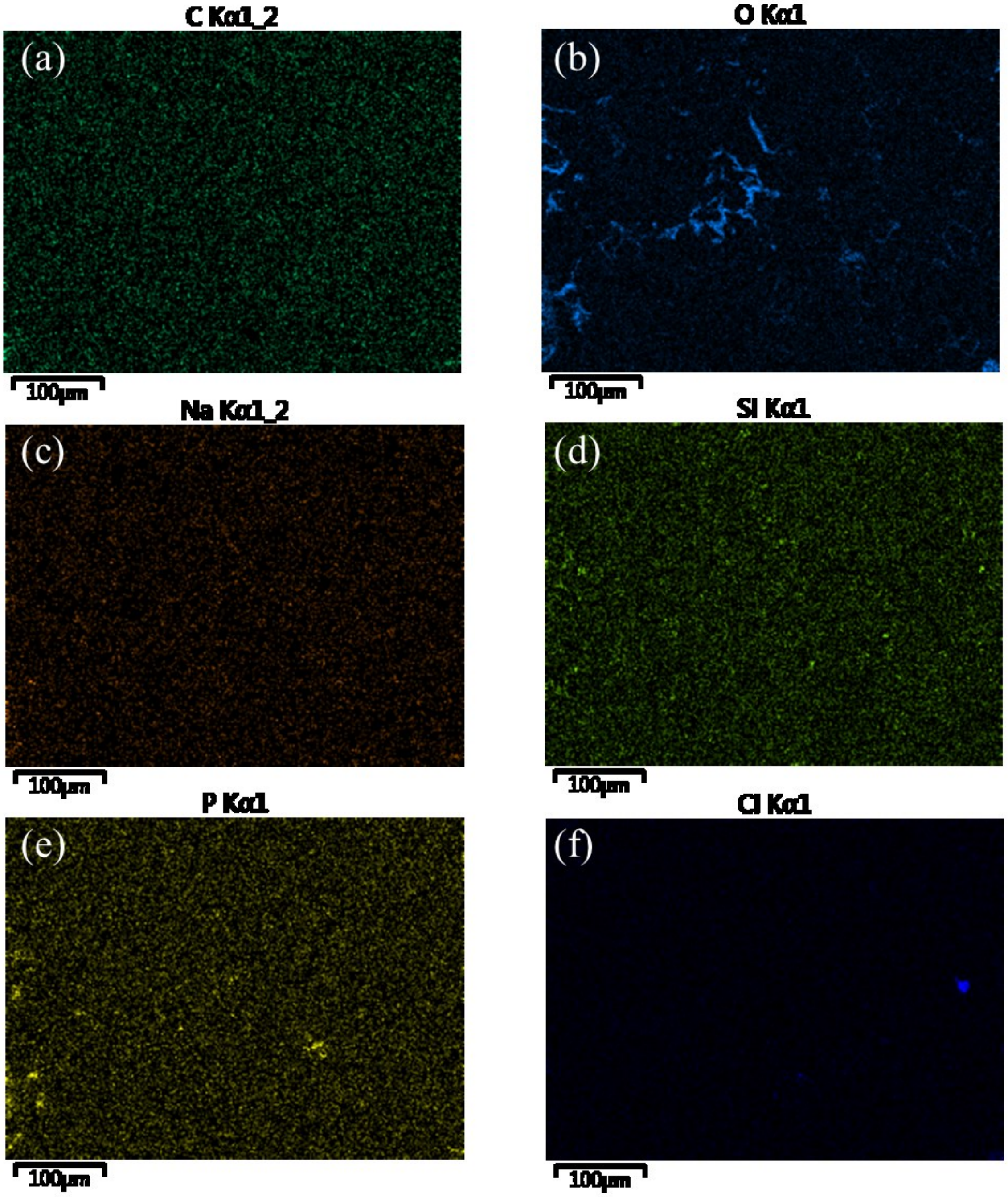

Figure 4.25: EDS elemental mappings of (a) C, (b) O, (c) Na, (d) Si, (e) P and (f) Cl on 20Fe after corrosion test

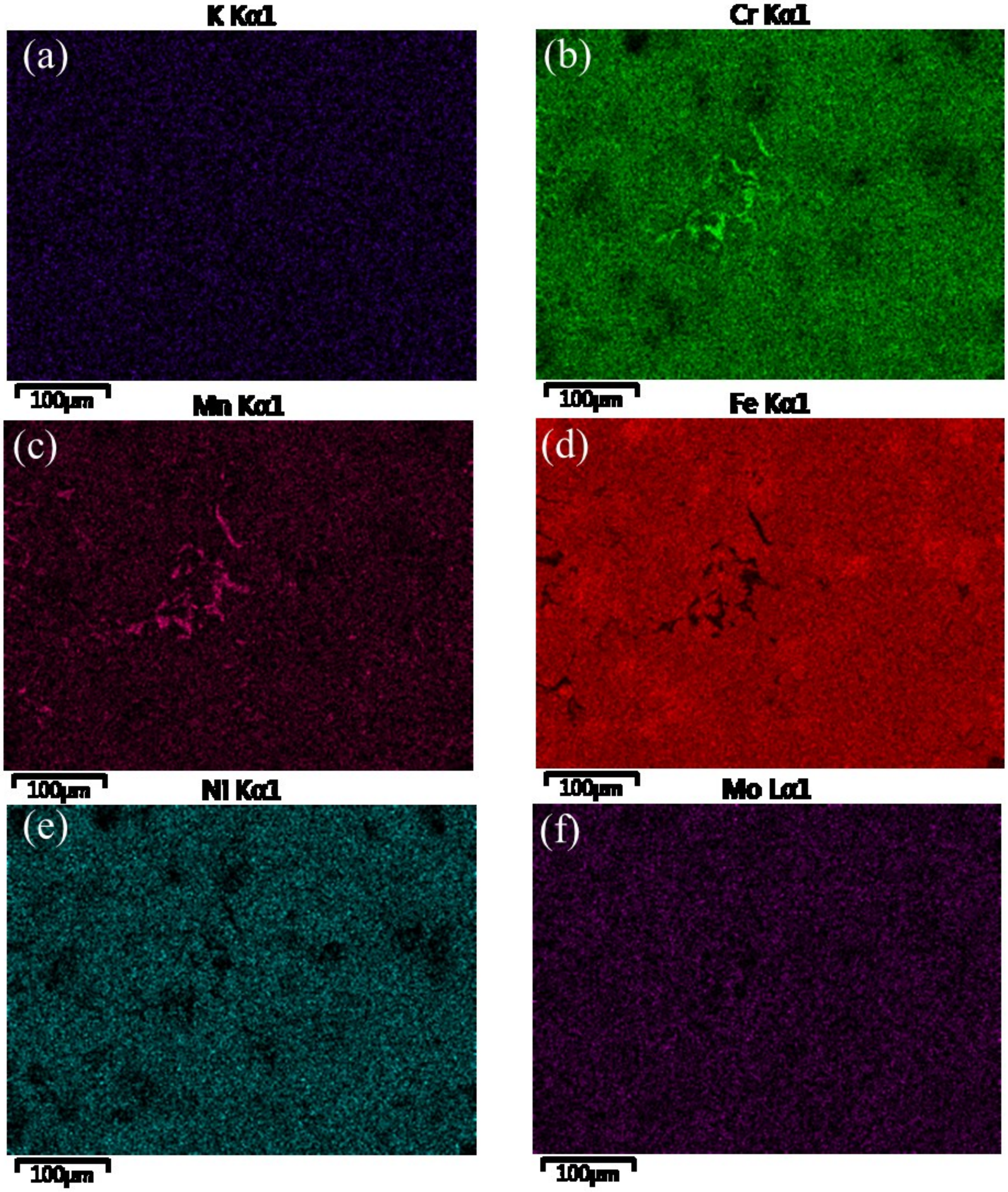

Figure 4.26: EDS elemental mappings of (a) K, (b) Cr, (c) Mn, (d) Fe, (e) Ni and (f) Mo on 20Fe after corrosion test

The 80wt%Fe coating, however, exhibits numerous pits on the degraded surface, as illustrated in Figure 4.27.

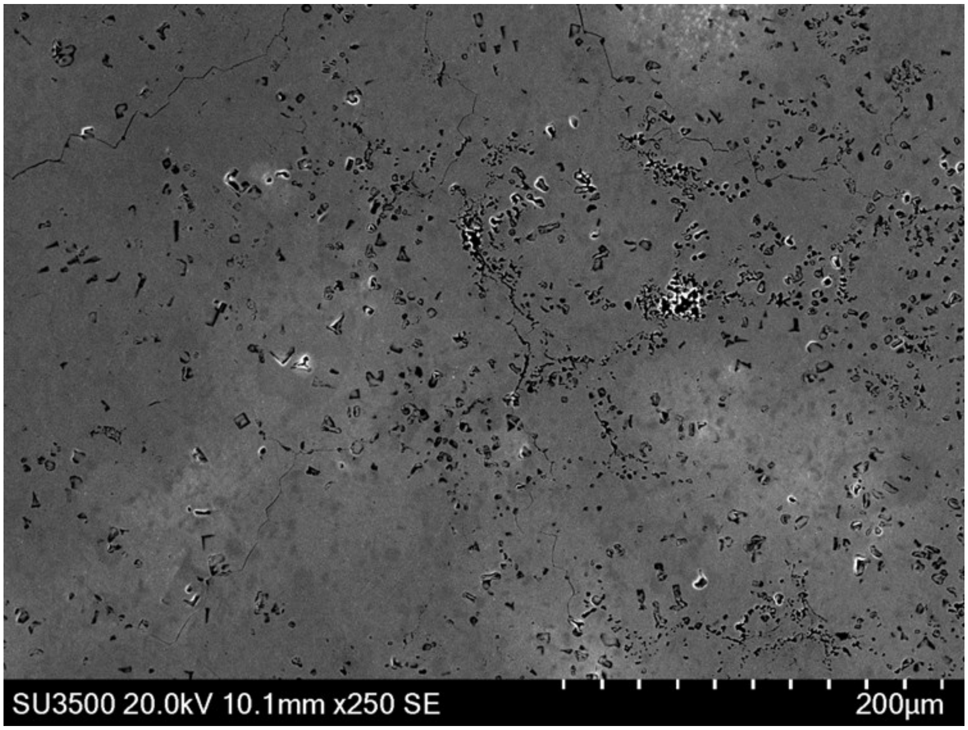

Figure 4.27: SEM image of degraded 80wt%Fe showing network of pits throughout the surface

Pits form a network on the surface of the 80wt%Fe with pores which disintegrates the surface. The EDS spectrum of Figure 4.27 does not indicate higher percent for CP Fe because a lot of CP Fe has been disintegrated and mixed to Hank's solution (Figure 4.28). The higher chlorine concentration on the 80wt%Fe surface is responsible for pits forming and is still present after cleaning. It is also seen on the EDS elemental map for chlorine (Figure 4.29(f)). Compared to EDS mapping with 20wt%Fe (Figure 4.25(f)), chlorine is observed on the surface where pits are observed. Apart from chlorine, higher phosphorus content in the 80wt%Fe coating is also observed than the 20wt%Fe coatings. Oxygen and carbon contents are not increased significantly as visible contaminants are cleaned before EDS observation. Therefore, it can be concluded that galvanic corrosion of 20wt%Fe with 316L coating initiates pits, the number of accelerates over time (Figures 4.23 and 4.27). It is also observed that oxidation starts from the weak parts of surface where cracks and pores are located. The existence of all other elements of the Hank's solution and the degraded surface of 80wt%Fe are depicted in Figures 4.29 and 4.30.

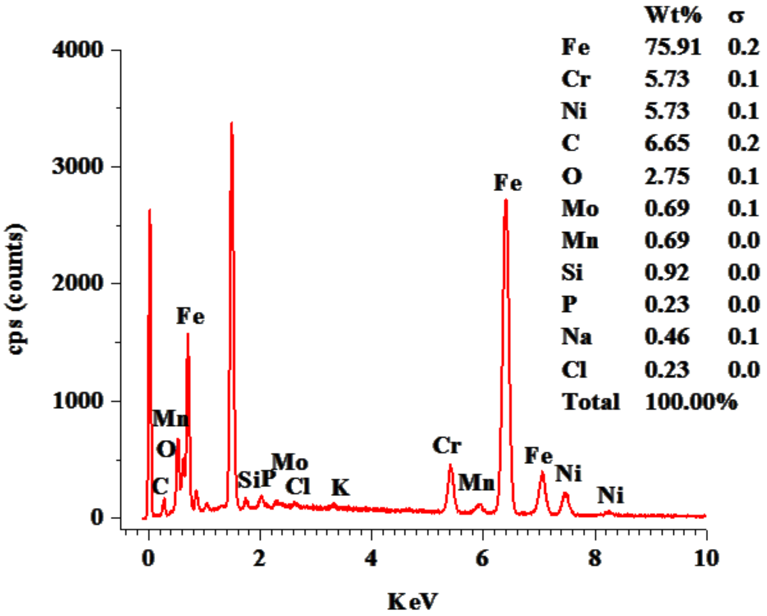

	Wt%	σ
Fe	75.91	0.2
Cr	5.73	0.1
Ni	5.73	0.1
C	6.65	0.2
O	2.75	0.1
Mo	0.69	0.1
Mn	0.69	0.0
Si	0.92	0.0
P	0.23	0.0
Na	0.46	0.1
Cl	0.23	0.0
Total	100.00%	

Figure 4.28: Energy dispersive spectral analysis on corroded 80wt%Fe surface

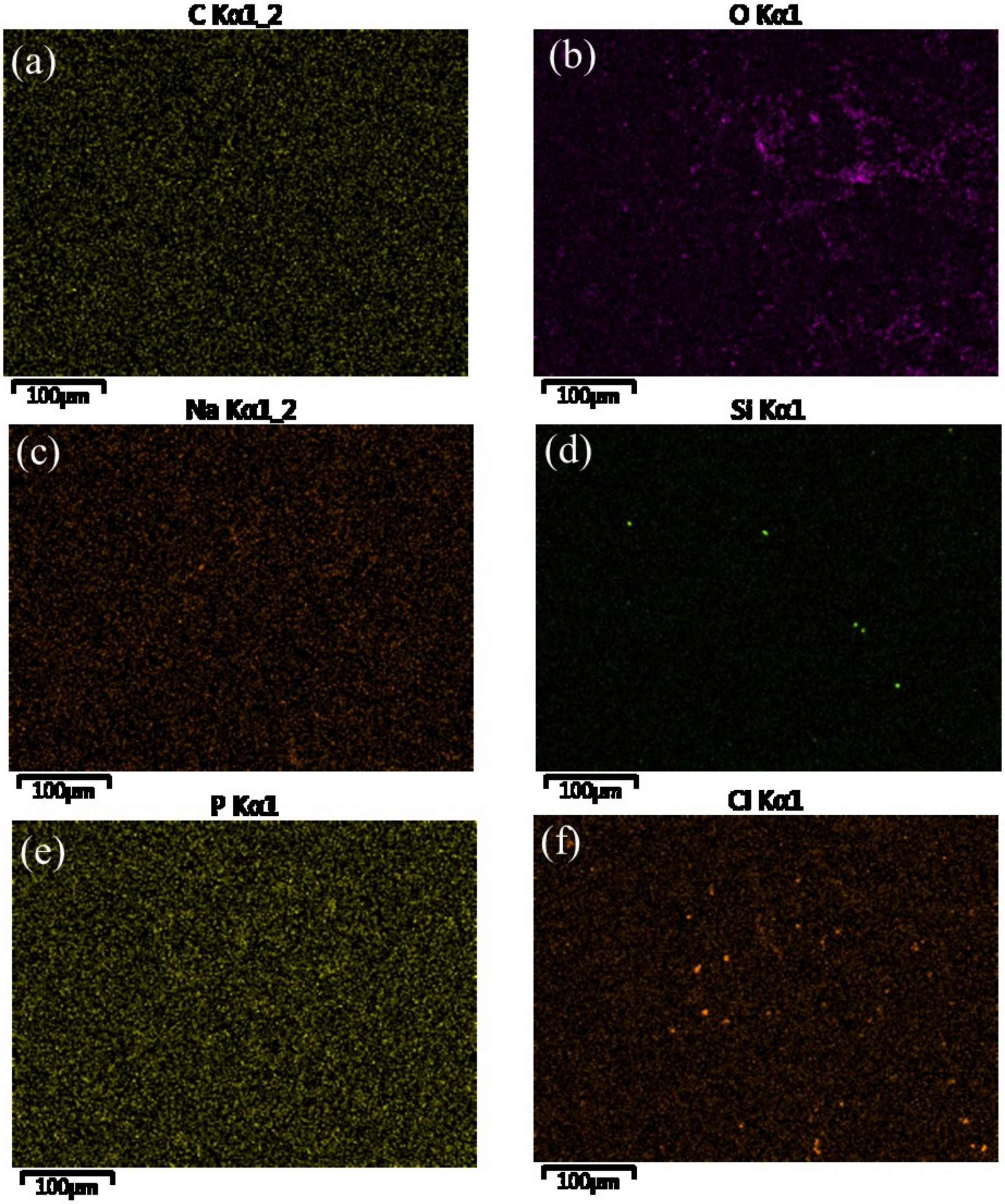

Figure 4.29: EDS elemental mappings of (a) C, (b) O, (c) Na, (d) Si, (e) P and (f) Cl on 80wt%Fe after corrosion test

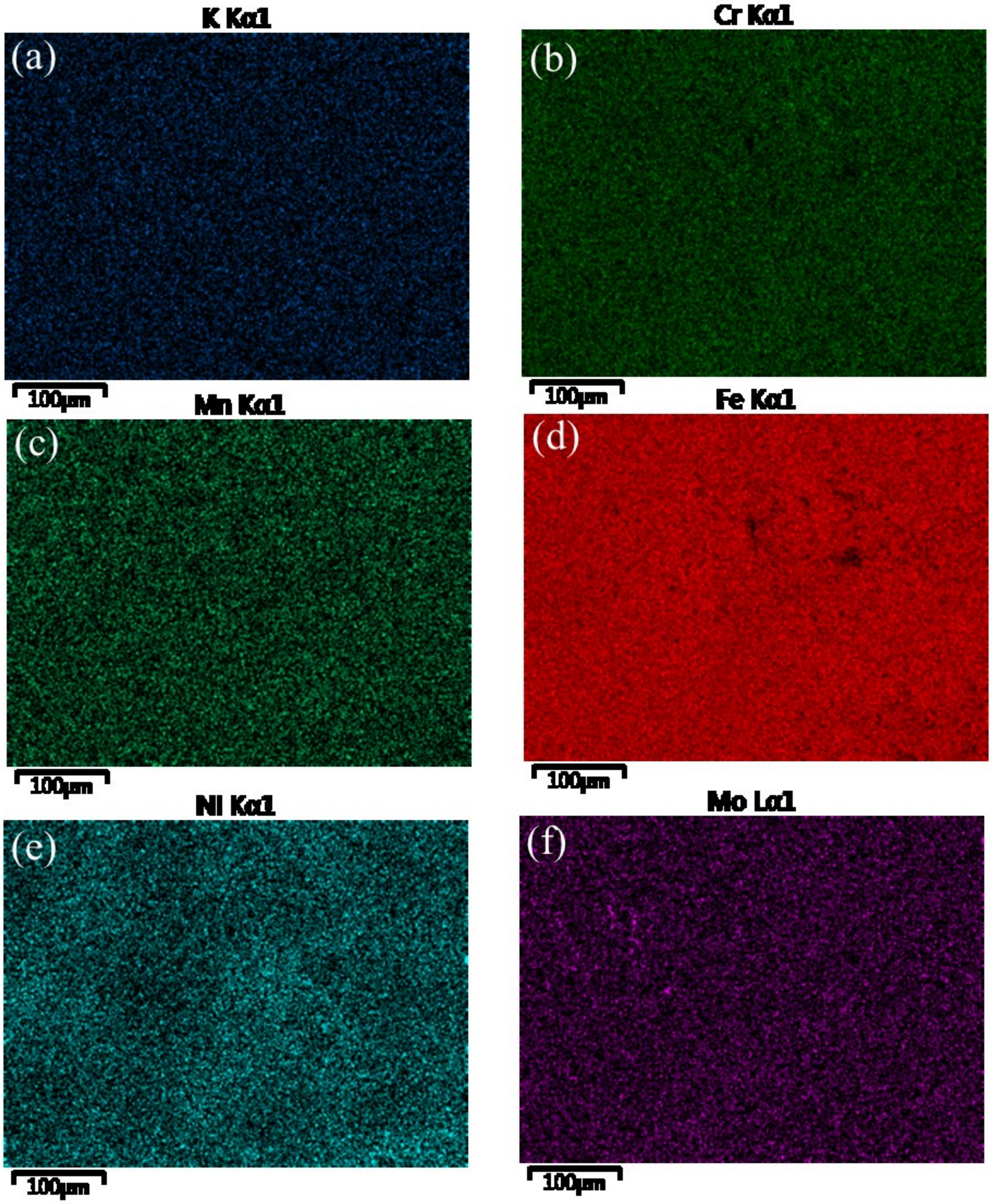
K Kα1

Cr Kα1

Mn Kα1

Fe Kα1

Ni Kα1

Mo Lα1

Figure 4.30: EDS elemental mappings of (a) K, (b) Cr, (c) Mn, (d) Fe, (e) Ni and (f) Mo on 80wt%Fe after corrosion test

A higher CP Fe percentage cannot resist degradation; due to the fact that it lacks chromium and molybdenum, which contribute to form protective oxide layers on stainless steel. Low magnification images of heat treated 80wt%Fe coatings immersed after 5 weeks in Hank's solution exhibits large pits (Figure 4.31). This disintegration also indicates that irons are preferentially degraded during the immersion test.

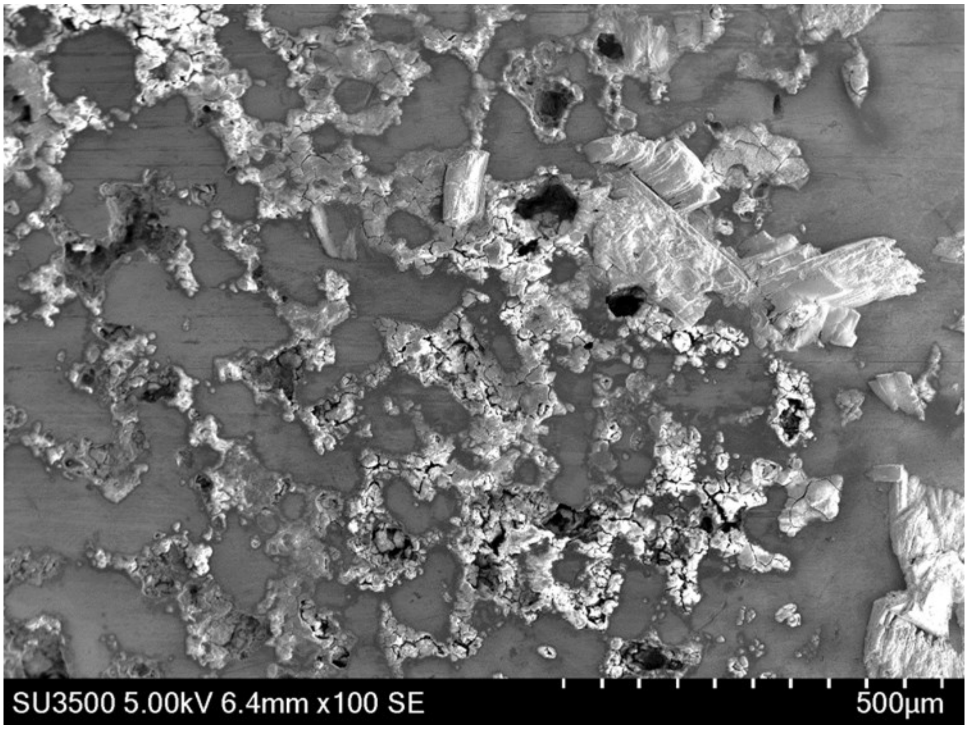

Figure 4.31: 80wt%Fe coating after 5 week immersion test showing disintegration of the surface from large pits

Although 80wt%Fe exhibited a higher corrosion rate, it is associated to the lowest corrosion due to microgalvanic effect. The 20wt%Fe coatings exhibit the highest corrosion due to microgalvanic effect, but the SEM images cannot differentiate the effect of microgalvanic corrosion on 20wt%Fe coatings.

4.4 Empirical Equation for Corrosion Rate Estimation of Mixed Coatings

The corrosion rates obtained with the immersion and polarization tests are used to generate an empirical equation which can estimate corrosion rate based on CP Fe percentage. A polynomial best fit curve is plotted on the average corrosion rates obtained from immersion test and potentiodynamic polarization technique and are represented in Figures 4.32 and Figure 4.33, respectively. Based on the nature of the corrosion rate, a simple polynomial equation is proposed as follows:

$$CR = A + Bx + Cx^2 \qquad [4.11]$$

Here, *CR* and *x* represent the corrosion rate and CP Fe weight percentages, respectively. *A*, *B* and *C* are the empirical constants. Table 4.7 lists the values of constants to be used for estimating corrosion rate.

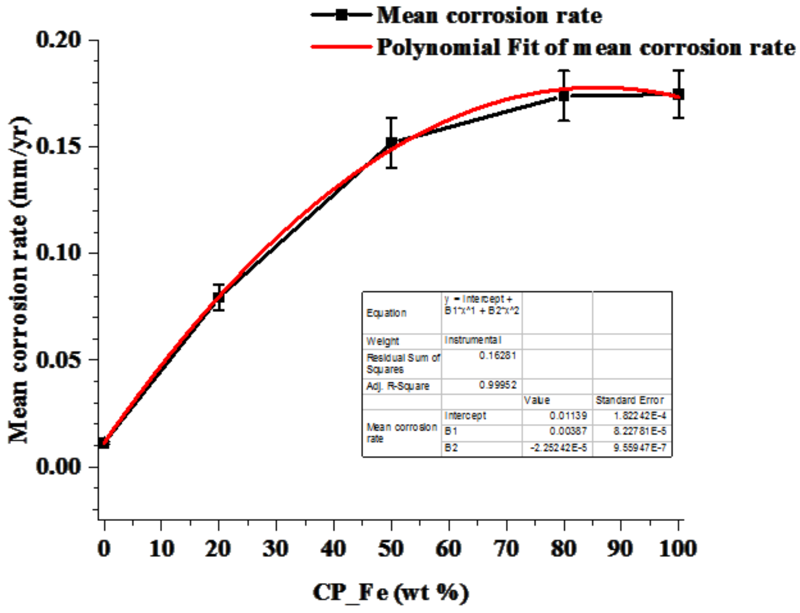

Equation	y = Intercept + B1*x^1 + B2*x^2		
Weight	Instrumental		
Residual Sum of Squares	0.16281		
Adj. R-Square	0.99952		
		Value	Standard Error
Mean corrosion rate	Intercept	0.01139	1.82242E-4
	B1	0.00387	8.22781E-5
	B2	-2.25242E-5	9.55947E-7

Figure 4.32: Polynomial fit for annealed immersion corrosion tests showing average corrosion rate

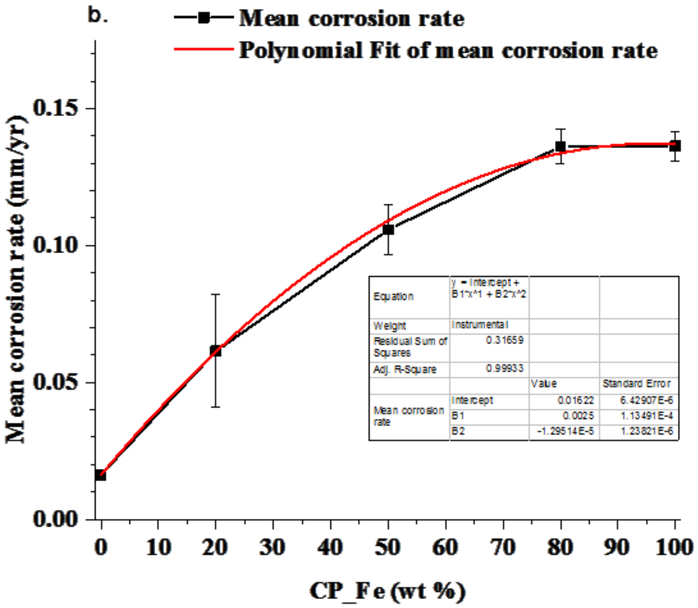

Figure 4.33: Polynomial fit for annealed polarization corrosion tests showing average corrosion rate

Table 4.7: Empirical constants for the quadratic model

Constant	Values	
	Immersion test	**Polarization test**
A	$11.39\times10^{-3}\pm1.82\times10^{-4}$	$16.22\times10^{-3}\pm6.43\times10^{-6}$
B	$3.87\times10^{-3}\pm8.23\times10^{-5}$	$2.50\times10^{-3}\pm1.13\times10^{-4}$
C	$-2.25\times10^{-5}\pm9.56\times10^{-7}$	$-1.30\times10^{-5}\pm1.24\times10^{-6}$

Empirical equations exhibit R^2 values greater than 0.99 for both cases which indicate a good fit curve for corrosion rate estimation by empirical equation. However, an exponential empirical equation is also generated to obtain a better fit of the corrosion rates with a fewer amounts of constants. Based on the immersion corrosion rate, an exponential equation is proposed as follows:

$$CR = CR_{max}(1 - exp^{(-ax)}) \qquad [4.12]$$

Figure 4.34 illustrates a best fit curve based on Equation 4.12:

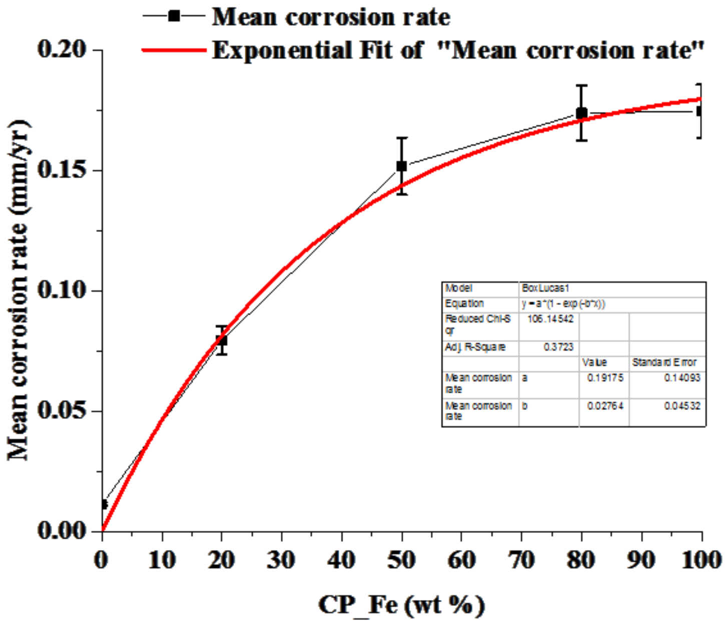

Figure 4.34: An exponential fit for immersion corrosion tests showing the average corrosion rate

Figure 4.34 exhibits that the exponential Equation 4.12 can predict the average corrosion rate if only one coefficient value is known. It does not provide a good R^2 value (R^2=0.37) but corrosion rate can be estimated within the standard deviation of experimental value.

4.5 Corrosion Mechanism

The corrosion mechanism of the mixed coating during the corrosion test in Hank's physiological solution can be generalized into four steps:

1. Initial red-ox reaction:

Anodic dissolution of iron (main composition of the mixed and pure coatings) results in the oxidation of metallic ions can be described by:

$$Fe \rightarrow Fe^{2+} + 2e^{-} \qquad [4.13]$$

Cathodic reaction consumes the electrons produced during the oxidation:

$$O_2 + 2H_2O + 4e^{-} \rightarrow 4OH^{-} \qquad [4.14]$$

2. Oxides and hydroxide layer formation:

The top, middle and bottom layers of the oxidized surface is due to hydrated Fe_2O_3, Fe_3O_4 and FeO, respectively [31]. Here, iron forms insoluble hydroxides and oxides by reacting with hydroxyl ions liberated from the cathodic reaction:

$$2Fe + 4OH^- \rightarrow 2Fe(OH)_2 \rightarrow 2FeO.2H_2O \qquad [4.15]$$

$$4Fe(OH)_2 + O_2 + 2H_2O \rightarrow 4Fe(OH)_3 \rightarrow 2Fe_2O_3.6H_2O \qquad [4.16]$$

3. Pit formations:

The exposed oxide layers are affected by iron chlorides from physiological solution which forms hydroxides and acid by hydrolyzation:

$$Fe^{2+} + 2Cl^- \rightarrow 2FeCl_2 \qquad [4.17]$$

$$FeCl_2 + H_2O \rightarrow Fe(OH)_2 + HCl \qquad [4.18]$$

4.6 Conclusion

In summary, this chapter presented the following conclusions:

a. Iron oxide layers reduce corrosion rate after a certain time period (18 days or so) during the immersion test.

b. Annealed 80wt%Fe coatings exhibit a 0.23 mmpy corrosion rate after 18 days of immersion, which is comparable to other iron-based degradable materials. Instead, microgalvanic effect is found to be the lowest due to the lower cathodic area which decreases their corrosion rate closer to CP Fe. 20wt%Fe coatings exhibit the highest corrosion rate due to micro-galvanic effect, but lower corrosion rates of the constituent materials (316L and CP Fe) and lower porosity after annealing reduces the corrosion rate of 20wt%Fe. The corrosion rates obtained from the polarization test also supports this notion as the corrosion rates found from both tests are similar.

c. Annealing reduces the microgalvanic effect of the 20wt%Fe and the overall corrosion rate decreases by almost 50% as compared to the corrosion rate of the as-sprayed samples. The reduction of porosity decreases the surface area of the coating and resultantly reduces the overall corrosion rate. The 80wt%Fe exhibits the highest overall corrosion rate even after heat treatment which is a result of the higher percentage of CP Fe in the 80wt%Fe coatings. The microgalvanic effect and porosity reduction did not accelerate the corrosion rate.

d. The galvanic corrosion test of the mixed coatings with respect to 316L at 1:1 area ratio indicated that galvanic corrosion of 80wt%Fe/316L couple exhibited the highest corrosion rate among the mixed coatings. It also indicated that the reduction of porosity did not decrease the rate of mass loss of the 80wt%Fe coatings.

e. Corrosion initiates from the defective areas (cracks and pores) of the coating where oxide layers form on the surface. Pitting is results due to the presence of chloride ions in physiological solution which attacks the surface not covered with oxide layers.

Chapter 5. **Stent Fabrication and Future Work**

5.1 Introduction

In this chapter the process of stent fabrication is considered following the successful coating on plane substrates by cold spray. The degradation and mechanical properties found for the plane coatings lead to the conclusion that the optimum coatings for stent fabrication utilized powder mixtures during the coating process. Based on the mechanical and corrosion tests described in the previous chapters, it was found that the 80wt%Fe coatings were suitable candidates to be used to fabricate a degradable stent. The present chapter describes the stent fabrication procedure, current status and the future work to be done to initiate the in-vivo trials using stents fabricated from mixed coatings.

5.2 Experimental Details

Coatings were sprayed on rods to form the raw material required for producing stents. There are two differences between spraying onto a rod and spraying onto a plate. First, the rod must be rotated on a mandrel, as shown in Figure 5.1, in contrast with a plate that can remain stationary. Secondly, the spray gun traces out a 1D motion for spraying onto a rod whereas the spray gun motion follows a 2D path for spraying onto a plate. Although coating onto a rod is not uncommon, some trial and error is necessary to optimize this process. Another factor to consider is that the deposition efficiency will be less when spraying onto a rod since the rod surface is not flat and some powders will deflect off of the rod.

When the powder is sprayed onto a 5-8 mm diameter rod substrate, some of the powder at the edges of the spray cone will be lost due to the small diameter of the rod. This loss increases as the rod diameter decreases. The gun traverse speed (GTS) used for plane coatings is transferred to robot speed for rod coatings. GTS may be converted to motor speed (rps or rpm) by following the simple equation:

$$GTS = \pi \times D \times rps \qquad [5.1]$$

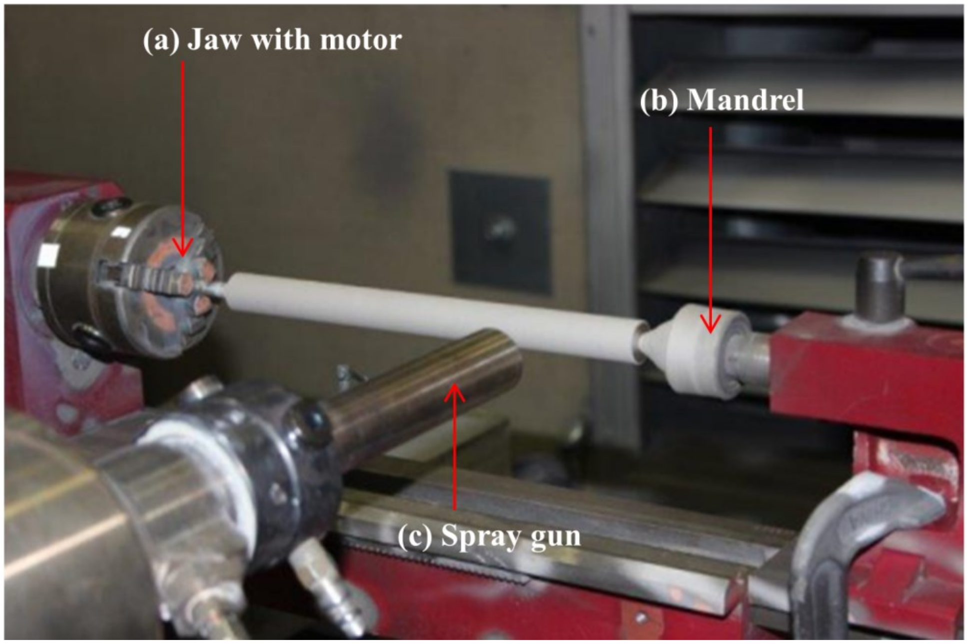

Figure 5.1: Cold spray with rods showing (a) jaw with a motor (b) mandrel and (c) spray gun

A motor speed of 11.94 or 19.1 rps is necessary for an 8 or 5 mm diameter rod, respectively.

The robot speed is calculated with the assumption that one revolution of the rod will correspond to the plate step size. Hence the robot speed may be calculated as follows:

$$Robot\ speed = \frac{Step\ size}{Time\ for\ one\ revolution\ (sec)} \qquad [5.2]$$

The step size used for a plane coating is 2 mm and the time for one revolution used for an 8 mm rod is 11.94 sec^{-1}. So, the robot speed used for an 8 and 5 mm rod is 23.87 and 38.2 mm/sec, respectively. Due to variations in the microhardness of the various powder lots, the cold spray parameters must be adjusted for each powder lot to optimize the coating efficiency. The parameters must also be adjusted so that the rod rotational speed is not too high because high rotational speed may cause the rod to be eccentric. High rotational speeds make the deposition process less efficient because of the difficulty to deposit particles onto a curved surface rotating at a high speed. The final process parameters used for the rod coatings are given in Table 5.1 below:

Table 5.1: Parameters used for rod coatings

Powder Lot	**Rod Dia (mm)**	**Gas Temp. (°C)**	**Gas Pressure (MPa)**	**Stand-off (mm)**	**Robot Speed (MPa)**	**Feed Rate (gm/min)**	**Rod Rotational Speed (rpm)**
1	8	700	4	80	23.87	24.1	716
2	5	700	4	80	38.20	36	1100
3	5	700	4.9	40	4.8	33	139

The KINETICS 4000 cold spray system was utilized for lot 1 coatings. There was a clogging issue with the 80wt%Fe coatings that lead to use the Plasma Giken® cold spray system PCS-800 for the subsequent coatings shown in Figure 5.1. Lot 1 coating was not grit blasted because buckling was observed with lot 1 coatings on an aluminum 6061 rod. Aluminum is used as a substrate to deposit lot 1 powders but due to its severe potential adverse effects, mild steel was used as a substrate for the subsequent spray processes. Aluminum substrates are removed from the coating by using slow diamond cutter and grind to remove the traces of aluminum on the coating to be characterized for the corrosion and microstructural tests. Chemical compositions of the coatings did not exhibit any traces of aluminum.

However, lot 2 and 3 substrates were grit blasted to increase the adhesion of the coating. In addition, the lot 3 substrates were preheated with two passes of nitrogen gas for better coating deposition. The substrates were six inches in length, with a coating length of approximately 3 to 4 inches. The resulting coating thicknesses varied between 1.5 and 2 mm. A typical rod after cold spray deposition is shown in Figure 5.2.

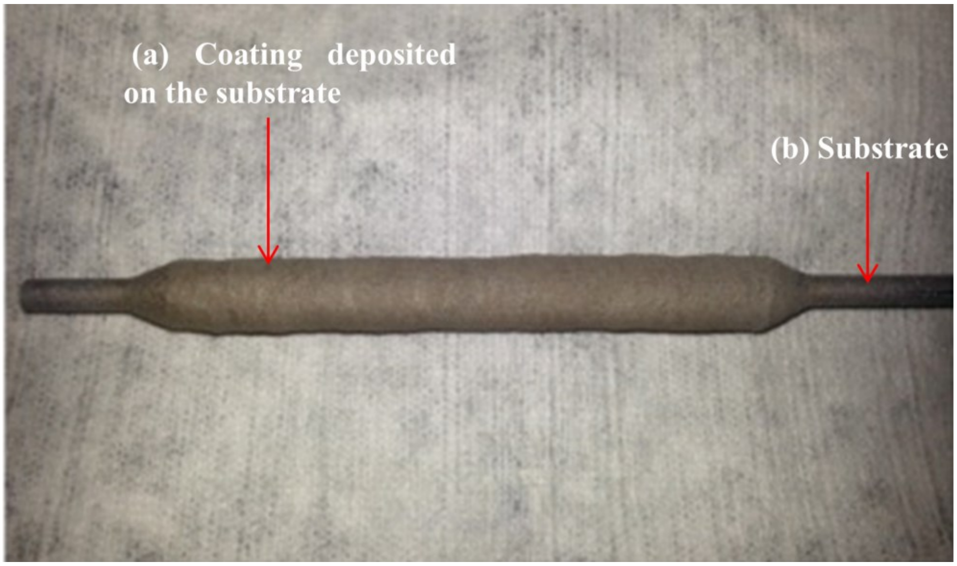

Figure 5.2: 80wt%Fe mixed powders deposited on a rod substrate showing (a) coating deposited on the substrate and (b) substrate

5.3 Manufacturing Process of Stents

Based on the spray parameters listed in Table 5.1, aluminum Al6061 substrates were chosen first after considering that the heat treatment at 1100°C will cause the substrate to melt leaving only the coating after heat treatment. Coatings were annealed after spraying in a temperature-controlled ThermCraft box furnace. In the first attempt, several 2 mm thick coatings surrounding rods were annealing at 1100°C by hanging them from the top holes of the ThermCraft box furnace. A similar annealing operation was performed as presented in subsection 3.2.2. Following this procedure, it was found that the aluminum expanded during the heat treatment and destroyed the coatings, as shown in Figure 5.3(a). In addition, heat treatment of the coating surrounding an aluminum rod induces diffusion of aluminum inside the coating at high temperature. Hence, electrical discharge machining (EDM) was employed on the remaining coatings to remove the rod from the coating. A hole was drilled through the middle of the rod and then an EDM wire was inserted. Then the EDM method was used to cut the substrate to a diameter of 8 mm and then flatten the top surface to remove the surface nonuniformities that result from the spraying process. To fabricate a stent, the tubes were laser cut with the desired stent cell design. The use of conventional laser cutting techniques would result in heat-affected zones, leading to an overall increase of grain growth, affecting the mechanical properties of the material. Femto lasers use ultrafast, single step laser gun that employ a fraction of the energy of standard laser which minimize thermal damage. Indeed, conventional laser imparts an important amount of energy as heat and exhibits thermal damage which requires post processing. The reasons to employ the femtosecond laser to fabricate degradable stents are as follows [104]:

1. Since femto second laser has no heat effect on the machined material, the material has no damage due to the thermal defects and stay as dissimilar metals. Therefore post processing and relevant post-operating costs are negligible as compared to other processes.
2. Machining is performed through ionization which separates molecular bonds without increasing the applied heat. Therefore, it enables to cut harder metal which usually requires more heat to be cut by conventional laser machining.
3. It is used in medical device manufacturers due to their configurability to machine parts in a very precise tolerance.

Therefore, a femto laser was used for the cutting process (SPECTRAlytics, Dassel, USA) to avoid the high heat associated with conventional laser cutting and potential associated alloying. The fabricated stent-like structure was cut to 0.8 cm in length; with a strut thickness of approximately 145 µm. Stents with thinner struts exhibit a reduced restenosis rate and better stent strut coverage as compared to the stents with thicker struts [105]. However, a strut thickness of 145 micron is selected as a thickness for the stent prototype. Strut thickness needs to be reduced in order to fabricate coronary stents. Figure 5.3(b) shows a photograph of the resulting stent minitube after EDM and femto laser cutting.

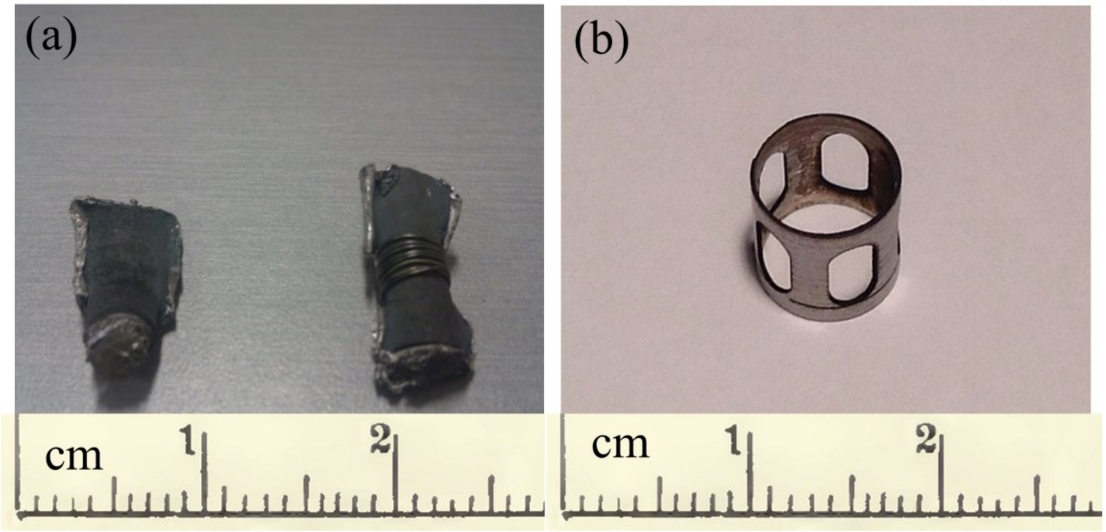

Figure 5.3: (a) Heat treatment effort of coatings with rod and (b) stent minitubes prepared after femto laser cutting

These stents did not maintain their integrity after laser cutting due to the absence of heat treatment. To provide a more rigid substrate for the coating onto a rod, a second coating attempt was made with a 1020CR mild steel rod selected instead of an aluminum substrate. In addition, center-less grinding (Avitech tools Inc., Montreal, QC, Canada) was used after heat treatment to obtain a polished surface finish. The coating of the various lot powders was performed according to the spray parameters shown in Table 5.1. The coatings with the rod were annealed at 1100°C for 1 hour after cold spray in a ThermCraft box furnace under an argon atmosphere. Similar annealing conditions were used as described in subsection 3.2.2. The post-processing required for stent fabrication was a three-step procedure, combining center-less grinding, electrical discharge machining (EDM) and laser cutting with electro-polishing.

Electropolishing is an electrochemical process which reduces surface imperfections by applying direct electrical current to the metal sample and another metal both immersed in an electrolyte. Current flow through the sample brightens, smooths, deburrs and passivates the exposed surface by dissoluting the sample [106].

The surface discontinuities that result from conventional laser cutting, machining and electrical discharge machining (EDM) initiates stress concentrations and metallurgical conditions at the cut surface. Stress concentration initiates fracture at a much lower stress than for an electropolished surface. Therefore, it can affect the mechanical and corrosion performance of medical devices. In principle, electropolishing restores the surface to an undamaged condition by removing undesirable metallurgical condition from the surface [107].

The final coating thickness after center-less grinding process was approximately 200-250 µm. Upon completion of center-less grinding, electrical discharge machining (EDM) was utilized to separate the coating from the rod substrate. Finally, femto laser and electropolishing was used to cut the minitubes with the desired stent cell design. The stents were cut between 1.5-2 mm in length; with a strut thickness of approximately 145 µm.

Figure 5.4(a) is the image after EDM processing and Figure 5.4(b) shows the first completed stent minitube that was fabricated by this procedure. Even after annealing for 1 hour at 1100°C, the ductility was relatively low for stent operation and the stents was not functional as it could not be deployed. Annealing at higher temperatures was determined to be necessary to fabricate a stent with high ductility. The stent fabrication process is summarized in the flowchart shown in Figure 5.5.

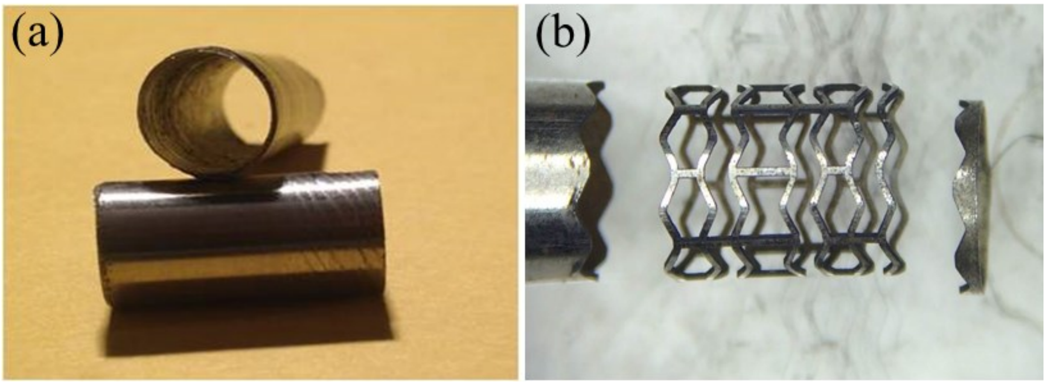

Figure 5.4: (a) Minitubes after EDM and (b) laser cut stents

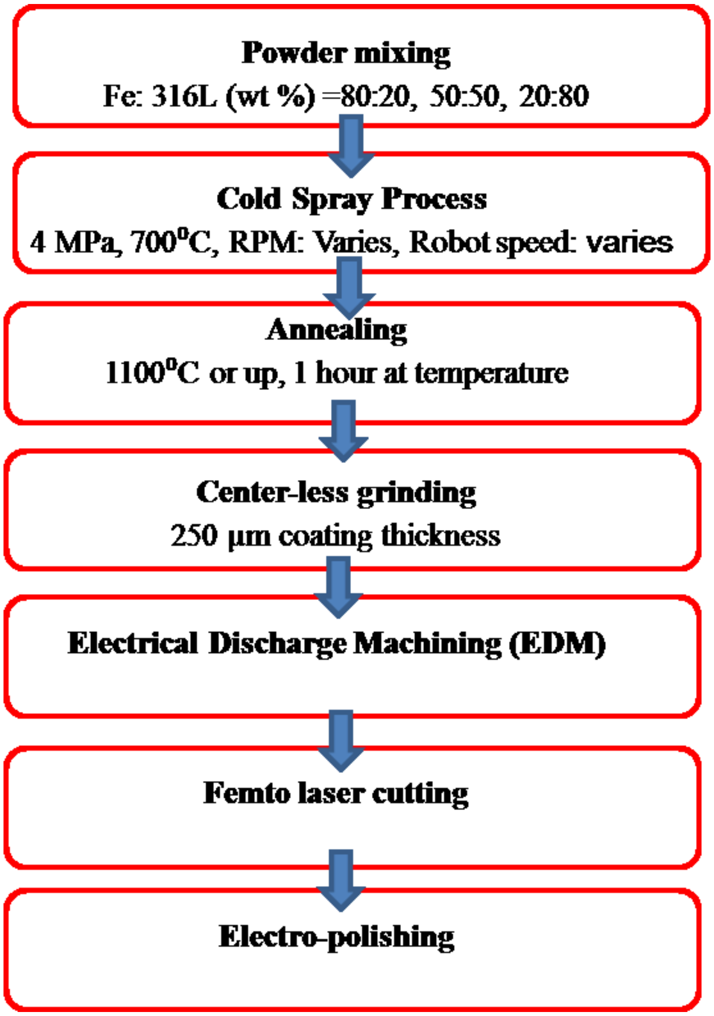

Figure 5.5: Flow chart for stent fabrication

5.4 Recommendations for the Future Plan

The production of lot 2 coatings has been completed with static immersion testing. Lot 3 coatings are currently being used for stent fabrication. The required heat treatment for lot 3 coatings performed in a Type F21100 tube furnace (Barnstead/Thermolyne Corporation, Iowa, USA) utilized a temperature of 1150°C for annealing. Due to the high annealing temperature, a pure alumina tube insert was used, which has a melting point of 1750°C. The temperature is monitored and controlled using a DIGI-SENSE® Temperature Controller (Cole-Parmer Instrument Co., Illinois, USA). The substrates are mounted in ceramic discs and placed in the center of the alumina tube insert at room temperature. Oxidation control was implemented by flowing argon gas. To remove excess air from the oven chamber, argon gas is allowed to flow for 15 minutes prior to annealing. The oven is then allowed to reach the prescribed temperature. Ramp-up time to reach the required annealing temperature is approximately 90 minutes, after which the temperature is held constant for one hour. The specimens are cooled at a controlled rate to room temperature with a continued flow of argon gas.

The post-processing required for stent fabrication is a three-step procedure, combining center-less Grinding, electric discharge machining (EDM) and laser cutting with electro-polishing after the annealing remains same. Figure 5.6 depicts the stent fabricated from lot 3 coatings.

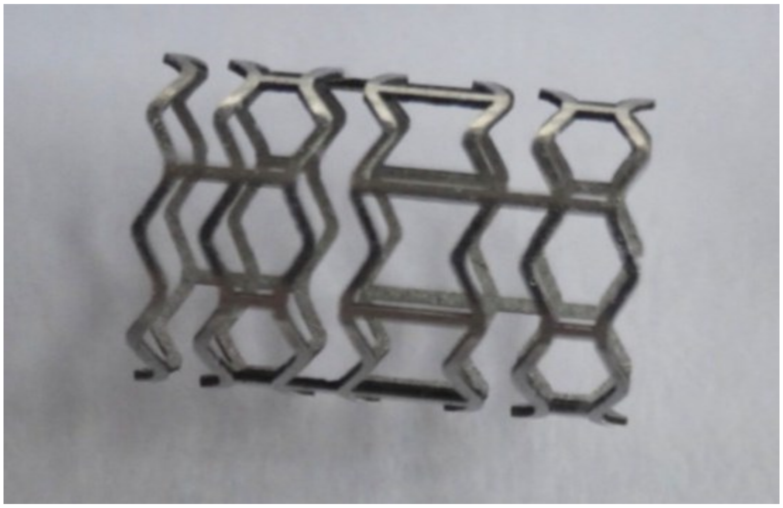

Figure 5.6: Laser cut stent after electro-polishing from 80wt%Fe mixed coating with a stent thickness of about 150 µm

Chapter 6. **Discussion**

In the present research, powder mixtures were cold-sprayed onto a substrate consisting of either a plate or a rod for the goal of fabricating biodegradable stents. Current industrial techniques use alloying to fabricate materials for permanent stents. Sintering and electroforming techniques are also currently been studied to fabricate materials for the degradable stents [30]. Alloying still can be considered superior for the industrial use for the fabrication of degradable stents for ductility but cold spraying is a potential alternative because of its small grain size. It has more parameters to be controlled as compared to electroforming and alloying, but this can be minimized by optimizing the process parameters for the specific set of powders [30].

Tensile test results indicated that the 20wt%Fe and 80wt%Fe lot 3 coatings resulted in tensile strengths of 584 and 629.1 MPa, respectively. Although the 80wt%Fe lot 3 coatings had about one third of the ductility (*i.e.,* 8%) in comparison with the 20wt%Fe lot 3 coatings, conversion of shear strength to tensile strength of lot 1 coatings indicated that the mixed coatings had a tensile strength of 596-604 MPa with an 80-90% reduction in area. This corresponds to a maximum of 15% less than the percent reduction in area obtained with 316L coatings. Based on the average corrosion rate of annealed 80wt%Fe specimens (~0.52 mg/cm^2/day), the corrosion rate of a stent with a total surface area of 0.45-1.00 cm^2 [108] would be approximately 0.23-0.52 mg/day. Hence, assuming a corrosion rate of 0.52 mg/day would imply that a stent with a mass of 150-300 mg would survive about 288-576 days. Similarly, assuming a corrosion rate of 0.23 mg/day, a stent with a mass of 150-300 mg would survive for 641-1282 days. In this chapter, the difficulties and challenges encountered during the present work as well as the limitations of the techniques used are presented. Based on the experience gained, the prospects for the fabrication of biodegradable stents are discussed.

6.1 Difficulties

The following difficulties were encountered during the present research:

1. Very high cooling rates during powder processing may generate martensite even at low carbon levels of CP Fe and 316L. It is very difficult to inhibit the formation of martensite. This transformation increases the microhardness of the powders and decreases the deposition efficiency of the coating process.
2. A reduction of austenite during the strain induced transformation from austenite to martensite is observed as a result of the cold spray process.
3. The tensile tests required to determine the ductility of the mixed materials are very costly.
4. Reducing the diameter of the rod used as a substrate during the cold spraying process decreases the deposition efficiency as a result of powder loss which in turn increases the cost of preparing a given sample.
5. CP Fe has an affinity to oxidize even at room temperature. The variation in the composition for powder lots kept in closed containers for long time periods suggests that CP Fe powder stock should always be stored under vacuum conditions.

6.2 Challenges

The following challenges were experienced during the present work:

1. The galvanic corrosion test of mixed coatings and 316L did not directly indicate the effect of microgalvanic corrosion between 316L and CP Fe particles inside the mixed coatings. The use of a scanning probe method was also used for determination of galvanic corrosion of the two different materials. However, the interparticle microgalvanic corrosion within a mixed coating was not determined by any corrosion measurement technique, but rather could only be implied from the general corrosion rate measuring techniques.
2. It is likely that the shape of the substrate (rod or plate) will influence the microstructural properties of the coating since different spray parameters are used

for plates and rods. The high microhardness of the CP Fe lot 3 powders and high motor speed for small diameter rods required a change in the spray parameters to ensure an adequate deposition efficiency. When spray coating onto rods, the microstructure of successive layers may also vary, and the radial variation in the microstructural properties of coatings on rods should be investigated in future work.

3. The coatings on rods had a diameter of about 5 mm, which was subsequently machined with an electrical discharge technique. Since coronary stents have a smaller diameter (typically 2 – 3 mm diameter) using the same technique to fabricate a stent at this scale will be challenging.
4. It is difficult to maintain the cylindrical symmetry of coatings on small diameter rods due to the impact of powders during the deposition process and the high rotational speed of the rods. These effects may cause the coating to have an eccentric shape.

6.3 Limitations

The limitations of the techniques used in the current research are given in the following:

1. The as-received iron powders contain high levels of impurities (Mn, Si, etc.) and low levels of elemental iron due to processing constraints. Armco® grade CP Fe particles are available and have a higher purity, but have a higher cost.
2. Good control over the composition, size, microstructure and morphology of the particles used should be maintained, since all of these factors will influence the deposition efficiency.
3. The CP Fe powders, which have a high microhardness, exhibit substantially lower deposition efficiencies than for 316L powders. However, when the particles are mixed, the subsequent deposition efficiency of the mixed coatings measured experimentally cannot be readily predicted theoretically.
4. The tensile strength and ductility of lot 1 coatings were estimated using the regression factors obtained from the lot 3 coatings, which introduces a degree of uncertainty in the results.

5. The pH of the in-vitro tests must be maintained at a value of 7.4-7.5 to mimic the physiological conditions of human blood plasma. Recent studies have used a method to maintain a constant range of pH (7.4-7.5) by adding gaseous CO_2 to the physiological solution. The addition of gaseous CO_2 forms bicarbonate ions which reduces the pH of the physiological solution sensed by a pH meter [98]. However, many groups have performed in-vitro tests with the pH ranging between 7.4-7.8 [109, 110].
6. Implanted stent covered with blood and cells in addition to dynamic body physiological condition due to blood flow reduces corrosion rate of pure [111] and electroformed iron [109] in vivo as compared to the corrosion rate in vitro. However, in-vivo tests for Fe-based degradable metals were not part of the thesis objectives.

6.4 Future work

Based on the present work, the following tests are recommended for future work:

1. Post-processing heat treatment should be performed on cold-sprayed rods for 1 hour at 1150°C to achieve a satisfactory ductility of the as-sprayed coating.
2. Dynamic degradation tests of the mixed coatings should be carried out to investigate the potential of the annealed composite to be used as a degradable stent.
3. The structure at the grain level of the mixed coatings was not characterized and tests should be carried out to obtain the grain size and orientation to determine the effect of the heat treatment on the coating microstructure.
4. Stent degradation tests should be performed using both static immersion and dynamic immersion protocols to compare the corrosion behavior of the plates and stents.
5. A degradation model should be developed for the mixed 316L/CP Fe coatings to assist in estimating the corrosion rate of the stent materials for various mixed conditions.

6. Following in-vitro degradation testing, pre-clinical trials should be initiated using animal models to assess the potential strength, ductility, corrosion rate and biocompatibility of the novel stents produced.
7. The effect of the mixed powder spraying ratio on the degradation properties should be determined to optimize the properties of the sprayed coatings for use as a degradable stent.
8. The 316L and CP Fe powders have different properties and the cold sprayability of the CP Fe powder has not yet been optimized. It may be possible to optimize the deposition of CP Fe powders and then prepare a mixed material by spraying a certain thickness with 316L and CP Fe independently using their optimum spray conditions. The spray technique may reduce the losses currently incurred with spraying mixed powders and also may avoid the loss of austenite which occurs during mixing.
9. Alternative techniques to fabricate stents should be investigated. For example, rather than coating directly onto a rod, a thin foil made by spraying onto a plane substrate could then be annealed and wrapped directly around a rod. If thicker coatings need to be prepared (~5 mm), EDM can be applied to fabricate a cylindrical shape but residual stresses [112] will likely be the main obstacle in preparing thick coatings.
10. CP Fe was selected as the most reactive powder based on the galvanic table considering toxicity, availability, and the mechanical properties of the metals. However, more reactive metals may be used as a long term plan for degradable stent fabrication.

Chapter 7. **Conclusions**

The initial hypothesis in this thesis was that it is possible to synthesize new metallic biodegradable stents using an intermixture of dissimilar metals by exploiting the galvanic effect. Furthermore, it was proposed that the degradation rate of the new materials may be controlled by controlling the relative proportions of the mixed powders.

In order to verify the feasibility of producing a biodegradable stent using the cold spray method, several important questions must first be answered. The first question to be addressed is whether or not it is possible to thoroughly mix the particular dissimilar powders chosen for the cold spray process. Although, in general, it is difficult to uniformly mix powders that have a wide variation in particle size and density, given the relatively similar properties of CP Fe and 316L, it was shown in Chapter 2 that a rolling mixer or a rotating tumbler are capable of thoroughly and uniformly mixing the powders. Image analysis after mixing by a rotating tumbler for one hour indicates that the particles are thoroughly mixed and the mixture retains the same mass percentages of the components as before mixing.

The next question to be addressed is whether or not the mixed powders will adhere to the substrate during the cold spray process to form a coherent layer. This question was addressed in Chapter 2 where it was shown that it is possible to cold-spray a mixture of 316L/CP Fe powders with a judicious choice of the spray parameters (gas temperature of 700°C, gas pressure of 4 MPa and a stand-off distance of 80 mm). In general, it was found that the ability to cold spray a particular powder mixture is influenced by the powder composition, size, microstructure and phase content. The higher hardness and body-centered crystal structure instead of higher velocity may be attributed to the lower deposition efficiency (DE) of the single component CP Fe as compared to the DE of 316L (33% vs 72%). Composite powders result in higher DE than the CP Fe powder, but the chemical composition of the mixed metals and strain-induced transformation from austenite to martensite cannot explain the difference between the experimental and expected DE values. A significant improvement in DE (66%) is attained with 80wt%Fe mixed metals, but this improvement is not reflected with the 20wt%Fe and 50wt%Fe powders where the higher amount of 316L possibly deposits better than the 80wt%Fe. However, the low deposition efficiency did not influence the porosity of the mixed metal layer formed (which was less than 1.3%). It may be attributed to the cubic crystallographic properties of the two powders due to the ease of plastic flow of these two cubic crystallographies. The increase in microhardness after impact is lower in CP Fe (1.2 vs. 1.72) than 316L possibly due to the transformation of austenite to martensite during mixing and cold spray. It was found that the martensitic transformation included a loss of austenite during mixing with a further loss due to strain-induced transformation during the cold spray process. It was found that the powder composition must be maintained in order to replicate the results. It was shown that 80wt%Fe lot 3 powders resulted in zero DE for the particular spray conditions, but a slight increase in spray intensity (i.e., gas temperature of 750°C, gas pressure of 4.9 MPa and a stand-off distance of 40 mm) resulted in a DE of 50% for the mixed powders. Such a deposition efficiency is only possible when the powders achieve impact velocities that are higher than the critical velocities at the specific spray conditions.

Once it was demonstrated the possibility of forming a coherent layer by cold spraying a powder mixture, the next question that arises is whether or not the layer will corrode with time, which is the essential requirement for a biodegradable stent. This question was addressed in Chapter 4 where it was demonstrated that a mixed-metal layer exhibited a controllable corrosion rate (0.25 mmpy) which was higher than commercially pure Armco® iron (0.10 mmpy). A typical increase in corrosion rate may be attributed to the relatively low as-sprayed porosity of the mixed metals and the controllability to the formation of iron oxide layers which reduces the corrosion rate of the mixed metals. It was found that a higher cathodic area induced a higher microgalvanic effect for 20wt%Fe than 80wt%Fe coatings. The lower corrosion rate of the constituent coatings (316L and CP Fe) and low porosity after heat treatment reduces the corrosion rate of the 20wt%Fe coatings to almost 50% as compared to the as-sprayed samples. The higher weight percentage of CP Fe in the 80wt%Fe coating induced a typical (0.23 mmpy) corrosion rate due to the higher dissolution of CP Fe in the electrolyte. The corrosion mechanism was found to be a combined effect of defective areas (cracks and pores) of the coating forming oxide layers and pitting due to chloride ions in the electrolyte. SS316L portion of the stent made of the mixed coating starts to disintegrate as well. It is observed on the degraded surface of the mixed coating that 316L starts to disintegrate.

The next question after the demonstration of the corrosion properties of the layer is whether or not the mechanical properties, and particularly the ductility, of the mixed-metal layer satisfy the requirements of the operation of a stent. This question was answered affirmatively in Chapter 3, and, in particular, the 20wt%Fe lot 3 coatings had a sufficient ductility (23% approximately) and tensile strength (580 MPa, approximately) to serve as a potential candidate material for the biodegradable stent application. The critical ductility obtained for the 80wt%Fe lot 1 coatings (8% approximately) was attributed to the high porosity and microhardness of the powders which required higher spray intensities to deposit the powders. Another requirement was to determine how to obtain the sample shear strength and percent regression in area if a sufficient amount of material was not available for a conventional tensile test. A regression factor was used to connect the shear and tensile strength obtained from the annealed coatings which exhibited a satisfactory tensile strength (597-605 MPa, approximately) and percent reduction in area which corresponds to the ductility of the single component coating. In addition, it was found that annealing reduced the number of pores, work hardening, and improved the shear strength due to the combined effects of recrystallization, sintering of unbounded particles or reduction of dislocations. Hence, it can be stated that mixed-metal layers possess satisfactory mechanical properties as required for the operation of a stent.

Now it can be stated that the fabricated material layers from spraying mixed metals have sufficient corrosion properties and ductility for stent operation. Hence, the final question is whether it is actually possible to fabricate a stent from the cold-sprayed layer. To answer this question, a protocol was described in Chapter 5 which demonstrated that it is possible to fabricate stents from the fabricated layers.

A prototype process has been developed to demonstrate the feasibility of fabricating a biodegradable stent, although to make stents on a commercial scale, the process must be adapted for mass production. In the process described in the present work, a stent can be fabricated from the coating in a three-step procedure, combining electrical discharge machining to prepare thin (150-200 micron) slices, rolling of the thin slices to generate the stent and laser cutting to thin them to desired thickness followed by electro-polishing to remove cutting residues. Successful completion of stent fabrication with this design could lead to mass production of the degradable stent from the plate coatings.

References

1 Lim, G.B.: ‘Public health: Global Burden of Cardiovascular Disease’, Nature Reviews Cardiology, February, 2013, 10, (2), pp. 59

2 Plank, B.G., Doling, M.J., and Knight, P.A.: ‘Coronary Artery Disease’, in Bisognano, J.D. (Ed.): ‘Manual of Outpatient Cardiology’ (Springer-Verlag London Limited, 2012), pp. 179-216

3 Dotter, C.T., and Judkins, M.P.: ‘Transluminal Treatment of Arteriosclerotic Obstruction: Description of a New Technic and a Preliminary Report of Its Application’, Circulation, 1964, 30, pp. 654-670

4 Dotter, C.T.: ‘Transluminally-placed Coilspring Endarterial Tube Grafts. Long-term Patency in Canine Popliteal Artery.’, Investigative Radiology, 1969;4:329-332, 4, pp. 329-332

5 Dotter, C.T., Buschmann, P.A.C., M. K. McKinney MK, R., and Rösch, J.: ‘Transluminal Expandable Nitinol coil stent grafting: preliminary report. ’, Radiology, 1983, 147(1), (1), pp. 259-260

6 Gruntzig, A.: ‘Transluminal Dilatation of Coronary-Artery Stenosis’, Lancet, 1978, 1, pp. 263

7 Guiteras-Val, P., Varas-Lorenzo, C., Garcia-Picart, J., Martí-Claramunt, V., and Augé-Sanpera, J.M.: ‘Clinical and Sequential Angiographic Follow-up Six Months and 10 Years After Successful Percutaneous Transluminal Coronary Angioplasty’, The American Journal of Cardiology, 1999, 83, (6), pp. 868-874

8 Palmaz, J.C., Sibbitt, R.R., Reuter, S.R., Tio, F.O., and Rice, W.J.: ‘Expandable Intraluminal Graft: a Preliminary Study’, Radiology, 1985, 156, pp. 73-77

9 Serruys, P.W., Strauss, B.H., Beatt, K.J., Bertrand, M.E., Puel, J., Rickards, A.F., Meier, B., Goy, J., Vogt, P., Kappenberger, L., and Sigwart, U.: ‘Angiographic Follow-up after Placement of a Self-Expanding Coronary-Artery Stent’, The New England Journal of Medicine, 1991, 324, (1), pp. 13-17

10 Schömig, A., Neumann, F., Kastrati, A., Schühlen, H., Blasini, R., Hadamitzky, M., Walter, H., Zitzmann-Roth, E., Richardt, G., Alt, E., Schmitt, C., and Ulm, K.: ‘A Randomized Comparison of Antiplatelet and Anticoagulant Therapy after the Placement of Coronary-Artery Stents’, The New England Journal of Medicine, 1996, 334, pp. 1084-1089

11 Moliterno, D.J.: ‘Healing Achilles — Sirolimus versus Paclitaxel’, The American Journal of Medicine, 2005, 353, pp. 724-727

12 Garg, S., and Serruys, P.W.: ‘Coronary Stents: Current Status’, Journal of the American College of Cardiology, 2010, 56, (10), pp. S1-S42

13 Hamilos, M.I., Papafaklis, M.I., Ligthart, J.M., Serruys, P.W., and Sianos, G.: ‘Stent Fracture and Restenosis of a Paclitaxel-Eluting Stent’, Hellenic Journal of Cardiology, 2005, 46, pp. 439-442

14 Cosgrave, J., and Dangas, G.D.: ‘Drug-Eluting Stent Restenosis’, in Colombo, A., and Stankovic, G. (Eds.): ‘Problem Oriented Approaches in Interventional Cardiology’ (Informa Healthcare, 2007), pp. 151-162

15 Stahli, B.E., Camici, G.G., and Tanner, F.C.: ‘Drug-Eluting Stent Thrombosis’, Therapeutic Advances in Cardiovascular Disease, 2009, 3, (1), pp. 45-52

16 Camenzind, E., Steg, P., and Wijns, W.: ‘Stent Thrombosis Late After Implantation of First Genaration Drug Eluting Stents’, Circulation, Mar 20, 2007, 115, (11), pp. 1440-1455
17 Lim, H.B., Hur, G., Kim, S.Y., Kim, Y.H., Kwon, S.U., W.R.Lee, and Cha, S.J.: ‘Coronary Stent Fracture: Detection with 64-section Multidetector CT Angiography in Patients and in Vitro’, Radiology, 2008, 249, (3), pp. 810-819
18 Nakazawa, G., Finn, A.V., Vorpahl, M., Ladich, E., Kutys, R., Balazs, I., Kolodgie, F.D., and Virmani, R.: ‘Incidence and Predictors of Drug-Eluting Stent Fracture in Human Coronary Artery A Pathologic Analysis’, Journal of the American College of Cardiology, 2009, 54, (21), pp. 1924-1931
19 Kang, W.C., C. Moon II, Ahn, T.H., and Shin, E.K.: ‘Multiple Stent Strut Fracture-Induced Restenosis in a Diffuse Long Lesion Treated with Overlapping Heterogeneous Drug-Eluting Stent’, International Journal of Cardiology, 2008, 130, pp. e30-e33
20 Chakravarty, T., White, A.J., Buch, M., Naik, H., Doctor, N., Schapira, J., Kar, S., Forrester, J.S., Weiss, R.E., and Makkar, R.: ‘Meta-Analysis of Incidence, Clinical Characteristics and Implications of Stent Fracture’, The American Journal of Cardiology, 2010, 106, (8), pp. 1075-1080
21 Nair, R.N.: ‘Coronary Stent Fracture :A Review of the Literature’, Cardiac Catheterization Laboratory Director, 2011, 1, (1), pp. 32-38
22 Levi, D.S., and Chang, A.L.: ‘Biodegradable Implants’, in da Cruz, E., Ivy, D., and Jaggers, J. (Eds.): ‘Pediatric and Congenital Cardiology, Cardiac Surgery and Intensive Care’ (Springer-Verlag London Limited, 2014), pp. 1219-1235
23 Ramcharitar, S., and Serruys, P.W.: ‘Fully Biodegradable Coronary Stents Progress to Date’, American Journal of Cardiovascular Drugs, 2008, 8, (5), pp. 305-314
24 Waksman, R.: ‘Biodegradable Stents: They Do Their Job and Disappear’, The Journal of Invasive Cardiology, 2006, 18, (2), pp. 70-74
25 Stack, R.S., Califf, R.M., Phillips, H.R., Pryor, D.B., Quigley, P.J., Bauman, R.P., Tcheng, J.E., and Greenfield, J.C.: ‘Interventional Cardiac Catheterization at Duke Medical Center’, The American Journal of Cardiology, 1988, 62, pp. 3F-24F
26 Tamai, H., Igaki, K., Kyo, E., Kosuga, K., Kawashima, A., Matsui, S., Komori, H., Tsuji, T., Motohara, S., and Uehata, H.: ‘Initial and 6-Month Results of Biodegradable Poly-l-Lactic Acid Coronary Stents in Humans’, Circulation, 2000, 102, pp. 399-404
27 Tamai, H.: ‘Biodegradable stents four year follow-up’, Presentation at TCT, 2004
28 Tanimoto, S., Bruining, N., van Domburg, R.T., Rotger, D., Radeva, P., Ligthart, J.M., and Serruys, P.W.: ‘Late Stent Recoil of the Bioabsorbable Everolimus-Eluting Coronary Stent and its Relationship With Plaque Morphology’, Journal of the American College of Cardiology, 2008, 52, (20), pp. 1616-1620
29 ASTM-F138-2013a: ‘Standard Specification for Wrought 18Chromium-14Nickel-2.5Molybdenum Stainless Steel Bar and Wire for Surgical Implants (UNS S31673)’ (ASTM International, West Conshohocken, PA)
30 Moravej, M., and Mantovani, D.: ‘Biodegradable Metals for Cardiovascular Stent Application: Interests and New Opportunities’, International Journal of Molecular Sciences, 2011, 12, (7), pp. 4250-4270

31 Hermawan, H.: ‘Design, Development and Validation of Degradable Metal Alloys used in Endovascular Surgery’, Université Laval, 2009

32 Emsley, J.: ‘The Elements’ (Oxford: Clarendon Press; 1998)

33 Moravej, M.: ‘Development and Validation of Metal Materials for Biodegradable Cardiovascular Stents by Electrolytic Deposition’, Université Laval, 2011

34 Heublein, B., Rohde, R., Kaese, V., Niemeyer, M., Hartung, W., and Haverich, A.: ‘Biocorrosion of Magnesium Alloys: A New Principle in Cardiovascular Implant Technology?’, Heart, 2003, 89, (6), pp. 651-656

35 Di Mario, C., Griffiths, H., Goktekin, O., Peeters, N., Verbist, J., Bosiers, M., Deloose, K., Heublein, B., Rohde, R., Kasese, V., Ilsley, C., and Erbel, R.: ‘Drug-Eluting Bioabsorbable Magnesium Stent ’, Journal of interventional cardiology, 2004, 17, (6), pp. 391-395

36 Erne, P., Schier, M., and Resink, T.J.: ‘The Road to Bioabsorbable Stents: Reaching Clinical Reality?’, Cardiovascular and Interventional Radiology, 2005, 29, pp. 11-16

37 Di Mario, C., Griffiths, H., Goktekin, O., Peeters, N., Verbist, J., Bosiers, M., Deloose, K., Heublein, B., Rohde, R., Kasese, V., Ilsley, C., and Erbel, R.: ‘Drug-Eluting Bioabsorbable Magnesium Stent’, Journal of Interventional Cardiology, 2004, 17, (6), pp. 391-395

38 Bosiers, M., and Investigators, A.M.S.I.: ‘AMS INSIGHT-Absorbable Metal Stent Implantation for Treatment of Below-the-Knee Critical Limb Ischemia: 6-Month Analysis’, Cardiovascular and Interventional Radiology, 2009, 32, (3), pp. 424-435

39 Peuster, M., Hesse, C., Schloo, T., Fink, C., Beerbaum, P., and von Schnakenburg, C.: ‘Long-term Biocompatibility of a Corrodible Peripheral Iron Stent in the Porcine Descending Aorta’, Biomaterials, 2006, 27, (28), pp. 4955-4962

40 Waksman, R., Pakala, R., Baffour, R., Seabron, R., Hellinga, D., and Tio, F.O.: ‘Short-term Effects of Biocorrodible Iron Stents in Porcine Coronary Arteries’, Journal of interventional cardiology, 2008, 21, (1), pp. 15-20

41 Peuster, M., Beerbaum, P., Bach, F.-W., and Hauser, H.: ‘Are Resorbable Implants about to become a Reality?’, Cardiology in the Young, 2006, 16, pp. 107-116

42 Pierson, D., Edick, J., Tauscher, A., Pokorney, E., Bowen, P., Gelbaugh, J., Stinson, J., Getty, H., Lee, C.H., Drelich, J., and Goldman, J.: ‘A Simplified in vivo Approach for Evaluating the Bioabsorbable Behavior of Candidate Stent Materials’, Journal of Biomedical Materials Research Part B-Applied Biomaterials, 2012, 100B, (1), pp. 58-67

43 Wu, C., Qiu, H., Xu, L., Ye, J., Yang, Z., Qian, X., Meng, X., Cui, Y., Song, L., and Gao, R.: ‘Inhibitory Effect of Iron on in vitro Proliferation of Smooth Muscle Cells’, Chinese Medical Journal, 2013, 126, (19), pp. 3728-3731

44 Wu, C., Qiu, H., Hu, X., Ruan, Y., Tian, Y., Chu, Y., Xu, X., Xu, L., Tang, Y., and Gao, R.: ‘Short-term Safety and Efficacy of the Biodegradable Iron Stent in Mini-Swine Coronary Arteries’, Chinese Medical Journal, 2013, 126, (24), pp. 4752-4757

45 Schinhammer, M., Haenzi, A.C., Loeffler, J.F., and Uggowitzer, P.J.: ‘Design Strategy for Biodegradable Fe-based Alloys for Medical Applications’, Acta Biomaterialia, 2010, 6, (5), pp. 1705-1713

46 Papyrin, A., Kosarev, V., Klinkov, S., Alkimov, A., and Fomin, V.: ‘Cold Spray Technology’ (Amsterdam ; London : Elsevier, 2007)

47 Dykhuizen, R.C., and Smith, M.F.: 'Gas Dynamic Principles of Cold Spray', Journal of Thermal Spray Technology, 1998, 7, (2), pp. 205-212
48 Karen, L., Taylor, J.K., Brochu, M., and Jodoin, B.: 'Cold Spray Application of Metallic/Bio-Ceramic Composite Powders', in Marple, B., Hyland, M., Lau, Y.-C., Li, C.J., Lima, R.S., and Montavon, G. (Eds.): 'Thermal Spray 2007: Global Coating Solutions' (ASM International, Materials Park, 2007)
49 Ajdelsztajn, L., Schoenung, J.M., Jodoin, B., and Kim, G.E.: 'Cold Spray Deposition of Nanocrystalline Aluminum Alloys', Metallurgical and Materials Transactions A, 2005, 36, (3), pp. 657-666
50 Jeong, D.H., Gonzalez, F., Palumbo, G., Aust, K.T., and Erb, U.: 'The Effect of Grain Size on the Wear Properties of Electrodeposited Nanocrystalline Nickel Coatings', Scripta materialia, 2001, 44, pp. 493-499
51 Champagne, V.K.: 'The Cold Spray Materials Deposition Process: Fundamentals and Applications' (Cambridge : Woodhead ; Boca Raton : CRC Press, 2007)
52 Dahotre, N.B., and Harimkar, S.P.: 'Laser Fabrication and Machining of Materials' (New York, N.Y. : Springer Science Business Media, ©2008)
53 Schmidt, T., Gartner, F., Assadi, H., and Kreye, H.: 'Development of a Generalized Parameter Window for Cold Spray Deposition', Acta Materialia, 2006, 54, (3), pp. 729-742
54 Hussain, T., McCartney, D.G., Shipway, P.H., and Zhang, D.: 'Bonding Mechanisms in Cold Spraying: The Contributions of Metallurgical and Mechanical Components', Journal of Thermal Spray Technology, 2009, 18, (3), pp. 364-379
55 Hussain, T., Yue, S., and Li, C.: 'Characteristics of Feedstock Materials in Modern Cold Spray: Materials, Process, and Applications', in Villafuerte, J. (Ed.): 'Modern Cold Spray: Materials, Process, and Applications ' (Springer, NY, 2015 (In Press))
56 Wong, W., Rezaeian, A., Irissou, E., Legoux, J.G., and Yue, S.: 'Cold Spray Characteristics of Commercially Pure Ti and Ti-6Al-4V', Thermec 2009 Supplement: 6th International Conference on Processing & Manufacturing of Advanced Materials, 2010, 89-91, pp. 639-644
57 Assadi, H., Gartner, F., Stoltenhoff, T., and Kreye, H.: 'Bonding Mechanism in Cold Gas Spraying', Acta Materialia, 2003, 51, (15), pp. 4379-4394
58 Gartner, F., Stoltenhoff, T., Schmidt, T., and Kreye, H.: 'The Cold Spray Process and its Potential for Industrial Applications', Journal of Thermal Spray Technology, 2006, 15, (2), pp. 223-232
59 http://www.hsu-hh.de/download-1.4.1.php?brick_id=gVtoSCPVB2riK4xO, accessed December,14, 2014
60 Poncin, P., and Proft, J.: 'Stent Tubing: Understanding the Desired Attributes', in Shrivastava, S. (Ed.): 'Medical Device Materials: Proceedings of the Materials and Processes for Medical Devices Conference' (ASM International, 2003), pp. 253-259
61 Al-Mangour, B., Vo, P., Mongrain, R., Irissou, E., and Yue, S.: 'Effect of Heat Treatment on the Microstructure and Mechanical Properties of Stainless Steel 316L Coatings Produced by Cold Spray for Biomedical Applications', Journal of Thermal Spray Technology, 2013, 23, (4), pp. 641-652
62 Vo, P., Irissou, E., Kudapa, S., and Nestler, M.: 'Strength and Wear Properties of Stainless Steel Coatings Produced by Cold Spray with Various Powder Sizes', in Lima,

R.S., Agarwal, A., Hyland, M.M., Lau, Y.C., Mauer, G., McDonald, A., and Toma, F.L. (Eds.): 'Proceedings of the International Thermal Spray Conference' (ASM International, 2013)

63 Villa, M., Dosta, S., and Guilemany, J.M.: 'Optimization of 316L Stainless Steel Coatings on Light Alloys using Cold Gas Spray', Surface and Coatings Technology, 2013, 235, pp. 220-225

64 Verstraeten, S.V., Aimo, L., and Oteiza, P.I.: 'Aluminium and Lead: Molecular Mechanisms of Brain Toxicity', Archives of Toxicology, 2008, 82, (11), pp. 789-802

65 ASTM-G82-98-2009: 'Development and Use of a Galvanic Series for Predicting Galvanic Corrosion Performance' (ASTM International, West Conshohocken, PA)

66 Yue, S., Wong, W., Aydin, H., Mongrain, R., Barua, R., Vo, P., and Dolbec, R.: 'Improving Cold Sprayability: Mixed Metal Powders' (ASM International, 2015)

67 Cinca, N., Lima, C.R.C., and Guilemany, J.M.: 'An Overview of Intermetallics Research and Application: Status of Thermal Spray Coatings', Journal of Materials Research and Technology, 2013, 2, (1), pp. 75-86

68 Al-Mangour, B., Mongrain, R., Irissou, E., and Yue, S.: 'Improving the Strength and Corrosion Resistance of 316L Stainless Steel for Biomedical Applications using Cold Spray', Surface & Coatings Technology, 2013, 216, pp. 297-307

69 Alissa, E.M., and Ferns, G.A.: 'Heavy Metal Poisoning and Cardiovascular Disease', Journal of Toxicology, 2011, pp. 1-21

70 http://www.atsdr.cdc.gov/toxguides/toxguide-4.pdf, accessed October 13, 2014

71 http://www.matweb.com/search/DataSheet.aspx?MatGUID=ff6d4e6d529e4b3d97c77d6538b29693, accessed October 12, 2014

72 http://www.matweb.com/search/DataSheet.aspx?MatGUID=8909140a76074049809ad74d536ed606, accessed October 11, 2014

73 http://www.clufix.com/gb/images2/plaquette_revetements_en.pdf#page=7, accessed October 14, 2014

74 Hou, X., and Jones, B.T.: 'Inductively Coupled Plasma/Optical Emission Spectrometry', in Meyers, R.A. (Ed.): 'Encyclopedia of Analytical Chemistry' (John Wiley & Sons Ltd, Chichester, 2000), pp. 9468-9485

75 ASTM-E1019-2011: 'Standard Test Methods for Determination of Carbon, Sulphur, Nitrogen and Oxygen in Steel, Iron, Nickel and Cobalt Alloys by Various Combustion and Fusion Techniques' (ASTM International, West Conshohocken, PA)

76 Peymandar, M., Schmuck, S., Schweinichen, P., and Senk, D.: 'Interfacial Reactions between Slag and Melt in the New World of High Manganese Steels', in Yurko, J., Zhang, L., Allanore, A., Wang, C., Spangenberger, J.S., Kirchain, R.E., Downey, J.P., and May, L.D. (Eds.): 'EPD Congress 2014' (Wiley Online Library, 2013)

77 Tisza, M.: 'Physical Metallurgy for Engineers' (ASM International and Freund Publishing House Limited, 2001)

78 http://www.matweb.com/search/DataSheet.aspx?MatGUID=654ca9c358264b5392d43315d8535b7d, accessed Octoer 24, 2014

79 http://www.matweb.com/search/datasheet.aspx?MatGUID=a2d0107bf958442e9f8db6dc9933fe31, accessed October 23, 2014

80 Menendez, E., Sort, J., Liedke, M.O., Fassbender, J., Surinach, S., Baro, M.D., and Nogues, J.: 'Controlled Generation of Ferromagnetic Martensite from Paramagnetic Austenite in AISI 316L Austenitic Stainless Steel', Journal of Materials Research, 2009, 24, (2), pp. 565-573

81 McGuire, M.F.: 'Stainless Steels for Design Engineers' (Materials Park, Ohio : ASM International, 2008)

82 Dan, W.J., Li, S.H., Zhang, W.G., and Lin, Z.Q.: 'The Effect of Strain-induced Martensitic Transformation on Mechanical Properties of TRIP Steel', Materials & Design, 2008, 29, (3), pp. 604-612

83 Yue, S., Wong, W., Aydin, H., Mongrain, R., Barua, R., Vo, P., and Dolbec, R.: 'Improving Cold Sprayability: Mixed Metal Powders'. Proc. International Thermal Spray Conference and Exposition, Long Beach, CA, USA, May 11-14, 2015 2015 pp. Pages

84 Ungár, T.: 'The Meaning of Size Obtained from Broadend XRD Diffraction Peaks', Advanced Engineering Materials, 2003, 5, (5), pp. 323-329

85 Lucas, G.E., Odette, G.R., and Sheckherd, J.W.: 'Shear Punch and Microhardness Tests for Strength and Ductility Measurements', in Corwin, W., and Lucas, G.E. (Eds.): 'The Use of Small-Scale Specimens for Testing Irradiated Material' (ASTM International, 1986)

86 Lucas, G.E., Odette, G.R., and Sheckherd, J.W.: 'Shear Punch and Microhardness Tests for Strength and Ductility Measurements', ASTM International, 1986 pp. Pages

87 Aydin, H.: 'Effect of Microstructure on Static and Dynamic Mechanical Properties of Third Generation Advanced High Strength Steels', McGill University, 2013

88 Hamilton, M.L., Toloczko, M.B., and Lucas, G.E.: 'Recent Progresses in Shear Punch Testing', in Ullmaier, H., and Jung, P. (Eds.): 'Miniaturized Specimens for Testing Irradiated Materials' (ASM International, 1995), pp. 46-58

89 Zhen, Z., Xi, T.F., and Zheng, Y.F.: 'A Review on in vitro Corrosion Performance Test of Biodegradable Metallic Materials', Trans. Nonferrous Met. Soc. China, 2013, 23, (8), pp. 2283-2293

90 Fontana, M.G.: 'Corrosion Engineering' (Tata McGraw-Hill, 2005)

91 Schinhammer, M.: 'Development and Characterization of Biodegradable Fe-based Alloys for Temporary Medical Applications', ETH Zurich, 2012

92 ASTM-G31-72-2011: 'Standard Practice for Laboratory Immersion Corrosion Testing of Metals' (ASTM International, West Conshohocken, PA)

93 ASTM-G59-97-2009: 'Standard Test Method for Conducting Potentiodynamic Polarization Resistance Measurements' (ASTM International, West Conshohocken, PA)

94 ASTM-G71-81-2009: 'Standard Guide for Conducting and Evaluating Galvanic Corrosion Tests in Electrolytes' (ASTM International, West Conshohocken, PA)

95 Baboian, R.: 'Corrosion Tests and Standards: Application and Interpretation' (ASTM International, 2005)

96 Deshpande, K.B.: 'Validated Numerical Modelling of Galvanic Corrosion for Couples: Magnesium Alloy (AE44)-Mild Steel and AE44-Aluminium Alloy (AA6063) in Brine Solution', Corrosion Science, 2010, 52, (10), pp. 3514-3522

97 Bauer, A.: 'Stainless Steel in Waters: Galvanic Corrosion and its Prevention' (Nickel Institute http://www.nickelinstitute.org)

98 Schinhammer, M., Hofstetter, J., Wegmann, C., Moszner, F., Loeffler, J.F., and Uggowitzer, P.J.: 'On the Immersion Testing of Degradable Implant Materials in Simulated Body Fluid: Active pH Regulation Using CO2', Advanced Engineering Materials, 2013, 15, (6), pp. 434-441

99 Talha, M., Behera, C.K., Kumar, S., Pal, O., Singh, G., and Sinha, O.P.: 'Long Term and Electrochemical Corrosion Investigation of Cold Worked AISI 316L and 316LVM Stainless Steels in Simulated Body Fluid', RSC Advances, 2014, 4, (26), pp. 13340-13349

100 Bardal, E.: 'Corrosion and Protection' (Springer-Verlag London Limited, 2003)

101 Tang, Y.-C., Katsuma, S., Fujimoto, S., and Hiromoto, S.: 'Electrochemical Study of Type 304 and 316L Stainless Steels in Simulated Body Fluids and Cell Cultures', Acta Biomaterialia, 2006, 2, (6), pp. 709-715

102 Jiménez, Y.S., Gil, M.T., Guerra, M.T., Baltes, L.S., and Rosca, J.C.M.: 'Interpretation of Open Circuit Potential of Two Titanium Alloys for a Long Time Immersion in Physiological Fluid', Bulletin of the Transilvania University of Braşov, 2009, 2, (51), pp. 197-204

103 Karimi, S., Nickchi, T., and Alfantazi, A.M.: 'Long-term Corrosion Investigation of AISI 316L, Co-28Cr-6Mo, and Ti-6Al-4V Alloys in Simulated Body Solutions', Applied Surface Science, 2012, 258, (16), pp. 6087-6096

104 http://info.raydiance.com/blog/topic/femtosecond-laser-stent-cutting, accessed June 7th, 2015

105 Soucy, N.V., Feygin, J.M., Tunstall, R., Casey, M.A., Pennington, D.E., Huibregtse, B.A., and Barry, J.J.: 'Strut Tissue Coverage and Endothelial Cell Coverage: a Comparison between Bare Metal Stent Platforms and Platinum Chromium Stents with and without Everolimus-eluting Coating', EuroIntervention, 2010, 6, (5), pp. 630-637

106 Sojitra, P., Engineer, C., Kothwala, D., Raval, A., Kotadia, H., and Mehta, G.: 'Electropolishing of 316LVM Stainless Steel Cardiovascular Stents: An Investigation of Material Removal, Surface Roughness and Corrosion Behaviour', Trends Biomater. Artif. Organs, 2010, 23, (3), pp. 115-121

107 Hanke, L., and Bayha, E.: 'Surface Characterization for Optimizing Electropolishing for Medical Devices': 'Medical Device Materials: Proceedings of the Materials & Processes for Medical Devices Conference 2003 (ASM International)', pp. 81-86

108 Bornapour, M., Muja, N., Shum-Tim, P., Cerruti, M., and Pekguleryuz, M.: 'Biocompatibility and Biodegradability of Mg-Sr Alloys: The Formation of Sr-substituted Hydroxyapatite', Acta Biomaterialia, 2013, 9, (2), pp. 5319-5330

109 Moravej, M., Purnama, A., Fiset, M., Couet, J., and Mantovani, D.: 'Electroformed Pure Iron as a New Biomaterial for Degradable Stents: In vitro Degradation and Preliminary Cell Viability Studies', Acta Biomaterialia, 2010, 6, (5), pp. 1843-1851

110 Hermawan, H., Purnama, A., Dube, D., Couet, J., and Mantovani, D.: 'Fe-Mn Alloys for Metallic Biodegradable Stents: Degradation and Cell Viability Studies', Acta Biomaterialia, 2010, 6, (5), pp. 1852-1860

111 Moravej, M., Amira, S., Prima, F., Rahem, A., Fiset, M., and Mantovani, D.: 'Effect of Electrodeposition Current Density on the Microstructure and the Degradation of Electroformed Iron for Degradable Stents', Materials Science and Engineering B, 2011, 176, pp. 1812-1822

112 Suhonen, T., Varis, T., Dosta, S., Torrell, M., and Guilemany, J.M.: 'Residual Stress Development in Cold Sprayed Al, Cu and Ti Coatings', Acta Materialia, 2013, 61, (17), pp. 6329-6337

113 http://www.corrosion-doctors.org/Principles/Conversion.htm, accessed September 28, 2014

Appendix A

Corrosion rate conversion [113]:

	mA.cm^{-2}	mmpy	mpy	mg.cm^{-2}.day^{-1}
mA.cm^{-2}	1	$3.28\frac{m_a}{n\rho}$	$3.28\frac{m_a}{n\rho}$	$0.895\frac{m_a}{n}$
mmpy	$0.306\frac{n\rho}{m_a}$	1	39.4	0.274ρ
mpy	$0.00777\frac{n\rho}{m_a}$	0.0254	1	0.00694ρ
mg.cm^{-2}.day^{-1}	$1.12\frac{n}{m_a}$	$\frac{3.65}{\rho}$	$\frac{144}{\rho}$	1

Appendix B

Manufacturer’s specification sheet of 316L and CP Fe powders of lot 1 (2012):

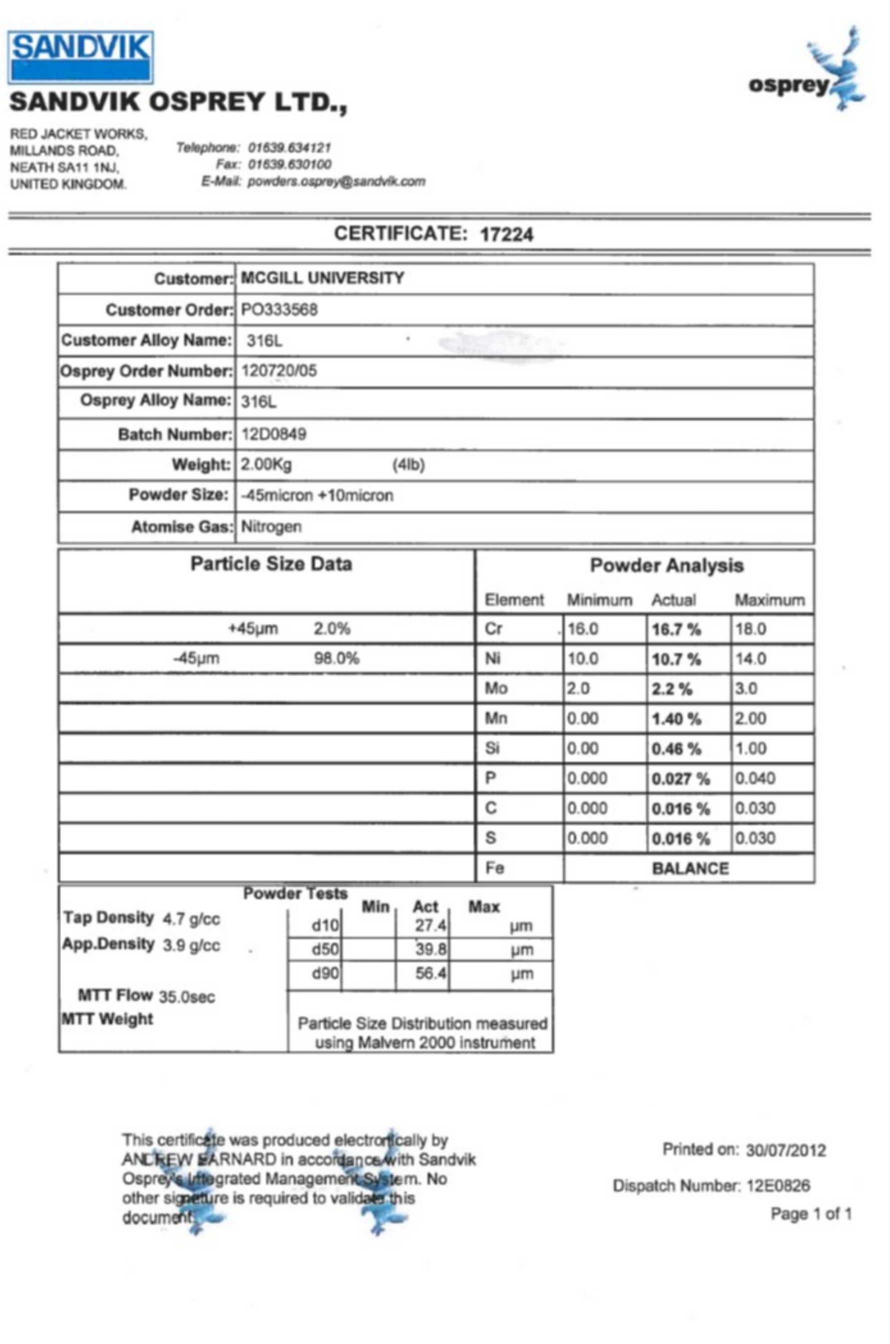

SANDVIK

SANDVIK OSPREY LTD.,

RED JACKET WORKS,
MILLANDS ROAD,
NEATH SA11 1NJ,
UNITED KINGDOM.

Telephone: 01639.634121
Fax: 01639.630100
E-Mail: powders.osprey@sandvik.com

osprey

CERTIFICATE: 17224

Customer:	**MCGILL UNIVERSITY**
Customer Order:	PO333568
Customer Alloy Name:	316L
Osprey Order Number:	120720/05
Osprey Alloy Name:	316L
Batch Number:	12D0849
Weight:	2.00Kg (4lb)
Powder Size:	-45micron +10micron
Atomise Gas:	Nitrogen

Particle Size Data		**Powder Analysis**			
		Element	Minimum	Actual	Maximum
+45µm	2.0%	Cr	16.0	**16.7 %**	18.0
-45µm	98.0%	Ni	10.0	**10.7 %**	14.0
		Mo	2.0	**2.2 %**	3.0
		Mn	0.00	**1.40 %**	2.00
		Si	0.00	**0.46 %**	1.00
		P	0.000	**0.027 %**	0.040
		C	0.000	**0.016 %**	0.030
		S	0.000	**0.016 %**	0.030
		Fe	**BALANCE**		

Powder Tests

Tap Density 4.7 g/cc
App.Density 3.9 g/cc
MTT Flow 35.0sec
MTT Weight

	Min	**Act**	**Max**
d10		27.4	µm
d50		39.8	µm
d90		56.4	µm

Particle Size Distribution measured using Malvern 2000 instrument

This certificate was produced electronically by ANDREW BARNARD in accordance with Sandvik Osprey's Integrated Management System. No other signature is required to validate this document.

Printed on: 30/07/2012
Dispatch Number: 12E0826
Page 1 of 1

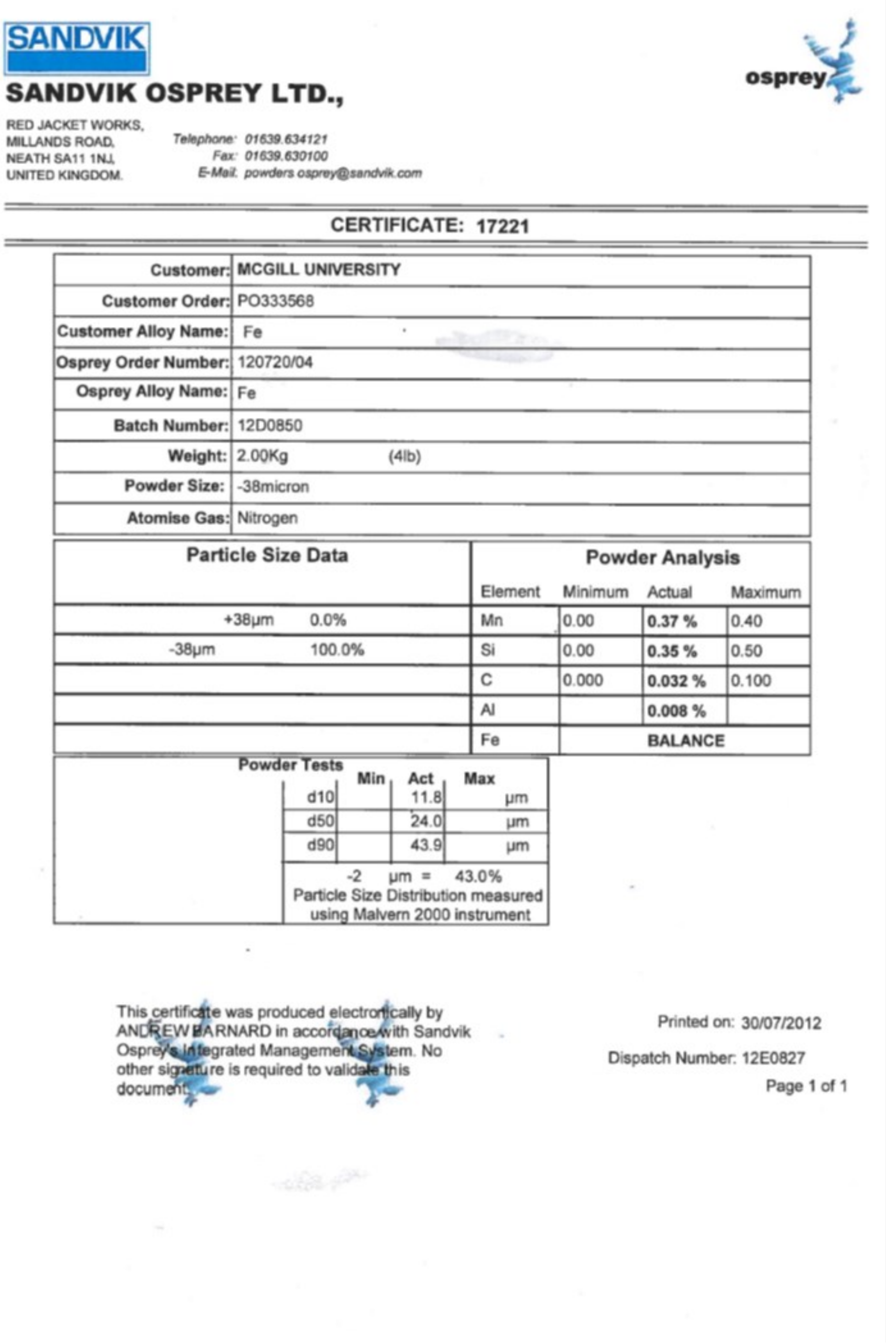

SANDVIK

SANDVIK OSPREY LTD.,

osprey

RED JACKET WORKS,
MILLANDS ROAD,
NEATH SA11 1NJ,
UNITED KINGDOM.

Telephone: 01639.634121
Fax: 01639.630100
E-Mail: powders.osprey@sandvik.com

CERTIFICATE: 17221

Customer:	**MCGILL UNIVERSITY**
Customer Order:	PO333568
Customer Alloy Name:	Fe
Osprey Order Number:	120720/04
Osprey Alloy Name:	Fe
Batch Number:	12D0850
Weight:	2.00Kg (4lb)
Powder Size:	-38micron
Atomise Gas:	Nitrogen

Particle Size Data

+38µm	0.0%
-38µm	100.0%

Powder Analysis

Element	Minimum	Actual	Maximum
Mn	0.00	**0.37 %**	0.40
Si	0.00	**0.35 %**	0.50
C	0.000	**0.032 %**	0.100
Al		**0.008 %**	
Fe		**BALANCE**	

Powder Tests

	Min	Act	Max	
d10		11.8		µm
d50		24.0		µm
d90		43.9		µm

-2 µm = 43.0%
Particle Size Distribution measured using Malvern 2000 instrument

This certificate was produced electronically by ANDREW BARNARD in accordance with Sandvik Osprey's Integrated Management System. No other signature is required to validate this document.

Printed on: 30/07/2012

Dispatch Number: 12E0827

Page 1 of 1

Appendix C

Manufacturer’s specification sheet of 316L and CP Fe powders of lot 2 (2013):

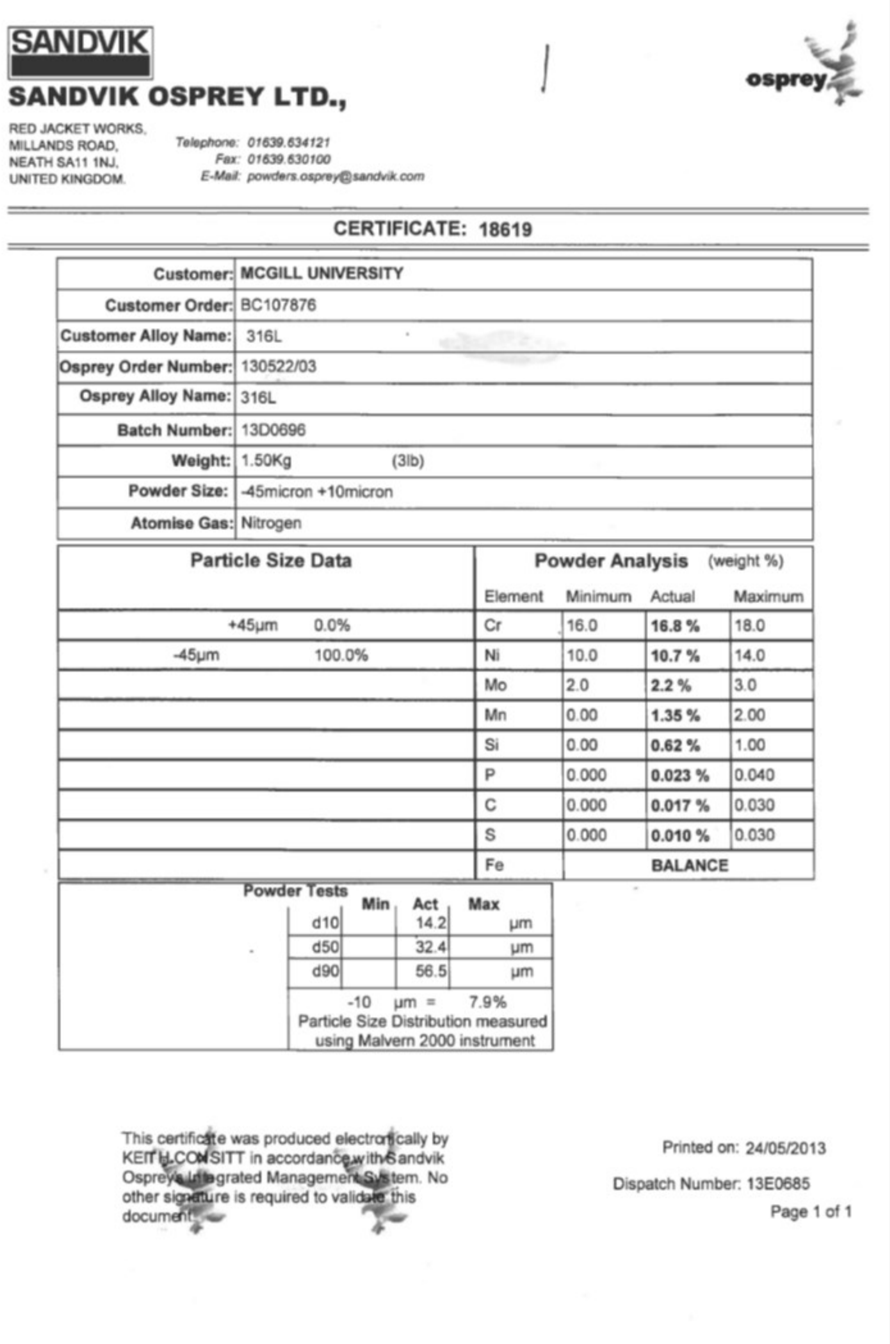

SANDVIK

SANDVIK OSPREY LTD.,

RED JACKET WORKS,
MILLANDS ROAD,
NEATH SA11 1NJ,
UNITED KINGDOM.

Telephone: 01639.634121
Fax: 01639.630100
E-Mail: powders.osprey@sandvik.com

osprey

CERTIFICATE: 18619

Customer:	**MCGILL UNIVERSITY**
Customer Order:	BC107876
Customer Alloy Name:	316L
Osprey Order Number:	130522/03
Osprey Alloy Name:	316L
Batch Number:	13D0696
Weight:	1.50Kg (3lb)
Powder Size:	-45micron +10micron
Atomise Gas:	Nitrogen

Particle Size Data

+45µm	0.0%
-45µm	100.0%

Powder Analysis (weight %)

Element	Minimum	Actual	Maximum
Cr	16.0	**16.8 %**	18.0
Ni	10.0	**10.7 %**	14.0
Mo	2.0	**2.2 %**	3.0
Mn	0.00	**1.35 %**	2.00
Si	0.00	**0.62 %**	1.00
P	0.000	**0.023 %**	0.040
C	0.000	**0.017 %**	0.030
S	0.000	**0.010 %**	0.030
Fe		**BALANCE**	

Powder Tests

	Min	Act	Max
d10		14.2	µm
d50		32.4	µm
d90		56.5	µm

-10 µm = 7.9%
Particle Size Distribution measured using Malvern 2000 instrument

This certificate was produced electronically by KEITH.CONSITT in accordance with Sandvik Osprey's Integrated Management System. No other signature is required to validate this document.

Printed on: 24/05/2013

Dispatch Number: 13E0685

Page 1 of 1

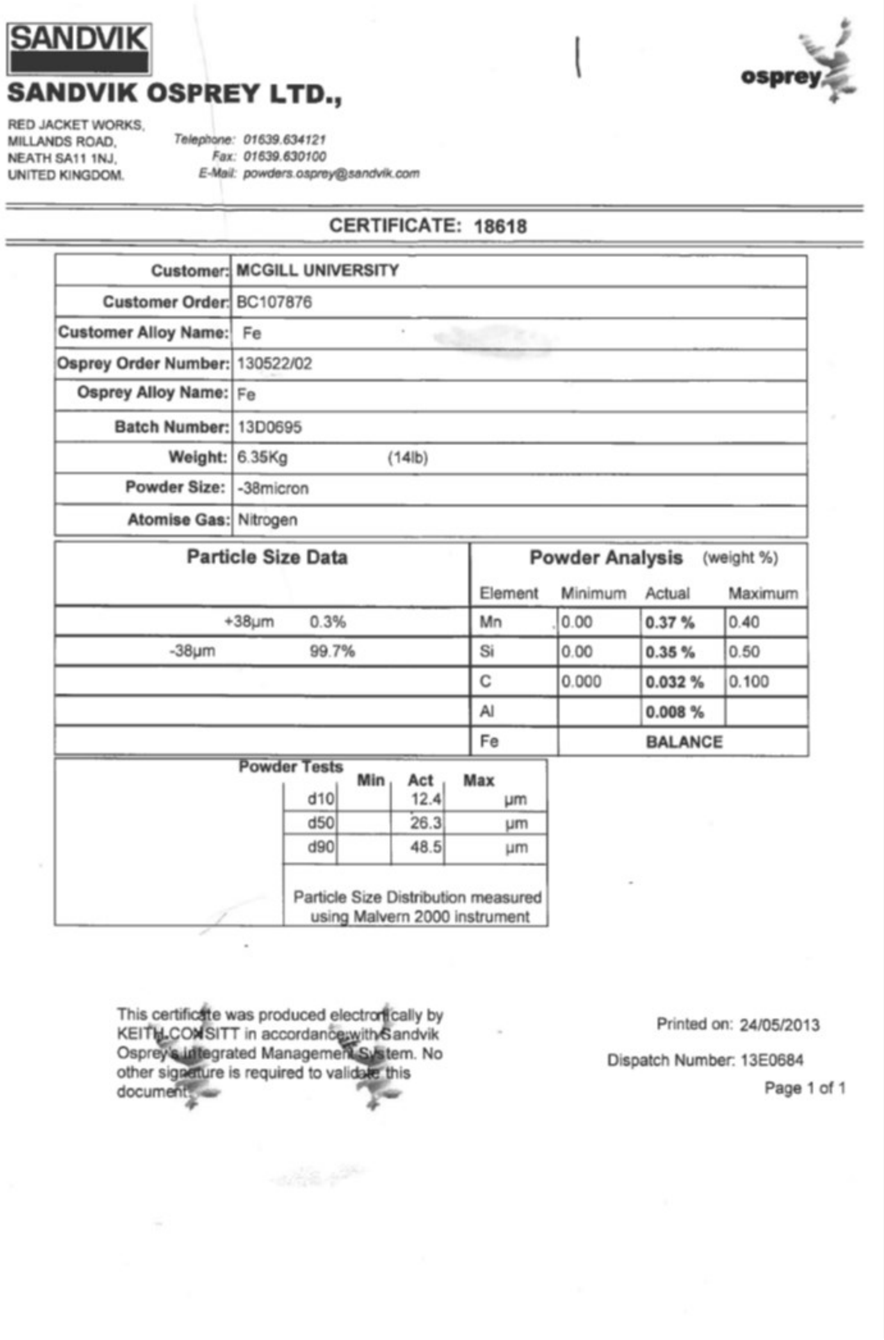

SANDVIK

SANDVIK OSPREY LTD.,

RED JACKET WORKS,
MILLANDS ROAD,
NEATH SA11 1NJ,
UNITED KINGDOM.

Telephone: 01639.634121
Fax: 01639.630100
E-Mail: powders.osprey@sandvik.com

osprey

CERTIFICATE: 18618

Customer:	**MCGILL UNIVERSITY**
Customer Order:	BC107876
Customer Alloy Name:	Fe
Osprey Order Number:	130522/02
Osprey Alloy Name:	Fe
Batch Number:	13D0695
Weight:	6.35Kg (14lb)
Powder Size:	-38micron
Atomise Gas:	Nitrogen

Particle Size Data

+38µm	0.3%
-38µm	99.7%

Powder Analysis (weight %)

Element	Minimum	Actual	Maximum
Mn	0.00	**0.37 %**	0.40
Si	0.00	**0.35 %**	0.50
C	0.000	**0.032 %**	0.100
Al		**0.008 %**	
Fe		**BALANCE**	

Powder Tests

	Min	Act	Max
d10		12.4	µm
d50		26.3	µm
d90		48.5	µm

Particle Size Distribution measured using Malvern 2000 instrument

This certificate was produced electronically by KEITH CONSITT in accordance with Sandvik Osprey's Integrated Management System. No other signature is required to validate this document.

Printed on: 24/05/2013

Dispatch Number: 13E0684

Page 1 of 1

Appendix D

Manufacturer’s specification sheet of 316L and CP Fe powders of lot 3 (2014):

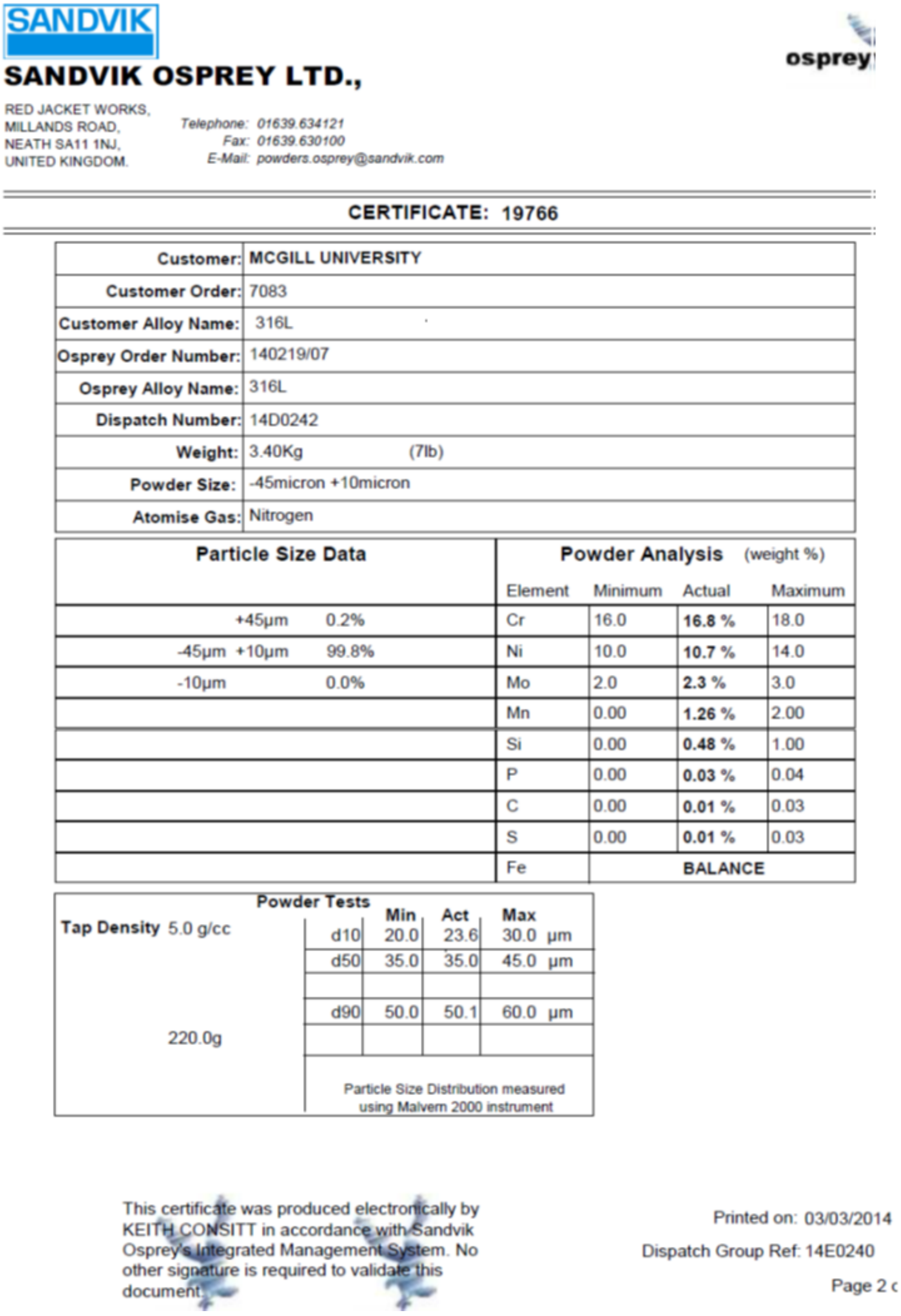

SANDVIK

SANDVIK OSPREY LTD.,

osprey

RED JACKET WORKS,
MILLANDS ROAD,
NEATH SA11 1NJ,
UNITED KINGDOM.

Telephone: 01639.634121
Fax: 01639.630100
E-Mail: powders.osprey@sandvik.com

CERTIFICATE: 19766

Customer:	**MCGILL UNIVERSITY**
Customer Order:	7083
Customer Alloy Name:	316L
Osprey Order Number:	140219/07
Osprey Alloy Name:	316L
Dispatch Number:	14D0242
Weight:	3.40Kg (7lb)
Powder Size:	-45micron +10micron
Atomise Gas:	Nitrogen

Particle Size Data		**Powder Analysis** (weight %)			
		Element	Minimum	Actual	Maximum
+45µm	0.2%	Cr	16.0	**16.8 %**	18.0
-45µm +10µm	99.8%	Ni	10.0	**10.7 %**	14.0
-10µm	0.0%	Mo	2.0	**2.3 %**	3.0
		Mn	0.00	**1.26 %**	2.00
		Si	0.00	**0.48 %**	1.00
		P	0.00	**0.03 %**	0.04
		C	0.00	**0.01 %**	0.03
		S	0.00	**0.01 %**	0.03
		Fe		**BALANCE**	

Powder Tests

Tap Density 5.0 g/cc

220.0g

	Min	**Act**	**Max**
d10	20.0	23.6	30.0 µm
d50	35.0	35.0	45.0 µm
d90	50.0	50.1	60.0 µm

Particle Size Distribution measured using Malvern 2000 instrument

This certificate was produced electronically by KEITH CONSITT in accordance with Sandvik Osprey's Integrated Management System. No other signature is required to validate this document.

Printed on: 03/03/2014
Dispatch Group Ref: 14E0240
Page 2 c

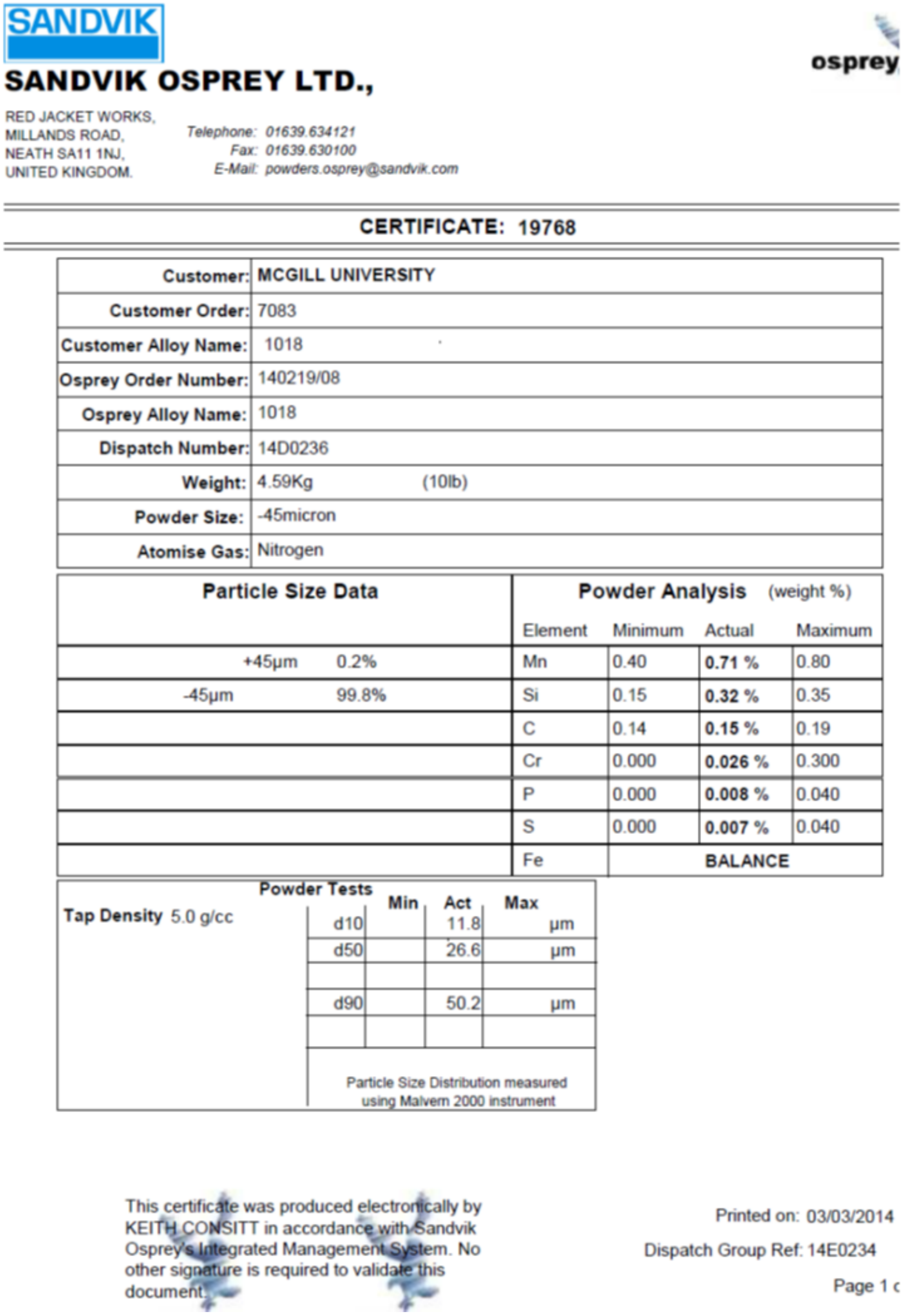

SANDVIK

SANDVIK OSPREY LTD.,

osprey

RED JACKET WORKS,
MILLANDS ROAD,
NEATH SA11 1NJ,
UNITED KINGDOM.

Telephone: 01639.634121
Fax: 01639.630100
E-Mail: powders.osprey@sandvik.com

CERTIFICATE: 19768

Customer:	**MCGILL UNIVERSITY**
Customer Order:	7083
Customer Alloy Name:	1018
Osprey Order Number:	140219/08
Osprey Alloy Name:	1018
Dispatch Number:	14D0236
Weight:	4.59Kg (10lb)
Powder Size:	-45micron
Atomise Gas:	Nitrogen

Particle Size Data

+45µm	0.2%
-45µm	99.8%

Powder Analysis (weight %)

Element	Minimum	Actual	Maximum
Mn	0.40	**0.71 %**	0.80
Si	0.15	**0.32 %**	0.35
C	0.14	**0.15 %**	0.19
Cr	0.000	**0.026 %**	0.300
P	0.000	**0.008 %**	0.040
S	0.000	**0.007 %**	0.040
Fe		**BALANCE**	

Powder Tests

Tap Density 5.0 g/cc

	Min	Act	Max
d10		11.8	µm
d50		26.6	µm
d90		50.2	µm

Particle Size Distribution measured using Malvern 2000 instrument

This certificate was produced electronically by KEITH CONSITT in accordance with Sandvik Osprey's Integrated Management System. No other signature is required to validate this document.

Printed on: 03/03/2014

Dispatch Group Ref: 14E0234

Page 1 c

Appendix E

Manufacturer's specification sheet of Hank's physiological solution:

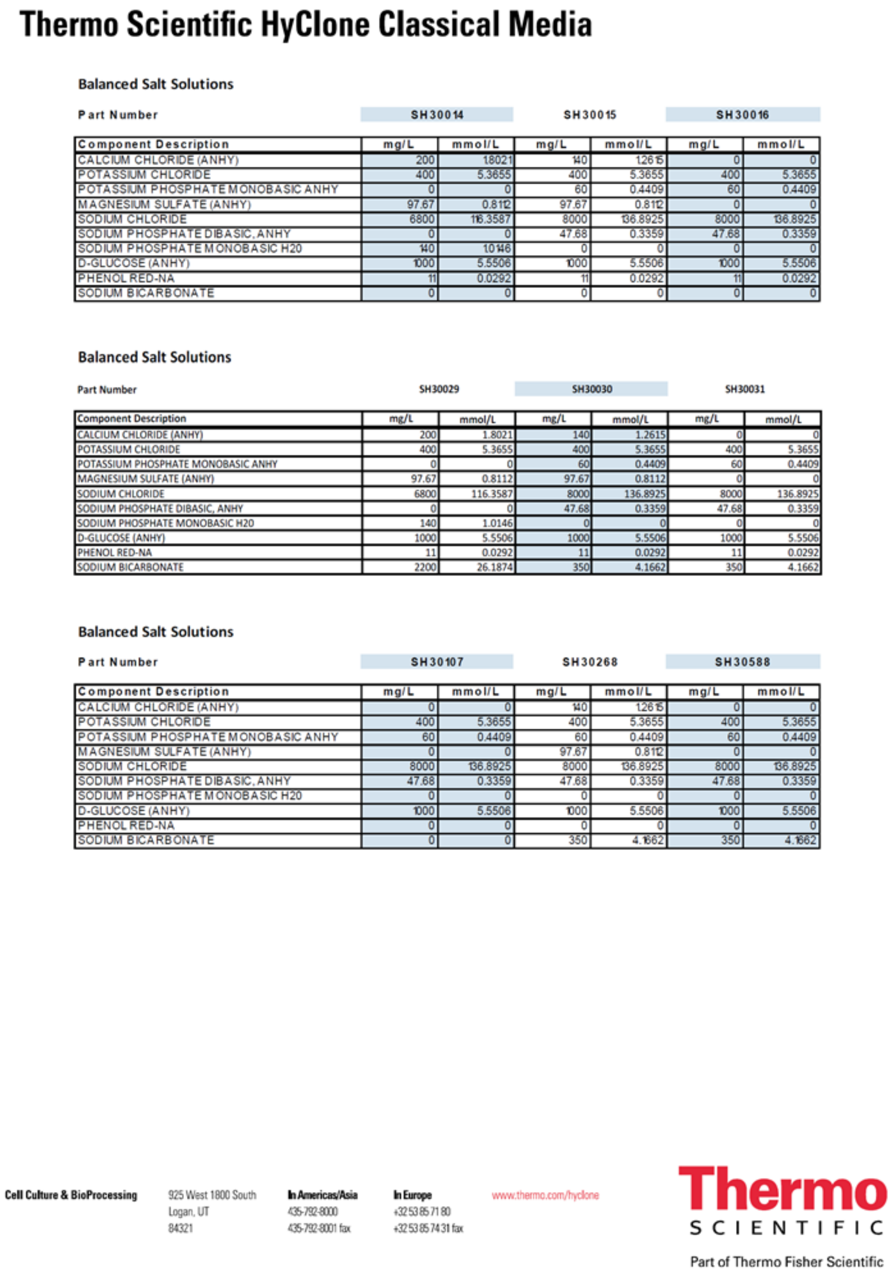

Thermo Scientific HyClone Classical Media

Balanced Salt Solutions

Part Number	SH30014		SH30015		SH30016	
Component Description	**mg/L**	**mmol/L**	**mg/L**	**mmol/L**	**mg/L**	**mmol/L**
CALCIUM CHLORIDE (ANHY)	200	1.8021	140	1.2615	0	0
POTASSIUM CHLORIDE	400	5.3655	400	5.3655	400	5.3655
POTASSIUM PHOSPHATE MONOBASIC ANHY	0	0	60	0.4409	60	0.4409
MAGNESIUM SULFATE (ANHY)	97.67	0.8112	97.67	0.8112	0	0
SODIUM CHLORIDE	6800	116.3587	8000	136.8925	8000	136.8925
SODIUM PHOSPHATE DIBASIC, ANHY	0	0	47.68	0.3359	47.68	0.3359
SODIUM PHOSPHATE MONOBASIC H20	140	1.0146	0	0	0	0
D-GLUCOSE (ANHY)	1000	5.5506	1000	5.5506	1000	5.5506
PHENOL RED-NA	11	0.0292	11	0.0292	11	0.0292
SODIUM BICARBONATE	0	0	0	0	0	0

Balanced Salt Solutions

Part Number	SH30029		SH30030		SH30031	
Component Description	**mg/L**	**mmol/L**	**mg/L**	**mmol/L**	**mg/L**	**mmol/L**
CALCIUM CHLORIDE (ANHY)	200	1.8021	140	1.2615	0	0
POTASSIUM CHLORIDE	400	5.3655	400	5.3655	400	5.3655
POTASSIUM PHOSPHATE MONOBASIC ANHY	0	0	60	0.4409	60	0.4409
MAGNESIUM SULFATE (ANHY)	97.67	0.8112	97.67	0.8112	0	0
SODIUM CHLORIDE	6800	116.3587	8000	136.8925	8000	136.8925
SODIUM PHOSPHATE DIBASIC, ANHY	0	0	47.68	0.3359	47.68	0.3359
SODIUM PHOSPHATE MONOBASIC H20	140	1.0146	0	0	0	0
D-GLUCOSE (ANHY)	1000	5.5506	1000	5.5506	1000	5.5506
PHENOL RED-NA	11	0.0292	11	0.0292	11	0.0292
SODIUM BICARBONATE	2200	26.1874	350	4.1662	350	4.1662

Balanced Salt Solutions

Part Number	SH30107		SH30268		SH30588	
Component Description	**mg/L**	**mmol/L**	**mg/L**	**mmol/L**	**mg/L**	**mmol/L**
CALCIUM CHLORIDE (ANHY)	0	0	140	1.2615	0	0
POTASSIUM CHLORIDE	400	5.3655	400	5.3655	400	5.3655
POTASSIUM PHOSPHATE MONOBASIC ANHY	60	0.4409	60	0.4409	60	0.4409
MAGNESIUM SULFATE (ANHY)	0	0	97.67	0.8112	0	0
SODIUM CHLORIDE	8000	136.8925	8000	136.8925	8000	136.8925
SODIUM PHOSPHATE DIBASIC, ANHY	47.68	0.3359	47.68	0.3359	47.68	0.3359
SODIUM PHOSPHATE MONOBASIC H20	0	0	0	0	0	0
D-GLUCOSE (ANHY)	1000	5.5506	1000	5.5506	1000	5.5506
PHENOL RED-NA	0	0	0	0	0	0
SODIUM BICARBONATE	0	0	350	4.1662	350	4.1662

Cell Culture & BioProcessing

925 West 1800 South
Logan, UT
84321

In Americas/Asia
435-792-8000
435-792-8001 fax

In Europe
+32 53 85 71 80
+32 53 85 74 31 fax

www.thermo.com/hyclone

Thermo
SCIENTIFIC
Part of Thermo Fisher Scientific